Measurement cell for sound speed in liquids: Pulse-echo buffer rod method

THESIS FOR THE DEGREE

MASTER OF SCIENCE

IN

MARINE MEASUREMENT SYSTEMS

ACOUSTICS

BY

HANNAH DYVEKE SKOGHEIM BENUS

DEPARTMENT OF PHYSICS AND TECHNOLOGY

UNIVERSITY OF BERGEN

MAY, 2022

Abstract

In the field of instruments for measurements, process monitoring and control, ultrasonic flow meters (USFMs) are one of the fastest-growing technologies [1]. USFMs have been developed for measuring both flow rate and water cut in pipes, including XSENS Flow Solutions' "XACT flow rate and fraction meter for liquids" [2]. Such measurements, with their corresponding uncertainties, are of increasing importance to the oil and gas industry. For correct water cut measurements provided by a USFM, the instrument is dependent on high precision sound velocity measurements of the individual liquid components that constitute the emulsion.

The main objective of this thesis is to develop a measurement cell based on the pulse-echo buffer rod method for high-precision sound velocity measurements with a relative expanded uncertainty of less than 1000 ppm = 0.1% (95% confidence level). Due to the measurement cell's intended use in industrial applications, a number of dimensional and environmental preferences were established in advance by XSENS Flow Solutions [2]. These preferences had to be taken into account when designing the measurement cell, and constrained the possibility of achieving the desired uncertainty in this project.

Several uncertainty sources have been identified during the project. They are a consequence of 1) the dimensional constraints, 2) coherent noise sources due to buffer rods 3) overall uncertainty contributions. A detailed uncertainty budget has been carried out to account for all identified uncertainty contributions, resulting in a relative expanded uncertainty of 2231 ppm at 45.7^oC, primarily due to uncertainty in the sample length.

The constructed measurement cell has been used for sound velocity measurements in distilled water, saline water, and vegetable oil for a temperature span of T = 20^oC to T = 45^oC. Compared to theoretical models, accurate sound velocity measurements were acquired, resulting in deviations as low as 7 ppm for saline water, and 20 ppm for distilled water. An adaptation of Khimunin's diffraction correction model has been introduced in the project for diffraction correction through several mediums. The accurate experimental sound velocity measurements motivated a preliminary analysis of the diffraction correction model through simulations in COMSOL with promising results.

Acknowledgment

The project presented in this master thesis is a cooperation between the University of Bergen and XSENS Flow Solutions. The project started in January 2021, and most of the work was carried out between August 2021 and to end of May 2022.

First and foremost, I would like to thank my supervisor Prof. Per Lunde from the Department of Physics and Technology, and co-supervisor, Tarjei Rommetveit from XSENS Flow Solutions, for taking me on as their master's student. Thank you both for the invaluable help throughout the project, for introducing me to the physics behind acoustics, and for the patience and guidance you have provided along the way. Per Lunde, for introducing me to the theory behind acoustics and inspiring me to learn more. Tarjei Rommetveit, for teaching me how to apply theoretical physics in practice, as a colleague and as a supervisor.

I would further like to thank everyone in the Acoustics group. A special thanks to Eivind Nag Mosland for help with the topic of diffraction correction. The time you set aside for performing simulations and helping me understand the topic has been invaluable. I also want to express my gratitude to Mathias Sæther and Audun Oppedal Pedersen for their assistance and fruitful discussions in the experimental work.

Thanks to the staff at the Mechanical Workshop at the Dept. for Physics and Technology for manufacturing the measurement cell and helping me when problems arose. I also wish to express my gratitude to the Department of Chemistry for setting aside time to teach me about the chemical processes of liquids and providing me with liquid samples. Lastly, thanks to my amazing, wonderful family and friends for the patience, support, and reassuring words throughout the project. My family for always inspiring me to archive my goals, and my friends for all the good memories created throughout my years as a student- none mentioned, none forgotten. You have all made the hard work and long days worthwhile.

Hannah D. S. Benus

Bergen, 05.05.2022

Contents

List of symbols

Symbol	Description	Unit
ν	Poissions ratio	
c_{td}	Theoretical sound velocity in distilled water	m/s
c_{ts}	Theoretical sound velocity in saline water	m/s
t_A	Transit time of the signal reflcted at the buffer/sample interface	s
t_B	Transit time of the signal reflected at the sample/reflector interface	s
Δt	Total transit time, $t_B - t_A$	s
c_s	Experimental sound velocity in liquid sample	m/s
c_b	Compressional sound velocity in Plexiglas buffer	m/s
c_{shear}	Shear sound velocity in Plexiglas buffer	m/s
D	Buffer length at temperature T_0	m
L_0	Sample length at temperature T_0	m
L	Sample length as a function of temperature	m
K_T	Thermal expansion coefficient	
α	Linear thermal expansion coefficient	$^oC^{-1}$
a_{eff}	Effective transducer radius	m
θ_{3dB}	Half power angle	rad
f	Frequency	Hz
ω	Angular frequency	rad/s
k	Wavenumber	m^{-1}
T	Temperature	^oC
P	Pressure	bar
R_i	Pressure reflection coefficient	
T_i	Pressure transmission coefficient	
H^{diff}	Diffraction correction	

Chapter 1

Introduction

1.1 Background and motivation

Acoustic sensors and instruments are getting more advanced and prominent every year. Due to the possibility of non-intrusive testing and monitoring, acoustic sensors play a crucial role in several fields like medical and industrial research, amongst others. Flow measurements, non-destructive testing, seismic surveys, medical ultrasound, and sonars are only some of the applications where new developments are made every year.

In the field of instruments for measurements, process monitoring and control, ultrasonic flow meters (USFMs) are one of the fastest-growing technologies [1]. Due to its non-intrusive and non-invasive nature, as well as its fast response and high accuracy, it is one of the most common flow measurement devices [3]. Ultrasonic flow meters based on transit-time, measure the difference between sound waves sent upstream and downstream in a pipe, which is directly proportional to the sound velocity of the medium in question [4]. This can, in turn, be used to measure the flow rate in pipes. USFMs have further been developed for measuring the water cut in pipes, including XSENS Flow Solutions' "XACT flow rate and fraction meter for liquids" [2]. Such measurements, with their corresponding uncertainties, are of increasing importance to the oil and gas industry.

For suppliers and refineries, the quality of crude oil exchanged is evaluated according to the water cut measurement, thus the fraction of water in crude oil [5]. It is further a critical part of production control and management [5], and the instrument's trustworthiness is hence paramount. For correct water cut measurements provided by a USFM, the instrument is dependent on high precision sound velocity measurements of the individual liquids components that constitute the emulsion.

For water, the temperature and pressure dependency can usually be determined using existing theoretical models, provided that the sound velocity at a specific temperature and salinity can be measured accurately. For crude oils, however, few such models exist, and the models are almost always dependent on the exact composition of the oil in hand [6]. To ensure high accuracy of the water cut measurements, high-precision sound velocity measurements as a function of temperature and pressure are thus needed.

In this work, the pulse-echo buffer rod method will be evaluated and tested as a candidate method for measuring sound velocity in liquids at high precision. The design and measuring method was described by Øyvind Nesse in his dissertation [7] and will be used as a basis throughout the project. The resulting measurement cell will be used by XSENS Flow Solutions [2] as a sound velocity reference base for their patented high precision USFMs.

1.2 Related work

Different ultrasonic systems are widely used in various fields of science and engineering to measure the acoustic properties of liquids and gases. Numerous sources are found on measuring methods applied for measuring acoustic properties and the corresponding accuracy, advantages and limitations. In 1998, a feasibility study was carried out at Christian Michelsen Research [8] prior to developing a method for high-precision sound velocity measurements for natural gas under pressure, which included an extensive review of available literature and available measurement methods. In 2007, Norli [9] introduced an updated literature survey, including a synopsis of [8], to research the exciting sound velocity measurement methods to propose a method for measuring the sound velocity in natural gas under pressure. Although the discussions from the papers above are specified for gases, many of the discussed methods are just as applicable for liquids. This topic is thus a subject of extensive research. It is usually divided into two categories: *resonator methods* which is based on standing waves in cavities, and *transient methods* using transient sound fields to characterise the medium [8, 9]. Under the category of transient methods, the use of a buffer-rod to obtain acoustic properties, as for this project, is a widely discussed approach[10].

Depending on the acoustic property of interest, methods where a buffer-rod is utilised may differ in terms of the shape and composition of the buffer and measurement cell, as well as the amount of transducers used [10]. For amplitude measurements, in relation to the determination of the reflection coefficient and attenuation of the medium in question, a synopsis of buffer-rod techniques can be found in [10] and [11].

The pulse-echo buffer rod method, first introduced by Papadakis et al. [12], is a classic method due to its robustness, simplicity, and low-cost [13]. A sound pulse generated by the transducer propagates through a buffer rod, through the sample liquid and onto a reflector. Some of the sound energy is reflected as echos at the interfaces, and the transit time between the echos can be used to calculate the sound velocity. The principle design is sketched in Fig. 1.1, from [7]. The presence of the buffer rod eliminates any direct contact between the transducer and the liquid sample, thus protecting it from any high pressures and corrosive liquids. It is also a simple and robust design and has no moving parts, which is often preferred. Further, propagation delays in the buffer, coupling agent, and delays due to electrical and mechanical conversions cancel out [8]. Although the design is simple and has no moving parts, problems arise when applying buffer rods. Unwanted echoes due to twice traversed buffer propagation, mode converted waves, and overall reflections from the edges may act as coherent noise. They can overlap with the main echoes, significantly reducing the Signal-to-Noise ratio

(SNR) and the accuracy of the sound velocity measurements. This is reported in several studies using buffer-rods, both for sound velocity measurements [14, 15], and for amplitude measurements [13, 16]. In cases of small dimensions, the most dominating source of uncertainty is, however, often the propagation path since it can be challenging to determine the path length with adequate precision. One established method is to calibrate the propagation path with a known liquid sample [7, 10, 15, 17, 18].

Calibrating the path length was done by McClements and Farley in 1990[19], using the pulse-echo buffer rod method with a Plexiglas buffer and a frequency of 2.1 MHz. They achieved a claimed accuracy of 0.5 m/s using different concentrations of NaCl at 20^oC.

The pulse-echo buffer rod method was further used by Nesse [7] to study the phase velocity and attenuation in several emulsions. Two measurement cells were created, one for low-frequency (250-900 kHz) range and one for high-frequency (1.4-14 MHz) range measurements. The path length was calibrated against a known liquid sample. Diffraction effects were assumed negligible, and a total uncertainty of 1 m/s was reported.

Acquiring high-precision sound velocity measurements without calibrating the measurement cell is considerably more difficult. In 2005, Benedetto et al. [20] created a sound velocity cell based on the double-reflected pulse-echo method, thus a single transducer placed between two parallel reflectors, operating at 5 MHz. By measuring the distance between the transducer and reflectors with a coordinate measuring machine, an overall estimated uncertainty of 0.1% was obtained throughout a temperature span of $0-120^oC$ and for pressures up to 90 MPa.

Solberg [21] created a measurement cell based on the three-way pulse method. The method was proposed by Lunde and Vestrheim [8], and utilises two transducers on either side of a measurement chamber. The sound velocity is obtained by measuring the transit time between the direct propagation and the three times reflected propagation, using the transducers themselves as reflectors. Solberg measured the path length with a caliper and obtained a relative expanded uncertainty of 0.16% (95 % confidence level, k = 2) for tap water at room temperature, using a transducer operating at 500 kHz.

As the measurement cell is to work under the same conditions as the USFM, a frequency range of 200-500 kHz is preferred to account for dispersion effects in crude oils. Most of the reported sound velocity cells operate far outside of this range [15, 17, 19, 22], and many possible design implementations are thus not applicable. For the candidate method, Nesse's low-frequency measurement cell has therefore been used as a tentative design for further development. The design is presented in Fig. 1.1.

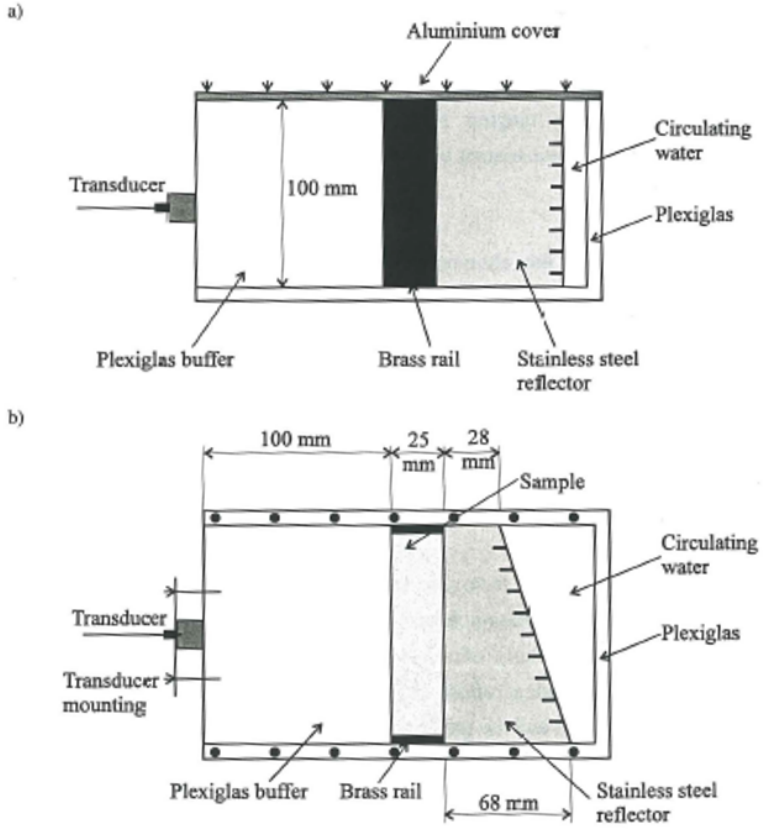

Figure 1.1: Schematic drawing of the measurement cell created in [7] based on the pulse-echo buffer rod method; a) side view b) top view.

1.3 Objective

This project aims to create a measurement cell utilising the pulse-echo buffer rod method to measure the sound velocity in single- and dual-phase liquids with a relative expanded uncertainty (95% confidence level) below 1000ppm as a function of temperature and 1 atm. A documented and traceable uncertainty budget will be carried out by considering and identifying possible uncertainty sources which can affect the total uncertainty of the sound velocity in the liquid medium.

Due to the industrial application of the project, several criteria were set in advance. To account for relevant dispersion effects and attenuation when measuring the sound velocity in castor oils, the preferable operating frequency range was set to 200-500kHz. Further, the measurement cell had to be small, light and easy to transport, and is is to measure single and dual-phase liquids under atmospheric pressure conditions within a temperature span of 20-60^oC. As liquids behave differently upon heating, a sound velocity range of 1250 - 1580 m/s is selected to account for saline water and crude oils at high temperatures. To act as a reference base, it is vital to control and calculate the measurement uncertainty, where a relative expanded uncertainty below 1000ppm = 0.1 % at 95% confidence level is preferred within relevant environmental parameters. Because coherent noise sources may interfere due to the set criteria, two signal processing methods will be evaluated in terms of accu-

racy; the zero-crossing method based on direct transit time measurements and the Fourier spectrum method.

As a long-term goal, this research will lay a foundation for developing high-precision sound velocity cells for measuring single- and dual-phase liquids under high temperature and pressure conditions for industrial applications.

1.4 Thesis outline

This thesis consists of 8 chapters with including appendices. In **Chapter 1**, the motivation of the project, previous work and objective is presented. In **Chapter 2**, the pulse-echo measurement method will be introduces, and theory relevant for the sound velocity measurements will be presented. **Chapter 3** is divided into two parts, where the first part will describe the experimental setup and measurement methods relevant for measuring the sound velocity. The second part contains considerations done prior and the development process toward creating the measurement cell, and will present the final result. **Chapter 4** consists of simulations and numerical analysis, used for accurate determination of the sound velocity. In **Chapter 5**, all relevant uncertainty models for experimental and theoretical sound velocity measurements will be presented, together with a sensitivity analysis. **Chapter 6** will present the experimental results and associated uncertainties when applicable. **Chapter 7** is an overall discussion, and **Chapter 8** draws the conclusion and recommendations for further work. **Appendices** include Matlab scripts, detailed calculations and uncertainty standards.

Chapter 2

Theory

Chapter 2 provides the theoretical background of this work and contains five main sections with subsections. In Section 2.1, a short description of the theoretical sound velocity in different liquid mediums relevant to the project will be presented. Section 2.2 describes the principle of the pulse-echo buffer rod method, and the equation to calculate the sound velocity will be derived in the time and frequency domain. The correction terms needed in the sound velocity calculations are presented in Section 2.3. Beam pattern and transducer radius will be presented in Section 2.4, and in Section 2.5, a model for thermal expansion in the measurement cell will be described.

2.1 Sound velocity

Sound waves can travel through any gases, liquids or solids and will be affected by the medium's physical properties [23]. Some mediums can further be dispersive, where higher frequency waves travel faster than lower frequency waves. A sound wave will thus not retain its initial shape when propagating through a dispersive medium[24]. Three characteristic sound velocities may therefore be defined. The *phase velocity* is the velocity of a mono frequency wave where all points have equal phase [8]. The *group velocity* is the velocity at which an envelope of waves with slightly different frequency propagates [25], and the signal onset can be used to find the *signal velocity* [8].
Suppose the sound velocity is to be calculated in a dispersive medium. In that case, the phase velocity at the carrier frequency is generally desired, which is found by measuring the stationary part of the signal [8]. If the media is independent of frequency, thus nondispersive, the signal, phase, and group velocities are all equal [8].

Sound velocity in solids can further be separated into compressional and shear waves. In compressional waves, particle displacement is parallel to the direction of the wavefront, while shear waves have a particle displacement perpendicular to the wavefront [23]. Shear waves, in contrast to compressional waves, can only exist in solids [23]. The relationship between shear and compressional waves in solid material can be expressed through Poisson's ratio, ν, given as [26]

$$\nu = \frac{1}{2} \cdot \frac{\left(\frac{c_c}{c_{shear}}\right)^2 - 2}{\left(\frac{c_c}{c_{shear}}\right)^2 - 1}, \tag{2.1}$$

where c_c and c_{shear} are the compressional and shear sound velocities, respectively.

This project aims to calculate the compressional sound velocity in single and dual-phase liquids under different temperature conditions. It is thus necessary to be able to verify the results and compare the results with theoretical models. A short description of the sound velocity in water is thus presented in the following.

2.1.1 Sound velocity in water

The sound velocity in water is mainly dependent on temperature, salinity and pressure. During this project, distilled water will be used as a reference medium. This being non-saline water and a non-dispersive medium, the sound velocity will only be dependent on temperature and pressure. As a result, a simplified expression provided by Kinsler et al. [23] for calculating sound velocity in distilled water will be adapted in this project. The equation is given as

$$c_{td} = 1402.7 + 488\frac{T}{100} - 482\left(\frac{T}{100}\right)^2 + 135\left(\frac{T}{100}\right)^3 + \left(15.9 + 2.8 \cdot \frac{T}{100} + 2.4\left(\frac{T}{100}\right)^2\right) \cdot \frac{P_G}{100}, \tag{2.2}$$

where c_{td} is the theoretical sound velocity in distilled water (subscript td for theoretical, distilled). The temperature T is given in ^oC and P_G is the gauge pressure in bar [27],

$$P_G = P - P_{atm} = P_M - \rho_w g h, \tag{2.3}$$

where P_M is the measured ambient pressure, $\rho_w g h$ is the hydrostatic pressure, and $P_{atm} \equiv 1.01325$ bar is the standard atmospheric pressure [27]. Eq. (2.2) has an uncertainty of 0.05% (500ppm) for $0 < T < 100^oC$ and $0 < P_G < 200$ bar [23]. No confidence level is provided, and a confidence level of 95% is thus assumed. The density of distilled water, ρ_w

The density of pure water, ρ_w, as a function of temperature can be expressed by the Kell formulation [28]. In this project, however, the density is set to constant $\rho_w = 998 kg/m^3$, corresponding to density in water at 20^oC [28]. The change in sound velocity due to a change in density is assumed negligible, which is calculated to be a valid assumption in Section 6.1.3.

Generally, sound velocity in saline water increases with increased salinity [23]. Several theoretical equations exist for calculating the sound velocity in saline water, where common ones are the ones often referred to as the UNESCO equation [29] and the Del Grosso equation[30]. The equations, however, have different ranges of validity. Only the UNESCO equation will be adequate within the operating range for both salinity and temperature in this project. It has a temperature range of $0 - 40^oC$, a salinity range of 0-40 ppt (parts per thousand), and a 0 to 1000 bar pressure range [31]. Due to concerns regarding the validity of the UNESCO equation with distilled water [32], the equation has not

been used for the distilled water measurements.
The original UNESCO algorithm was formulated by Chen and Millero [29] but was later recalculated by Wong and Zu [31] following the adoption of the International Temperature Scale of 1990[33]. Their form of the UNESCO equation will be used in this project, given as

$$c_{ts}(S,T,P) = Cw(T,P) + A(T,P)\cdot S + B(T,P)\cdot S^{3/2} + D(T,P)\cdot S^2, \tag{2.4}$$

where c_{ts} is theoretical sound velocity in saline water (subscript ts for theoretical, saline), S is salinity given in parts per thousand (ppt), T is temperature in ^oC, and P = $P_M + \rho_s gd$ is the measured pressure added with the hydrostatic pressure in bar. Cw(T, P), A(T, P), B(T, P) and D(T, P) are different expressions, together containing 42 different numerical values. The remainder of the equation is therefore presented in Appendix B.

An uncertainty in the model itself has been hard to find, but following the article of Leroy et. al. [32], it is set to be 0.15 m/s. The confidence level is not stated, and is thus assumed 68% as it is based on experimental measurements.

The density of saline water, ρ_s is a function of temperature, salinity, and ρ_w [34]. In this project, the density is set to constant $\rho_s = 1013.2 kg/m^3$, which in Section 6.1.3 is shown to be a valid assumption.

2.2 Pulse-echo buffer rod measurement method

2.2.1 Principle of the pulse-echo buffer rod method

The principle of the pulse-echo buffer rod method is shown in Fig. 2.1. A transducer, acting as both a transmitter and a receiver, sends out an acoustic signal which propagates through a solid buffer. At the buffer/sample interface, the signal is partially reflected and partially transmitted. The transducer acquires the reflected part of the acoustic signal, now acting as a receiver, and yields the *first echo*. The transmitted part of the signal propagates through the sample before it is reflected at the sample/reflector interface. It then propagates back to the transducer, yielding the *second echo*. The first and second echo will in the following be named Signal A = S_A and Signal B = S_B respectively.

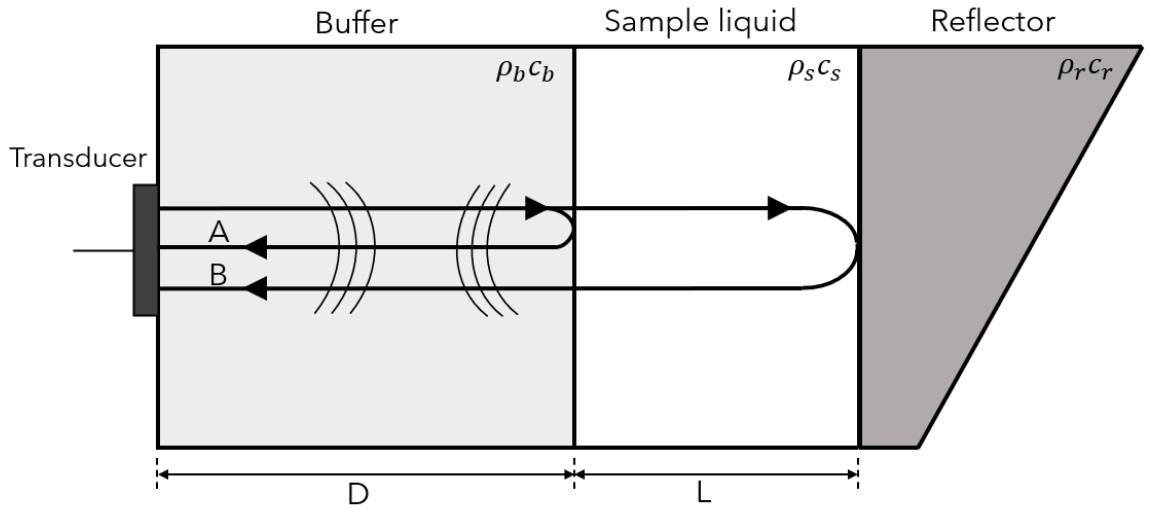

Figure 2.1: Illustration of the principle of the pulse-echo buffer rod method.

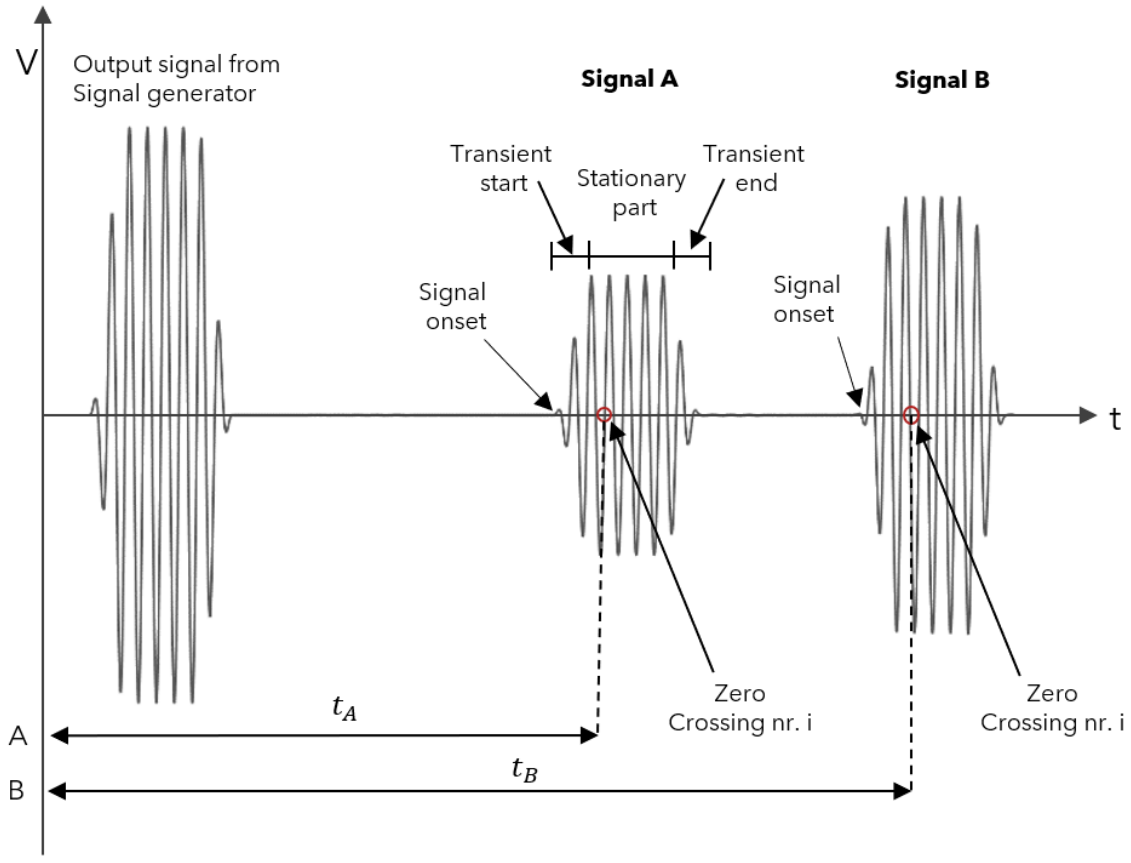

Figure 2.2: Schematic illustration of Signal A and B, used for transit time determination, together with identification of different parts of the pulse. Illustration inspired by [8].

2.2.2 Sound velocity in time domain

The sound velocity can be found by measuring the two-way transit time in the sample liquid. Fig. 2.3 shows the system setup of the measurement cell. This system setup will be used to derive an equation for the sound velocity in the time domain. A similar approach was presented in Lunde and Vestrheim's feasibility study [8]. Their notations will be applied here, adjusted to the measurement setup used in this project.
A set of idealized assumptions will be used to develop the model, such as negligible phase shifts upon reflection at the buffer/liquid interface and liquid/reflector interface due to plane wave propagation [8]. The noise due to electronic switching when switching between transmitter and receiver is also assumed negligible.

It will be shown in the following that t_j in the system model presented in Fig. 2.3 corresponds to the total transit time, where subscript j = A, B denote the transit time for Signal A and Signal B (cf. Fig.2.1).

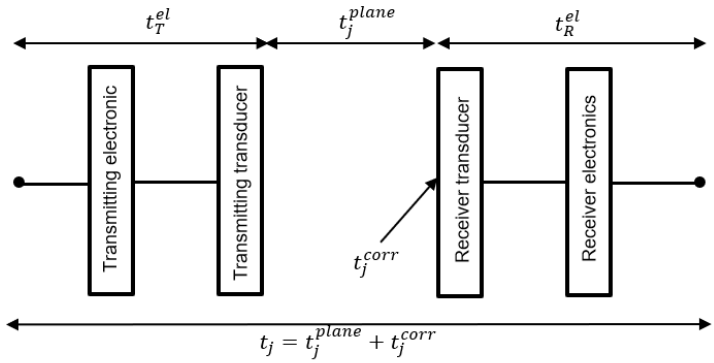

Figure 2.3: System model of the experimental setup. Illustration inspired by [8].

The signal generator and the transmitting electronics excites the transmitting transducer with a voltage pulse. This pulse is converted to particle velocity which propagates through the buffer where the pulse is partially reflected and partially transmitted, shown in Fig. 2.1.

The reflected pulse at the buffer/sample interface, propagates back to the transducer where it is converted to a voltage pulse by the transducer. The voltage pulse is sent through the receiving electronics and is detected by the oscilloscope. The received pulse, shown as Signal A in Fig. 2.2, can then be used to calculate the transit time of Signal A, t_A, by measuring zero-crossing number i in a characteristic part of the pulse. The characteristic part can either be the signal onset, the transient part or stationary part, cf. Fig. 2.2. The measured transit time of zero-crossing number i for signal A, t_A, can thus be expressed as

$$t_A = 2 \cdot t_{plane}^{buffer} + t_A^{corr}, \tag{2.5}$$

where t_{plane}^{buffer} is the plane wave travel time through the buffer with length D, and

$$t_A^{corr} = t^{el,T} + t^{el,R} + t_A^{rem}. \tag{2.6}$$

In equation 2.6,

- $t^{el,T}$ = travel time through transmitting cables, T/R-switch and transmitting transducer,
- $t^{el,R}$ = travel time through receiving cables, T/R-switch and receiving transducer,
- t_A^{rem} = travel time of t_A due to remaining effects not included in $t^{el,T}$ or $t^{el,R}$, further explained in Section 2.3.

The transmitted pulse at the buffer/sample interface, propagates through the sample liquid and is reflected at the reflector. It then propagates back to the transducer where it is converted to a voltage pulse. The voltage pulse is then sent through the receiving electronics and is detected by the oscilloscope as signal B in Fig. 2.2. The measured transit time of zero-crossing number i for Signal B, t_B, can thus be expressed as

$$t_B = 2 \cdot t_{plane}^{buffer} + 2 \cdot t_{plane}^{sample} + t_B^{corr}, \tag{2.7}$$

where t_{plane}^{sample} is the plane wave travel time through the liquid sample with length L, and

$$t_B^{corr} = t^{el,T} + t^{el,R} + t_B^{rem}. \tag{2.8}$$

In Eq. (2.8), t_B^{rem} is the travel time in t_B due to remaining effects not included in $t^{el,T}$ or $t^{el,R}$. These effects will be explained in Section 2.3. Time delays due to the transmitting and receiving electronics and transducer, $t^{el,T}$ and $t^{el,R}$ can be assumed to be the same for t_A and t_B [35].

The difference in arrival between Signal A and Signal B, defined Δt, can be expressed as

$$\Delta t = t_B - t_A. \tag{2.9}$$

Inserting Eqs. (2.5) and (2.7) into Eq. (2.9) yields

$$\Delta t = 2 \cdot t_{plane}^{sample} + t_B^{corr} - t_A^{corr}. \tag{2.10}$$

By inserting for the correction factors, Eqs. (2.6) and (2.8), into Eq. (2.10), Δt can be expressed as

$$\Delta t = 2 \cdot t_{plane}^{sample} + t_B^{rem} - t_A^{rem}. \tag{2.11}$$

Since

$$t_{plane}^{sample} = \frac{L}{c_s}, \tag{2.12}$$

where $L = L_0 \cdot K_T$ is the sample length as a function of temperature, with L_0 equal to the sample length at T_0, and K_T the thermal expansion of the sample area, the sound velocity in the liquid sample, c_s,

can be found using Eqs. (2.11) and (2.12) as

$$c_s = \frac{2L}{\Delta t - \Delta t^{rem}}, \tag{2.13}$$

where

$$\Delta t^{rem} = t_B^{rem} - t_A^{rem}. \tag{2.14}$$

The change in propagation length, L, due to thermal expansion will be treated in Section 2.5.

2.2.3 Sound velocity in frequency domain

A short burst may be favourable when one wants to avoid coherent noise contributions. Although the sound velocity can be calculated with the time-domain model using a short burst by measuring the signal onset or the transient part of the signal (cf. Fig. 2.2), the accuracy of the sound velocity calculations with direct transit time measurements can be limited if the signal does not have a steady-state region [36, 37].
Therefore, an alternative method will be presented based on finding the group velocity of the pulse in the frequency domain. The model is based on the work in Sæther's dissertation [14] and will be adapted to the current project.

In this method, the propagation will be described with a plane wave propagation and a diffraction term, thus a correction due to the assumption of plane wave propagation. It is thus assumed that phase delays due to other sources than transmitting and receiving electronics, defined Δt^{rem} in time-domain calculations, only consist of diffraction correction. In Section 2.3, this is explained in detail and shown to be a valid assumption.
The on-axis propagation is defined along the sound-axis of the transducer, thus the z-axis shown in Fig. 2.4.

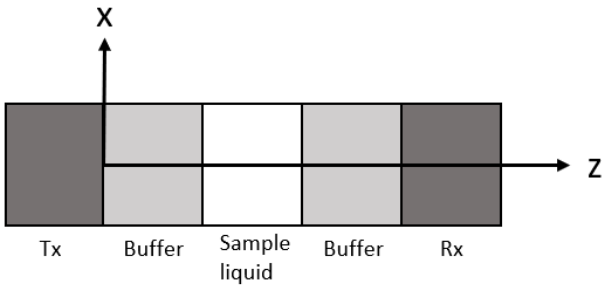

Figure 2.4: Direction of propagation in the system model, here shown for Signal B. Tx = Rx is the transducer, acting as both the transmitter and receiver. Illustration inspired by [14].

From Fig. 2.1, a system model can be set up for both Signal A and Signal B in the frequency domain, presented as a block diagram in Fig. 2.5. Each block represents the transfer function of a component in the measurement setup shown in Fig. 2.3. Between each block is a node, and either a voltage V, on-axis particle velocity v, or the on-axis sound pressure p is defined at each node[14]. The variables

are labelled with a number after the order in the system they appear, together with either letter A or B, corresponding to Signal A and Signal B, respectively. All variables are presented in the frequency domain.

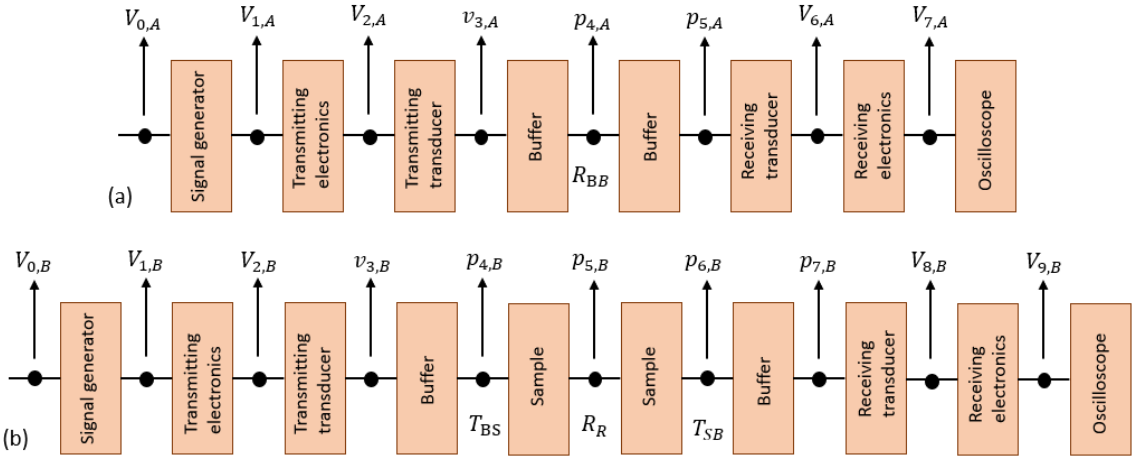

Figure 2.5: System model of the pulse-echo buffer rod method presented as a block diagram where a) Signal A and b) Signal B. Illustration inspired by [14].

For Signal A, Fig. 2.5a), the voltage signal in on the signal generator, transmitting electronics and transmitting transducer are denoted $V_{0,A}$, $V_{1,A}$ and $V_{2,A}$ respectively, where the transmitting electronics include T/R-switch and coaxial cables. The signal generator's emf is assumed to be the same as the input voltage signal[14].

The particle velocity at the transducer's front surface, acting as a transmitter, is denoted $v_{3,A}$, $p_{4,A}$ is the on-axis sound pressure at the buffer/sample interface and $p_{5,A}$ is the free-field pressure at the transducer's front surface, acting as a receiver, in the absence of the transducer. $V_{6,A}$ and $V_{7,A}$ are the pressure-wave induced input voltages on the receiving electronics and the oscilloscope, where the receiving electronics are the cables and T/R-switch. R_{BB} is the plane wave pressure reflection coefficient at the buffer/sample interface, [23]

$$R_{BB} = \frac{\rho_s c_s - \rho_b c_b}{\rho_s c_s + \rho_b c_b}, \tag{2.15}$$

where ρ_b is the density in the buffer, ρ_s is the sample's density, and c_b and c_s are the compressional sound velocities in the buffer and sample respectively.

Using Fig. 2.5, the transfer function for Signal A can be written

$$\frac{V_{7,A}}{V_{0,A}} = \frac{V_{1,A}}{V_{0,A}} \cdot \frac{V_{2,A}}{V_{1,A}} \cdot \frac{v_{3,A}}{V_{2,A}} \cdot \frac{p_{4,A}}{v_{3,A}} \cdot \frac{p_{5,A}}{p_{4,A}} \cdot \frac{V_{6,A}}{p_{5,A}} \cdot \frac{V_{7,A}}{V_{6,A}}. \tag{2.16}$$

Diffraction correction for Signal A can be expressed as [38]

$$H_A^{\text{diff}} = \frac{\langle p_{5,A} \rangle}{p_{5,A}^{pl}}, \tag{2.17}$$

where $\langle p_{5,A} \rangle$ is the average pressure over a "measurement area" equal to the transducer surface at distance d = 2D, and $p_{5,A}^{pl}$ is plane wave pressure at the same distance[1] ,

$$p_{5,A}^{pl} = v_{3,A} \cdot \rho_b c_b \cdot e^{-i2k_b D} \cdot R_{BB}, \tag{2.18}$$

assuming no unwanted reflections. In Eq. (2.18), D is the buffer length and $k_b = \omega / c_b$ is the buffer wave number with c_b equal to the buffer sound velocity, $\omega = 2\pi f$, where f is the frequency. Eq. (2.16) can thus be expressed as:

$$\frac{V_{7,A}}{V_{0,A}} = \frac{V_{1,A}}{V_{0,A}} \cdot \frac{V_{2,A}}{V_{1,A}} \cdot \frac{v_{3,A}}{V_{2,A}} \cdot \rho_b c_b \cdot e^{-i2k_b D} \cdot R_{BB} \cdot \frac{\langle p_{5,A} \rangle}{p_{5,A}^{pl}} \cdot \frac{V_{6,A}}{\langle p_{5,A} \rangle} \cdot \frac{V_{7,A}}{V_{6,A}}. \tag{2.19}$$

For Signal B, Fig. 2.5b), $V_{0,B}$, $V_{1,B}$ and $V_{2,B}$ are the voltage signal on the signal generator, transmitting electronics and transmitting transducer respectively. The signal generator's emf is assumed to be the same as the input voltage signal [14]. The transmitting electronics include the coaxial cables and the T/R-switch. Further, $v_{3,B}$ is the particle velocity at the transducer's front surface, acting as a transmitter. The on-axis sound pressure at the buffer/sample interface, the sample/reflector interface and the sample/buffer interface are denoted $p_{4,B}$, $p_{5,B}$ and $p_{6,B}$ respectively. $p_{7,B}$ is the free-field pressure at the transducer's front surface, acting as a receiver, in the absence of the transducer. The pressure-wave induced input voltage on the receiving electronics is denoted $V_{8,B}$, and $V_{9,B}$ is the input voltage on the oscilloscope. With normal incidence, the plane wave pressure transmission coefficients from the buffer into the sample, T_{BS}, and from the sample into the buffer, T_{SB}, are given as [23]

$$T_{BS} = \frac{2\rho_s c_s}{\rho_s c_s + \rho_b c_b}, \qquad T_{SB} = \frac{2\rho_b c_b}{\rho_s c_s + \rho_b c_b}. \tag{2.20}$$

The plane wave pressure reflection coefficient at the reflector, R_R, can further be expressed as

$$R_R = \frac{\rho_r c_r - \rho_s c_s}{\rho_r c_r + \rho_s c_s}, \tag{2.21}$$

where ρ_r is the density, and c_r is the compressional sound velocity of the reflector.

As for Signal A, the transfer function for Signal B can be written

$$\frac{V_{9,B}}{V_{0,B}} = \frac{V_{1,B}}{V_{0,B}} \cdot \frac{V_{2,B}}{V_{1,B}} \cdot \frac{v_{3,B}}{V_{2,B}} \cdot \frac{p_{4,B}}{v_{3,B}} \cdot \frac{p_{5,B}}{p_{4,B}} \cdot \frac{p_{6,B}}{p_{5,B}} \cdot \frac{p_{7,B}}{p_{6,B}} \cdot \frac{V_{8,B}}{p_{7,B}} \cdot \frac{V_{9,B}}{V_{8,B}}. \tag{2.22}$$

The diffraction correction for signal B can be written as [23]

$$H_B^{\text{diff}} = \frac{\langle p_{7,B} \rangle}{p_{7,B}^{pl}}, \tag{2.23}$$

where $\langle p_{7,B} \rangle$ is the average pressure over a "measurement area" equal to the transducer surface at

[1] Section 2.3.1 will introduce diffraction correction and provide a more detailed explanation.

distance d = 2D + 2L, and $p_{7,B}^{pl}$ is the plane wave propagation at the same distance,

$$p_{7,B}^{pl} = v_{3,B} \cdot \rho_b c_b \cdot e^{-i2k_b D} \cdot T_{BS} \cdot T_{SB} \cdot e^{-i2k_s L} \cdot R_R, \tag{2.24}$$

assuming no unwanted reflection. Further, $k_s = \omega / c_s$ is the sample wave number, and L is the sample length as a function of temperature, i.e. $L = L_0 \cdot K_T$. Eq. (2.22) can thus be expressed as

$$\frac{V_{9,B}}{V_{0,B}} = \frac{V_{1,B}}{V_{0,B}} \cdot \frac{V_{2,B}}{V_{1,B}} \cdot \frac{v_{3,B}}{V_{2,B}} \cdot \rho_b c_b \cdot e^{-i2k_b D} \cdot T_{BS} \cdot T_{SB} \cdot e^{-i2k_s L} \cdot R_R \cdot \frac{\langle p_{7,B} \rangle}{p_{7,B}^{pl}} \cdot \frac{V_{8,B}}{\langle p_{7,B} \rangle} \cdot \frac{V_{9,B}}{V_{8,B}}. \tag{2.25}$$

By dividing Eq. (2.25) with Eq. (2.19), the following expression is obtained:

$$\frac{\frac{V_{9,B}}{V_{0,B}}}{\frac{V_{7,A}}{V_{0,A}}} = \frac{\frac{V_{1,B}}{V_{0,B}} \cdot \frac{V_{2,B}}{V_{1,B}} \cdot \frac{v_{3,B}}{V_{2,B}} \rho_b c_b e^{-i2k_b D} T_{BS} T_{SB} e^{-i2k_s L} R_R \cdot \frac{\langle p_{7,B} \rangle}{p_{7,B}^{pl}} \cdot \frac{V_{8,B}}{\langle p_{7,B} \rangle} \cdot \frac{V_{9,B}}{V_{8,B}}}{\frac{V_{1,A}}{V_{0,A}} \cdot \frac{V_{2,A}}{V_{1,A}} \cdot \frac{v_{3,A}}{V_{2,A}} \cdot \rho_b c_b \cdot e^{-i2k_b D} \cdot R_{BB} \cdot \frac{\langle p_{5,A} \rangle}{p_{5,A}^{pl}} \cdot \frac{V_{6,A}}{\langle p_{5,A} \rangle} \cdot \frac{V_{7,A}}{V_{6,A}}}. \tag{2.26}$$

One can further assume that $\frac{V_{1,B}}{V_{0,B}} = \frac{V_{1,A}}{V_{0,A}}$, $\frac{V_{2,B}}{V_{1,B}} = \frac{V_{2,A}}{V_{1,A}}$, $\frac{v_{3,B}}{V_{2,B}} = \frac{v_{3,A}}{V_{2,A}}$, $\frac{V_{9,B}}{V_{8,B}} = \frac{V_{7,A}}{V_{6,A}}$, $\frac{V_{8,B}}{\langle p_{7,B} \rangle} = \frac{V_{6,A}}{\langle p_{5,A} \rangle}$ and $V_{0,A} = V_{0,B}$. Eq. (2.26) thus reduces to:

$$\frac{V_{9,B}}{V_{7,A}} = \frac{T_{BS} \cdot T_{SB} \cdot e^{-i2k_s L_0} \cdot R_R \cdot \frac{\langle p_{7,B} \rangle}{p_{7,B}^{pl}}}{R_{BB} \cdot \frac{\langle p_{5,A} \rangle}{p_{5,A}^{pl}}} = \frac{T_{BS} \cdot T_{SB} \cdot e^{-i2k_s L} \cdot R_R \cdot H_B^{diff}}{R_{BB} \cdot H_A^{diff}}. \tag{2.27}$$

To find the speed of sound of the sample, one has to find the phase of Eq. 2.27

$$\angle \left(\frac{V_{9,B}}{V_{7,A}} \right) = \angle \left(\frac{T_{BS} T_{SB} e^{-i2k_s L} R_R H_B^{diff}}{R_{BB} H_A^{diff}} \right) \tag{2.28}$$

Phase shifts upon reflection and transmission can be neglected due to plane wave propagation[8]. Eq. (2.28) thus reduces to

$$\angle \left(V_{9,B} \right) - \angle \left(V_{7,A} \right) = \angle \left(H_B^{diff} \right) - \angle \left(H_A^{diff} \right) - 2k_s L. \tag{2.29}$$

Applying Eq. (2.12), and knowing that $k_s = \omega / c_s$, an expression for c_s can be found through Eq. (2.29):

$$c_s = \frac{2L}{\left(\frac{\angle (V_{7,1})}{\omega} - \frac{\angle (V_{9,2})}{\omega} + \frac{\angle \left(H_B^{diff} \right)}{\omega} - \frac{\angle \left(H_A^{diff} \right)}{\omega} \right)}. \tag{2.30}$$

In Section 3.4.3, Eq. (2.30) will be used to calculate the sound velocity using the Fourier spectrum method.

To simplify Eq. (2.30), it is shown in [39] that one can define $t_A \equiv -\angle \left(V_{7,A} \right) / \omega$, $t_B \equiv -\angle \left(V_{9,B} \right) / \omega$, $t_A^{diff} \equiv -\angle \left(H_A^{diff} \right) / \omega$ and $t_B^{diff} \equiv -\angle \left(H_B^{diff} \right) / \omega$. Eq. (2.30) can thus be expressed in the time domain

as

$$c_s = \frac{2L}{t_B - t_A + t_A^{diff} - t_B^{diff}}. \tag{2.31}$$

The change in length due to thermal expansion, L = $L_0 \cdot K_T$, will be treated in Section 2.5.

2.3 Non-ideal characteristics

When measuring the sound velocity in the time domain, a correction time, t^{corr} was introduced for Signals A and B. As the difference between t_A and t_B is used, the transit time in the cables, electronics and transducer can be neglected. The correction terms will thus consist of t_A^{rem} and t_B^{rem} for Signals A and B respectively.
Several factors may contribute to a time delay in the measured transit times. Diffraction correction, thus the deviation from the assumption of a plane wave model of propagation, and possible phase shifts due to thermal and viscous boundary layers at the sample/buffer interface are possible correction terms that will be studied in the following. A short description will further be provided about mode-converted waves, which will be treated as an uncertainty in this project. Additional factors include, but are not limited to:

- Possible imperfect symmetry in the transducer itself or in the mounting of the transducer [40], not accounted for.
- Possible coherent noise contributions from echos in the measurement cell other than mode-converted waves, treated as an uncertainty in Section 6.8.2.
- Transit time delays due to thermal and viscous boundary layers at the buffer/sample interface are assumed to be negligible [35].
- Temperature-related effects on the dimensions of the measurement cell, discussed in Section 2.5.

Other unknown contributions are not accounted for.
The correction term for Signal A, t_A^{rem}, is in this project assumed to only be affected by diffraction correction,

$$t_A^{rem} = t_A^{diff}. \tag{2.32}$$

For Signal B, the transit time will be affected by both diffraction correction and boundary layer correction upon reflection at the sample/buffer interface,

$$t_B^{rem} = t_R + t_B^{diff}, \tag{2.33}$$

where t_R is the time shift due to boundary layer correction, and t_B^{diff} is the diffraction correction in Signal B. However, as will be evident in Section 2.3.2, the boundary layer corrections can be neglected.

Δt^{rem} in Eq. (2.14) thus reduces to

$$\Delta t^{rem} = \Delta t^{diff} = t_B^{diff} - t_A^{diff}. \tag{2.34}$$

In Eq. (2.34), Δt^{diff} is the time domain diffraction correction.

2.3.1 Diffraction correction

Waves propagating from the transmitting transducer are often regarded as plane waves when they are more spherical. The diffraction correction must be calculated to account for the deviation from the general assumption of plane wave propagation.

This section introduces the theory related to diffraction correction in this project. In Section 4.1, simulations will be conducted, which in turn is compared to the theory and assumptions presented here.

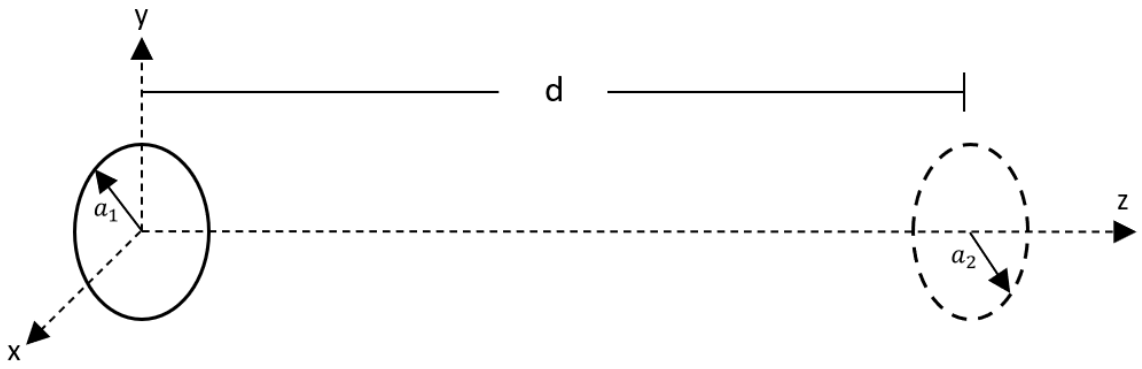

Figure 2.6: Illustration of a plane piston transmitter (left) and a measurement area (right). They are coaxially aligned with parallel faces, with a distance z = d between them. The transmitter is placed on z = 0 in a xy-plane and propagates sound waves in the +z-direction towards the measurement area. Figure inspired by [41].

There are several methods to correct for the deviation from plane-wave propagation. In Fig. 2.6, a sound source in an infinite fluid medium is coaxially aligned to a receiving circular measurement area. The sound source is a plane, circular piston vibrating uniformly mounted in an infinite rigid baffle, "the baffled piston model"[42]. The measurement area, thus the observation area as there is no physical receiver present, has a radius a_2 equal to the radius of the sound source, a_1. Thus $a_1 = a_2 = a$, illustrated in Fig. 2.6.

BPDC model - single fluid medium

For a single fluid medium, Khimunin expressed the deviation from plane-wave propagation for a uniformly vibrating plane piston as [38]

$$H^{diff} = \frac{\langle p \rangle_A}{p^{plane}}, \tag{2.35}$$

where p^{plane} is the plane-wave pressure at distance z = d, and $\langle p \rangle_A$ is the average sound pressure over the measurement area (in the absence of the receiver) at distance z = d, with area equal to the sound source, $A = \pi a^2$. Applying Williams baffled piston model, Eq. (2.35) becomes [42, 38, 43]

$$H^{diff}(d,f) = 1 - \frac{4}{\pi}\int_0^{\pi/2} exp\Big[-ikd\Big(\sqrt{1+4\Big(\frac{a}{d}\Big)^2 cos^2\theta} - 1\Big)\Big] sin^2\theta d\theta, \tag{2.36}$$

where θ is the integration variable, $k = \omega/c$ is the wave number and c is the sound velocity in the fluid medium. Eq. (2.36) must be solved numerically, which is shown in Appendix A.

The diffraction correction is often written with the dimensionless quantity [44]

$$S \equiv \frac{d}{a^2/\lambda} = \frac{2\pi d}{ka^2}. \tag{2.37}$$

Eq. (2.37) can be solved for d and inserted into Eq. (2.36), yielding an expression for the diffraction correction written with the dimensionless quantities S and ka [45],

$$H^{diff}(S,ka) = 1 - \frac{4}{\pi}\int_0^{\pi/2} exp\Big[-i\frac{(ka)^2 S}{2\pi}\Big(\sqrt{1+\Big(\frac{4\pi}{S\cdot ka}\Big)^2 cos^2\theta} - 1\Big)\Big] sin^2\theta d\theta. \tag{2.38}$$

Khimunin's diffraction correction is based on the baffled piston model and will henceforth go under the name "baffled piston diffraction correction" (BPDC), following notations in [46].

Diffraction correction in the pulse-echo solid buffer method

In this project, there are two signals of interest, S_A and S_B, as explained in Section 2.2.1. Consequently must the diffraction correction for the respective signals be calculated.

Signal A corresponds to the two-way propagation in the Plexiglas buffer. To calculate the diffraction correction for Signal A, the buffer/sample interface is assumed to be a plane infinite perfectly reflecting surface, an assumption further discussed in Section 4.1. The propagation distance used in the diffraction correction model is thus only the two-way propagation length in the buffer, thus d = 2D. The diffraction correction of Signal A, H_A^{diff} is thus found using the BPDC model (Eq. (2.38)), with

$$S = S_A = \frac{2\pi \cdot 2D}{k_b a_{eff}^2}, \tag{2.39}$$

where a_{eff} is the effective transducer radius (Section 2.4). The corresponding time shift has been shown in [39] to be expressed as

$$t_A^{diff} = -\frac{\angle H_A^{diff}}{\omega}. \tag{2.40}$$

Eq. (2.40) can be inserted into Eq. (2.34) to calculate Δt^{diff}.

Signal B will transmit into the buffer, propagate through the buffer, through the sample liquid, before it is reflected at the reflector. The BPDC model is restricted to a single fluid medium, and the model has thus been adapted by the author in cooperation with [35], and will be named "baffled piston

diffraction correction - multiple fluid" (BPDC-MF) model. To the authors knowledge, the model has not been used before.

Fig. 2.7 illustrates the propagation of Signal B. The signal generated by the transmitter first propagates through the buffer with length d = D. At the buffer/sample interface, the sound pulse has deviated from plane wave propagation, corresponding to a deviation in phase of ϕ_{B1}, determined by the distance D and the sound velocity c_b.
The sound pulse is then transmitted into the sample liquid. As the sound pulse propagates through the sample liquid, the deviation in phase will keep increasing from ϕ_{B1}, but at a rate determined by the new sound velocity, c_s. At the reflector interface, a plane infinite perfectly reflecting baffle is again assumed, and the diffraction length in the sample liquid will correspond to twice the sample length, d = 2L. After propagating twice the sample length, thus at the sample/buffer interface, the increased deviation from plane wave is calculated, corresponding to a deviation in phase of ϕ_{B2}.
The sound pulse is then transmitted into the buffer, propagates through the buffer before it is detected at the receiver again. Starting at ϕ_{B2}, the deviation in phase will increase at a rate again determined by the sound velocity and propagation distance. At the receiver, the deviation in phase will be ϕ_{B3}, corresponding to the total deviation in phase of Signal B.

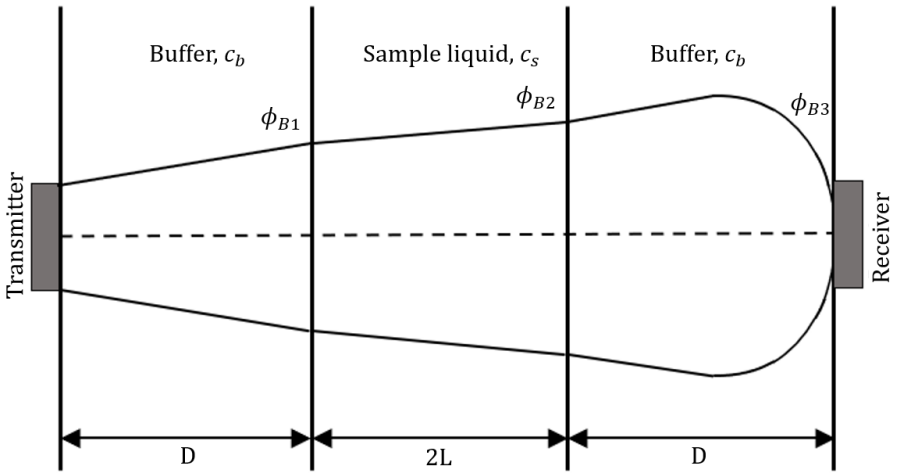

Figure 2.7: Illustration of the BPDC-MF model for calculating the diffraction correction in Signal B.

For each sampled waveform, two diffraction corrections are calculated as a function of distance d using Eq. (2.38) with f = 500 kHz and $a = a_{eff}$. The first diffraction correction, shown as the blue curve in Fig. 2.8, is calculated using $c = c_b$. The second calculation is performed using the sample's sound velocity, $c = c_s$, and is shown as the red curve in Fig. 2.8. Both curves start at d = 0. These two curves are used to calculate the total diffraction correction for signal B, following three steps. The first step is to calculate ϕ_{B1}, found at distance d = D using the blue curve. In the red curve, the corresponding distance is located where the deviation in phase is ϕ_{B1}, shown in Fig. 2.8. From this distance, the sound wave propagates the length $d = 2 \cdot L$, which results in ϕ_{B2}. In the final step, the phase ϕ_{B2} is located on the blue curve. The sound wave propagates the length d = D and the resulting

phase, $\phi_{B3} = \angle H_B^{diff}$ is calculated. When the deviation in phase due to diffraction for Signal B is calculated, the corresponding time shift can be found using [39]

$$t_B^{diff} = -\frac{\angle H_B^{diff}}{\omega}, \tag{2.41}$$

which, together with t_A^{diff}, can be used to calculate Δt^{diff} using Eq. (2.34).

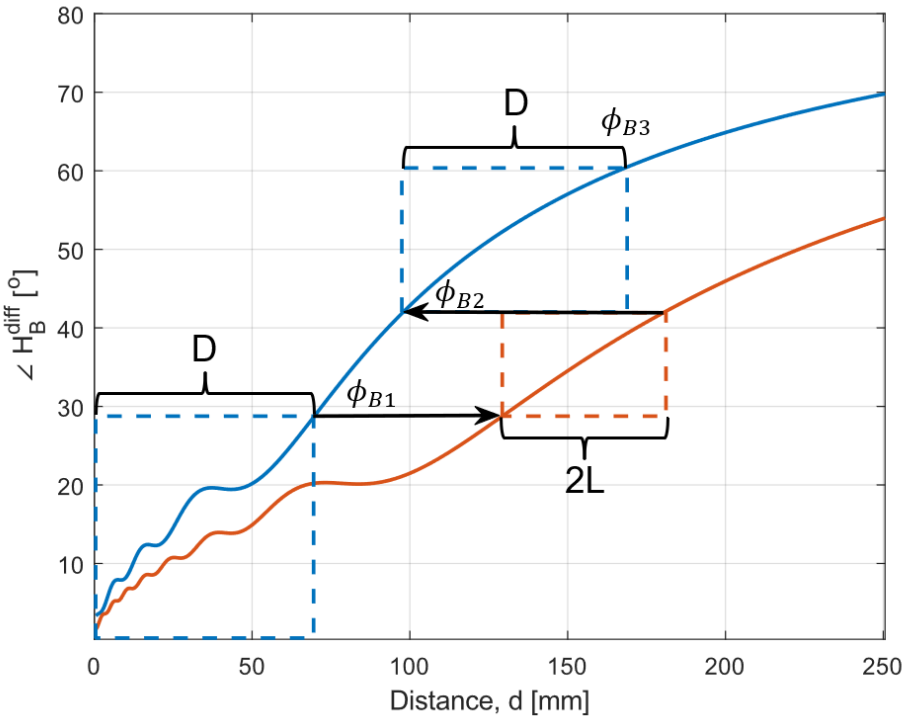

Figure 2.8: The total diffraction correction calculation in signal B using the BPDC-MF model. The blue curve is the calculated deviation in phase with c_b = 2711 m/s and the red curve is the calculated deviation in phase with c_s = 1480 m/s used as an example, both calculated as a function of distance. Further, D = 70.1 mm and L = L_0 = 25.18 mm.

2.3.2 Boundary layer correction

At the boundary between a fluid and a rigid surface, thin thermal and viscous boundary layers are generated when sound waves are reflected [47]. Inside these boundary layers, the acoustic impedance of the liquid is altered, causing a phase shift and a corresponding time shift [48].

In the candidate method (cf. Fig 2.1), such boundary layers will be generated at the sample/buffer interface. To account for such effects, a complex pressure reflection coefficient, $\hat{R}$ will be calculated, following [9]. From Kinsler and Frey [23], the complex reflection coefficient is expressed as

$$\hat{R} = \frac{p_r}{p_i}, \tag{2.42}$$

where p_i is the complex pressure amplitude of the incident wave and p_r is the complex pressure

amplitude of the reflected wave. Assuming plane wave at normal incidence, and a finite specific impedance, the complex reflection coefficient becomes [48]

$$\hat{R} = \frac{\hat{z} - \rho_s c_s}{\hat{z} + \rho_s c_s}, \tag{2.43}$$

where z is the finite specific impedance of the surface, ρ_s is the density and c_s is the sound velocity in the medium of the incident wave. The complex specific impedance can further be expressed as [48]

$$\hat{z} = e^{i\pi/4}\rho_s c_s \sqrt{\frac{\rho_s c_s^2}{\omega\mu}} \frac{\sqrt{Pr}}{\gamma - 1}. \tag{2.44}$$

Here, μ is the shear viscosity of the medium and γ is the ratio of specific heats of the medium. Further, Pr is the Prandtl number given as $Pr = C_p\mu/\kappa$, where C_p and κ is the specific heat at constant pressure and the thermal conductivity in the medium respectively.

By inserting Eq. (2.44) into Eq. (2.43), the increase in travel time due to thermal and viscous boundary layer, t_R, can be calculated using

$$t_R = \frac{\angle\hat{R}}{\omega}, \tag{2.45}$$

where $\angle\hat{R}$ is the phase of the complex reflection coefficient.

The tabulated values needed for calculating the complex specific impedance has been found in Tables 4.2 to 4.6 in Nesse's dissertation [7] for several liquid samples at 21.9^oC. Using the tabulated values together with f = 500 kHz, the time shift due to thermal and viscous boundary layers can be calculated, and the results are presented in Table 2.1.

Table 2.1: Tabulated sound velocity and density values for different liquid samples at 21.9^oC [7], and resulting calculated time shifts due to thermal and viscous boundary layers

Liquid sample	**Sound velocity,** c_s **[m/s]**	**Density,** $\rho[kg/m^3]$	**Time shift,** t_R **[ps]**
Exxol D80	1314.4	796.0	36.256
Exxol D100	1342.9	812.0	34.094
Hexadecane	1359.6	772.2	34.346
Dodecane	1290.4	748.4	37.284
Distilled water	1488.0	997.8	1.4528

In Table 2.1, it is evident that time shifts due to thermal and viscous boundary layers increases with decreasing density and sound velocity. Although the emulsions presented in Table 2.1 will not be used in this project, it gives an adequate representation of the time shift in emulsions.

It will be shown in Section 4.1 that the diffraction correction, Δt^{diff}, corresponds to approx. $2.7{\cdot}10^{-8}$ - $3.1{\cdot}10^{-9}$ for a sound velocity span of 1320-1480 m/s. From the calculated time shifts presented in Table 2.1, it is thus evident that the time shifts due to thermal and viscous boundary layers can

be neglected for all liquids sample presented. The incremental changes in the respective variables with increasing temperatures are further assumed to be negligible within the temperature span of the project.

2.3.3 Mode-converted waves

At the boundary between two media, where one of them is a rigid elastic solid, it is until now assumed that all waves are at normal incidence. At normal incidence, the transmitted and reflected waves will both be of the same type as the incident wave [49]. However, when the angle of incidence is oblique, another type of wave will be generated. This phenomenon is referred to as mode conversion and is the process of converting wave energy from shear to compressional, or vice versa [10]. Mode conversions will occur upon reflection at the boundary between the Plexiglas buffer and the sample liquid. A compressional wave will travel in one direction through the buffer, and a shear wave with a lower sound speed in the opposite direction [23]. Due to sound velocity differences, the mode-converted wave may act as a coherent noise source and is further assessed in Section 3.5.3. These mode-conversions and the implication they may have on the signal of interest have been identified and discussed by several authors[14, 16, 50].

2.4 Beam pattern and effective transducer radius

In the following, it is assumed that the transducer can be described with "the baffled piston model" (cf. Section 2.3.1). This is an idealized assumption as the transducer in the project will be mounted in a finite baffle, as well as vibrating non-uniformly.
When an acoustic wave propagates from a source, it creates a directive pattern according to Fig. 2.9. This pattern shows that the beam is composed of a main lobe, where most of the energy is located, and side lobes. The main lobe is the signal of interest and propagates normal to the transducer along the sound-axis, thus in +z direction. The side lobes will propagate at an angle from the plane, limited by the nodes at angles θ_n, where n defines node number n [23].

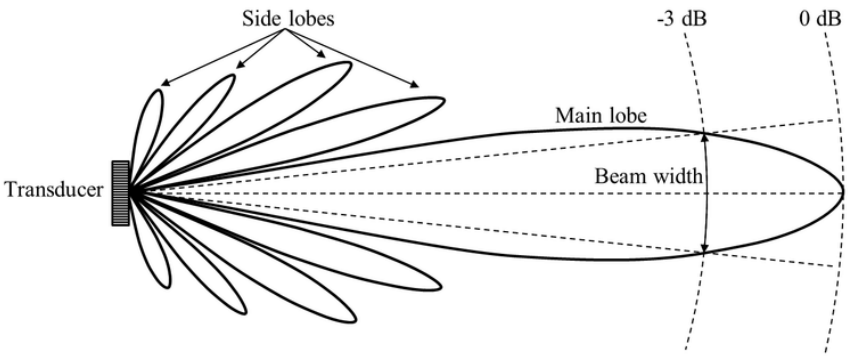

Figure 2.9: Illustration of the far-field beam pattern of a single transducer. Illustration is from [51] p. 25.

The shape of the main lobe and side lobes in Fig. 2.9, will only be present if the wave propagates in the far field [23]. It is therefore necessary to define a distance where the signal propagates from near field to far field, given as the Rayleigh-distance, r_R, [23]

$$d > r_R \equiv \frac{A}{\lambda} = \frac{\pi a^2}{\lambda} = \frac{\pi a^2 f}{c}, \tag{2.46}$$

where A = πa^2, $\lambda = c/f$ is the wavelength, and d is distance from the transmitter to the measurement area, illustrated in Fig. 2.6.

Eq. (2.46) shows that the Rayleigh distance will increase with increasing frequency, and is inversely proportional to the speed of sound in the medium. When far field is achieved, the directional factor ("Bessel directivity") can be described as [23]

$$H(\theta) = \left| \frac{2J_1(kasin\theta)}{kasin\theta} \right| \tag{2.47}$$

where J_1 is the first order Bessel function of the first kind. This can then be used to find out how the beam radiation pattern will look like. The pressure nodes can be found at angles θ_m given by [23]

$$kasin\theta_m = j_{1m} \tag{2.48}$$

where j_{1m} is the value of the argument of J_1 that reduces the above Bessel function to zero, i.e. $J_1(j_{1m}) = 0$ [23].

Each pressure node has an associated pressure lobe, where the angular locations are determined by H(θ). The values for the pressure lobes and nodes can be found in Appendix A.5 in [23], where it is found that $H(\theta) \approx 0$ for the first time when $j_{11} = 3.83$. The main lobe is thus contained within the node given by [23]:

$$kasin\theta_1 = j_{11} \iff \theta_1 = sin^{-1}\Big(\frac{j_{11}}{ka}\Big) = sin^{-1}\Big(\frac{3.83}{ka}\Big). \tag{2.49}$$

In this project, the "3 dB angle" or the "half power angle" will be used to specify the beam width, and can be calculated using [23]

$$H^2(\theta) = 0.5, \tag{2.50}$$

or

$$\theta_{3dB} \approx sin^{-1}\Big(\frac{1.6163}{ka}\Big), \tag{2.51}$$

where θ_{3dB} is the the 3 dB angle. The beam width can then further be defined as $2 \cdot \theta_{3dB}$. Through simulations presented in Section 4.2, the side lobes will be studied in detail applying the theory above.

The baffled piston model, described in Section 2.3.1, assumes that the entire front face of the transducer moves uniformly [23]. A transducer's center may move with a larger amplitude than its boundaries, which makes the surface move non-uniformly [45]. This deviation can be accounted for by using the effective transducer radius. The effective transducer radius can be found by solving for a in Eq. 2.51, thus

$$a_{eff} = \frac{c}{\omega} \cdot \frac{1.6163}{sin\theta_{3dB}}. \tag{2.52}$$

2.5 Thermal expansion

This section will present the thermal expansion of the sample area when it is subjected to increased temperatures.

In general, a material, or an object will expand in all directions when exposed to increasing temperatures, as seen in Fig. 2.10 a), where the orange dotted line shows the expanded boundaries. This also applies to a hole inside a material or an object, as shown in Fig. 2.10 b). Because the object expands, the hole inside of the object also expands.

Suppose an object has a length x_0 at an initial temperature T_0. The change in length of the object upon a temperature increase ΔT can be found through [27]

$$\Delta x = x_0 \alpha \Delta T. \tag{2.53}$$

Here, $\Delta T = T - T_0$, where T_0 is the initial temperature and T is the measured temperature, and α is the linear thermal expansion coefficient of the given material. $\Delta x = x - x_0$ is the final length subtracted with the initial length. Solving for x yields

$$x = x_0\big(1 + \alpha(T - T_0)\big) = x_0\big(1 + \alpha\Delta T\big) = x_0 \cdot K, \tag{2.54}$$

where $K = 1 + \alpha\Delta T$ will serve as an abbreviation for the general increase in x_0 with temperature.

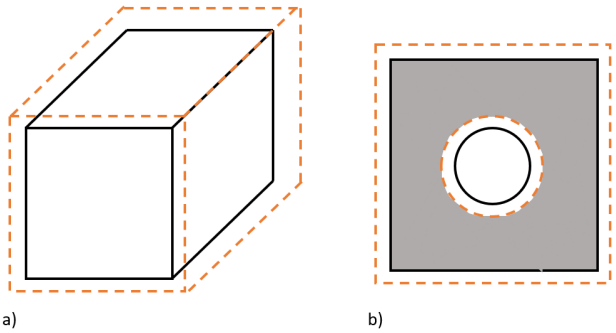

Figure 2.10: Illustration of thermal expansion in a material: a) a solid piece of material will expand in all directions b) a whole inside an object will expand at the same rate as the material surrounding it.

However, the above equation will only hold for a single material or object. The materials that make up the measurement cell in the project will expand at different rates according to their linear thermal expansion coefficients when heated up. The cell is made out of Aluminium Alloy 6082 and Plexiglas which has linear thermal expansion coefficients of $\alpha_a = 24{\cdot}10^{-6}/^oC$ and $\alpha_p = 70{\cdot}10^{-6}/^oC$ respectively [52, 53].

The Plexiglas is attached to the aluminium using bolts, as shown in Fig. 2.11. In theory, when the measurement cell is heated up, the aluminium will expand in all directions, increasing the length of the sample area. However, the aluminium is attached with bolts to the Plexiglas buffer. The bolts will consequently halter the expansion due to forces acting on both the Plexiglas and the aluminium.

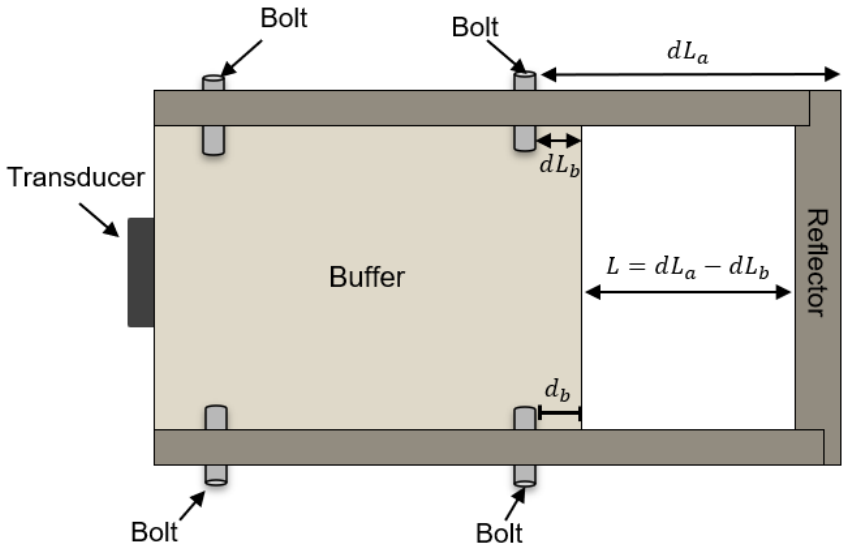

Figure 2.11: Illustration of the expansion of the sample area due to thermal expansions in the materials surrounding the bolts. Sketch is illustrated as seen from the top. Dimensions are not to scale.

The change in sample length due to buffer expansion will be equal to the expansion to the right of the bolt, named distance d_b. Further, the expansion of the aluminium chassis, dL_A, will be limited by the bolt placement, where at temperature T_0, the distance is given as

$$L_A = L_0 + d_b, \tag{2.55}$$

where L_0 is the sample length at T_0. The change in the sample length due to the aluminium expansion will consequently only be dependent on the expansion on the right side of the bolt, as shown in Fig. 2.11.

With an increase in temperature, ΔT, the new sample length, L, will be equal to the difference between the increase in L_A, dL_A, and the increase in d_b, dL_b

$$L = dL_a - dL_b. \tag{2.56}$$

Using Eq. 2.54, the linear thermal expansion of the aluminium chassis can be expressed as

$$dL_a = L_A + (L_A)\alpha_a \Delta T, \tag{2.57}$$

and the expansion of the buffer can be expressed as

$$dL_b = d_b + d_b \cdot \alpha_p \Delta T. \tag{2.58}$$

Inserting Eqs. (2.56), (2.57) and (2.58) into Eq. (2.56), results in the expression for the new length as a function of temperature

$$L = L_0 + \Delta T \cdot \Big((L_0 + d_b) \cdot \alpha_a - d_b \cdot \alpha_p \Big). \tag{2.59}$$

Following Eq. (2.54), the above equation can be reduced to

$$L = L_0 \cdot K_T, \tag{2.60}$$

where K_T will be the general expansion of L_0 with a temperature change ΔT, and can be expressed as

$$K_T = 1 + \Delta T \cdot \Big(\alpha_a + \frac{d_b}{L_0} (\alpha_a - \alpha_p) \Big). \tag{2.61}$$

The calculations above, however, only holds for the areas surrounding the bolts. It was decided to strategically place the bolts so as to prevent or limit acoustic interference due to reflections from the bolt surface, meaning that the middle of the Plexiglas buffer is not secured by bolts. Upon heating, the Plexiglas buffer might experience stress forces around the acoustic axis, causing the middle to bulge as shown in Fig. 2.12. Such an expansion will decrease the length of the sample area, causing an error in the sound velocity measurements.

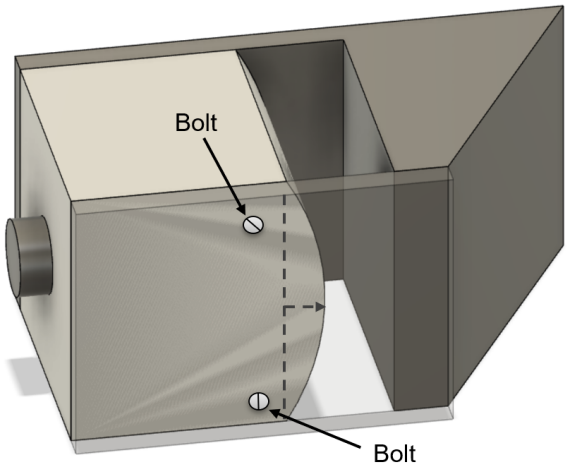

Figure 2.12: Simplified illustration of the possible thermal expansion of the sound axis in the Plexiglas buffer due to a temperature increase. The expansion is exaggerated and the dimensions are not to scale.

For the candidate project, a sample length of $L_0 = 25.18mm$ is measured (ref. Section 6.2). Based on Eq. (2.12) and a sound velocity of $c_s = 1481m/s$, if the sample length is reduced by 0.01 mm, a sound velocity change of 0.6 m/s can be calculated. The bulging of the Plexiglas buffer can thus be a potential source of sound velocity error. However, this expansion is hard to quantify and even harder to measure without high precision tools. It will thus only be treated in further discussions in Chapter

7.

The diffraction correction model presented in Section 2.3.1 is dependent on the buffer length which is secured by bolts on both sides (Fig. 2.11). In this project, no equation has been created for the thermal expansion of the buffer, and the uncertainty in this is assumed negligible, as it will be shown in Section 6.8 that the uncertainty in diffraction correction only accounts for ≈ 1% of the total uncertainty budget.

2.6 Fourier Transform

The Fourier transform can be used to analyze time-domain signal in the frequency domain, which will be used in Section 3.4.3 in this project. Fourier synthesis further constructs time signals from a frequency response by using the inverse Fourier transform [54].
The Fourier transform, $X(\omega)$ and the invers Fourier transform, $x(t)$ can be expressed as [25]

$$\begin{aligned} X(\omega) &= \int_{-\infty}^{\infty} x(t) e^{-i\omega t} dt, \\ x(t) &= \frac{1}{2\pi} \int_{-\infty}^{\infty} X(\omega) e^{i\omega t} d\omega \end{aligned} \tag{2.62}$$

In digital processing, the Fourier transform can be discretized in the time domain and frequency domain; $t = n\Delta t$ and f = $r\Delta f$. Δt and Δf are the intervals between two samples in the time or frequency domain, and n and r are integers[54]. The discrete Fourier transform (DFT) and the inverse DTF are defined as [55]

$$\begin{aligned} X[r] &= \sum_{n=0}^{N-1} x[n] e^{-\frac{2\pi k}{N} n} \\ x[n] &= \frac{1}{N} \sum_{n=0}^{N-1} X[r] e^{\frac{2\pi k}{N} n} \end{aligned} \tag{2.63}$$

The DFT is usually calculated using the fast Fourier transform (FFT) [54]. This is done in this project using a pre-defined algorithm in Matlab [56].

Chapter 3

Experimental setup and measurement methods

This chapter describes the experimental setup and measurement method used in this project. The chapter consists of five main sections with included subsections and can roughly be divided into three parts. The first part, Sections 3.1, 3.2 and 3.3 concerns the measurements and experimental setups needed to measure the sound velocity. The second part, Section 3.4, will discuss the signal processing methods applied. A detailed description of the design of the measurement cell and considerations made prior to construction will be included in Section 3.5.

3.1 Measurements of acoustic properties

Throughout the project, sound velocity measurements, noise measurements, and other acoustic properties will be measured. A block diagram of the setup used for these measurements is presented in Fig. 3.1, and a picture is presented in Fig. 3.2.
A transducer is clamped onto the measurement cell and serves as both a transmitter and a receiver using a T/R-switch (transmitting/receiving). The transducer is excited using a signal generator, and the received signal is monitored through an oscilloscope. Inside the measurement cell is a temperature probe connected to a computer using an adapter. Software for digital filtering, storage and communication is developed by the author in Matlab, presented in Appendix D.2.

The measurement cell is immersed in a water bath for sound velocity measurements at increasing temperatures. A heater is inside this water bath, which heats the water bath through a temperature controller. The temperature controller monitors the temperature inside the water bath through a temperature sensor. The author has identified neither the name nor brand of the temperature sensor. However, since the sensor only measures the water bath temperature, its uncertainty and specifications will not affect the measured sound velocity. A pump further circulates the water, so the temperature is evenly distributed.

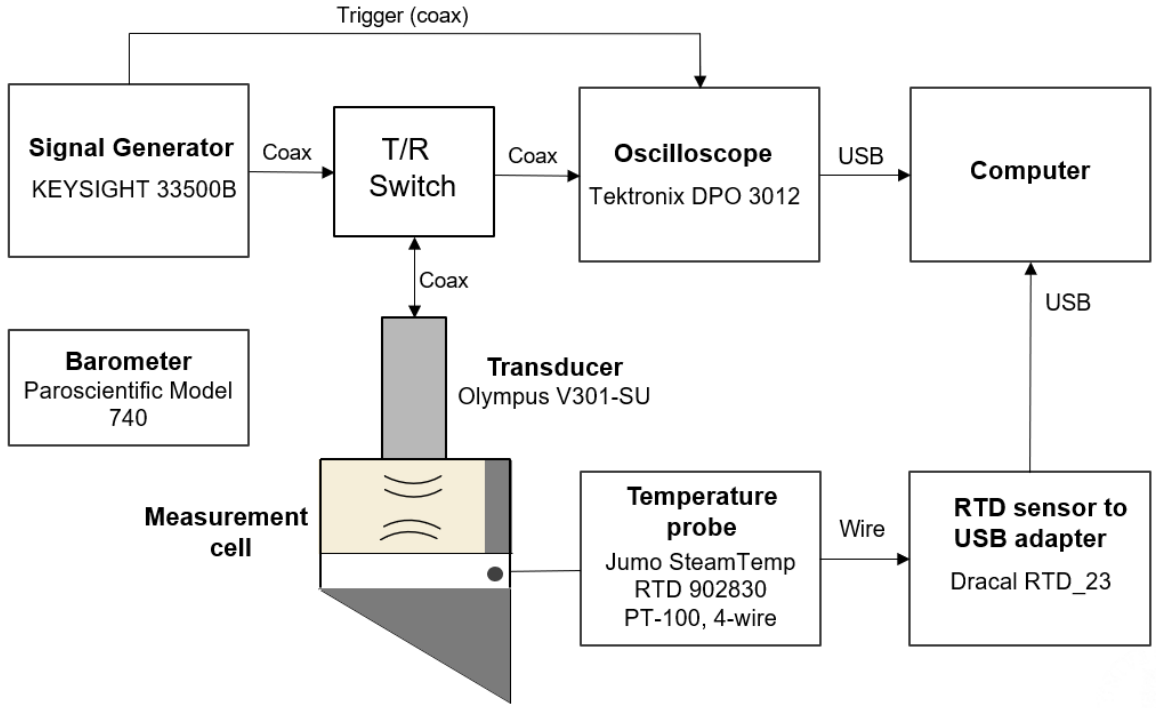

Figure 3.1: Measurement setup A. Block diagram of the measurement setup when measuring acoustic properties and noise sources

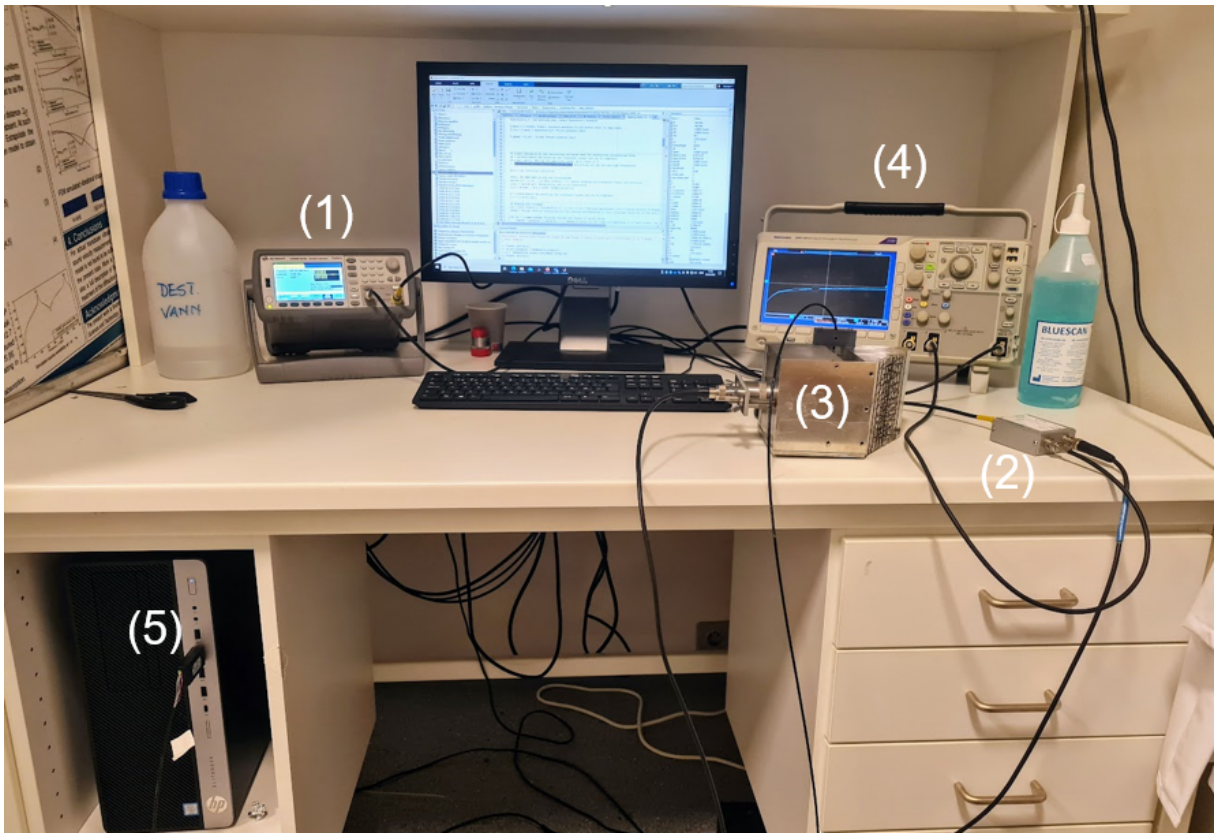

Figure 3.2: Picture of measurement setup A. (1) Signal generator. (2) T/R-switch. (3) Measurement cell, including transducer and temperature probe (4) Oscilloscope (5) RTD sensor to USB adapter.

The whole setup for these measurements is presented in Fig. 3.3, and a list of all components utilised is presented in Table 3.1. In the following subsections, details of the different components will be presented.

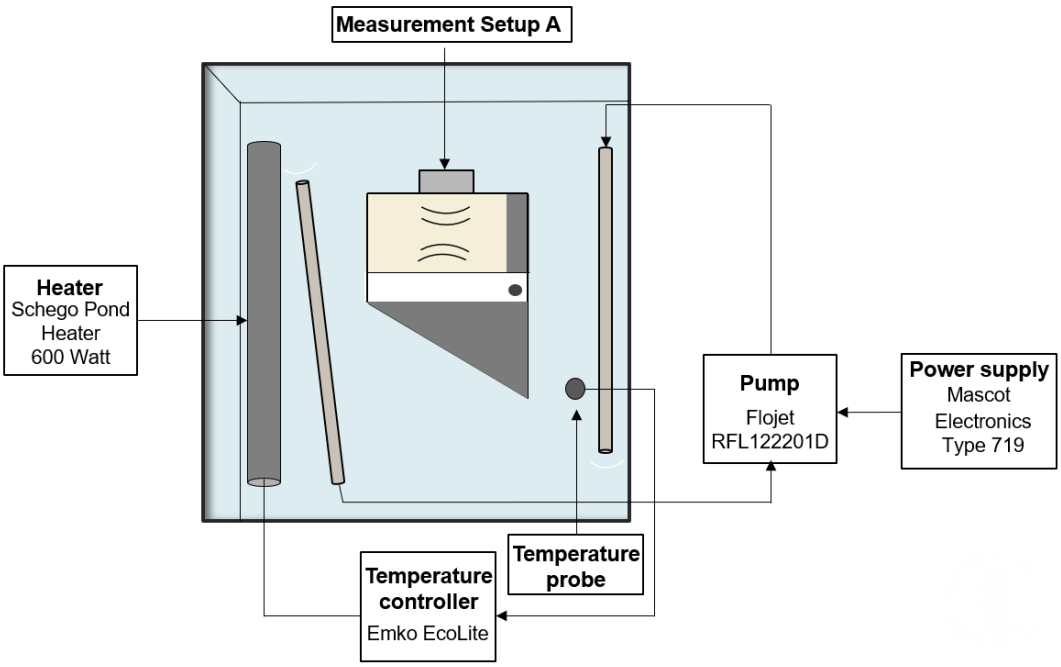

Figure 3.3: Measurement setup B. Illustration of the measurement setup utilised when measuring the sound velocity in the liquid sample with increasing temperature.

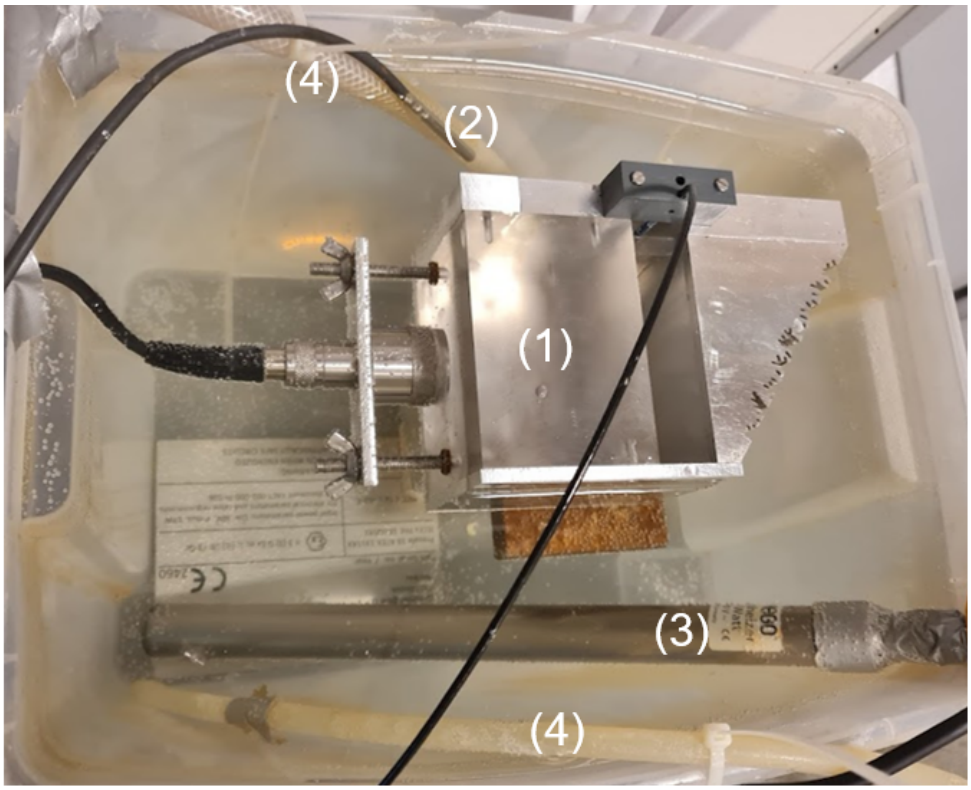

Figure 3.4: Picture of measurement setup B. (1) Measurement setup A. (2) Temperature probe. (3) Heater. (4) Tubes. Temperature controller, power supply and pump is not included.

Table 3.1: List of components used when measuring various acoustic properties and noise.

Component	**Manufacturer**	**Model**	**Serial Number**
Measurement setup A			
Signal generator	Keysight	33511B	MY57300358
T/R Switch	Electronic workshop/IFT, UiB	-	-
Transducer	Panametrics	V301-SU	179296
Measurement cell	Workshop/IFT, UiB	-	-
Oscilloscope	Tektronix	DPO 3012	C024018
Barometer	Paroscientific	740-30A-CE	67325
RTD sensor to USB adapter	Dracal	RTD_23	E16381
Temperature probe	Jumo SteamTemp RTD	902830	00445084
Couplant	Bluescan Utrasound gel	446-1	-
Distilled water	Department of Chemistry, UiB	-	-
Measurement setup B			
Water pump	FLOJET	RLF122201D	13K24200
Power Supply	Mascot Electronics	Type 719	176381
Temperature control unit	EMKO	Eco Lite	-
Temperature probe	n/a	n/a	-
Heater	SCHEGO	Teichheizer 600 Watt	-
Physical measurements			
Digital caliper	MarCal	16EWR	-

3.1.1 Signal generator

In the experimental setup, Keysight 33511B, 20 MHz Function/Arbitrary Trueform Waveform Generator was utilised. The datasheet can be found in [57].

Using the waveform generator, a sinusoidal burst was generated with 2-10 periods, depending on the purpose of the experiment. For the sine function, the frequency range is 1 μHz to 20 MHz with 1 μHz resolution. The accuracy of the frequency is ±(1 ppm of setting + 15 pHz) in one year, at temperature $23^oC \pm 5^oC$. Throughout the project, a frequency of 500 kHz has been used. Assuming a calibration within the last year (calibration data not available) and room temperature of around 22^oC, the frequency accuracy is within ±0.5 Hz.

Further, the amplitude range is $1mV$ to 10 V (into 50Ω) with a four-digit resolution. The accuracy is ±(1% of setting in V_{pp}) ± $(1mV)$. To create a burst with the largest possible amplitude, the amplitude was set to 10 V. No non-linearity's were observed in the project due to the large voltage amplitude.

Table 3.2 summarises the parameters of the signal generator set throughout the experiments.

Table 3.2: Settings for Keysight 33511B used in experiments

Function	Frequency	Amplitude	Offset	Burst Cycles	Burst Period	Phase	Delay
Sine (Burst)	500 kHz	10 V	0 V	2-10	10 ms.	0^o	0 s.

A BNC splitter was connected to the output of the waveform generator. Through coaxial cables, one end was connected to the T/R switch, while the other end was directly connected to the oscilloscope to study the reference signal. Further, a trigger signal was sent to the oscilloscope through the sync output via a coaxial cable.

3.1.2 T/R Switch

The T/R-switch (Transmit/Receive) is a typical diode bridge based switch produced at the electronic workshop at the Department of Physics and Technology (IFT).
A regular diode has a knee voltage, also known as a cut-in voltage, where the current increases rapidly above this point. This minimum voltage is required for a diode to work [58, 59]. As can be seen in Fig. 3.5, there are three diodes in series with the signal generator in the forward direction. For the transmitting signal in the project, the voltage must thus be three times the knee voltage, which for regular silicon diodes, as used in this switch, is 0.7 V [59]. The amplitude of the received signal is, however, not within the overall minimum voltage amplitude criteria of the diodes. The diodes will act as an open circuit, and the received signal will thus be picked up by the oscilloscope instead.

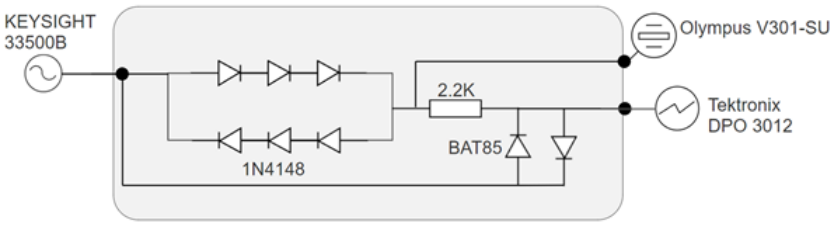

Figure 3.5: Electronic circuit diagram for the T/R-Switch applied in the project

The knee voltage, which make the diodes suitable for use as switches, also causes non-linear effects at the received signal[58]. These effects are clearly visible in the project, and are eliminated through filtering. This is shown in Section 3.4.4.

3.1.3 Transducer

Throughout the project, only one transducer would be needed, which would act as both the transmitter and the receiver. To find a suitable transducer for the project, factors like center frequency, radius, type of transducer and connector type had to be considered.

After consulting with XSENS Flow Solutions[2], a frequency of 500 kHz was assumed to be sufficient concerning possible dispersion effects in crude oils (ref. Section 7.1) as the operational frequency of their flow meters are lower.

The experimental setup utilized in Fig. 3.3 required a watertight transducer. Generally, immersion transducers, as opposed to standard contact transducers, are designed for liquid environments and have watertight connectors [60].

With the above requirements, the choice fell on Panametrics Ultrasonic Immersion Transducer type V301-SU, with the transducer dimensions shown in Fig. 3.6. The technical specifications by the manufacturer are listed in Table 3.3, and the transducer properties are listed in Table 3.4. The transducer can withstand water temperatures up to 50^oC which sets the approximate boundary for maximum temperature throughout the project [61].

It is in Section 6.5.1 shown that the measurement cell also can operate at frequencies below the operating frequency of f = 500 kHz, resulting in accurate measurements down to 375 kHz and a deviation of $\approx$ 1.5 m/s at 275 kHz. Accurate measurements are also obtained at 600 kHz (Section 6.5.1).

Table 3.3: Transducer specifications [61]

Transducer Type	**Frequency** [KHz]	**Nominal element size**		**Unfocused transducer part number**
		[mm]	[inch]	VIDEOSCAN
Large Case Diameter (LCD)	500	25.4	1.0	V301-SU

The nominal element diameter is 25.4 mm, shown in the left sketch in Fig. 3.6. The effective element radius and directivity in water are found experimentally, where the experimental setup for measuring the effective element radius is described in Section 3.3. As the effective radius is hard to measure in a solid [14], the effective radius in water in applied throughout the project.

A test form (with correct serial number) for the specific transducer used in the project could not be located. Solberg [21] used the same transducer model with a different serial number, and a test form of that transducer is enclosed at the end of Solberg's thesis. This will be used as a general indication of the bandwidth and resonance frequency of the transducer in hand. A summary of the findings is presented in Table 3.4.

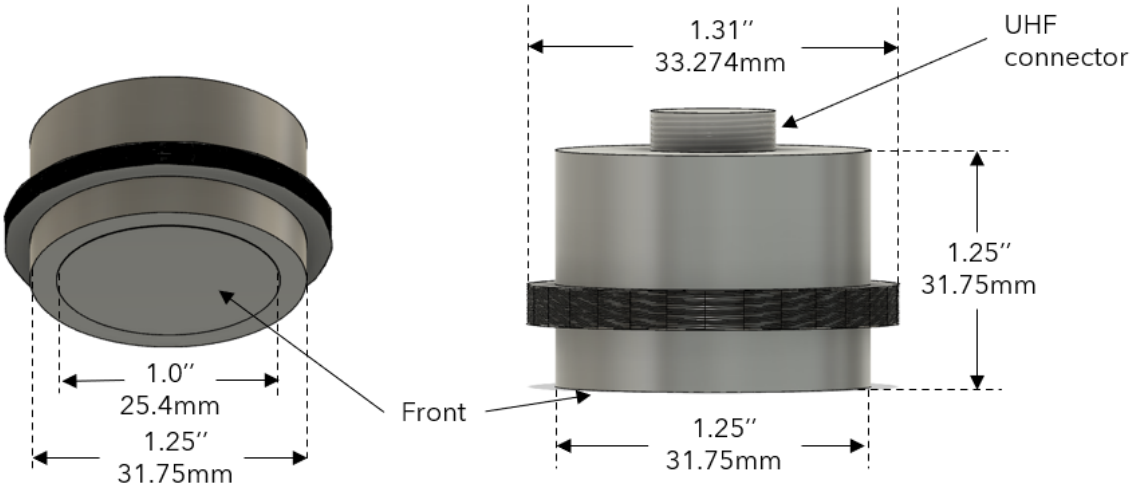

Figure 3.6: Transducer V301-SU dimensions [61].

With the chosen frequency f = 500 kHz, $a = a_{eff}$, and measured sound velocity in the Plexiglas buffer, c_b = 2711 m/s at room temperature (Section 6.3), the Rayleigh distance can be calculated using Eq. (2.46), resulting in r_R = 89.5 mm.

Table 3.4: Experimental transducer properties calculated from the results in section6.4.*From [21].

					6 dB Bandwidth	
Transducer type	a_{eff}	Center freq.*	Peak freq.*	θ_{3dB}	Lower freq.*	Upper freq.*
V301	12.43 mm	0.48 MHz	0.47 MHz	3.5^oC	0.33 MHz	0.64 MHz

The transducer is connected to the T/R switch using a coaxial cable with a waterproof UHF connector at one end and a BNC connector at the other end. The transducer is mounted on the Plexiglas buffer using an installed attachment shown in Fig. 3.7b. To facilitate the transmission of sound energy from the transducer into the buffer, a couplant of type Bluescan Ultrasonic gel is applied to the transducer surface.

3.1.4 Measurement cell

The workshop at the Department for Physics and Technology at UiB constructed the measurement cell used in this project based on the authors design, shown in Fig. 3.7. A transducer was clamped on the measurement cell and a temperature probe was inserted into the sample area. In Section 3.5, the dimensions and specifications are explained in detail.

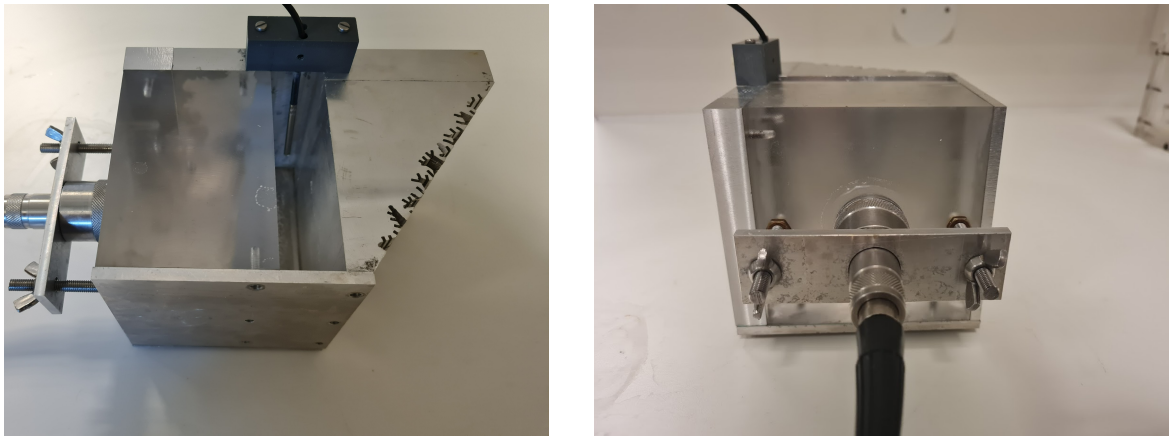

(a) Top view

(b) Front view

Figure 3.7: Picture of the measurement cell used in the project with transducer and temperature probe. Dimensions and specifications are given in section 3.5.

3.1.5 Oscilloscope

A Tektronix DPO3012 Oscilloscope [62], was used to monitor and log the received signals. The oscilloscope was connected to the T/R switch as well as the output signal from the signal generator using coaxial cables, and was further connected to the computer via USB. Through a Matlab-script (Appendix D.2), data points were sampled for further processing.
The oscilloscope has 2 analog channels, 100MHz bandwidth, 16 bits vertical resolution and a sample rate of 2.5 GHz. It was externally triggered by the signal generator.

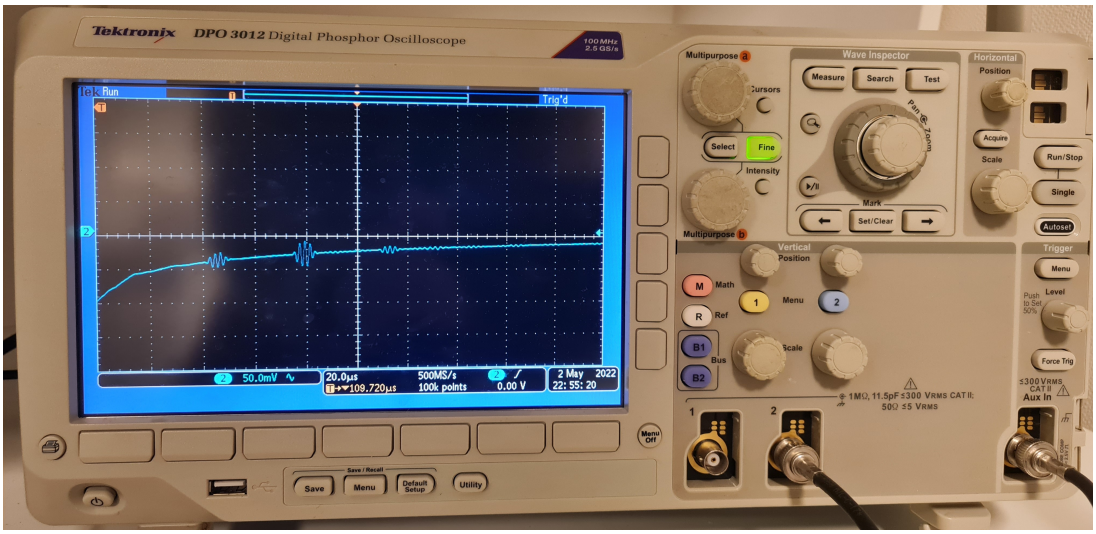

Figure 3.8: Picture of the Tektronic DPO3012 Oscilloscope with a typical waveform.

When extracting the data from the oscilloscope onto the computer, only the data displayed would be extracted. It was thus essential to make sure that the oscilloscope screen showed the data of interest. Therefore, the data of interest filled the display and was enlarged as much as possible without causing

any saturation. The signal was then averaged 512 times using the built-in average function to reduce incoherent noise. The resulting waveform can be seen in Fig. 3.8.

The range of the oscilloscope in the horizontal direction is 1 ns/div to 1000 s/div where the corresponding time accuracy is ± 10 ppm for a 1 ms interval or larger. In the vertical direction, the range is 1 mV/div to 10 V/div (1MΩ), and the corresponding accuracy is ±1.5% for larger than 5 mV/div. To get the signal of interest into frame, the horizontal and vertical sensitivity was set to 20μs and 50.0 mV respectively. This corresponded to a 500MHz sample rate, which was set automatically. Further, the waveform was set to be split into 100k sampling points which were exported to MATLAB for further processing.

3.1.6 Pressure measurements

To measure the barometric pressure, a freestanding barometer is used, shown in Fig. 3.9. The barometer is a Paroscientific Model 740 barometer [63] with an accuracy of 0.015% of reading at room temperature, and a resolution of 10^{-5} bar. The barometer is not incorporated into the measurement circuit, and thereby the signal processing script. Consequently must the pressure be read manually before, during, and after a measurement series. No significant changes in pressure has been observed during a measurement series, and it is thus assumed that the uncertainty due to observational fluctuations in analog pressure readings (ref. Table 6.4) accounts for the uncertainty due to not logging the pressure continuously.

Figure 3.9: Picture of Paroscientific Model 740 barometer.

3.1.7 Temperature measurements

A temperature sensor with high precision is required to be sure that the temperature in the sample liquid is known.

JUMO STEAMTemp Temperaturgiver RTD (902830), article number 00445084 [64] is chosen for this

project. It is a 4 wire RTD, waterproof, has a diameter of 4mm and a length of 50mm. The diameter is small enough to have room on all sides of the sensor, inflicting no extra heat from the metal chassis, as the chassis is believed to get hotter faster than the sample liquid. A picture of the probe placement is shown in Fig. 3.7, and illustrated in Fig. 3.30. It further has a temperature range of -70^oC to +200^oC and an expanded uncertainty of 0.2^oC at T = 22.94^oC (95% confidence level, k = 2) [64], which is well below the required in the sensitivity analysis of $u(\Delta T)$ = 0.35^oC at 68% confidence level (Section 5.3). A PT100 temperature sensor is further given by the characteristic equation [65]

$$R = R_0(1 + \alpha T + \beta T^2), \tag{3.1}$$

where R i s the resistance of the temperature sensor, R_0 is the resistance at 0^oC, T is temperature in ^oC, and α and β are constants. For a regular platinum element, $\alpha = 3.9083 \cdot 10^{-3}/^oC$, $\beta = -5.775 \cdot 10^{-7}/^oC^2$ and $R_0 = 100\Omega$ [66].

When measuring the sound velocity with increasing temperatures, the measurement cell is placed in a water bath, as illustrated in Fig. 3.3, where the temperature of the water bath is controlled using an external temperature sensor. After calibrating the JUMO sensor, a discrepancy of $\approx 1.5^oC$ is found between the two sensors, which is accounted for throughout.
It should here be noted that due to the size of the water bath, spatial temperature variations were observed in the sample area throughout the measurement series. To minimise the spatial variations between set points, the sample area was stirred manually at even intervals. Changes in sound velocity upon stirring were not observed, and the measurement cell was stabilised for ten minutes at temperature set points to ensure no spacial temperature variations or flow present in the water.

Calibration of temperature sensor

To calibrate the temperature sensor, a dry-well calibrator is utilized. The temperature sensor is inserted into the dry-well and connected to a Fluke Super-DAQ temperature scanner through a temperature sensor multiplexer, as shown in Fig. 3.10. Inserted into the dry-well is also a reference PT100 element, JUMO 902150-30386. This reference temperature sensor element is calibrated per DIN EN60751, which is a worldwide standard in calibration of platinum resistance thermometers [65], with an uncertainty of 0.04^oC at 20^oC (95% confidence level) [67]. The measured temperature of the reference PT100 will thus be the reference temperature inside the dry-well.

The temperature scanner is set on an automated test sequence, thus enabling a series of calibrations without interference. In steps of 3^oC, the temperature sensor is calibrated from 18-60^oC. For each calibration step, 100 measurements were collected from both the reference probe and the PT100 using the USB output of the temperature scanner.

The tolerance band and stability limit are set to 0.15^oC and the soak-time to 6 minutes. This means that the temperature scanner will not take any measurements before the reference PT100 is within the stability limit for six consecutive minutes, achieving a stable temperature inside the dry-well. The

tolerance band refers to the temperature the reference probe must be within to start scanning.

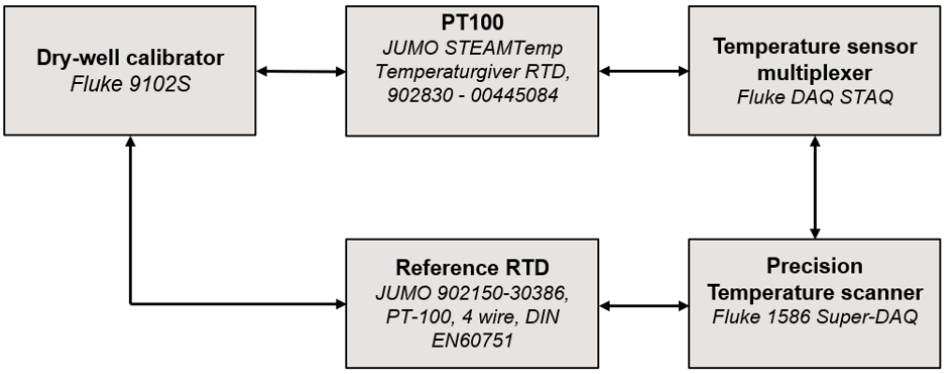

Figure 3.10: Block diagram of the measurement setup used when calibrating the JUMO STEAMTemp Temperaturgiver RTD.

Two series of measurements were done. In the first round, the coefficients α,β and R_0 in Eq. (3.1) are set to the standard coefficients for a regular platinum element. Using cftool in MATLAB, the measured average temperature of the reference probe is plotted against the average values for the measured temperature of the PT100, resulting in new variables, α and β, for the new characteristic equation.

These new variables are then used to run a new set of measurements. If the first series of measurements is done correctly and the correct variables are found, the measured temperature of the PT100-element should be almost identical to the reference probe. The calibration results are shown in Section 6.1.1.

After calibration, the uncertainty in temperature measurements using the PT100 temperature probe is calculated to U(T) = 0.324^oC at 60^oC (95% confidence level, k = 2), which includes a maximum deviation from calibration of 0.04^oC (100% confidence level, k = $\sqrt{3}$).

Solving for T in Eq. (3.1), results in an equation for the temperature as a function of resistance

$$T = \frac{-\alpha R_0 + \sqrt{\alpha^2 R_0^2 - 4\beta R_0 (R_0 - R)}}{2\beta R_0} \tag{3.2}$$

The temperature is measured for each measurement, and the corresponding resistance is calculated by using Eq. (3.1) with the general coefficients for a platinum element. Eq. (3.2) is then applied using the calculated resistance and the new coefficients to find the calibrated temperature. This is implemented into the data logging script (Appendix D.2).

3.1.8 Length measurements

When measuring the sound velocity, two dimensions of the measurement cell were of importance; the length of the sample area, L_0, and the length of the buffer, D.

Sample length, L_0

Because the buffer and the reflector were attached to the chassis, the placement of the buffer and reflector in relation to each other would make up the length of the sample area, L_0. L_0 was thus found after finishing the measurement cell.

The measurement cell was placed at room temperature (22.94^oC) for 24 hours to ensure no material expansion due to temperature gradients were present. The knife-edge faces of a MarCal 16EWR digital caliper [68] were used to measure the length of the sample area. By measuring the entire width of the sample area, the variation in length could be found. Ten repeatability measurements were taken at the approximate location of the sound axis, thus at the centre of the width. The results are presented in Section 6.5. However, as can be seen in Fig.3.11, the measured length of the sample area was constricted to only the top due to the length of the knife edges. Therefore, assumptions had to be made about how the length varied further down in the sample area based on the measurements of the buffer and reflector.

Figure 3.11: A picture illustrating the limitation on measurements due to the knife-edge's length using the digital caliper MarCal 16EWR.

Measurements were taken at increasing temperature as to see if any changes could be measured, but no changes within the resolution of the caliper could be found. Within the temperature span of the project, the increase in sample length due to thermal expansion falls within the uncertainty of the MarCal 16EWR digital caliper. The uncertainty is specified to be ±0.03mm by the manufacturer,

following DIN 862 standard [68]. Coverage factor k = 2 is assumed.

A combined standard uncertainty in sample length of $u(L_0) = 0.0252mm$ (95% confidence level, k = 2) is calculated, presented in Table 6.8.

Buffer and reflector measurements

Before the buffer was attached to the aluminium chassis, the length of the buffer, D, was measured. After setting the buffer to room temperature for 24 hours, the buffer's length, width, and height were measured using a MarCal 16EWR digital caliper. The buffer was rotated and measured at several places to ensure that the entire Plexiglas buffer block was covered. At the approximate location of the sound axis, ten repeatability measurements were taken of the length across the entire height of the buffer. The results are presented in Section 6.5. The dimensions of the reflector, on the other hand, could not be measured due to irregular surfaces. In cooperation with the Institute for Physics and Technology's workshop, the reflector surface was assumed to be plane with an uncertainty of $\pm 0.02mm$ (95% confidence level).

3.2 Sound velocity measurements in Plexiglas buffer

To accurately correct for diffraction, the compressional sound velocity in the Plexiglas buffer must be known. This section will present the method for measuring the Plexiglas buffer at room temperature and as a function of temperature. The results are presented in Section 6.3.

To accurately measure the compressional sound velocity of the Plexiglas buffer, c_b, the measurement setup shown in Fig. 3.1 was used, and the transducer was further excited with a ten-period pulse at 500kHz with a $10V$ peak-to-peak output amplitude.

If no sample is present, the plane wave reflection coefficient can be approximated to R $\approx$ 1 as $Z_{air} << Z_{buffer}$, where Z_{air} and Z_{buffer} correspond to the impedance of air and buffer respectively. The transit time between echos traversed in the Plexiglas buffer 2 and 4 times can then be used to measure the sound velocity. Following Eq. (2.13) with $\Delta t^{rem} = \Delta t^{corr}$ (ref. Section 2.3.1), this can be found through

$$c_b = \frac{2D}{t_{RB} + t_{B2}^{corr} - t_{B1}^{corr}}, \tag{3.3}$$

where D is the buffer length and t_{RB} is the average transit time between the arrival of the first and second reflection at the buffer/air interface, measured with the zero-crossing signal processing method (ref. Section 3.4.2). Further, t_{B1}^{corr} and t_{B2}^{corr} are the correction factors due to diffraction, which can be found by applying the BPDC model (Eq. (2.38)) for both pulses, where $d = 2 \cdot D$ and $d = 4 \cdot D$ for t_{B1}^{corr} and t_{B2}^{corr} respectively.

An 85x100x100 mm Plexiglas block was used to acquire the c_b as a function of temperature. The same type of Plexiglas was used as the buffer used in the project. The Plexiglas buffer in the project is fixed with bolts to the metal chassis, limiting the thermal expansion of the buffer. By immersing only

the buffer into the water bath, the buffer can expand without any applied stresses, and the thermal expansion can thus be compensated for through Eq. (2.54) with thermal expansion coefficient $\alpha_b = 70 \cdot 10^{-6}$ [53]. The V301 transducer was clamped onto the block, and the setup was then placed into the water bath setup, illustrated in Fig. 3.3. To avoid amplitude reduction due to sound transmission into the water bath, a plastic bag filled with air was secured on the backside of the buffer, shown in Fig. 3.12. The bag will act as a vacuum and reflect most of the propagating wave back to the transducer surface.

The signal generator was set to produce a ten-period pulse at 500 kHz with a 10 V peak-to-peak voltage amplitude. A temperature interval of 22^oC to 45^oC was chosen, and in steps of approximately 3^oC, the waveforms were collected, and the average compressional sound velocity was found using Eq. (3.3). To assume stable temperature conditions, the water bath was stabilized for 10 minutes between each setpoint.

Figure 3.12: Picture of the measurement setup used to measure the sound velocity in the Plexiglas as a function of temperature. A plastic bag filled with air is secured with tape on the back of the Plexiglas, and a transducer is clamped onto the front. The setup is immersed into the water bath

An attempt was made to measure the shear sound velocity in the Plexiglas buffer. As can be seen in Fig. 3.26, the amplitude is severely reduced compared to the signals of interest, which makes locating the zero-crossing between the pulses difficult. The sound velocity measurements were thus not seen as reliable, and the shear sound velocity was found by applying Eq. (2.1) with the experimental c_b, and $\nu = 0.4$ [23].

3.3 Setup for measuring the effective transducer radius

The effective transducer radius, a_{eff} (Section 2.4), was measured using the experimental setup shown as a block diagram in Fig. 3.13.

The V301-transducer was manually immersed into a water tank and aligned with a hydrophone through motion controllers in the vertical and horizontal planes. The angle of the transducer was further manually aligned through a rotation stage. The transducer and hydrophone were separated by a distance $\approx$ 64.5 mm, which assured far-field propagation, thus d > r_R. A picture of the measurement setup is shown in Fig. 3.14.

When the transducer and hydrophone were aligned, several measurements were performed. The signal generator was set to produce a 100-period sinusoidal burst with f = 500kHz and 10V peak-to-peak output amplitude. In steps of 0.1^o and 0.05^o, the rotation stage was set to rotate from -7^o to 7^o, corresponding to an approximate width of the main lobe. For each step, the amplitude was found in the stabilized part of the signal and averaged 125 times before the results were collected from the oscilloscope.

A beam pattern is found by plotting the recorded amplitude against the corresponding angle. By locating the θ_{3dB}-angle, a_{eff} can be calculated using Eq. (2.52).

The alignment of the hydrophone and transducer, rotation of the transducer under the measurement series, and the data collection and processing were all automated processes in Matlab using a series of scripts. The original scripts can be found in Magne Aanes' doctorate from 2014 [69] and have later been modified by Mathias Saether in the Acoustics Group at the University of Bergen.

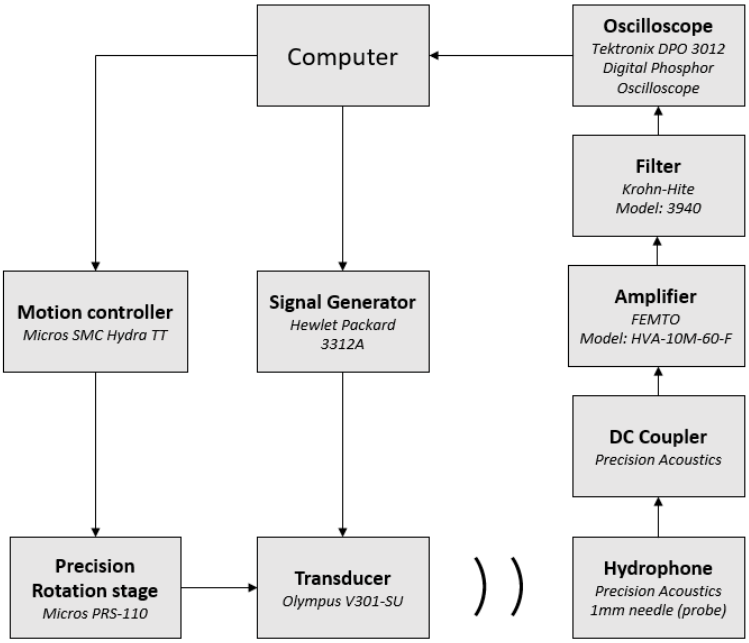

Figure 3.13: Block diagram of the measurement setup for finding the effective transducer radius.

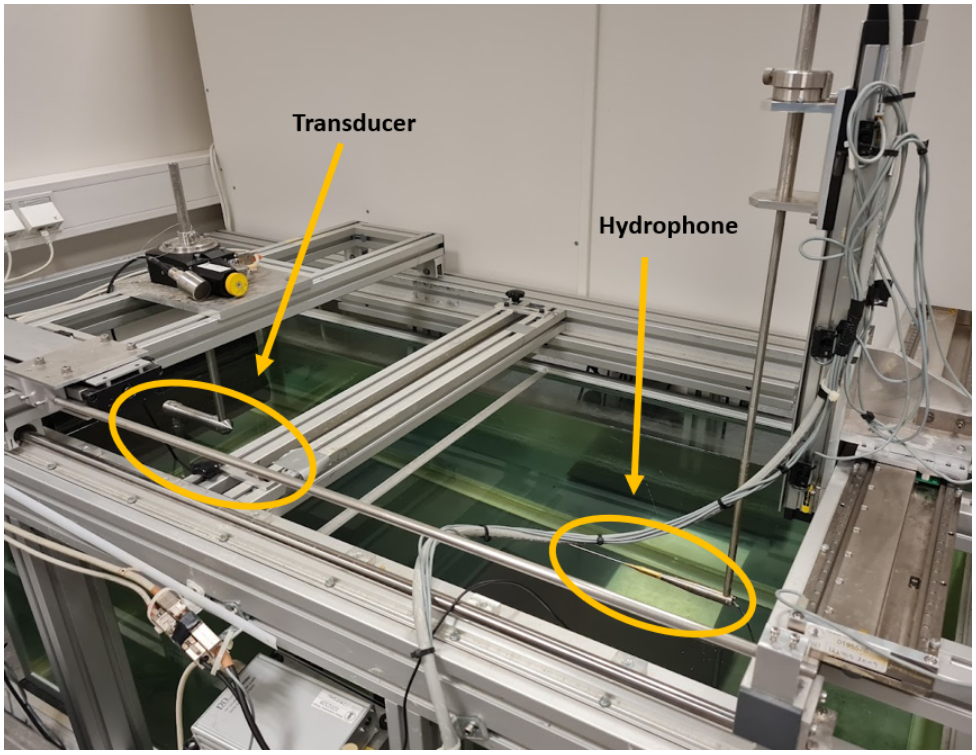

Figure 3.14: Picture illustrating the measurement setup, where the transducer and hydrophone are highlighted.

3.4 Signal processing

The sound velocity is commonly determined by calculating the transit time in a specific pulse feature. This can be the first peak, the start of the signal (signal onset), or one or several zero-crossings in a specific portion of the pulse [36].

However, several factors can change the shape of the propagating pulse, making it problematic to determine the velocity accurately. There are several methods to calculate the sound velocity, and in this project, two methods will be studied and later compared.

The first method does not have a defined name but will be named the Zero-crossing method (ZCM) in this project. It is a widely used method [9, 14, 21] and is based on measuring the transit-time using the same zero-crossings in two pulses of interest.

The second method studied here is the Fourier spectrum method (FSM) [14, 36, 50, 70, 71, 72]. Using a Fourier Transform, the signals are transformed into the frequency domain, where the unwrapped phase is used to calculate the speed of sound. One advantage of this method is the ability to use short pulses. However, one must ensure that the pulses are long enough that the centre frequency is well-defined [72].

This section will first present the sampling parameters used for signal processing. The theory of both methods will then be discussed, along with implementing them. Lastly, a few remarks will be made about the digital filters used in this project.

3.4.1 Sampling parameters

As to give an overview of the parameters used for the signal output and data collection, a table summarizing the variables is given here. These variables will be the same for both signal processing methods.

Table 3.5: Parameters used throughout the data collection.

Nr. of bits	Horizontal res.	Vertical res.	Sampling freq.	Output voltage	Signal Freq.	Burst period
16	20 μs	50 mV	500 MHz	10 V	500 kHz	10.0 ms

The oscilloscope screen in Fig. 3.8, shows the horizontal and vertical resolution and the typical waveform used throughout the project, where the vertical resolution is set to maximum without reaching saturation. The waveform was further set to be split into 100 k sampling points and exported to MATLAB for further processing. Other parameters will be given when applicable.

3.4.2 Zero-crossing method

In the Zero-crossing method, the sound velocity is determined by measuring $t_B - t_A$ by direct transit time measurements of Signals A and B. Signals A and B are defined in Section 2.2.1, along with the corresponding t_A and t_B. The transit time is calculated at a point where the sampled signal crosses the zero voltage line, known here as a zero-crossing. This zero-crossing can either be in the transient part, the steady-state (stationary) part of the signal onset, illustrated in Fig. 2.2. Using zero-crossing number i, where i = 1,2,3..., for Signals A and B, the time between the arrival of the pulses can be calculated. This is shown in Fig. 2.2, where zero-crossing number i is marked in red. The signal onset is found at i = 1. This can be used to calculate the speed of sound as it is less prone to dispersion effects [37], but the accuracy of this method is debated [36, 37]. At the start of the signal, the energy is low, and any coherent acoustic interference (ref. Section 3.5.3) in this area could lead to inaccurate measurements [14]. Further, the signal onset can be hard to locate [36].
In this project, the average sound velocity will be calculated using several zero-crossings in the steady-state portion of the signal, thus the portion of the signal with a defined frequency and amplitude. The resulting transit time will be more robust against noise sources by averaging over several zero-crossings.

To calculate the transit time using the Zero-crossing method, the zero-crosses must be located. Since the values are discrete, few to no point intersect at these zero-crosses. However, the signal-to-noise ratio (SNR) is calculated to be 37dB (Section 3.4.5), thus an almost linear part of the sine-wave around zero can be assumed. Linear interpolation as a method for calculating the zero-crosses is therefore assumed to be sufficient.
Locating the zero-crossing at one point using linear interpolation is illustrated in Fig. 3.15. The slope

of the straight line, m, from the points before and after the zero-crossing can be found by [73]

$$m = \frac{V_{i+1} - V_i}{t_{i+1} - t_i}, \tag{3.4}$$

where $s_i = (t_i, V_i)$ is the sampled time and voltage before the zero-crossing, and $s_{i+1} = (t_{i+1}, V_{i+1})$ is the sampled time and voltage after the zero-crossing. In linear interpolation, the zero-cross can be assumed to lay on a straight line between points s_i and s_{i+1}. Thus can the slope be defined as

$$m = \frac{V_{i+1} - 0}{t_{i+1} - t_{0,i}}, \tag{3.5}$$

where the zero-crossing is defined in point $s_{zc} = (t_{0,i}, 0)$, thus at the zero voltage line at time $t_{0,i}$. The time of the zero-crossing can then be calculated:

$$t_{0,i} = t_{i+1} - \frac{V_{i+1}}{m}. \tag{3.6}$$

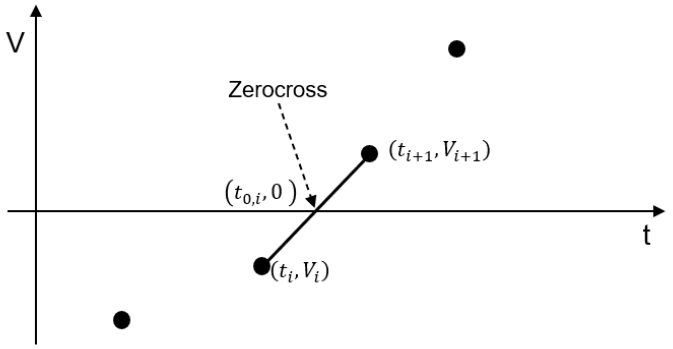

Figure 3.15: Example of calculated zero-cross using linear interpolation

In Matlab, the zero-crosses are calculated by multiplying V_n with V_{n+1}. A zero-cross is located between the discrete points if the resulting number is negative.

Locating all zero-crosses in the received signal is necessary to separate the signal of interest from the noise. This is done by summing all the discrete amplitude values between two zero-crosses. The zero-crosses corresponding to pulses can be separated from zero-crosses corresponding to noise by setting a voltage threshold value. It is crucial to find a threshold higher than the noise level but low enough to detect the start of the signal.

When the start of the signal is located, the steady-state portion of the signal can be found by studying the waveform and defining the zero-crossings of interest. Using the same zero-crosses for Signal A and Signal B, $t_B - t_A$ can be calculated and inserted into Eq. (2.13). This is done for each zero-crossing throughout the steady-state portion of the signal before the average sound velocity is calculated. Although averaging reduces the variation in sound velocity due to noise sources, the discrepancies will still be an uncertainty assessed in Section 6.8.2.

This work uses the zero-crossing method for liquid samples using a six-period pulse as the primary signal processing method. It has further been used when measuring the sound velocity of the Plexiglas buffer. The signal processing method will further be compared to the Fourier Spectrum Method, introduced in the next chapter, using both a two-period pulse and a six-period pulse. For the two-period pulse, the average sound velocities using zero-crosses number 4 and 5, illustrated in Fig. 3.16a have been found, as the accuracy of the signal onset has been debated [36, 37]. For the six-period pulse, the average sound velocity is found using the whole steady-state part of the signal, illustrated in Fig. 3.16b. In Section 6.5, these zero-crosses are shown to be an accurate representation of the steady-state portion of the signal.

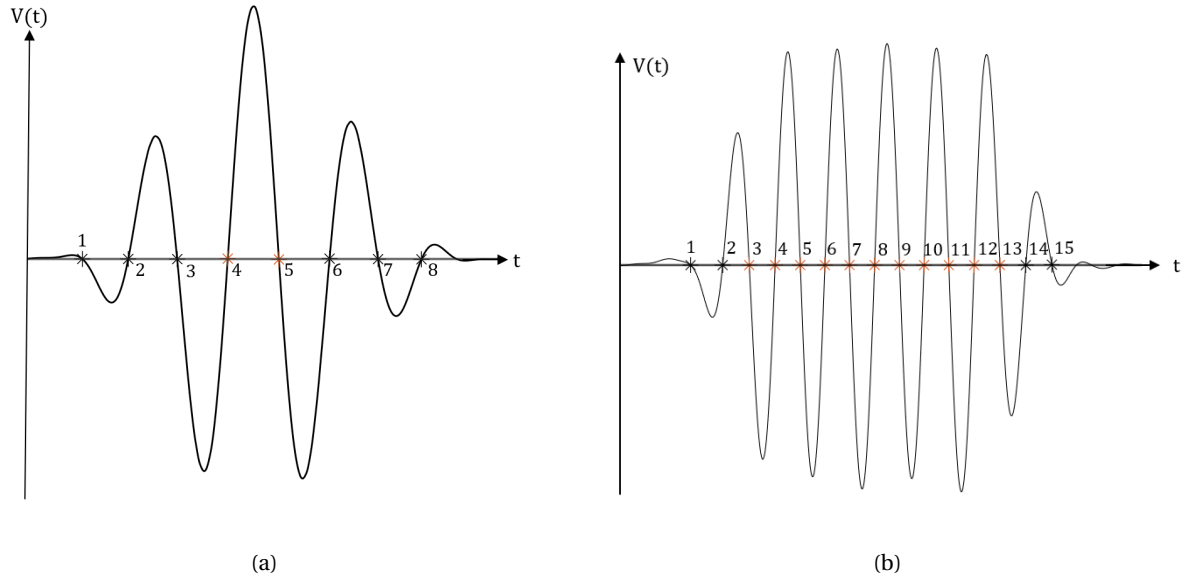

(a) (b)

Figure 3.16: Illustration of a two-period pulse (a) and a six-period pulse (b) with corresponding marked zero-crosses, where the red zero-crosses are used for sound velocity measurements in this project.

The disadvantage with this method is the need for a signal with a steady-state to be able to assume propagation of a continuous wave, an assumption needed in the theory described in Sections 2.3.1 and 2.4. To achieve a steady-state, a several-period pulse is needed. As will be evident in Sections 3.5.3 and 3.5.5, such a pulse can result in coherent interference from several sources, decreasing the accuracy of the measurements.

3.4.3 Fourier Spectrum method

The Fourier spectrum method (FSM) [14, 50, 70, 72] will in this project be used as the second method for calculating the sound velocity. It is based on using the unwrapped phase angle of the DFT (Eq. (2.63)) of the signals and will be explained by showing an example using distilled water as a liquid sample. The case of applying a two-period pulse and applying a six-period pulse will be discussed. The approach is based on the method explained in Mathias Saether's dissertation [14], and the theory is presented in Section 2.2.3.

The waveform used as an example is acquired with the experimental setup shown in Fig. 3.1 with a 500 kHz two-period 10 V peak-to-peak voltage amplitude. Further parameters used are listed in Table 3.5. Distilled water at T = 24.03^oC is used as a sample, which results in c_{td} = 1494.0 m/s (ref. Eq. (2.2)). In Fig. 3.17a, the original response used is shown after filtering and eliminating the output from the signal generator (ref. Fig. (2.2)).

When measuring the sound velocity, the first step is identifying and isolating the pulses of interest. The start of the signals will be defined by the start of the first peak, where the start is defined at the zero-crossing using the zero-crossing method (cf. section above). The zero-crossing will further define the end of the signal at the end of the last peak in the last period. In Fig. 3.17a, the first and last black mark shows the start and the end of the signals, where the voltage signals are the time domain signals, $V_{7,A}(t)$ and $V_{9,B}(t)$, corresponding to the pulses S_A and S_B respectively. The pulses are extracted and zero-padded with 100 000 samples, where the result is shown in Fig. 3.17b. Abruptly truncating the signal can lead to potential aliasing effects [14], but it is later shown that these potential effects are negligible and will be treated as an uncertainty.

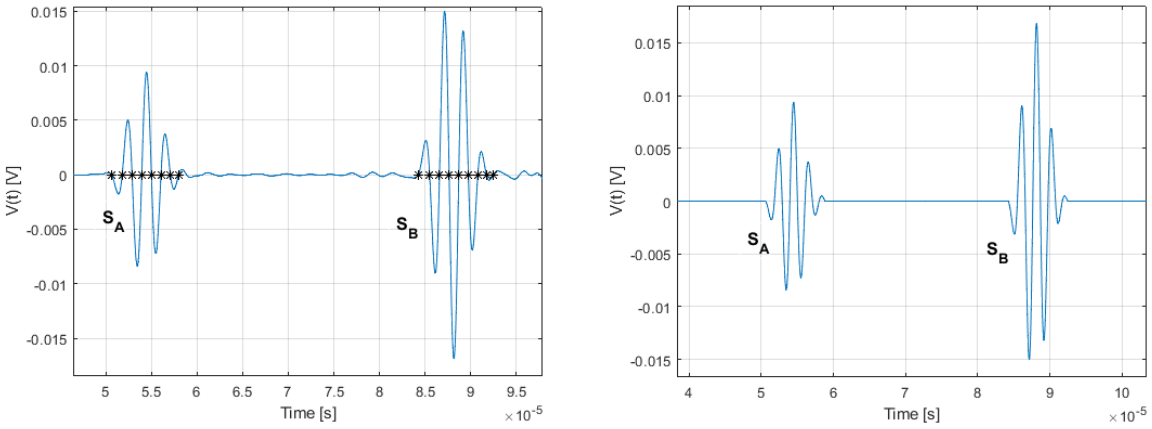

Figure 3.17: a) Received response after filtering for a two-period 500 kHz signal. The marked zero-crosses indicate the start and end of Signals A and B. Measurement is taken with the setup shown in Fig. 3.1 with distilled water and a 2 period 500 kHz pulse. b) Isolated pulses based on the signal in Fig. a)

Each signal is then individually isolated for further processing and zero-padded with 100 000 samples each. They are then circularly rotated to the beginning of the sample window to avoid the 2nπ phase ambiguity [70], with time shifts t_A^{shift} and t_B^{shift} for signals A and B, respectively. The time-shifted signals are then Fourier transformed using Eq. (2.63), where Fig. 3.18 a) and c) present the magnitude of the DFT, and b) and d) the wrapped phase angle.

Using Matlab, the phase of the DFT is presented as the wrapped phase angle, which means that it is presented between an interval of $\pm\pi$. If the actual phase is outside this interval, the phase value is increased or decreased with multiples of 2π to keep the value between $\pm\pi$ or $\pm 180^o$ [74]. In Fig. 3.18 b) and d), which shows the wrapped phase of the DFT of the shifted pulses, sudden phase changes from $-\pi$ to $+\pi$ can be observed. In an infinitely long measurement window, these phase changes would be exactly 2π [14]. In this project, they are approximately 2π (± 3.12) due to the frequency resolution

when sampling a finite response.

The next step is to unwrap the phase, which is done through Matlab using the command *unwrap* [56]. If there is a phase change greater than or equal to π, the command shifts the angle by adding multiples of 2π until the phase difference is less than π. The unwrapped phase is shown in Fig. 3.18 c) and e). The frequencies below 250kHz and above 700 kHz were filtered out due to noise. The phase spectrum between 250 kHz and 700 kHz is thus shown.

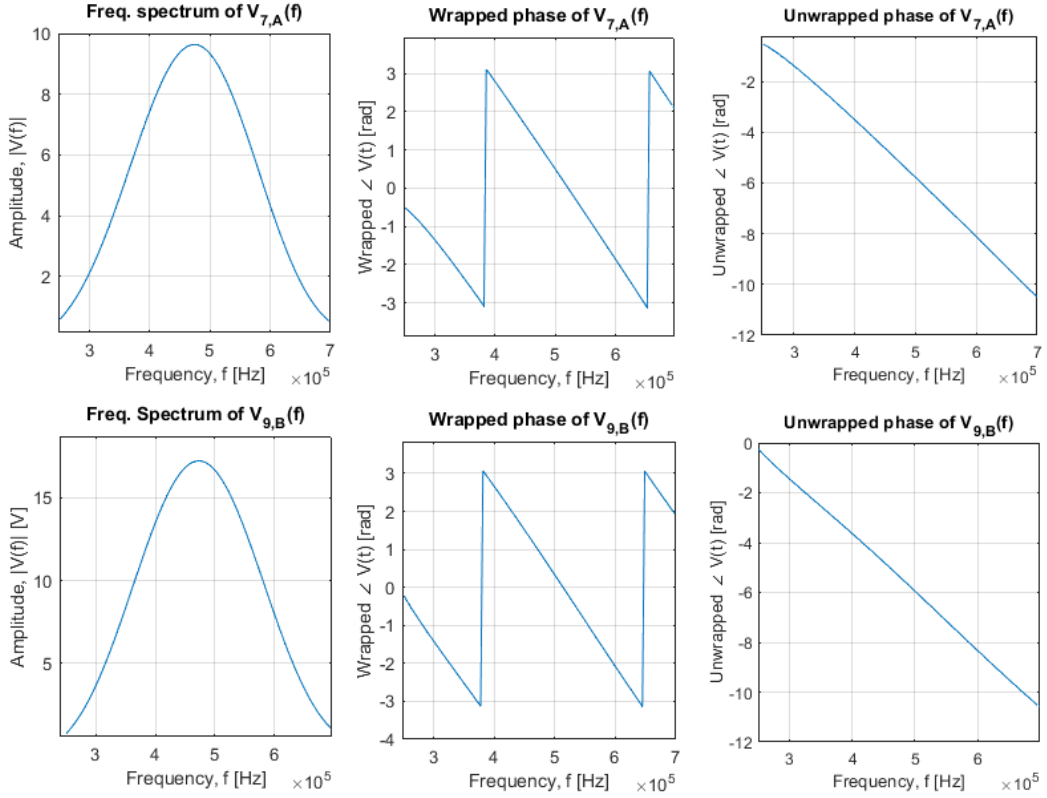

Figure 3.18: The unwrapping process of the two-period pulses in Fig. 3.17a. Figs. b) and e) shows the wrapped phase, and Figs. c) and f) shows the unwrapped phase of $V_{7,A}(f)$ and $V_{9,B}(f)$ respectively. Figs. a) and d) shows the magnitude spectrum's of signal A and B.

The phase angle of the shifted signals above, $\angle V_{7,A}^{shift}$ and $\angle V_{9,B}^{shift}$ are related to $\angle V_{7,A}$ and $\angle V_{9,B}$ by [14]

$$\begin{aligned} \angle V_{7,A} &= -\omega t_A^{shift} + \angle V_{7,A}^{shift} \\ \angle V_{9,B} &= -\omega t_B^{shift} + \angle V_{9,B}^{shift}. \end{aligned} \tag{3.7}$$

In Eq. (3.7), ωt_A^{shift} and ωt_B^{shift} are the corresponding phase shifts due to the time shifts t_A^{shift} and t_B^{shift} respectively. $\angle V_{7,A}^{shift}$ and $\angle V_{9,B}^{shift}$ are found using the unwrapped phase from Fig. 3.18.
Using Eq. (3.7) together with Eq. (2.30), the sound velocity can be measured as a function of frequency. For comparison with the zero-crossing method presented above, the sound velocity at f = 500 kHz will be extracted. The resulting sound velocity is presented in Fig. 3.22a.

The results above provide an accurate method to determine the sound velocity in a two-period signal. However, with a longer pulse length, the center frequency will be more defined and the bandwidth of the signal will decrease. This is evident in Fig. 3.19 b) and e) upon comparing the magnitude spectra with Fig. 3.18. In Fig. 3.19, the same experimental setup is applied as for the two period pulse (ref. Fig. 3.17b, with a six-period pulse at f = 500 kHz, using distilled water at $24.05^{o}C$. The same signal processing method is applied, where the phase of the DFT is presented in Fig. 3.19 b) and d), and the wrapped phase angle in c) and e).

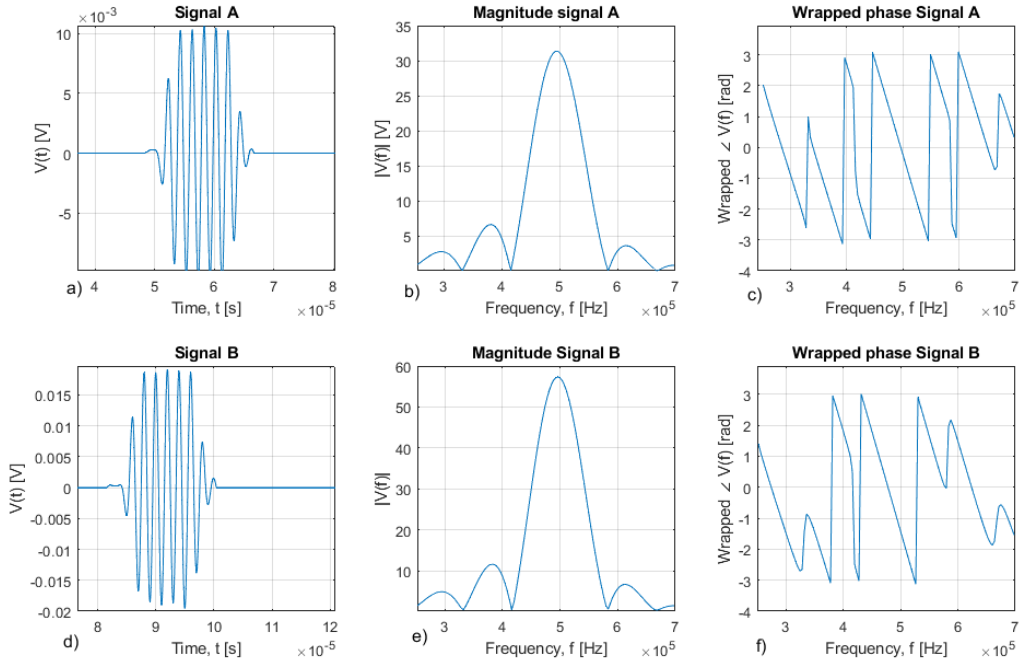

Figure 3.19: The isolated, zero-padded and circularly rotated signals A and B are shown in Fig. a) and d) with a six-period 500 kHz pulse. The corresponding frequency spectras are shown in b) and e), and the wrapped phase is presented in c) and f) for signal A and B respectively.

A consequence of the decrease in bandwidth, is that low frequency signal-to-noise (SNR) areas will appear. In the low SNR areas, identified by the dips between peaks in Fig. 3.19 b) and e), the wrapped phase does not reach $\pm\pi$. When unwrapping the phase, these areas will result in discontinuities, observed in Fig. 3.20. At the first dip, right after 300 kHz, the wrapped phase is $\neq \pi$, and a discontinuity in the unwrapped phase can be seen at that point. The discontinuities will further provide inaccurate sound velocity measurements, as can be observed in Fig. 3.21. These phase unwrapping problems upon low SNR have been discussed by several other authors [75, 76, 77].

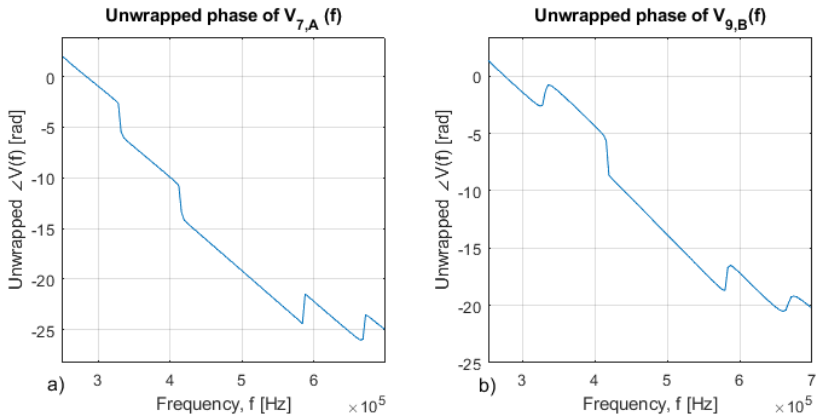

Figure 3.20: The unwrapped phase of a) $V_{7,A}(f)$, and b) $V_{9,B}(f)$ of Signals A and B in Fig. 3.19 respectively.

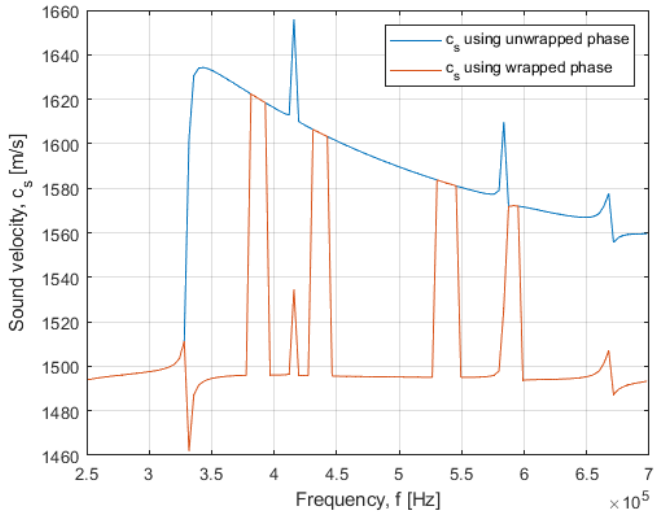

Figure 3.21: Sound velocity as a function of frequency using the wrapped (red) phase, and the unwrapped (blue) phase for the six-period pulse shown in Fig. 3.19

Fig. 3.21 shows, however, that the sound velocity obtained using the wrapped phase is inaccurate with almost 100 m/s, which is of such magnitude that the sound velocity can be discarded. This definite error is an inherent benefit of the FSM in general [78], which makes it easy to determine when accurate velocity measurements are acquired.

In Figs. 3.19 and 3.21, it can however be seen that the wrapped phase at f = 500 kHz is accurate due to the large SNR. The wrapped phase has been seen to represent all measurements in the relevant measurement series accurately. It has thus been decided to use the wrapped phase for sound velocity measurements when applying the FSM with six periods, and a solution for accurately unwrapping has not been further investigated.

To illustrate how the speed of sound changes from abruptly truncating the signal at the last zero-cross to linearly trailing off the signal for the two-period and six-period pulse, the sound velocities are calculated in both cases for both signals using the method described above. The results are shown in Fig. 3.22, where both scenarios are displayed for both signals. The resulting sound velocities are

shown in Fig 3.23.

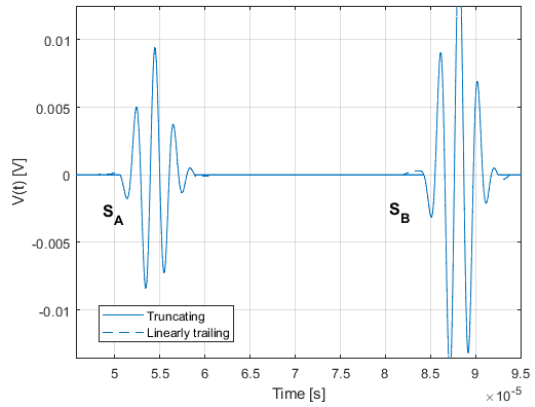

(a) Two-period signal

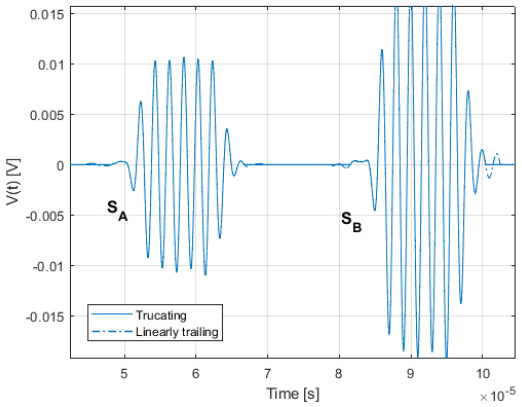

(b) Six-period signal

Figure 3.22: Signal 3.17a (a) and Signal 3.19 (b) isolated by linearly trailing the signal, and by truncating the signal.

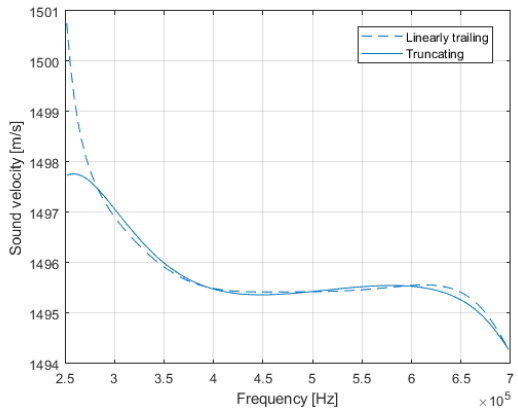

(a) Two-period signal

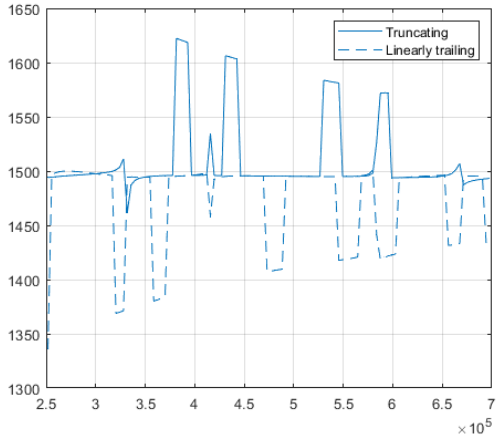

(b) Six-period signal

Figure 3.23: The calculated sound velocity using the Fourier Spectrum method for both scenarios shown in Fig. 3.22a at 24.03^oC and 1 atm (a) and Fig. 3.22b at 24.05^oC at 1 atm (b). The resulting sound velocities are not corrected for diffraction

It can in Fig. 3.23b be noticed that the sound velocity as a function of frequency changes between the two scenarios. However, at f = 500 kHz, thus at the frequency of interest when comparing the method to the ZCM, the sound velocities are almost identical. For the truncated signal, a sound velocity of c_s = 1495.192 m/s is measured, while for the linearly trailed, c_s = 1495.184 m/s. Using Eq. (2.12), this will correspond to an uncertainty in transit time due to truncating the signal of

$$u(\Delta t)^{6period}_{trunc} = \frac{2 \cdot 25.18 \cdot 10^{-3}}{1495.184} - \frac{2 \cdot 25.18 \cdot 10^{-3}}{1495.192} = 1.802 \cdot 10^{-10} s, \tag{3.8}$$

where the sample length is measured in Section 3.1.8. It should be noted that these values are not corrected for diffraction. Corrected for diffraction (ref. Section 2.3.1), the sound velocities are measured to c_s = 1493.802 m/s for the truncated, and c_s = 1493.798 m/s for the linearly trailed, against a

theoretical sound velocity at 24.05^oC and 1 atm of c_{td} = 1494.07 m/s. This corresponds to a deviation of ≈ 180 ppm for both scenarios, which is a promising result for later sound velocity measurements.

The same approach can be used for the two-period signal, Fig. 3.23a. A deviation can be seen between the two scenarios as a function of frequency as for the six-period pulse. At 500 kHz the sound velocity of the truncated signal (not corrected for diffraction) is c_s = 1495.32 m/s, and the linearly trailed is 1495.28 m/s. Using the same method as above, this corresponds to $u(\Delta t)_{trunc}^{2period}$ = $9.01 \cdot 10^{-10}$ s. Corrected for diffraction, the truncated sound velocity corresponds to c_s = 1493.95 m/s, while the linearly trailed gives c_s = 1493.91 m/s. Using T = 24.04^oC and 1 atm, c_{td} = 1494.0 m/s. This corresponds to a deviation of 60 ppm, which is even more promising than for the six-period pulse.

The difference in sound velocity for both the two-period and six-period pulse is small enough to conclude that truncating the signal is sufficient. The total transit time uncertainty due to truncating the signal when using FSM is further assessed in Section 6.8.2.

A comparison between the zero-crossing method and the Fourier spectrum method is shown in Section 6.5, and the resulting choice of signal processing method is discussed in Section 7.2.

3.4.4 Filtering

As will be evident in the experimental part of the project, a waveform at the oscilloscope contains both the acoustic signal of interest and noise. Therefore, filtering out as much noise as possible is essential to increase the Signal to Noise ratio (SNR).

Two coherent noise sources must be accounted for; the coherent noise with the same frequency as the wanted signal and the coherent noise with frequencies above or below the wanted signal. Coherent noise with the same frequency as the wanted signal is discussed in Section 3.5.3. The noise with frequencies above or below the wanted signal can be filtered out using a causal FIR-filter, a filter where each sample is a weighted sum of the present and past inputs [54]. A bandpass filter is chosen in this project to remove both the upper and lower frequencies.

Initially, an analogue Krohn-Hite Model 3940 filter was implemented in the measurement circuit, with 200 kHz and 800 kHz cut-off frequencies. When the analogue filter was incorporated into the measurement circuit, the waveform became too "dynamic" where its amplitude and phase fluctuated and thus lacked sufficient stability for accurate sampling. This was believed to be due to the strong DC-component present from the T/R-switch. Changing the cut-off frequencies of the filter was further tried without success. A digital filter was therefore chosen. As the waveform had to be sampled quite often, a filter with a low computational cost was needed. Further, due to the Fourier Spectrum method being dependent on the unwrapped phase of the signal, the filter could not cause any phase distortions. Matlab has a pre-designed digital filter named *bandpass* which is a casual minimum-order FIR-filter [56]. It further compensates for the phase delay introduced by the filter itself [56]. With a centre frequency of 500kHz, the cut-off frequencies are 200kHz and 800kHz. The default value of the stopband attenuation is 60dB [56], which has been tested to be computationally

efficient for the project.

A large DC-component is present in the analogue signal due to the T/R-switch. The DC-component results in a steep step response and a discontinuity where the derivative is undefined due to an infinite amount of frequency components present. Although the bandpass filter filters out most unwanted frequencies, fluctuations due to the DC-component will still be present after filtering, shown in Fig. 3.24a, and enlarged in Fig. 3.24b. The blue curve shows the original signal before filtering, named Waveform A, and the yellow curve shows the signal after filtering, applying the *bandpass* filter, named Waveform B. Due to the fluctuations still present in Waveform B, the waveform is cut right after the discontinuity, shown as a black dotted line in Fig. 3.24a, and manipulated, assuring that the first sample starts at the zero voltage line. The DC-component can then be removed by filtering the signal through the bandpass filter. The result is shown as the red curve in Figs. 3.24a and 3.24b and is named Waveform C.

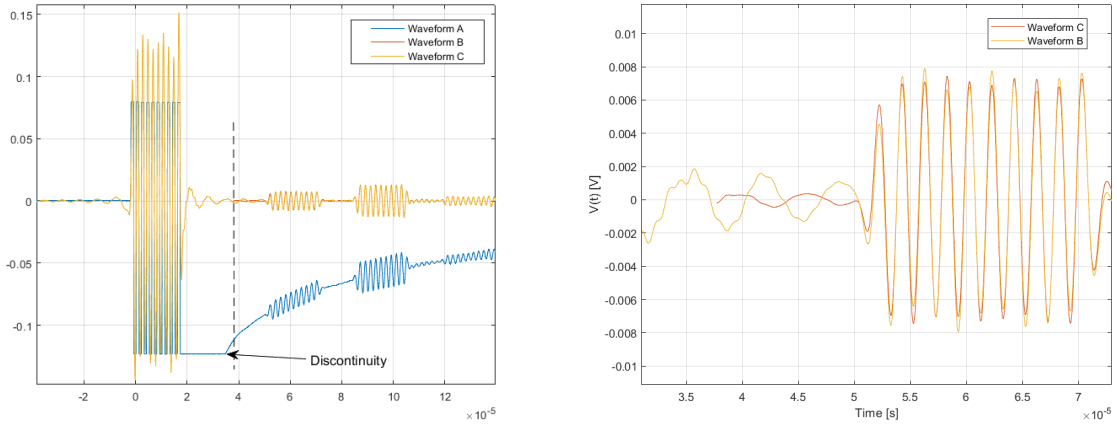

(a) (b)

Figure 3.24: a) Waveform A shows an original measured signal from the measurement cell described in Section 3.5, using f = 500kHz, 10V peak-to-peak amplitude, and 10 periods. Waveform B is the processed signal after applying band-pass filter. Waveform C is the filtered, processed signal after removing the discontinuity in the original signal. Fig. b) shows an enlarged part of Fig. a).

From Fig. 3.24b, it is evident that if only the portion of the pulse after the discontinuity is chosen (Waveform C), the signal is significantly improved in terms of fluctuations between the output transducer-signal and the first pulse. This method is therefore implemented in the data collection script when measuring the sound velocity. It should be noted that when measuring the sound velocity, the signal on the oscilloscope is enlarged (cf Fig.3.8) and the discontinuity is not visible. However, the signal must still be cut as explained above before further processing.

Although the bandpass filter claims to compensate for the phase distortion, it is important to see how much distortion there will be after filtering. The phase of waveform C in Fig. 3.24 is thus calculated before and after filtering. The resulting change in phase due to the applied filters is shown in Fig. 3.25.

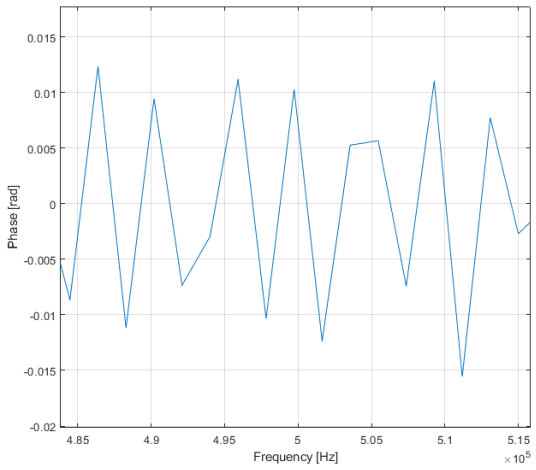

Figure 3.25: Calculated phase distortion in waveform C as a function of frequency when applying the predesigned filter *bandpass* in Matlab.

There will be a slight distortion in phase due to the applied filter. Several other built-in Matlab filters are studied to see if this phase distortion can be reduced or eliminated without success. An uncertainty in transit time when calculating the Fourier Spectrum method due to phase distortions thus is set to 0.01 rad, corresponding to $u(\Delta t)_{ph} = 3.18 \cdot 10^{-9}$ s.

3.4.5 Noise

Different noise sources can affect the acoustic signals used to calculate the sound velocity in the liquid, which may lead to a decrease in accuracy. It is thus crucial to identify the noise sources and minimize their influence on the signals of interest.

Signal-to-Noise ratio (SNR)

Noise affects the signal, decreasing the accuracy of the calculated sound velocity when determining the sound velocity from the received pulses. As can be seen in Section 6.8.2, the accuracy of the sound velocity decreases with increasing noise. Therefore, the ratio of signal to noise should be kept as high as possible.
The signal-to noise ratio, SNR, is defined as the power of signal to the power of noise, commonly specified in decibels [4]

$$SNR = 10log\left(\frac{W_S}{W_N}\right) = 20log\left(\frac{V_{RMS}^S}{V_{RMS}^N}\right)[dB], \tag{3.9}$$

where W_S and W_N is the power of signal and noise respectively, V_{RMS}^S is the root-mean-square (RMS) voltage of the signal and V_{RMS}^N is the RMS voltage of the noise.

For a sampled signal, the RMS voltage of the noise in Eq. (3.9) may be expressed as [4]

$$V_{RMS}^{N} = \sqrt{\frac{1}{N}\sum_{n=1}^{N} V_{n,N}^{2}}, \tag{3.10}$$

and the same for the RMS of the signal.

Incoherent noise contributions

Incoherent noise, also known as random noise, is composed of both temporal and spatially random noise, which could appear anywhere in the waveform [79].

The SNR due to incoherent noise is usually improved by applying a bandpass filter, as explained in Section 3.4.4. However, this only eliminates noise outside a specific frequency range, and the incoherent noise could be anywhere on the frequency spectrum. The SNR is thus further improved by averaging multiple signal traces.

To calculate the V_{RMS}^{N} in the received signal, the unfiltered, original waveform, shown as the blue response in Fig. 3.24a is utilized, where the signal has been averaged 512 times. There is a strong DC-component present in the original waveform, which makes it hard to calculate the average voltage amplitude. The data points prior to the received transducer signal are thus utilized to measure the incoherent noise RMS value, V_{RMS}^{N}, by applying Eq. (3.10). The signal will further contain the same DC-component. Thus, to calculate the signal RMS value, it is assumed that the amplitude of the signal in Waveform C in Fig. 3.24a is the same as the unfiltered signal amplitude. This is not necessarily true, but it can give a rough estimate of V_{RMS}^{S}. For Signals A and B, a resulting SNR of 37 dB and 39 dB is calculated using Eq. (3.9). No significant changes in the SNR have been observed throughout the measurement series.

Coherent noise contributions

Coherent noise is noise sources with the same frequency as the carrier frequency of the signal of interest but with different amplitude and phase. The coherent noise source can thus not be eliminated with filtering or averaging. The different coherent noise sources in the project must therefore be identified and analysed to improve the SNR, shown in Fig. 3.26. The coherent noise can arise from several sources, e.g. reverberation, transducer echos, side lobe interference and acoustic cross-talk. By identifying the noise sources, adjustments can be made to reduce the effect the noise contributions have on the pulses of interest, increasing the accuracy of the sound velocity measurements.

Two pulse trains are studied using the experimental setup presented in Fig. 3.1 with f = 500 kHz and a 10 V output amplitude. One measurement is conducted in the absence of a liquid sample, enabling the investigation of the buffer contributions. The result is shown as the red response in Fig. 3.26. The blue response in Fig. 3.26 shows the response when distilled water is used as a liquid sample, thus the response used to measure the sound velocity in the liquid. To inspect each noise contribution

individually, a two-period burst is selected.

S_1 is the reflection from the buffer/sample interface, while S_3 is the reflection from the sample/reflector interface. Further, S_2 is a mode-converted wave that has propagated once as a compressional wave through the buffer and once as a shear wave, S_{cs} (Section 3.5.3). In Section 3.5.5, S_4 is identified as the reflector reverberation. Lastly, S_5 and S_6 correspond to the four times traversed pulse in the buffer and sample, respectively, explained in Section 3.5.3. Side-wall reflections have not been identified.

The pulses S_1 and S_3 are the signals of interest in this project. From Fig. 3.26, S_1 is well isolated and can easily be identified. Isolating S_3 can, however, become complicated if a longer pulse is chosen due to S_4 and S_5 being in proximity of the signal of interest. This is discussed in Section 3.5.6.

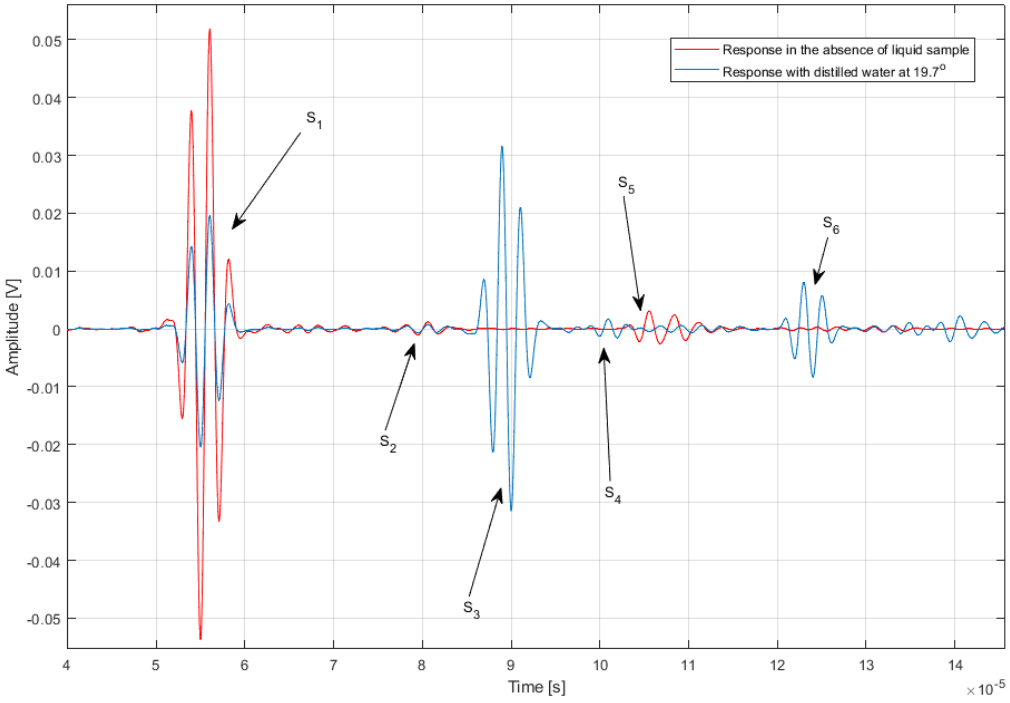

Figure 3.26: Measurements conducted using the experimental setup presented in Fig. 3.1, used for investigation of noise contributions. Red curve shows the response in the absence of a liquid sample. Blue curve shows response using distilled water at 19.7^oC as liquid sample.

3.5 Construction of the measurement cell

Multiple parameters need to be considered to construct the measurement cell used in this project. It is desirable to have low uncertainty. Consequently, the acoustic noise sources must be identified, and design implementation must be done based on these sources. The design must also account for an increase in temperature and a change in sound velocity in the sample. This section will discuss the design considerations and present the final result.

3.5.1 XSENS' preferences

XSENS Flow Solutions [2] set several preferences in advance. An operational frequency of f = 500 kHz was desired to account for possible dispersion effects in crude oils. The measurement cell was also intended to be small, lightweight, and easy to transport. All parts of the measurement cell, including buffer, reflector, and sample area, would thus have to be constructed accordingly. In addition, the sample area would have to be designed so that not much liquid would be required, with a limit of 0.5 litres. A measurement cell measuring precise sound velocity from 1250 m/s to 1580 m/s was preferred to accommodate sound velocities in crude oils and saline water at higher temperatures. Nesse's [7] measurement cell (ref. Fig.1.1) was used as a starting point, with the goal of making it smaller and lighter while obtaining as high a level of precision as possible.

The preferences above were thus all considered when constructing the measurement cell, together with the objective to measure the sound velocity with a relative expanded uncertainty of less than 1000 ppm.

3.5.2 Material considerations

When choosing the material for both the measurement cell and the buffer, many factors had to be considered. In this section, Table 3.6 will be used as a base for discussion.
Due to the principle behind the solid buffer method (Section 2.2.1), the solid buffer must have a different impedance than the liquid sample. However, if the material impedance is too high, most of the sound energy will be reflected. This will, in turn, decrease the amplitude, and thereby the SNR, of Signal B.

Table 3.6: Material properties of three common acoustic materials. Reflection coefficients are calculated against water at 20^oC. Thermal expansion coefficients, α, are found in [80]. The other values are from [23] p. 526. Shear sound velocity is calculated using Eq. (2.1) with tabulated values.

Material	Compressional sound velocity [m/s]	Shear sound velocity [m/s]	Density [kg/m^2]	Compressional Impedance [MRayl]	Poisson's ratio [-]	Youngs Modulus [GPa]	Reflection coefficient [-]	α [/^oC]
Aluminium	6300	3173	2700	17.0	0.33	71	0.84	21-24·10^{-6}
Plexiglas	2650	1082	1200	3.2	0.4	3.2	0.38	68-75·10^{-6}
Stainless steel	6100	2490	7770	47.0	0.28	195	0.94	(16-17.3)·10^{-6}

Thermal expansion and elasticity are two parameters of interest when constructing the chassis around the buffer. Suppose two materials are clamped together with different linear thermal expansion coefficients. The difference may cause thermal shock to the materials when heated up, causing the measurement cell to crack and leak. It is thus advantageous to ensure that the materials have similar thermal expansion coefficients.

Suppose the materials differ in terms of thermal expansion. In that case, Young's modulus indicates how the materials will interact with each other, as it is a measure of elasticity in a material. A stiff material has a high Young's modulus[81]. If a material has a large thermal expansion coefficient and

is clamped against material with a high Young's modulus, the material may crack due to the increased stress. Materials with a high Young's Modulus are further less malleable and thus difficult to work with when building the measurement cell.
The material properties listed in Table 3.6, together with the discussion above, support the use of Plexiglas as a buffer with an aluminium chassis.
The aluminum provided by the Department of Physics and Technology's workshop is Aluminium Alloy 6082 with a linear temperature expansion coefficient of $\alpha = 24 \cdot 10^{-6} m/(m^o C)$ [52, 82], while the Plexiglas used for the solid buffer has a linear temperature expansion coefficient of $\alpha = 70.0/^o C$ [53].

The uncertainties in α_A and α_p are not given and are thus found by calculating the standard deviation of several online tabulated coefficients. For Plexiglas, the thermal expansion coefficients found online are α_p = (68-75)$\cdot 10^{-6}$ $/^o C$ [80], and α_p= 70$\cdot 10^{-6}$ $/^o C$ [53], resulting in a standard deviation of $2.35 \cdot 10^{-6}/^o C$.

For Aluminium Alloy 6082, $\alpha_A = 24 \cdot 10^{-6}/^o C$ [52], $\alpha_A = 24 \cdot 10^{-6}/^o C$ [82], and $\alpha_A = 23.4 \cdot 10^{-6}/^o C$ [83], resulting in a standard deviation of $0.35 \cdot 10^{-6}/^o C$.

3.5.3 Considerations due to acoustic noise

Before the dimensions and shape of the measurement cell were finalised, a thorough analysis of the acoustic noise contribution was carried out.
In a solid-buffer measurement cell, the transducer will not only receive the signals of interest, S_A and S_B, but will also be prone to noise due to reflections, echos and shear waves. This can reduce the accuracy of the transit time measurements. These noise sources are coherent and can not be eliminated through averaging or filtering, and can only be limited or removed by choice in material, dimensions of the measurement cell and pulse length. This section will describe the different coherent noise sources and how they can be reduced, thus reducing the transit time uncertainty.

Echo from the main lobe

The sound velocity, using the pulse-echo buffer rod method, is found using Signals A and B (Section 2.2.1), where Signal A, S_A, is the twice traversed signal in the buffer and Signal B, S_B, has an additional propagation corresponding to twice the sample length. The sound velocity, however, may be susceptible to interference effects stemming from the signal that has traversed the buffer four times, S_{RB}, and the signal that has traversed the sample liquid four times, S_{RR}, illustrated with the orange and blue propagation paths respectively in Fig. 3.27.

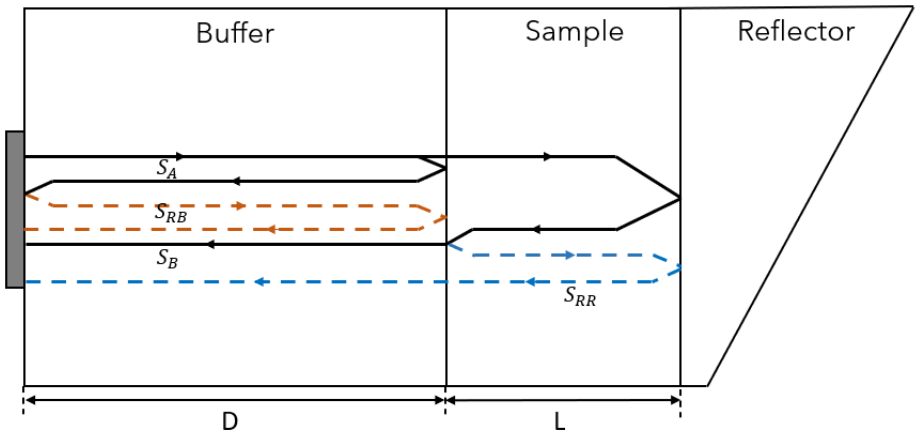

Figure 3.27: Illustration of the different sources to acoustic noise due to multiple travel times in the measurement cell, together with the signals of interest.

The second reflection inside the sample area, S_{RR}, will be neglected in the design of the measurement cell as the arrival time of the signal is much later than both S_A and S_B. It, however, has to be accounted for when choosing the pulse repetition frequency to make sure that no acoustic cross talk will occur. The second reflection inside the buffer, S_{RB}, is a possible concern. If the buffer sound velocity, c_b = 2650 m/s (ref. Table 3.6) and the sample sound velocity is within a sound velocity span of 1250 - 1580 m/s, $c_b \approx 2 \cdot c_s$. As a result, S_{RB} and S_A may arrive at the transducer surface simultaneously. As a result, S_{RB} may be a source of coherent noise, which is hard to separate from the signal of interest. The coherent noise source can be reduced or eliminated by choosing a buffer length, D, long enough to delay S_{RB} or by choosing a short sample length, L_0. In this project, S_{RB} is aimed to be placed after signal B, thus [16]

$$\frac{4D}{c_b} > \frac{2D}{c_b} + \frac{2L_0}{c_s} + \Delta t_{burst}, \tag{3.11}$$

where Δt_{burst} is the signal duration. This equation will be applied when determining the measurement cell dimensions.

Shear wave propagation

When measuring the sound velocity using the solid buffer method, mode-converted waves (ref. Section 2.3.3) are unavoidable due to the need for a solid buffer. It is here assumed that the transducer only produces compressional waves and thus will twice traversed shear wave propagation be neglected.

The only way to reduce the mode-converted waves' effect on the signal of interest is by the choice in pulse length, suitable buffer material and proper measurement cell dimension. Because the buffer is made of Plexiglas, the interference can only be limited by the buffer length, sample length and pulse length.

The mode-converted wave propagating as a compressional wave one way and shear wave the other way will henceforth be named S_{cs}. If the mode-converted signal is to arrive before signal B, then [16]

$$\frac{D}{c_{shear}} + \frac{D}{c_b} + \Delta t_{burst} < \frac{2D}{c_b} + \frac{2L_0}{c_s}. \tag{3.12}$$

Another option is to let S_{cs} arrive after S_B. This would, however, result in an unfeasible large measurement cell and is thus eliminated as an option. Eq. (3.12) will be applied in the following section to determine the dimensions of the measurement cell.

Side lobe interference

As shown in Fig. 2.9, the beam pattern of the transducer consists of a main lobe and several side lobes. Suppose the transducer is modelled as a baffled piston, and one assumes far-field propagation. In that case, the side lobes will propagate at angles determined by nodes calculated from the Bessel Directivity function, Eq. (2.47). Because the side lobes propagate at angles away from the main lobe, they will follow different propagation paths inside the measurement cell, resulting in possible coherent noise from reflections inside the measurement cell. The interference due to these reflections can be reduced by expanding the width of the buffer. However, these reflections depend on the size of the measurement cell, the temperature inside the buffer, and the sample liquid's sound velocity.

To be able to see how the side lobes evolve with different acoustic parameters and measurement cell dimensions, a simulation is created by the author, presented in Section 4.2. Based on the simulation result, a numerical analysis can be done on the magnitude of the coherent noise due to side lobe interference. This is carried out in Section 4.3.

3.5.4 Dimensional considerations

Based on XSENS's preferences (Section 3.5.1), choice of transducer element radii and frequency (Section 3.1.3), choice of material (Section 3.5.2) and the acoustic noise analysis (Section 3.5.3), the pulse length and dimensions of the measurement cell could be determined. Although XSENS preferred a small and manageable measurement cell, other factors mentioned had a great say if the measurement cell was to measure the sound velocity with an accuracy of less than 1000ppm.

The minimum length of the sample area was largely based on the sensitivity analysis presented in Section 5.3. If the measurement cell is to have a relative expanded uncertainty of less than 1000 ppm at 95% confidence level, Table 5.8 permits a relative standard uncertainty in sample length of 630 ppm at 68% confidence level. With a sample length of 25.00 mm, an expanded uncertainty of U(L_0) = 0.0316 mm is allowed, while decreasing the sample length to say, 20 mm, reduces the allowed expanded uncertainty to U(L_0) = 0.0252 mm. A smaller sample length would also result in challenging maintenance and cleaning due to physical constraints. The minimum sample length is thus set to 25 mm.

The coherent noise contributions, S_{RB} and S_{cs} are both depend on the dimensions of the measurement cell, the sound velocity of the sample, and the amount of periods. Therefore, to construct the measurement cell, an analysis was done, inspired by the analysis of Bjørndal et al. [16]. From Table 3.6, the compressional and the shear sound velocity in the buffer were set to c_b = 2650 m/s and c_{shear} = 1082 m/s respectively at room temperature. Two dimensional criteria were further set by solving for D in Eqs. (3.12) and (3.11). For the four times traversed signal, S_{RB}, to not overlap with signal B,

$$D > \frac{c_b}{2} \cdot \left(\frac{2L_0}{c_s} + \Delta t_{burst} \right). \tag{3.13}$$

Further, the mode-converted shear wave, S_{cs}, restricted the dimensions such that,

$$D < \frac{\frac{2L_0}{c_s} - \Delta t_{burst}}{\frac{1}{c_{shear}} - \frac{1}{c_b}}. \tag{3.14}$$

Two analysis were conducted, one for L_0 = 25.0 mm, and one for L_0 = 30.0 mm, presented in Figs. 3.28 and 3.29 respectively. For each sample length, two scenarios are studied. The first scenario being c_s = 1580 m/s, and the second when c_s = 1250 m/s, thus accounting for the entire sample sound velocity range of interest (ref. Section 3.5.1). For both scenarios, c_b, c_{shear}, and L_0 are constant. By accounting for all of the above considerations as a function of Δt_{burst}, the allowed buffer length can be found for each scenario. Further, by comparing the two analyses, the development of the coherent noise contributions can be found as a function of sample length. For clearer illustration, Figs. 3.28 and 3.29 are shown as a function of number of periods, $\Delta t_{burst} \cdot f$, where f = 500 kHz.

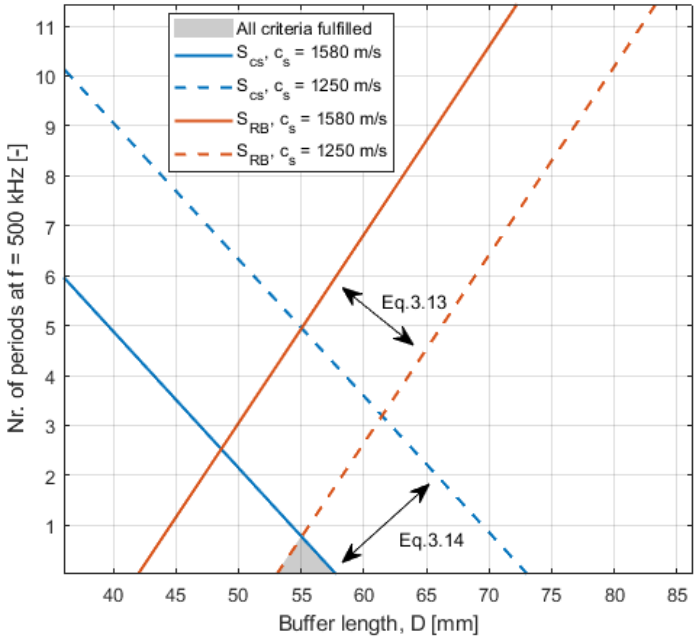

Figure 3.28: Allowed buffer length as a function of nr. of periods for L = 25.0 mm, based on the coherent noise sources where D > the red lines and D < blue lines. The range that fulfills all criteria (Eqs. (3.13) and (7.1)) for a sound velocity span of 1250-1580 m/s is marked in grey.

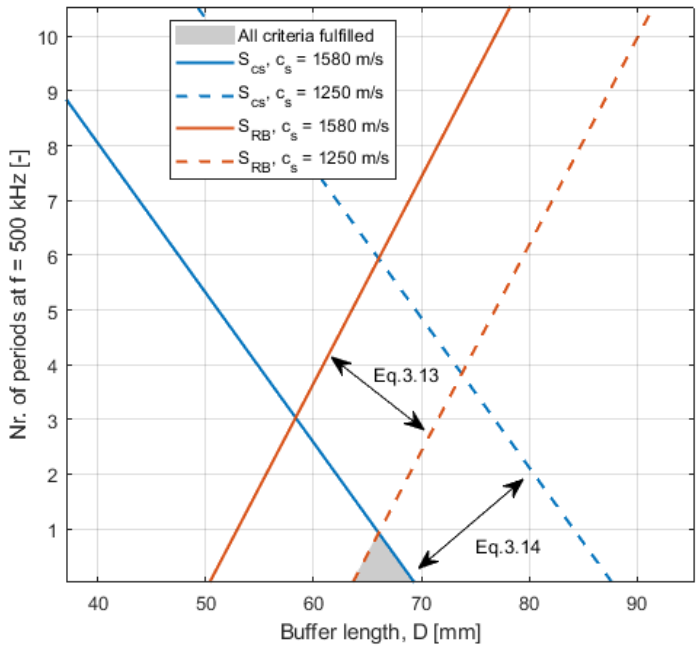

Figure 3.29: Allowed buffer length as a function of nr. of periods for L = 30.0 mm, based on the coherent noise sources where D > red lines and D < blue lines. The range that fulfills all criteria (Eqs. (3.13) and (7.1)) for a sound velocity span of 1250-1580 m/s is marked in grey.

From Figs. 3.28 and 3.29, the maximum allowed buffer length decreases as a function of sound velocity if the four times traversed buffer signal, S_{RB} is accounted for. The maximum allowed buffer length further increases as a function of sound velocity if the mode-converted signal, S_{cs}, is taken into account. The area where both criteria are fulfilled (Eqs. (3.13) and (7.1)), marked in grey, is limited by a less than one period pulse in both scenarios due to the coherent noise sources S_{RB} (at 1250 m/s) and S_{cs} (at 1580 m/s), with a narrow allowed buffer length span. A one-period pulse is not feasible, and it is thus evident that either the signal S_{RB} or the signal S_{cs} must be included as a permanent coherent noise source.

According to Fig. 11 in [16], the mode-converted signal has a significantly lower amplitude than the four times traversed signal. This was measured using a transducer in pulse-echo mode with f = 5 MHz, clamped on a Plexiglas buffer against air. Although the scenarios are not identical, it can be assumed that the amplitude of S_{cs} is lower than the amplitude of S_{RB}, and thus will S_{cs} be chosen as a permanent coherent noise source.

If the criteria set by Eq. (7.1) is removed, thus the coherent noise source S_{cs}, the coherent noise source limiting the dimensions and nr. of periods is S_{RB} at 1250 m/s. By comparing the figures, it is evident that an increase in sample length decreases the allowed nr. of periods and increases the required buffer length, both attributes not desired. A sample length of L = 25.0 mm is thus chosen.

By comparing Fig. 3.28 with Fig. 3.29, it can be seen that the allowed nr. of periods increases with increasing buffer length (when S_{cs} is neglected). It was, however, desirable to have a measurement cell as small as possible (cf. Section 3.5.1). From Fig. 3.28, a 70 mm buffer would allow for a ten period

pulse at 1580 m/s. At 1250 m/s, it would have to be decreased to six periods, but as can be seen in Fig. 3.33, a six-period pulse is sufficient to reach a steady-state.

From the above discussion, a sample length of L_0 = 25.0 mm, and a buffer length of D = 70 mm is chosen. The buffer is small enough for XSENS, while still large enough to utilize a number of periods corresponding to a steady-state for the entire sample sound velocity range. This buffer length sets a lower limit of six periods at 1250 m/s but can be increased with increasing sound velocity to ten periods at 1580 m/s. It can further be noted that if the Fourier spectrum method is used with a two-period pulse and the dimensions above, the minimum sound velocity at which the four times traversed buffer signal S_{RB} will not interfere with the signal of interest S_B, is > 1100 m/s.

Due to side lobe interference, a wide measurement cell is beneficial [7, 14]. Nesse [7] applied a 100 mm wide buffer, and through ray-tracing simulations explained further in Section 4.2, it is evident that a decrease in buffer width of less than 100 mm would increase the coherent noise contributions due to side lobe interference. The buffer width was thus chosen to be 100 mm. As part of the final design, 5 mm are added to the height to accommodate a lid, resulting in a final buffer height of 105 mm. The final dimensions of the measurement cell is shown in Fig. 3.30.

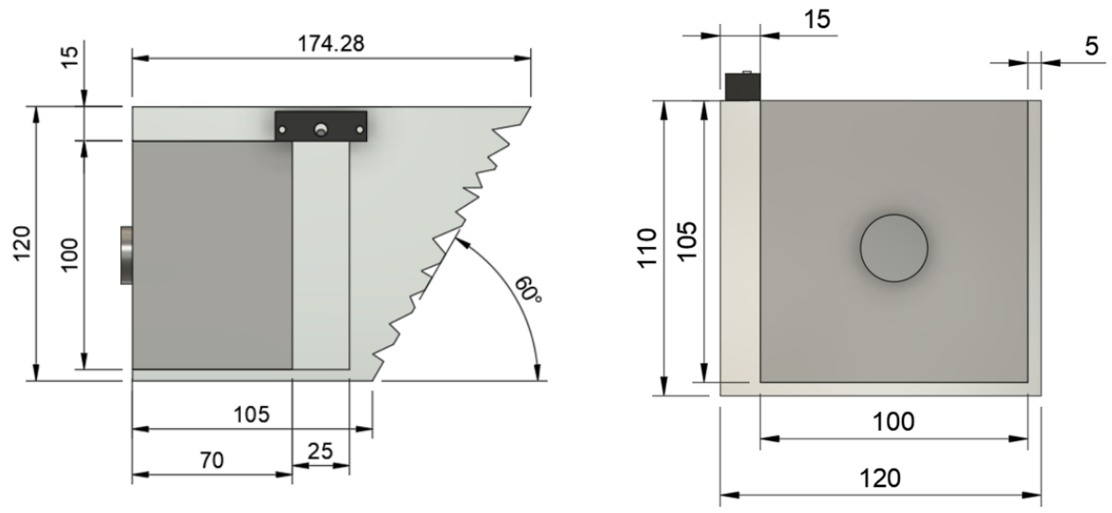

(a) Top view

(b) Front view

Figure 3.30: Dimensions and design of the constructed measurement cell.

3.5.5 Reflector design

At the sample/reflector interface, however, the incident sound wave is partially reflected and partially transmitted, where the transmitted signal is reflected at the reflector's end.

As discussed in Section 3.5.2, the reflector is made from aluminium, which has a compressional sound velocity of 6300m/s, using the tabulated data in Table 3.6. A sound pulse propagating through aluminium will consequently travel four times faster than distilled water at room temperature. If the travel time through the reflector is shorter than the acoustic signal, this might result in coherent noise

contributions [7].As a result, the reflector had to be designed to eliminate or reduce this possible source of coherent noise.

A typical reflector in the solid buffer method is angled at the end, that guides the signal towards the side wall. [7]. If cuts are made at the back face of the reflector, the signal is more distorted, reducing the chances of reflector reverberation. This design is hence chosen in this project.

Being restricted by the size of the measurement cell, the reflector dimensions must be calculated based on the minimum travel time needed to avoid or limit coherent noise. Using trigonometric rules and the sound velocity in aluminium, the dimensions of the reflector was calculated. The result is presented in Fig. 3.30.

A suspected noise interference due to the reflector was observed when the experimental measurements were carried out, indicated with an arrow in Fig. 3.32. The measurement cell was consequently acoustically investigated by moving the transducer from the centre of the buffer to the edges, shown in Fig. 3.31. By monitoring the unfolding of the noise signal as a function of transducer position, the noise source could be identified. Due to the reflector being angled, a transducer placed on the left side of the measurement cell (positions A/C) should, in theory, receive delayed noise due to the increased propagation length in the reflector. The opposite then holds for the right side (positions B/D).

Using the experimental setup shown in Fig. 3.1 and a short 500kHz burst, three pulse trains were measured: response from the original transducer position, position A and position B. The result is presented in Fig. 3.32 and shows a distinct change in the observed noise signal when the transducer is moved, and it can thus be concluded that the signal is, in fact, noise due to reflector reverberation. This noise signal was hence considered when choosing the appropriate number of periods in the pulse, presented in the next section.

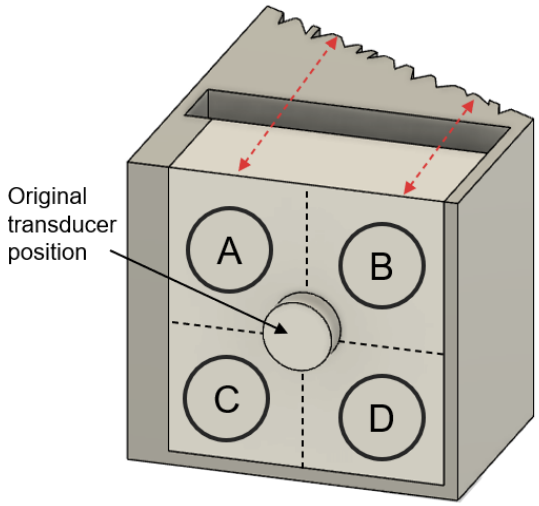

Figure 3.31: Illustration of transducer positions used in the reflector experiment.

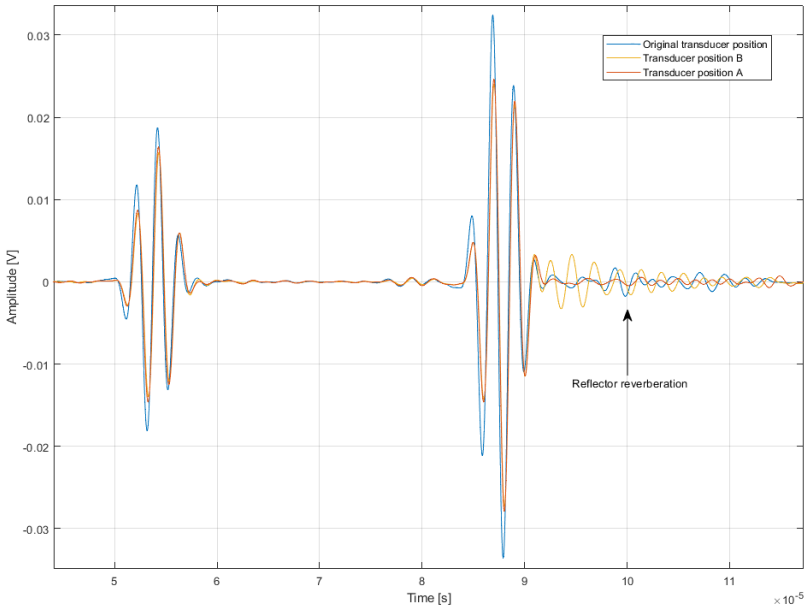

Figure 3.32: Resulting responses when the transducer is moved according to figure 3.31, enlarged around Signal B. Blue curve shows the original response when the transducer is centered.

3.5.6 Pulse length considerations

From Section 3.5.4, a pulse length of six periods at 1250 m/s and up to ten periods at 1580 m/s has been found to account for S_{RB} and S_{cs} with the dimensions set in the project.

However, from the reflector discussions above, the reflector reverberation is suspected of arriving shortly after signal B. The arrival of the reflector reverberation, the mode-converted wave S_{cs}, and the four times traversed buffer signal S_{RB} are thus all noise sources that will interfere with S_B if the pulse length is long enough.

Using the finalized measurement cell with the set dimensions shown in Fig. 3.30, two waveforms were acquired using a two-period and a six-period pulse. If a short burst is utilized, shown as the blue curve in Fig. 3.33, the coherent noise sources will not interfere with the signals of interest, S_A and S_B. This is, however, not the case for the six-period signal shown as the red curve in Fig. 3.33. It can be seen at the start of S_B that the mode-converted shear wave interferes with S_B. The end of S_B and the reverberation from the back of the reflector will further arrive at the transducer almost simultaneously.

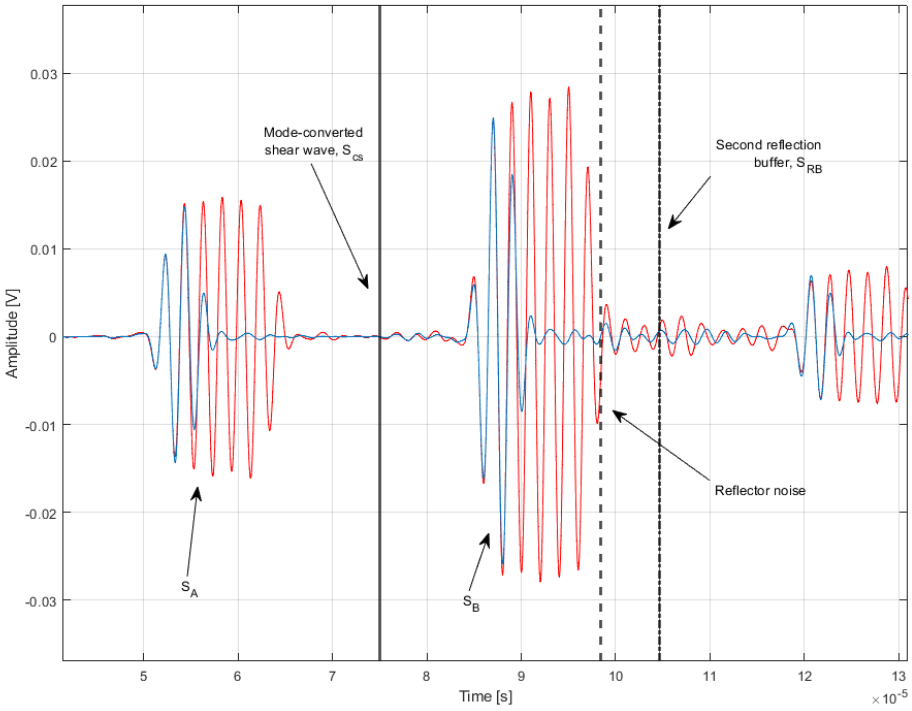

Figure 3.33: Illustration of the arrival noise contribution in comparison the signals of interest, S_A and S_B, for a two-period pulse (blue) and a six-period pulse(red)

Although a short burst seems like the natural choice from Fig. 3.33, a short burst will lack a steady-state, and the assumption of continuous waves can not be used, which is an assumption behind the theory presented in Sections 2.4 and 2.3.1.

In Section 6.5, three waveforms are acquired, with a pulse length of two, six and ten periods. The corresponding sound velocities are measured as a function of calculated zero-crosses in the pulse. It can from the results be seen that the zero-crossing method (Section 3.4.2) improves drastically when a steady-state is archived. If the pulse is increased beyond six periods, however, an apparent change in measured sound velocity can be found upon the arrival of the coherent noise sources. A six-period signal is thus the upper limit of the project independent on sample sound velocity and will be used throughout the project to be able to accurately compare the zero-crossings method with the Fourier spectrum method.

This is long enough to reach a steady-state while still short enough to avoid or reduce the uncertainty due to the largest coherent noise sources. The advantage of a 6-period pulse is also the ability to average over consecutive transit-times. A noise source in one part of the pulse will have a smaller effect on the average sound velocity than a noise source in the two-period pulse.

3.5.7 Temperature considerations

A temperature sensor would be needed to measure the sound velocity as a function of temperature. By directly immersing the temperature sensor in the sample area, unwanted reflections would be generated inside the cell, leading to possible errors in the sound velocity measurements. It was thus determined to increase the width of the sample area while leaving the buffer at the original width, which would result in a cavity where the sensor could be placed without disturbing the sound propagation.

The sensor could also not be placed in direct contact with the metal, as it was suspected that this would cause local heating of the sensor and thus inaccurate temperature measurements. The cavity was made rectangular and the sensor was placed a few millimeters from each wall to ensure that this would not happen in this project. The dimensions of the temperature sensor and thereby the type of sensor thus had to be decided first, explained in Section 3.1.7. The resulting placement of the temperature sensor is shown in Fig. 3.7.

Chapter 4

Simulations and Numerical Analysis

This chapter presents two different types of simulations and a numerical analysis. Section 4.1 presents a simulation performed in COMSOL to study the diffraction correction in the measurement cell used in the project. Section 4.2 will present a ray-tracing simulation of the side lobe propagation. In Section 4.3, a numerical analysis will be presented, used for assessing coherent noise sources.

4.1 Diffraction correction simulation

The Baffled piston diffraction correction (BPDC) model [38](Section 2.3.1) only considers a single fluid medium. In the candidate method, there are two signals of interest (cf. Fig. 2.1); Signal A is a two-way propagation through a solid buffer, and Signal B consists of propagation through several mediums. For signal A, the BPDC model can be used (under the assumption that the solid buffer can be approximated as a liquid). For signal B, the BPDC model is not sufficient and thus has the BPDC-MF (multiple fluid) model been introduced in Section 2.3.1, adapted from the BPDC model.

As will be evident later, accurate experimental sound velocity measurements are obtained compared to theoretical models. The diffraction correction model presented in Section 2.3.1, and the accuracy of the model, is thus of importance. Simulations enable more accurate sound propagations than those obtained through experiments. By comparing the diffraction in the sound propagation from simulations with the diffraction correction presented in this project, an indication of the accuracy of the BPDC-MF model can be determined. It should be noted that the results presented here are preliminary and should be investigated further. The simulations are all time-domain simulations conducted in COMSOL and were performed by Mosland [84].

Simulations in the time domain are performed with finite element methods, with the time domain being divided into steps named divisions per period, and the spatial domain is divided into small steps by mapped meshing, which provides quadrilateral elements [84]. Accuracy depends on mesh size and time step resolution, which must be sufficient for the solution to converge. However, in general, increasing the time and spatial resolution increases the computational cost significantly. Several studies have been done on the accuracy of the discretisation [14, 85, 86]. This is, however, not within

the scope of this project, and a convergence test is not performed. Thus are the simulations with the highest available elements per wavelength (EPW) and divisions per period (DPP) chosen to ensure the highest accuracy possible, which will vary for each simulation [84].

In this section, two simulations will be presented. The first simulation will simulate propagation in an elastic buffer, while the second simulation simulates a simplified model of the measurement cell in the project using an elastic Plexiglas buffer, a liquid sample and a hard boundary at the end which represents the reflector surface.

The sound source is modelled as a baffled piston by specifying a varying, uniform displacement of an area on the elastic buffer equal to the piston radius, u_{z0}. The receiver is sensitive to the average displacement, $\langle u_z \rangle$, over a measurement area the same size as the piston, where z is the direction of propagation. In the simulation, this is done by letting the surface boundary oscillate freely. In Comsol Multiphysics reference manual [87], this boundary condition is called "free" and will henceforth be used.

For each simulation performed, the deviation in arrival time due to diffraction effects is of interest. The resulting $\langle u_z \rangle$ is thus compared with a plane wave propagation, $u_{z,plane}$,

$$u_{z,plane} = \mathbf{u_{z0}} \cdot e^{i(\omega t - kz)}, \tag{4.1}$$

where $\mathbf{u_{z0}}$ is the amplitude of u_{z0}, $\omega = 2\pi f$ with f equal to the frequency of propagation, $k = \omega / c_s$, where c is the general sound velocity in the medium of propagation. This will result in a simulated diffraction correction, H_{sim}^{diff}, equal to

$$H_{sim}^{diff} = \frac{\langle u_z \rangle}{u_{z,plane}}. \tag{4.2}$$

By comparing the simulated arrival time, t_{sim}, to t_{plane}, the deviation in time due to diffraction effects can be calculated using the corresponding zero-crossings, named the plane-wave approach in the following. In Fig. 4.1, an example is shown. The simulated signal is two-way propagation inside the buffer, Signal A, and arrives at the transducer surface at time t_{sim}^{A}, followed by the plane wave propagation at time $t_{plane}^{A} = 2D/c_b$, where D is the length of the buffer and c_b is the buffer sound velocity. The zero-crosses for both pulses are located and used to calculate the deviation in time, $t_{A,sim}^{diff}$. Using $t_{A,sim}^{diff} = -\angle H_{A,sim}^{diff} / \omega$, the corresponding deviation in phase can be calculated.

In this example, an eight-period pulse is applied to the simulation with f = 500kHz. As shown in Fig. 4.1, the signal reaches a steady-state, meaning that an eight-period pulse is sufficient to assume a continuous wave. Thus will the excitation pulse for all simulations be an eight-period 500 kHz pulse where the two first and last periods are amplitude modulated, thus multiplied with $0.5 \cdot (1 - cos(2\pi t(4/f)))$ [84].

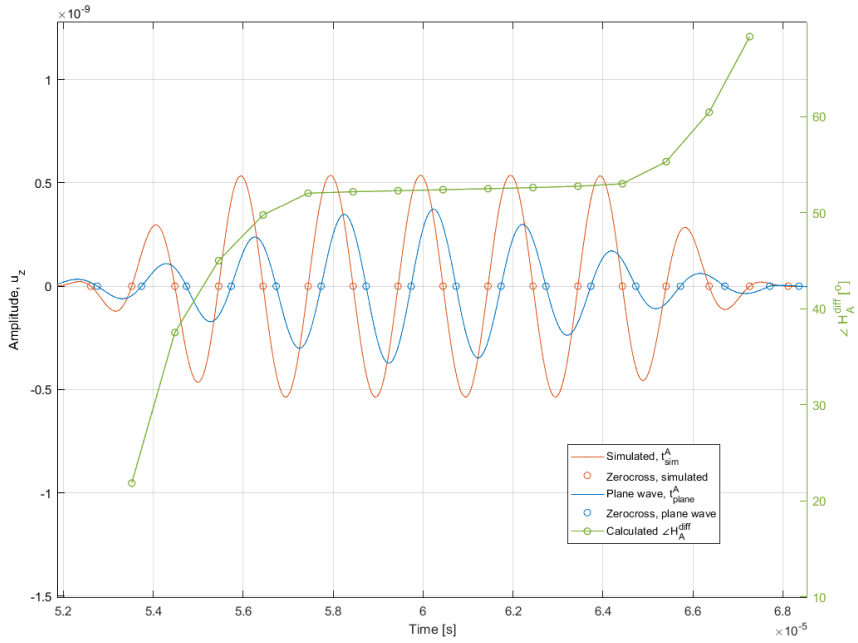

Figure 4.1: Red curve: simulated displacement at the receiver surface, $\langle u_z \rangle$ in time domain for the twice traversed propagation through an elastic Plexiglas buffer with D = 70.1 mm and c_b = 2711 m/s with 150 division per period and 10 elements per wavelength. Corresponding simulated plane wave propagation is shown as the blue curve. The green curve shows the resulting deviation in phase between the curves, $\angle H_A^{diff}$, in degrees. Simulation performed by Mosland [84]

When the deviation in phase is found, it is of interest to compare the results with the diffraction correction models. For Signal A, the BPDC model will be used (cf. discussion above), given by Eq. (2.35).

The same method as above will be applied to determine the simulated diffraction for Signal B, except that the distance travelled will now correspond to the two-way propagation inside the buffer and sample, with corresponding sound velocities. The resulting diffraction will be named $H_{B,sim}^{diff}$, and can be compared to the BPDC-MF model, Section 2.3.1. The BPDC-MF model is based on the BPDC model, and the same assumptions will thus apply.

It can further be noted that the COMSOL simulations differ from the BPDC and BPDC-MF models. The models are based on the assumption that the surface propagates perfectly within an infinite fluid medium, and sound pressure is measured at a distance 2d, over a measurement area equal to the receiver's size without the receiver present, illustrated in Fig. 4.2b). For the simulations, the propagation will correspond to the propagation of the measurement cell. It will thus propagate back to the receiver (without the receiver present) upon reflection at a rigid boundary, illustrated in Fig. 4.2a). The deviation from this assumption will be studied in simulation 1. Moreover, comparing diffraction in sound pressure with displacement is assumed to be valid and has not been investigated any further. This will be further discussed later in the section.

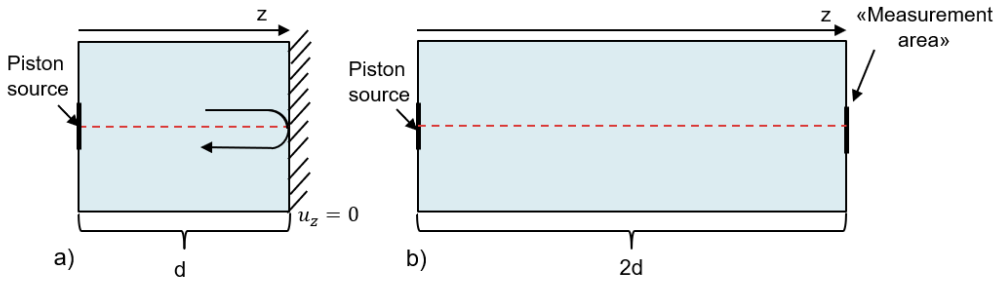

Figure 4.2: Comparison of the propagation path of a) COMSOL simulations b) BPDC/BPDC-MF model.

4.1.1 Simulation 1: Simulation using a solid buffer

When calculating the diffraction correction for the received signals in the measurement cell, it is assumed that the surfaces are all plane infinitely reflecting surfaces. A simulation is created by [84] to study the deviation from this assumption using an elastic Plexiglas buffer and a "sound hard boundary (wall)" as a reflecting surface. Sound hard boundary is the name in the Comsol Multiphysics reference manual [87] for a boundary at which the normal component of the displacement is zero, $u_z = 0$.

The sound source is modelled as a baffled piston (cf. discussion above), and the buffer is modelled as an elastic buffer. As a mesh, the standard conditions in COMSOL for elastic solids are used, thus 2nd order 8-node elements (Quadratic Serendipity) [84]. The boundary conditions of the buffer sides are free/vacuum, and the model is 3D-axisymmetric.
Due to possible sidewall interference, two simulations are conducted, corresponding to the two different schematics in Fig. 4.3. For both simulations, DPP = 150 and EPW = 10. The material parameters used are further given in Table 4.1.

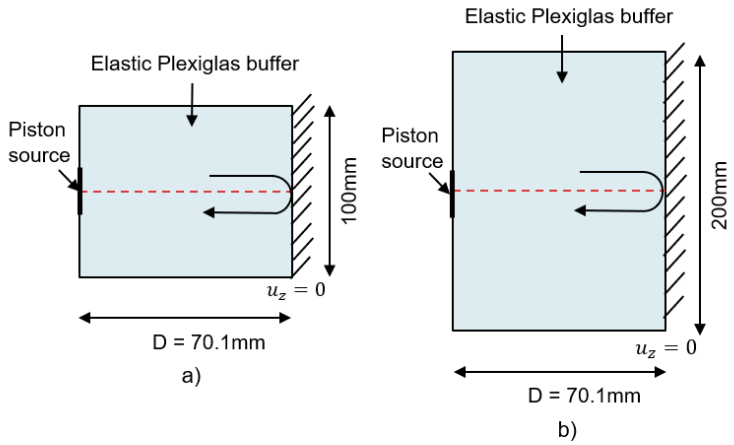

Figure 4.3: Simulation 1 in COMSOL: Elastic buffer and baffled piston as a source. Red line corresponds to the divide for a three-dimensional axisymmetric model. For both scenarios, the boundary conditions are the same, f = 500 kHz, and the piston radius, a = a_{eff} = 12.442mm. a) Buffer width = 100mm. b) Buffer width = 200mm.

Table 4.1: Parameters used throughout the simulations, given by Mosland [84].

Comp. sound velocity, c_b	**Buffer density,** ρ_b	**Poissons ratio,** ν	**Shear sound velocity** c_{shear}	**Piston radius, a**
2710 m/s	1190 kg/m^3	0.375	1210 m/s	12.44 mm

Using the plane-wave approach, the diffraction correction in the COMSOL simulations for both scenarios presented in Fig. 4.3 can be found. As this will only be propagation through a single medium, the BPDC model will be used for comparison, Eq. (2.38), with the parameters presented in Table 4.1 and d = 2D = 140.2 mm. Fig. 4.4 presents the calculated diffraction correction using both the BPDC model and the plane-wave approach.

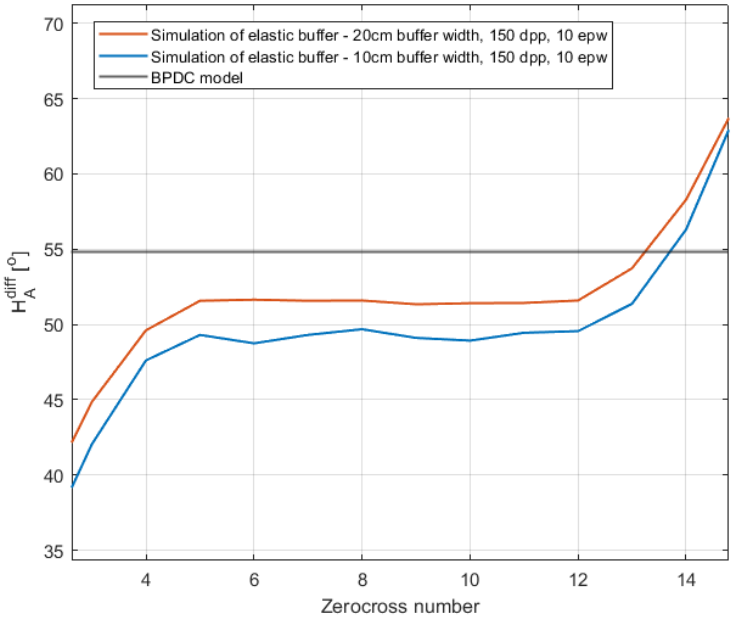

Figure 4.4: Calculated diffraction correction using the BPDC model (black), and using the plane wave approach for propagation through an elastic buffer with length 2D, with parameters presented in Table 4.1 and DPP = 150 and EPW = 10. Red curve corresponds to the 20 cm buffer width, while the blue curve corresponds to the 10 cm buffer width. Simulations performed by [84].

From Fig. 4.4, it is evident that the simulation using a narrow buffer provides a result that deviates more from the BPDC model than the wider buffer, where deviations of $\approx 5.7^o$ and $\approx 3.21^oC$ is found between the BPDC model and the narrow and wide buffer respectively. The narrow buffer may thus be influenced by shear waves and overall reflections from the side walls. Although some deviation might be present due to the assumption of a plane perfectly reflecting surface, additional deviation could be explained if the simulations have not converged. This can, however, not be proven unless more simulations are performed with higher EPW. Another explanation may be that time-domain simulations are generally less accurate than frequency-domain simulations [88], or due to the approximation of using the BPDC model on an elastic buffer.

4.1.2 Simulation 2: Simulation of the measurement cell

The solid buffer method, described in Section 2.2.1, is simulated by [84] using a simplified three-dimensional axisymmetric model with an elastic Plexiglas buffer, a liquid sample and a reflector (sound hard boundary).

The buffer is modelled as an elastic buffer. As a mesh, the standard conditions in COMSOL for elastic solids are used, thus 2nd order 8-node elements (Quadratic Serendipity). The boundary conditions on the sides of the buffer are free/vacuum [84]. For the fluid sample, 2nd order 9-node elements (Quadratic Lagrange) are applied as a mesh, where the sample is modelled as a fluid. The boundary condition of the liquid sample is a sound hard boundary (cf. discussion above), which will act as a reflector, while the boundary conditions on the sides are free/vacuum. At the solid-fluid interface, the displacement must be continuous throughout the boundary [89].

The sound source is modelled as a baffled piston (cf. discussion above). Also here, two different dimensions are used, and a sketch of the simulations can be seen in Fig. 4.5. The wider model, Fig. 4.5b), is more computational demanding [84]. A consequence of this is that the EPW and DPP must be decreased.

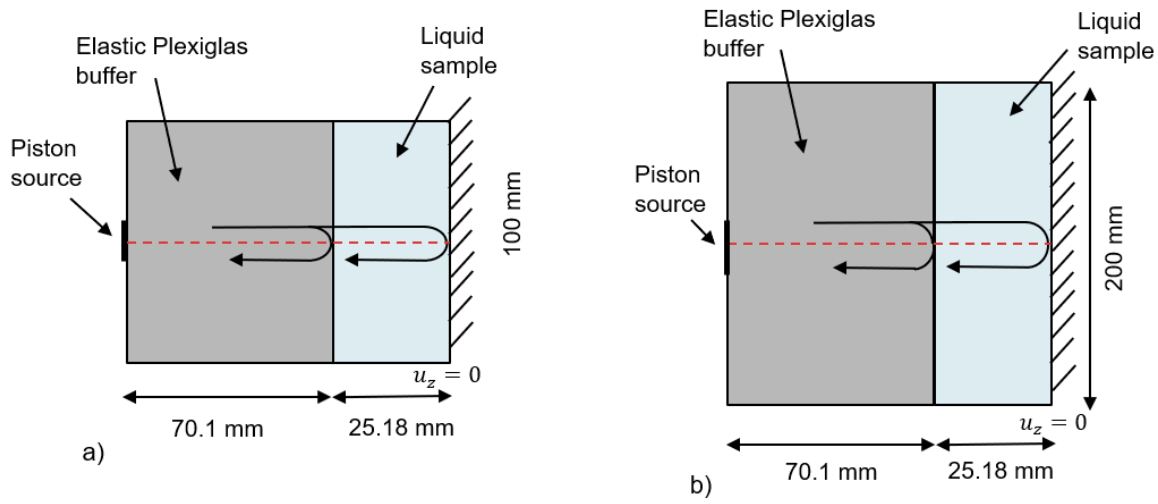

Figure 4.5: Dimensions utilized when simulating the solid buffer method in COMSOL. For both scenarios, the boundary conditions are the same, f= 500 kHz, and piston radius, a = 12.442mm. a) Buffer width = 100mm. b) Buffer width = 200mm.

The buffer parameters given in Table 4.1 will be used on the elastic buffer. Further, the simulations will be simulated in a liquid sound velocity span of c_s = 1320m/s - 1480 m/s. This sound velocity span will correspond to different crude oils at varying temperatures. The sample liquid density is thus set to 839.3 kg/m^3 for all simulations, corresponding to the density of Diesel (assuming constant density) [84].

A simulation is performed using 20 EPW and 300 DPP, and the simulation setup presented in Fig. 4.5a) is utilised to decrease the computational cost. For the simulations, the diffraction correction is

calculated using the plane-wave approach for both Signal A and B, thus $H_{a,sim}^{diff}$ and $H_{B,sim}^{diff}$ respectively. This is then compared to the diffraction correction calculated with the BPDC model for Signal A, H_A^{diff} with d = 2D, and the BPDC-MF model for Signal B, $\angle H_B^{diff}$ where d = 2D + $2L_0$. The results are presented in Fig. 4.6, together with the total diffraction correction for both methods, $\angle H^{diff}$ and $\angle H_{sim}^{diff}$.

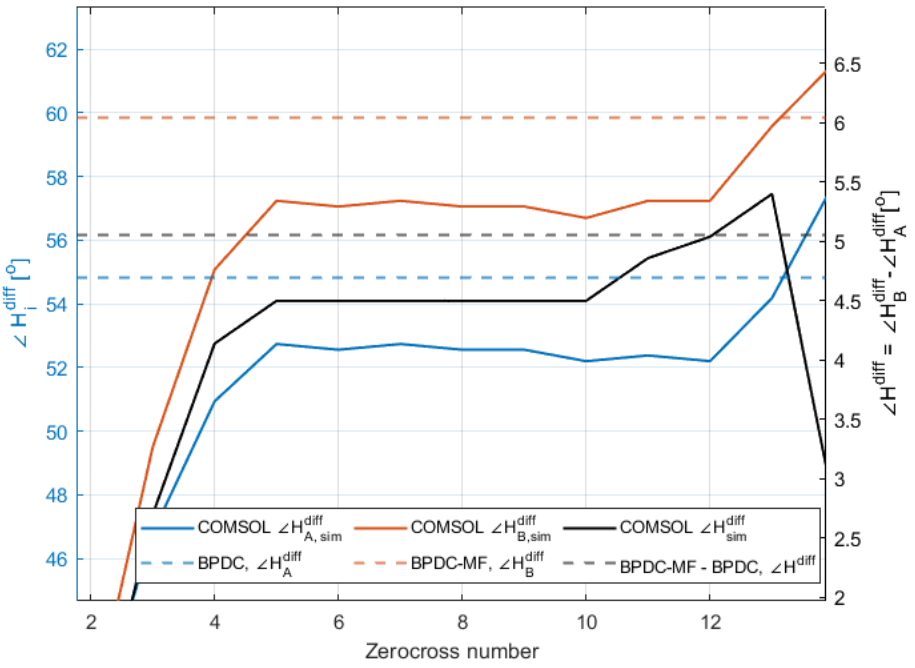

Figure 4.6: Difference in phase between the model used in the project and the COMSOL diffraction correction at sample fluid 1320 m/s, using 20 EPW mesh and 300 DPP, a = 12.44 mm and f = 500 kHz. The solid blue ($\angle H_{A,sim}^{diff}$) and red ($\angle H_{B,sim}^{diff}$) lines are calculated using the plane-wave approach. The solid black line is the total phase of the diffraction correction. Dashed lines correspond to the calculated diffraction based on Khimunin's diffraction correction model. Simulation performed by PhD candidate Eivind Nag Mosland [84]

The deviations between the COMSOL results and the diffraction correction model (BPDC/BPDC-MF) for Signals A and B are significant when inspecting them individually. A deviation between the BPDC model and the COMSOL simulation of $\approx 2.24^oC$ is found for Signal A, compared to $\approx 5.7^oC$ for Simulation 1 with width = 100 mm (as in this case). This may indicate that Simulation 1 has not yet converged. Further discrepancies can be due to the assumption of a perfectly reflecting surface for the BPDC model or the approximation of using the BPDC model on an elastic buffer.

For Signal B, a deviation of 2.8^oC between the simulation and the BPDC-MF model is found, where the largest contributor is believed to be the BPDC-MF model itself. Further deviations may be explained by the arguments presented for Signal A, which will also apply to Signal B. For both Signals A and B, some discrepancy is further believed to be sidewall interference, as it is evident in Simulation 1 that the width of the simulation causes a significant difference in the results.

Although the COMSOL simulations differ by more than 2^o from the diffraction correction models for individual signals, the combined diffraction corrections, $\angle H^{diff}$ and $\angle H_{sim}^{diff}$, compare favourably

with a deviation of only 0.5^o. This is found using zero-crossing numbers 5 to 10.

Due to computational costs, only one simulation was performed using 20 EPW and 300 DPP. It was, however, of interest to see how the diffraction changed with increasing sound velocity. To do so, the simulation setup shown in Fig. 4.5b) was utilized to decrease the noise due to reflections, and the resolutions were set to 14 EPW and 200 DPP. Three simulations were performed by [84] where the sound velocity in the liquid sample, c_s, was 1320, 1400 and 1480 m/s, all with sample liquid density $\rho_s = 839.3 kg/m^3$.

For each COMSOL simulation, the plane-wave approach was used to find the diffraction correction in Signals A and B, resulting in a total diffraction correction of $\angle H^{diff}_{sim}$. This was, in turn, compared to the total diffraction correction, $\angle H^{diff}$, using the BPDC and the BPDC-MF model for the same sample sound velocity span. The results are presented in Fig.4.7, together with the result in Fig. 4.6 (marked with a red circle).

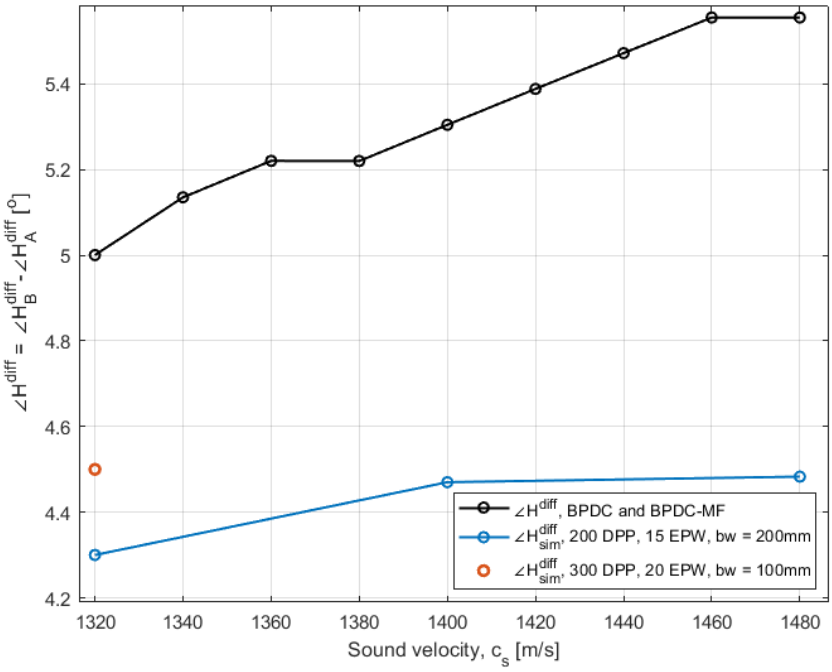

Figure 4.7: The phase of the diffraction correction as a function of sound velocity; theoretical and simulated. Blue curve: Simulated with DPP = 200, EPW = 15 and buffer width = 200 mm. Black curve shows the calculated phase using the diffraction correction model based on Khimunin's model. Result from Fig. 4.6 is shown for comparison. Simulation performed by Mosland [84]

From Fig. 4.7, it can be seen that an increase in sound velocity causes an increase in diffraction correction, both for $\angle H^{diff}$ and $\angle H^{diff}_{sim}$. As can be seen from the figure, the slope of the theoretical diffraction is steeper than the simulation. Thus, the deviation between the theoretical and simulated diffraction correction will increase, resulting in a maximum deviation of 1.07^o at 1480 m/s.

At 1320 m/s, the highest resolution COMSOL simulation provides a result closer to $\angle H^{diff}$. The deviation between the two simulations at 1320 m/s indicates that the signal has not yet converged using

200 DPP and 15EPW. Therefore, the actual deviation between $\angle H^{diff}$ and $\angle H^{diff}_{sim}$ might be even smaller than the results presented in Fig. 4.7.

Based on the discussions above, the total deviation between Khimunin's diffraction model and the diffraction correction in the current project is suspected to result from the assumption of a perfectly reflecting surface, the buffer being a solid rather than a fluid, side-wall interference, the model itself, simulations not having converged and other unknown sources. To avoid underestimating the uncertainty in the project due to diffraction correction, an uncertainty corresponding to the maximum deviation between the two curves in Fig. 4.7 is chosen, thus 1.07^o at 1480 m/s, corresponding to an uncertainty of $5.956 \cdot 10^{-9} s$, assuming 100% confidence level, k = $\sqrt{3}$, resulting in $u(\Delta t^{diff}) = 3.44 \cdot 10^{-9} s$.

Here, it should be noted that comparing $\angle H^{diff}$ with $\angle H^{diff}_{sim}$ is assumed to be valid in this project. Since these are only preliminary results, it has not been considered how (or if) this may affect the results. Given the uniqueness of the BPDC-MF model and the accurate sound velocity results presented in Chapter 6, it has been of interest to map the discrepancy with an independent method as a starting point for future work.

4.2 Simulation of side lobe propagations

A simulation program has been created through MATLAB using the theory in Section 2.4. It will simulate each side lobe's propagation through a measurement cell of choice through ray-tracing, making it possible to find out if, and to which degree, it will cause coherent noise at the transducer surface. If the signal-to-noise ratio (SNR) of the side lobes is high enough, the side lobes might be a source to coherent noise (Section 3.5.3). A numerical analysis will be presented in Section 4.3 which shows that a SNR of 40 dB will correspond to a time shift in the signal of interest of $3.2 \cdot 10^{-9}$ s (Table 4.2), which can be significant if the measurement cell is dependent on high-accuracy transit time measurements. It is thus of interest to see how the side lobes will propagate (during idealized conditions), which can be used as a consideration when designing the measurement cell. Through the simulation, this can be done by changing the frequency, radius of the transducer, size of the measurement cell and varying speed of sound of the buffer and in the sample area.

For the simulation to be valid, a set of idealized assumptions must be made. The sound source in the simulations will be modelled as a baffled piston (Section 2.3.1). Assuming continuous waves and far-field propagation, the directive pattern can thus described by the directional factor (Bessel directivity), Eq. (2.47). The main lobe and side lobes are then contained within the nodes described by Eq. (2.48).

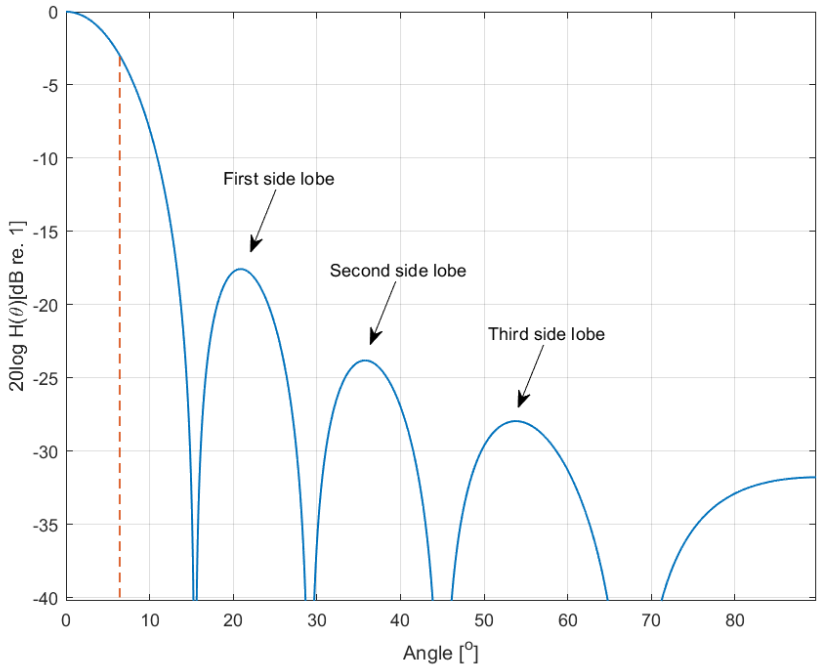

Figure 4.8: One-way directivity of transducer modelled with the directivity function, Eq. (2.47) where a = 12.43mm, $c = c_b = 2711$ m/s, f = 500kHz. Dashed red line shows the θ_{3dB} angle, calculated using Eq. (2.49).

In the following, a brief approach to the simulation is given through an example using this projects constructed measurement cell, followed by the simulated results.

Fig. 4.8 shows the main lobe and side lobes calculated using the Bessel directivity function, Eq. (2.47), with f = 500kHz, c = 2711 m/s (corresponding to c_b measured in Section 6.3) and $a = a_{eff} = 12.43$mm (Section 6.4). The figure shows that the main lobe and side lobes are contained within pressure nodes. Using Eq. (2.48), the angles of these pressure nodes can be found, which in turn can be used to define the angles that make up a specific side lobe.

In Fig. 4.9 an example of a propagation inside the measurement cell is shown, where θ is thought to be an arbitrarily angle inside a side lobe of the projects' measurement cell. The measurement cell is drawn as a Cartesian coordinate system, starting at 0 in the bottom left corner.

From Fig. 4.9, it can be observed that the ray propagates through the buffer with length l_1, where it hits the right edge of the buffer after a distance l_1', and propagates up to the sample area. Some of the sound will be reflected at the buffer/sample interface, shown as the dashed line, and some of it will transmit into the sample area before it is reflected at the reflector. The former one will be studied here.

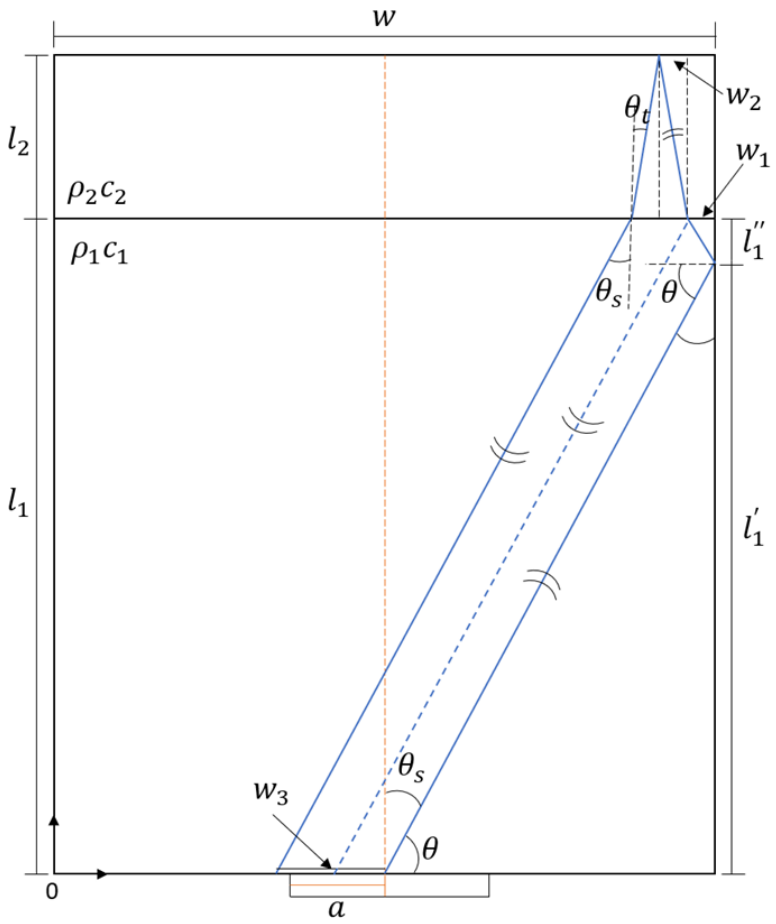

Figure 4.9: Illustration of propagation inside a measurement cell, where angles and dimensions are used to create the simulation.

If $l_1' < l_1$, as in Fig. 4.9, the ray will hit the side wall of the buffer at point:

$$l_1' = tan\theta \cdot \frac{w}{2}. \tag{4.3}$$

where w is the buffer width. Using geometric similarities and the law of specular reflection [23], one can further find out where the ray hits the buffer/sample-interface:

$$w_1 = tan\theta_s \cdot l_1'' = tan\theta_s \cdot (l_1 - l_1'), \tag{4.4}$$

where $\theta_s = 90^o - \theta$. The ray will now propagate from Plexiglas with impedance $z_1 = \rho_1 c_1$, into the samplewith impedance $z_2 = \rho_2 c_2$.
Snell's law of refraction states that [23],

$$\frac{sin\theta_i}{c_1} = \frac{sin\theta_t}{c_2}, \tag{4.5}$$

where θ_i is the angle of incidence (θ_s for the above example) with sound velocity c_1, and θt is the angle of transmission with sound velocity c_2. By rearranging Snell's law, the angle of propagation into

the sample area can be found

$$\theta_t = sin^{-1}\Big(\frac{sin\theta_s}{c_1} \cdot c_2\Big). \tag{4.6}$$

The resulting angle can then be used to find the location (with respect to the width) where the ray hits the reflector from the buffer/sample-interface, w_2.

$$w_2 = tan\theta_t \cdot l_2. \tag{4.7}$$

Because of geometric similarities, this angle will be equal on the way back to the buffer/sample-interface. Snells law is applied back into the buffer and the position where the ray hits back to transducer plane can be found:

$$\frac{w}{2} - w_3 = tan\theta_s \cdot l_1, \tag{4.8}$$

where w_3 will correspond to the width the ray has propagated in total with respect to the center of the transducer. After these lengths and widths are found, they are turned into coordinates in an xy-plane and plotted for simulation purposes. The total propagation length is further found using trigonometric rules. This method is quite cumbersome for large amounts of angles and the script which finds these parameters as well as calculating the propagation length is therefore made. The angles of the side lobes differ, and the propagation will thus change accordingly. This is taken under consideration in the simulation.

Figs. 4.10 and 4.11 shows examples of a simulated first and second side lobe inside a measurement cell respectively, where the length of the buffer is $l_1 = 70.1mm$ and the width is $w = 100mm$. Further, the sample length is $l_2 = 25.18mm$, $a = a_{eff}$ and the sound velocities are given as $c_b = c_1 = 2711m/s$ and $c_s = c_2 = 1481m/s$. These parameters are thus a scenario in the project using the created measurement cell with distilled water as sample liquid at 20^oC and 1 atm.

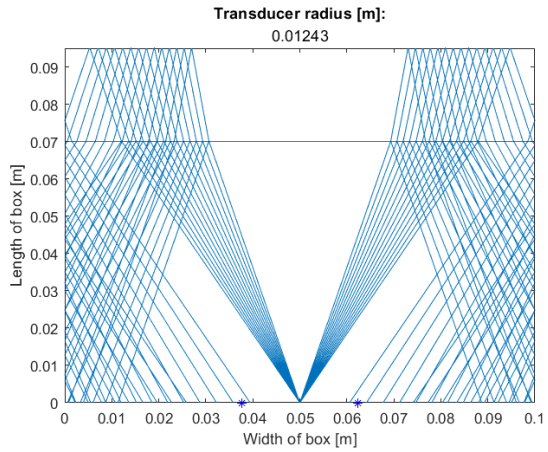

Figure 4.10: Simulation of first side lobe

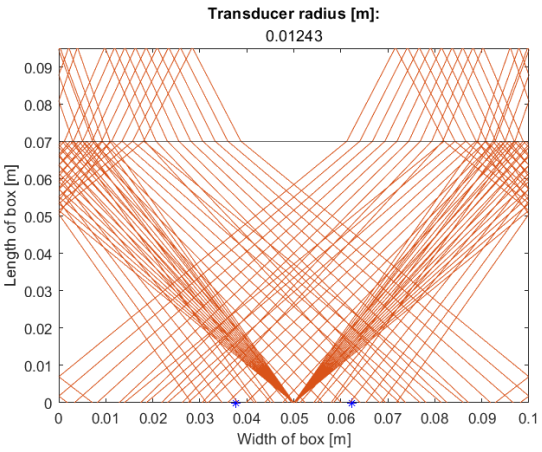

Figure 4.11: Simulation of second side lobe

From Fig. 4.10, it is evident that the noise from the first side lobe can be neglected. The transducer placement is indicated with two blue stars, and if no acoustic noise reflects between these two stars, noise due to the simulated side lobe can be disregarded. However, in Fig. 4.11, some side lobe interference at specific angles in the second side lobe can be observed. Using the total distance of the

reflected signals and dividing it by the velocity of the propagating medium, the total elapsed time of the interfering propagation can be calculated. By including the length of the pulse train and comparing the calculated time to the arrival of Signals A and B (Section 2.2.1), it can be discovered whether the specific propagation inside the side lobe will interfere with the propagation from the main lobe.

For the measurement cell dimensions simulated in Figs. 4.10 and 4.11, simulations are done for a sound velocity interval of 1250-1580 m/s. The results are not presented here, but shows that the first side lobe can be disregarded for the entire sound velocity range, while the second side lobe must be accounted for throughout as it will propagate back to the transducer within the time span of Signal B.

To assume a worst-case-scenario, the peak of the second side lobe, shown in Fig. 4.8 will be used which carries the most sound energy. As there is a two-way directivity in the measurement cell, $20logH^2(\theta)$ is calculated [23], which results in $20logH^2(\theta) = -47.6dB$. To find out what impact it may have on the transit time, a numerical analysis is presented in the next section.

4.3 Numerical analysis of coherent noise

To study how coherent noise will affect the sound velocity, a numerical analysis is carried out inspired by the report "Uncertainty model for Multipath Ultrasonic Transit Time Gas Flow Meters", written by Per Lunde, Kjell-Eivind Frøysa and Magne Vestrheim, pp. 165-167 [90]. The notations further follows [39].

Consider the signal of interest, given by

$$V_s(t) = A_S sin(\omega t), \tag{4.9}$$

and a noise signal propagating with the same frequency, delayed by the phase ϕ,

$$V_N(t) = A_N sin(\omega t + \phi). \tag{4.10}$$

It can be shown that the actual measured signal, $V_M(t)$, will be a superposition of $V_s(t)$ and $V_N(t)$, expressed as [21]

$$V_M(t) = A_M sin(\omega t + \phi), \tag{4.11}$$

with amplitude

$$A_M = A_S\sqrt{1 + \left(\frac{A_N}{A_S}\right) + 2\left(\frac{A_N}{A_S}\right)cos\phi}, \tag{4.12}$$

and a phase

$$\theta = tan^{-1}\left(\frac{(A_N/A_S)sin(\phi)}{1 + (A_N/A_S)cos(\phi)}\right) \tag{4.13}$$

Two factors will affect the significance of the noise signal; the amplitude of the noise and the phase difference between the signal of interest and the noise signal. Both variables will thus be investigated through a numerical analysis, calculated with the script presented in D.4.

The phase delay, ϕ, is varied from 0 to 180 degrees in 5000 steps. The amplitude A_M, the phase ϕ, and the amplitude ratio (A_M/A_S) are calculated for each step. The maximum, minimum, and standard uncertainty are found from the calculated variables. Through the standard uncertainty of the phase, $u(\hat{\theta})$, the standard uncertainty of the time fluctuations can be found:

$$u(\Delta t)_{coh.noise} = \frac{u(\hat{\theta})}{360 \cdot f}. \tag{4.14}$$

Several Signal-to-noise ratios (SNR), $20\log(A_N/A_S)$ are investigated, and the results are presented in Table 4.2

Table 4.2: Calculated standard deviation and max/min values for the amplitude ratio (C/A), phase difference, and time shift for a frequency of f = 500 kHz.

		SNR [dB]					
		10	**20**	**30**	**40**	**50**	**60**
Amplitude ratio, C/A [dB]	Std. unc.	2.0	0.6	0.2	0.06	0.02	0.006
	Max. dev	2.4	0.8	0.3	0.09	0.03	0.009
	Min. dev	-3.3	-0.9	-0.3	-0.09	-0.03	0.009
Phase, $\theta[^o]$	St.unc., $u(\hat{\theta})$	13.0	4.1	1.3	0.40	0.13	0.04
	Max. dev. & min. dev.	± 18.4	± 5.7	± 1.8	± 0.57	0.18	0.06
Time [ns]	Std. unc., $u(\Delta t)$	72.1	22.5	7.12	2.25	0.71	0.23
	Max. dev & min. dev.	± 102.4	± 31.9	± 10.1	± 3.18	± 1.01	± 0.32

The results in Table 4.2 are almost identical to those presented in Table 6.4 in [90], expect for the SNR of 10 dB, which are though to be rounding error. In [90], the resulting table was used to study the required SNR for transit time uncertainty. In this project, however, the table will be used to assess the time shift due to coherent noise contributions through a known SNR.

For the side lobe interference presented above, a SNR of 47.6 dB is found. Using the analysis above, this corresponds to a standard uncertainty of coherent noise due to side lobe interference of $u(\Delta t)_{sidelobe} = 9.4 \cdot 10^{-10} s$.

Chapter 5

Uncertainty models and sensitivity analysis

The project aims to reach a relative expanded uncertainty of the experimental sound velocity measurements below 1000 ppm = 0.1%(95% confidence level). This chapter will introduce the theoretical models needed for uncertainty calculations and a sensitivity analysis conducted prior to constructing the measurement cell. In Chapter 6, the measurement results will be presented, with the corresponding calculated uncertainties. Based on all calculated uncertainties, the experimental uncertainty in sound velocity will eventually be presented in Section 6.8.

This chapter is divided into four sections with subsections. Section 5.1 will provide a list of uncertainty notations used throughout the project. Section 5.2 will present the uncertainty model in experimental sound velocity, where each uncertainty contribution will be presented with a model of its own through subsections. Based on the uncertainty model, a sensitivity analysis will be presented in Section 5.3. The last section, Section 5.4, will present two theoretical sound velocity models for distilled and saline water, together with a model for the uncertainty in pressure.

The uncertainty models follows the *International Bureau of Weights and Measures* [91].

5.1 Uncertainty notations

Throughout the uncertainty analysis, several notations will be used. In Table 5.1, the notations are listed with explanation, and are based on notations used by Lunde and Frøysa [40] which follows [91]. A further description of the uncertainty standards and equations are given in Appendix C.

Table 5.1: Notations used throughout the uncertainty analysis, following the notations from [40].

Standard uncertainty (standard deviation) of measurand x	$u(x)$
Combined standard uncertainty of measurand x, where x is a function of several variables, $f(x) = f(x_1, x_2, ..., x_i)$	$u_c(x)$
Coverage factor	k
Relative standard uncertainty of measurand x	$E_x = \frac{u(x)}{x}$
Expanded uncertainty of measurand x	$U(x) = k \cdot u(x)$
Relative expanded uncertainty of measurand x	$k \cdot E_x$
Sensitivity coefficient of variable x_i	$\frac{\partial f(x)}{\partial x_i}$

5.2 Uncertainty model for the experimental sound velocity

In this section, a model for the uncertainty in the experimental sound velocity measurements will be presented. This model will be applied in Section 6.8 when the relative expanded uncertainty is calculated, and will further be used for the preliminary sensitivity analysis presented in the next section.

Using Eq. (2.13), the combined standard uncertainty for the experimental sound velocity, c_s, can be studied, assuming uncorrelated parameters

$$u_c^2(c_s) = \Big(\frac{\partial c_s}{\partial L_0} \cdot u(L_0)\Big)^2 + \Big(\frac{\partial c_s}{\partial t^{corr}} \cdot u(\Delta t^{corr})\Big)^2 + \Big(\frac{\partial c_s}{\partial \Delta t} \cdot u(\Delta t)\Big)^2 + \Big(\frac{\partial c_s}{\partial K_T} \cdot u(K_T)\Big)^2, \tag{5.1}$$

where $u_c(L_0), u_c(K_T), u_c(\Delta t)$ and $u_c(\Delta t^{corr})$ are the combined standard uncertainties of $L_0, K_T, \Delta t$ and Δt^{corr} respectively.
Eq. (2.13) is then differentiated with respect to the respective variables, which yields

$$\begin{aligned} u_c^2(c_s) = &\Big(\frac{2K_T}{\Delta t - \Delta t^{corr}} \cdot u_c(L_0)\Big)^2 + \Big(\frac{2K_T L_0}{(\Delta t - \Delta t^{corr})^2} \cdot u_c(\Delta t^{corr})\Big)^2 \\ &\Big(-\frac{2K_T L_0}{(\Delta t - \Delta t^{corr})^2} \cdot u_c(\Delta t)\Big)^2 + \Big(\frac{2 \cdot L_0}{\Delta t - \Delta t^{corr}} \cdot u_c(K_T)\Big)^2. \end{aligned} \tag{5.2}$$

Based on the discussion in Section 2.3, the diffraction correction is found to be the dominating factor in Δt^{corr}. It is therefore assumed that $\Delta t^{corr} \approx \Delta t^{diff}$. Δt^{diff} will further have an angle of $< \pi/2$, resulting in a displacement in time of less than a quarter of a period. If a frequency of 500kHz is assumed, $\Delta t^{corr} < 0.5\mu s$ and consequently $\Delta t^{corr} << \Delta t$. Based on the above arguments, Eq. (5.2) can be reduced to

$$u_c(c_s)^2 = \Big(\frac{2K_T}{\Delta t} \cdot u_c(L_0)\Big)^2 + \Big(-\frac{2K_T L_0}{(\Delta t)^2} \cdot u_c(\Delta t)\Big)^2 + \Big(\frac{2K_T L_0}{(\Delta t)^2} \cdot u_c(\Delta t^{corr})\Big)^2 + \Big(\frac{2L_0}{\Delta t} \cdot u_c(K_T)\Big)^2. \tag{5.3}$$

By applying Eq. (2.13), Eq. (5.3) can further be written as

$$u_c^2(c_s) = \frac{c_s^2}{L_0^2} \cdot u_c(L_0)^2 + \frac{c_s^2}{K_T^2} \cdot u_c(K_T)^2 + \frac{c_s^2}{(\Delta t - \Delta t^{corr})^2} \cdot u_c(\Delta t)^2 + \frac{c_s^2}{(\Delta t - \Delta t^{corr})^2} \cdot u_c(\Delta t^{corr})^2. \quad (5.4)$$

Dividing all the terms on c_s^2 enables the possibility to isolate the speed of sound on one side. By defining $E_c = u_c(c_s)/c_s, E_{L_0} = u_c(L_0)/L_0, E_{K_T} = u_c(K_T)/K_T, E_{\Delta t} = u_c(\Delta t)/\Delta t$ and $E_{\Delta t^{corr}} = u_c(\Delta t^{corr})/\Delta t^{corr}$, Eq. (5.4) can be expressed in terms of relative uncertainties, which yields

$$E_{c_s}^2 = E_{L_0}^2 + E_{K_T}^2 + \frac{(\Delta t)^2}{(\Delta t - \Delta t^{corr})^2} E_{\Delta t}^2 + \frac{\Delta t^{corr^2}}{(\Delta t - \Delta t^{corr})^2} E_{\Delta t^{corr}}^2, \quad (5.5)$$

Due to $\Delta t >> \Delta t^{corr}$, the equation can be approximated to

$$E_{c_s}^2 = E_{L_0}^2 + E_{K_T}^2 + E_{\Delta t}^2 + \frac{(\Delta t^{corr})^2}{(\Delta t)^2} E_{\Delta t^{corr}}^2, \quad (5.6)$$

which in terms of relative expanded uncertainty can be expressed as

$$k \cdot E_{c_s} = k \cdot \sqrt{E_{L_0}^2 + E_{K_T}^2 + E_{\Delta t}^2 + \frac{(\Delta t^{corr})^2}{(\Delta t)^2} E_{\Delta t^{corr}}^2}, \quad (5.7)$$

where k = 2 for a 95% confidence level and $\Delta t^{corr}/(\Delta t) = s_{\Delta t^{corr}}$ is the relative sensitivity coefficient of Δt^{corr} [40].

In the following, an uncertainty model will be presented for each uncertainty contribution in Eq. (5.2), together with an uncertainty model for the uncertainty in temperature, $u_c(T)$.

5.2.1 Combined standard uncertainty in temperature

The temperature will be measured throughout the measurement series using a JUMO STEAMTemp Temperaturgiver RTD (902830), as both the sound velocity and the uncertainty in sound velocity is dependent on the measured temperature.

Assuming all sensitivity coefficients are equal to 1, uncertainty in temperature can be modelled as

$$\begin{aligned} u_c^2(T) = u_c^2(T)_{cal} + u^2(T)_{calibdev} + u^2(T)_{element} + u^2(T)_{drift_{JS}} \\ + u^2(T)_{adapter} + u^2(T)_{var} + u^2(T)_{other}, \end{aligned} \quad (5.8)$$

where

$$u_c^2(T)_{cal} = u^2(T)_{Tref} + u^2(T)_{scanner} + u^2(T)_{drift_{tref}}. \quad (5.9)$$

A description of all uncertainty contributors are presented in Table 5.2.

Table 5.2: Description of the uncertainty contributions when measuring the temperature in the sample area using JUMO STEAMTemp Temperaturgiver RTD (902830)

Uncertainty contributor	**Description**
$u(T)_{calibdev}$	Deviation from the reference PT100 after calibration.
$u(T)_{element}$	Standard uncertainty of the JUMO STEAMTemp PT100 sensor.
$u(T)_{drift_{JS}}$	Standard uncertainty due to thermal drift and aging in JUMO STEAMTemp Pt100 sensor.
$u(T)_{adapter}$	Standard uncertainty due to RTD-USB adapter.
$u(T)_{var}$	Standard uncertainty due to observed temperature variation under stable temperature conditions during 1 minute.
$u_c(T)_{cal}$	Combined standard uncertainty due to calibration of the JUMO SteamTemp PT100 sensor.
$u(T)_{drift_{ref}}$	Standard uncertainty due to thermal drift and ageing of the reference PT100 element.
$u(T)_{scanner}$	Standard uncertainty due to the accuracy of Fluke Calibration 1586A SUPER-DAQ Precision Temperature Scanner.
$u(T)_{Tref}$	Standard uncertainty in the reference PT100 element used for calibrations.
$u(T)_{other}$	Standard uncertainty due mechanical vibrations of the RTD, radio frequency interference and other unknown sources.

5.2.2 Combined standard uncertainty in thermal expansion

When subjected to heat, the sample length will expand according to Eq. (2.61) and can be compensated for with a thermal expansion coefficient, K_T. The combined standard uncertainty for K_T can be modelled as

$$u_c^2(K_T) = \left(\frac{\partial K_T}{\partial \Delta T} u_c(\Delta T)\right)^2 + \left(\frac{\partial K_T}{\partial \alpha_a} u(\alpha_a)\right)^2 + \left(\frac{\partial K_T}{\partial \alpha_p} u(\alpha_p)\right)^2 + \left(\frac{\partial K_T}{\partial L_0} u_c(L_0)\right)^2 + \left(\frac{\partial K_T}{\partial d_p} u_c(d_p)\right)^2 \tag{5.10}$$

By differentiating Eq. (2.61) with respect to the respective variables, the uncertainty in K_T yields

$$u_c(K_T)^2 = \left(\alpha_a + \frac{d_b}{L_0}(\alpha_a - \alpha_p)\right)^2 \cdot u_c(\Delta T)^2 + \left(\Delta T\left(1 + \frac{d_b}{L_0}\right)\right)^2 \cdot u(\alpha_a)^2 + \left(\Delta T \frac{d_b}{L_0}\right)^2 \cdot u(\alpha_p)^2 + \left(\Delta T \frac{d_b}{L_0^2}(\alpha_p - \alpha_a)\right)^2 \cdot u_c(L_0)^2 + \left(\frac{\Delta T}{L_0} \cdot (\alpha_A - \alpha_p)\right)^2 \cdot u(d_p)^2, \tag{5.11}$$

Further, $u_c(\Delta T)$ is given as

$$u_c(\Delta T) = \frac{\partial \Delta T}{\partial T_0} \cdot u_c(T_0) + \frac{\partial \Delta T}{\partial T} u_c(T) \tag{5.12}$$

The uncertainty contributions are listed in Table 5.3.

Table 5.3: Description of the uncertainty contributors in thermal expansion.

Uncertainty contributor	**Description**
$u(T_0)$	Standard uncertainty in reference temperature T_0, ref. Eq. (5.8).
$u(T)$	Standard uncertainty in measured temperature T, ref. Eq. (5.8).
$u(\alpha_a)$	Standard uncertainty in Aluminium Alloy 6082 thermal expansion coeff.
$u(\alpha_p)$	Standard uncertainty in Plexiglas thermal expansion coeff.
$u_c(L_0)$	Combined standard uncertainty of the sample length,L_0 measured at temperature T_0.
$u_c(d_b)$	Combined standard uncertainty of the distance measured from the bolts, securing the Plexiglas buffer to the chassis, to the sample area L_0.

5.2.3 Combined standard uncertainty in sample length

Assuming that all sensitivity coefficients are equal to 1, the combined uncertainty of sample length, L_0, at temperature T_0 can be expressed as

$$u_c^2(L_0) = u^2(L_0)_{caliper} + u^2(L_0)_{rep} + u^2(L_0)_{stab} + u_c^2(L_0)_{vert} + u^2(L_0)_{other}, \tag{5.13}$$

where,

$$u_c^2(L_0)_{vert} = u_c^2(D) + u^2(R). \tag{5.14}$$

Assuming all sensitivity coefficients are equal to 1, $u_c^2(D)$ can further be expressed as

$$u_c^2(D) = u^2(D)_{caliper} + u^2(D)_{rep} + u^2(D)_{stab} \tag{5.15}$$

All uncertainty contributions are presented in Table 5.4.

Table 5.4: Description of the uncertainty contributions in Eq. (5.13).

Unc. contribution	**Description**
$u(L_0)_{caliper} = u(D)_{caliper}$	Standard uncertainty of the MarCal 16EWR digital caliper.
$u(L_0)_{rep}$	Standard uncertainty due to the repeatability of the measured L_0 in the propagation path
$u(L_0)_{stab} = u(D)_{stab}$	Standard uncertainty due to caliper stability and drift.
$u_c(L_0)_{vert}$	Combined standard uncertainty due to variations in the length L_0 in the vertical direction of the sample area.
$u(L_0)_{other}$	Standard uncertainty due to other unknown sources.
$u(R)$	Standard uncertainty of the reflector due to assumption of a plane surface.
$u_c(D)$	Combined standard uncertainty of the buffer length D.
$u(D)_{rep}$	Standard uncertainty due to the repeatability of the measured buffer length D in the propagation path.

5.2.4 Combined standard uncertainty in transit time

In Section 3.4, two different signal processing methods for calculating the transit time are presented. Each of these methods has a corresponding uncertainty, and the uncertainty in sound velocity due to uncertainty in transit time, $u_c(\Delta T)$, will thus vary depending on the signal processing method. Two different models will thus be presented; one for Zero-crossing method (ZCM) and one for the Fourier Spectrum method (FSM).
The combined standard uncertainty in transit time with the ZCM can be expressed as

$$\begin{aligned} u_c^2(\Delta t)_{ZCM} = u^2(\Delta t)_{osc} + u_c^2(\Delta t)_{coh.noise} + u^2(\Delta t)_{el} + u^2(\Delta t)_{res} \\ + u^2(\Delta t)_{pump} + u^2(\Delta t)_{var} + u^2(\Delta t)_{RFI} + u^2(\Delta t)_{other}, \end{aligned} \tag{5.16}$$

where

$$u_c^2(\Delta t)_{coh.noise} = u^2(\Delta t)_{sidelobe} + u^2(\Delta t)_{mode.conv.} + u^2(\Delta t)_{trav} + u^2(\Delta t)_{refl} \tag{5.17}$$

Further, the combined standard uncertainty in transit time with the FSM can be expressed as

$$\begin{aligned} u_c^2(\Delta t)_{FSM} = u^2(\Delta t)_{osc} + u^2(\Delta t)_{trunc} + u_c^2(\Delta t)_{coh.noise} + u^2(\Delta t)_{el} \\ + u^2(\Delta t)_{pump} + u^2(\Delta t)_{res} + u^2(\Delta t)_{RFI} + u^2(\Delta t)_{ph.dist} + u^2(\Delta t)_{other}. \end{aligned} \tag{5.18}$$

In both cases, all sensitivity coefficients are assumed to be 1. In Table 5.5, a description of all uncertainty contributors are presented.

Table 5.5: Description of the uncertainty contributors in transit time measurements. Uncertainty contributors for both FSM and ZCM are included.

Uncertainty contributor	**Description**
$u(\Delta t)_{osc}$	Standard uncertainty due to the time resolution of the oscilloscope.
$u_c(\Delta t)_{coh.noise}$	Combined standard uncertainty due to coherent noise.
$u(\Delta t)_{sidelobe}$	Standard uncertainty in coherent noise due to side lobe interference.
$u(\Delta t)_{mode.conv.}$	Standard uncertainty in coherent noise due to mode-converted waved.
$u(\Delta t)_{trav}$	Standard uncertainty in coherent noise due to four times traversed buffer signal.
$u(\Delta t)_{refl}$	Standard uncertainty in coherent noise due to reflector reverberation.
$u(\Delta t)_{ph.dist.}$	Standard uncertainty due to phase distortions in the applied filter.
$u(\Delta t)_{el}$	Standard uncertainty due to fluctuations/instability in power supply, cables and other electrical equipment.
$u(\Delta t)_{res}$	Standard uncertainty due to sampling frequency, incoherent noise and bit resolution.
$u(\Delta t)_{var}$	Standard uncertainty due to a spread in the measured time shifts for different periods throughout the pulse.
$u(\Delta t)_{RFI}$	Standard uncertainty due to radio frequency interference.
$u(\Delta t)_{trunc}$	Standard uncertainty due to the deviation between truncating the signal onset and end, and linearly trailing. Dependent on the number of periods in the signal.
$u(\Delta t)_{pump}$	Standard uncertainty due the pump noise.
$u(\Delta t)_{other}$	Standard uncertainty due to other unknown contributions.

To find $u^2(\Delta t)_{res}$, further analysis is needed. This will be presented in the following.

Uncertainty in transit time measurements due to bit resolution and incoherent noise

The uncertainty in the voltage amplitude can affect the calculated transit time when using zero-crosses. In this section, a model is presented which was described by Fosså [39] in his work. His approach and notations will be implemented with a few alterations.

The model addresses the uncertainty contributions from the bit resolution of the oscilloscope $u(V)_{bit}$, sampling frequency f_s and the incoherent noise $u(V)_{inc.noise}$, which will all affect the voltage amplitude. Although incoherent noise can be reduced by averaging the signal, some incoherent noise will still be present. Further, the bit resolution of the oscilloscope display limits the measured voltage by either rounding the value up or down. These uncertainties are therefore treated here.

In Section 3.4.2, linear interpolation is introduced. This will be used as a basis for the uncertainty model.

If both sensitivity coefficients are assumed to be equal to 1, the uncertainty in the voltage amplitude can be expressed as

$$u_c^2(V) = u^2(V)_{bit} + u^2(V)_{inc}, \tag{5.19}$$

where $u_c^2(V)$ is the combined standard uncertainty for the voltage amplitude, and $u^2(V)_{bit}$ and $u^2(V)_{inc}$ are the uncertainty contributions due to incoherent noise and bit resolution, respectively.
The RMS value of the incoherent noise is acquired using the approach in Section 3.4.5. Even though the incoherent noise may vary for each sampled waveform, it will for simplicity be treated as though it is constant throughout the project. The RMS value will be used to determine the standard uncertainty in voltage amplitude due to incoherent noise [39],

$$u(V)_{inc} = V_{RMS}^N, \tag{5.20}$$

where V_{RMS}^N is the RMS value of the incoherent noise, calculated using Eq. (3.10).
The maximum quantisation error and therefore the uncertainty in the voltage amplitude due to bit resolution can be expressed as [4]

$$u(V)_{bit} = \frac{\Delta V_q}{2}, \tag{5.21}$$

where ΔV_q is the quantization interval expressed as

$$\Delta V_q = \frac{V_{MAX} - V_{MIN}}{2^a - 1}, \tag{5.22}$$

where V_q is the range of the oscilloscope display and a is the number of bits used in the quantisation.

As explained in Section 3.4.2, a zero crossing is found by interpolating between two points. This is illustrated in Fig. 5.1. The voltage amplitude before the zero crossing is defined here as V_i where $i = 1, 2, .., n$ is the sample number, and the voltage amplitude after the zero crossing is defined as V_{i+1}. Similarly can the time of sample number i and number i + 1 be defined as t_i and t_{i+1} respectively.

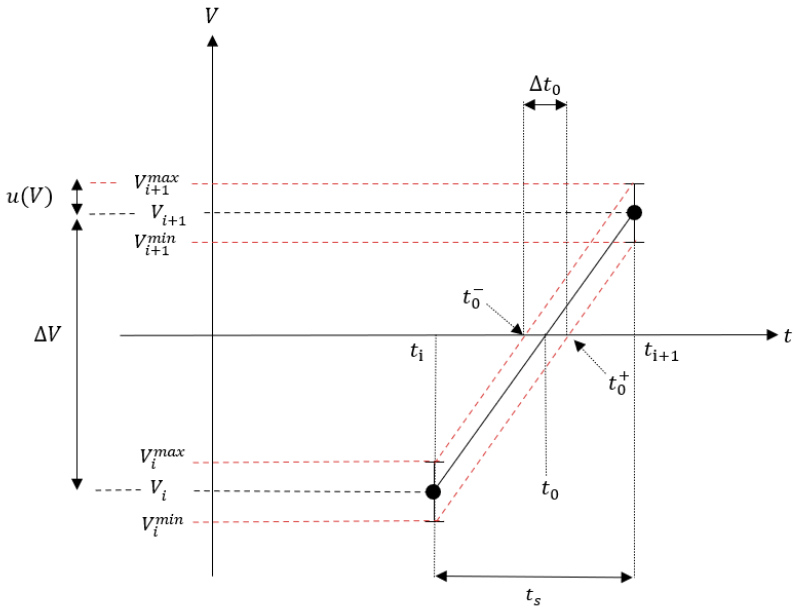

Figure 5.1: An illustration of how incoherent noise and bit resolution affect the calculation of zero-crosses involving linear interpolation. Figure inspired by Fig. 4.13 in [39].

To find out how the error in voltage amplitude affects the calculated zero-crossings, the maximum deviation from the zero crossing can be calculated. This is shown as the red lines in Fig. 5.1. The slope of the straight line for the maximum deviation from V_i, thus the line from coordinates (V_i^{max}, t_i)) to (V_{i+1}^{max}, t_{i+1}), can be found:

$$m^+ = \frac{V_{i+1}^{max} - V_i^{max}}{t_{i+1} - t_i}. \tag{5.23}$$

From Fig. 5.1, V_{i+1}^{max} corresponds to $V_{i+1} + u(V)$ and V_i^{max} corresponds to $V_i + u(V)$. Inserting this into Eq. (5.23) yield

$$m^+ = \frac{(V_{i+1} + u(V)) - (V_i + u(V)}{t_{i+1} - t_i)} = \frac{V_{i+1} - V_i}{t_{i+1} - t_i} = m, \tag{5.24}$$

where m is the slope between points (t_i, V_i) and (t_{i+1}, V_{i+1}). This can also be shown for the straight line from (V_i^{min}, t_i) to (V_{i+1}^{min}, t_{i+1}), where $V_i^{min} = V_i - u(V)$ and similarly for V_{i+1}^{min}.
Further, the uncertainty in time due to bit resolution and incoherent noise is illustrated in Fig. 5.1. The maximum and minimum deviation in voltage amplitude, results in time deviations t_0^- and t_0^+ respectively from the original zero crosssing using linear interpolation. The uncertainty can thus be expressed as

$$\Delta t_0 = t_0^+ - t_0^- = t_0 + e(t_o) - (t_0 - e(t_0)) = 2 \cdot u(t_0), \tag{5.25}$$

where $u(t_0) = t_0^+ - t_0 = t_0 - t_0^-$ is the uncertainty from the original zero crossing. In Section 3.4.2, an equation for the time of the zero crossing is found, Eq. (3.6). This can be implemented here

$$\Delta t_0 = t_0^+ - t_0^- = \left(t_i - \frac{V_i^{max}}{m}\right) - \left(t_i - \frac{V_i^{min}}{m}\right) = \frac{1}{m}\left(V_i^{min} - V_i^{max}\right). \tag{5.26}$$

From Eqs. (5.26) and (5.25),

$$\frac{1}{m}\left(V_i^{min} - V_i^{max}\right) = \Delta t_0 = 2 \cdot u(t_0). \tag{5.27}$$

Inserting $V_i^{min} = V_i - u(V)$ and $V_i^{max} = V_i + u(V)$ together with Eq. (5.24) into Eq. (5.27) and solving for $2 \cdot e(t_0)$ results in an equation for the error in the time of zero crossing,

$$\pm\, u(t_0) = \pm\left(\frac{(V_i - u(V)) - (V_i + u(V)}{2} \cdot \frac{t_{i+1} - t_i}{V_{i+1} - V_i}\right) = \pm u(V) \cdot \frac{t_s}{\Delta V}. \tag{5.28}$$

From Fig.5.1, $\Delta V = V_{i+1} - V_i$, and sampling period, t_s, can be expressed as

$$t_s = t_{i+1} - t_i = \frac{1}{f_s}. \tag{5.29}$$

Where f_s is the sampling frequency. The oscilloscope extracts 10000 samples per waveform as mentioned in Section 3.1.5. t_s, can thus be expressed as

$$t_s = \frac{t_{scope}^{max} - t_{scope}^{min}}{10000}, \tag{5.30}$$

where $t_{scope}^{max} - t_{scope}^{min}$ is the time display range of the oscilloscope when gathering data. This can thus vary depending on the time range of the signal of interest. The average error for the acquisition can

then be used to find the uncertainty in t_0:

$$u(\Delta t)_{res} \approx \overline{u}(t_0) = \frac{1}{N}\sum_{n=1}^{N} u_n(t_0). \tag{5.31}$$

where n = 1,2..,N corresponds to zero crossing number n. Thus is $u_n(t_0)$ calculated using Eq. (5.28) for each zero crossing to find the uncertainty in transit time. The uncertainty in transit time due to bit resolution is therefore found experimentally for each acquisition.

5.2.5 Combined standard uncertainty in correction term

In Section 2.3.2, it was shown that the uncertainty in the boundary layer correction, $u(\Delta t_R)$, could be neglected, and consequently will the time correction uncertainty only be dependent on the uncertainty in the BPDC-MF diffraction correction model presented in Section 2.3.1.

Assuming all sensitivity coefficients are equal to 1, the uncertainty in the diffraction correction is a combined uncertainty expressed as:

$$\begin{aligned} u_c^2(\Delta t^{diff}) = u^2(\Delta t^{diff})_{model} + u^2(\Delta t^{diff})_{a_{eff}} + u^2(\Delta t^{diff})_{c_b} + \\ u_c^2(\Delta t^{diff})_L + + u^2(\Delta u^2(\Delta t^{diff})_D + u^2(\Delta t^{diff})_{other}, \end{aligned} \tag{5.32}$$

The uncertainty in length, $u(L)$, can be expressed as

$$u_c^2(L) = (L_0 \cdot u_c(K_T))^2 + (K_T \cdot u_c(L_0))^2, \tag{5.33}$$

where $u_c(K_T)$ and $u_c(L_0)$ can be calculated using Eqs. (5.11) and (5.13). The uncertainty contributions are presented in Table 5.6, and a detailed description is presented below.

Table 5.6: Description of the uncertainty contributions in Eq. (5.32)

Uncertainty contribution	Description
$u(\Delta t^{diff})_{model}$	Standard uncertainty due to the deviation between the BPDC model and the BPDC-MF model
$u(\Delta t^{diff})_{a_{eff}}$	Standard uncertainty in Δt^{corr} due to the measured uncertainty in effective element radius, $u(a_{eff})$
$u(\Delta t^{diff})_{c_b}$	Standard uncertainty in Δt^{corr} due to the uncertainty in buffer compressional sound velocity, $u(c_b)$
$u(\Delta t^{diff})_L$	Standard uncertainty in Δt^{corr} due to $u_c(L)$, ref. Eq. (5.33)
$u(\Delta t^{diff})_D$	Standard uncertainty in Δt^{corr} due to $u(D)_{repeatability}$, ref. Table 5.4.
$u(\Delta t^{diff})_{other}$	Standard uncertainty due to other unknown contributions

Sensitivity coefficients are not calculated for the diffraction correction model used in this project as the resulting equations would be too complex for the scope of this thesis. Thus, to find out what

$u(a_{eff})$, $u_c(L)$, $u(c_b)$, and $u(D)$ correspond to in terms of $u_c(\Delta t^{diff})$, Δt^{corr} is first calculated as a function of a_{eff}, L, D, and c_b at temperature T, thus $\Delta t^{diff}\big(a_{eff}, c_b(T), D, L(T)\big)$, where a_{eff} and D are assumed constant with temperature. Δt^{diff} is then calculated with variables corresponding to the measured values added and subtracted with their corresponding uncertainties at 68% confidence level, while the other variables are held constant. The uncertainty in Δt^{diff} due to the respective variables will correspond to the maximum deviation between $\Delta t^{diff}\big(a_{eff}, c_b, D, L\big)$ and the calculated cases. Thus for $u(c_b)$,

$$u(\Delta t^{diff})^A_{c_b} = |\Delta t^{diff}\big(a_{eff}, c_b, D, L\big) - \Delta t^{diff}\big(a_{eff}, c_b + u(c_b), D, L\big)|, \tag{5.34}$$

$$u(\Delta t^{diff})^B_{c_b} = |\Delta t^{diff}\big(a_{eff}, c_b, D, L\big) - \Delta t^{diff}\big(a_{eff}, c_b - u(c_b), D, L\big)|, \tag{5.35}$$

where superscript A and B corresponds to the addition and subtraction of $u(c_b)$ respectively. The maximum value of the two corresponding uncertainties in Eqs. (5.34) and (5.35), will be the resulting uncertainty $u(\Delta t^{diff})_{c_b}$. These calculations are then done for $u(a_{eff})$, $u_c(L)$, and $u(D)$.

5.3 Sensitivity analysis

To archive a relative expanded uncertainty of the measured sound velocity of less than 1000ppm = 0.1%, it is crucial to understand how different measurement variables will impact the total uncertainty. This section will thus address how sensitive the total expanded uncertainty is to uncertainty contributions from the different measurement variables. The results will provide an indication of the largest uncertainty contributors, allowing them to be compensated for prior to creating the measurement cell. Many of the assumptions made in this section are thus preliminary. The approach to the sensitivity analysis is comparable to [21], and the calculations are based on the uncertainty model for c_s presented in Section 5.2, where Eq. (5.7) will be used for further analysis.

Distilled water will in this project be used as a reference medium, and will thus be used throughout the sensitivity analysis. As will be evident later, the uncertainty increases with increasing temperature. The maximum set temperature throughout the project will therefore be applied. In the sensitivity analysis, the following assumptions are made:

- f = 500 kHz
- T = 60^oC
- L_0 = 25.0 mm, sample length at room temperature
- c_s = 1551.1 m/s, sound velocity in distilled water at 60.0^oC using Eq. (2.2)
- T_0 = 24 ^oC, reference temperature
- $\alpha_P = 71.5 \cdot 10^{-6} K^{-1}$, mean value of temperature coefficient for Plexiglas in [92]

In the preliminary sensitivity analysis, it is further assumed that the thermal expansion, K_T, follows Eq. (2.54). The sample length due to thermal expansion at 60.0^oC will thus be L = 25.12 mm using the listed α_P. Further, $\Delta t = 2L/c_s \approx 32.4\mu s$.

Differentiating Eq. (2.54), the uncertainty in K_T can be expressed as

$$u(K_T) = \sqrt{(\Delta T \cdot u(\alpha_T))^2 + (\alpha_T \cdot u(\Delta T))^2}. \tag{5.36}$$

By defining $E_{K_T} = \frac{u(K_T)}{K_T}$, $E_{\alpha_T} = \frac{u(\alpha_T)}{\alpha_T}$ and $E_{\Delta T} = \frac{u(\Delta T)}{\Delta T}$, Eq. (5.36) can be expressed in terms of relative uncertainty,

$$E_{K_T} = \sqrt{\Big(\frac{\Delta T \alpha_T}{(1+\alpha_T \Delta T)} E_{\alpha_T}\Big)^2 + \Big(\frac{\alpha_T \Delta T}{(1+\alpha_T \Delta T)} E_{\Delta T}\Big)^2}. \tag{5.37}$$

which can be inserted into Eq. (5.7).

Initially, it is assumed that each term in Eq. (5.7) contributes equally to the total uncertainty. Each term is therefore named U and can be expressed as

$$k \cdot E_c = k\sqrt{4U^2}, \tag{5.38}$$

where k = 2. A total uncertainty of $2 \cdot E_c < 1000$ ppm at 95% confidence level is desired. Thus can each term in Eq. (5.38) at most contribute with 250 ppm at 68% confidence level. If $s_{\Delta t^{corr}} \cdot E_{\Delta t^{corr}}$ = 250 ppm, $E_{\Delta t^{corr}}$ can contribute with 16195 ppm assuming $\Delta t^{corr} < 0.5\mu s$ and $\Delta t \approx 32.4\mu s$.

In Table 5.7, a preliminary uncertainty budget is calculated which shows what the individual standard uncertainties must be if each term is to contribute equally in the case of c = 1551.1 m/s and T = 60^oC.

Table 5.7: Preliminary uncertainty budget nr.1 for the sound velocity using the pulse-echo buffer rod method when c_s = 1551.1 m/s and T = 60.0^oC, assuming each parameter contributes equally and $E_c \leq 1000\ ppm = 0.1\%$ (95% confidence level).

Variable	**Rel. standard uncertainty (68% c. l.)**	**Typical value**	**Standard uncertainty (68% c.l.)**	**Expanded uncertainty (95% c.l.)**
L_0	250 ppm	25.00mm	0.0063 mm	0.0126 mm
K_T	250 ppm	1.0027	0.00025	0.0005
Δt	250 ppm	32.3μs	0.00810 μs	0.0162 μs
Δt^{corr}	16129 ppm	0.5 μs	0.00810 μs	0.0162μs
c_s	500 ppm	1550 m/s	0.776 m/s	1.551 m/s

If $E_{K_T} \leq 250$ ppm (ref. Table 5.7), and it is assumed that α_T and ΔT contribute equally, Eq. (5.37) puts $(\frac{\alpha_T \Delta T}{1+\alpha_T \Delta T})^2 E_{\Delta T}^2$ = 125 ppm. If T = 60^oC, then $E_{\Delta T}$ = 44952 ppm and consequently will $u(\Delta T)$ = 1.75^oC. Such high temperature uncertainties will not be realistic throughout the project. A type A PT100 temperature probe has an uncertainty of 0.27^oC (95% confidence level) at 60^oC [65]. If E_{K_T} = 50

ppm, then $u(\Delta T) = 0.351^oC$ (68% confidence level), which should be sufficient, considering a possible increase in uncertainty due to calibration.

Further, a standard digital caliper at the Department for Physics and Technology's workshop has an accuracy of 0.03mm (assumed 95% confidence level)[68]. Thus must $u(L_0)$ be larger than 0.015 mm at 68% confidence level, assuming that no high-accuracy measuring tools are provided.

In Table 5.8 in Fosså [39], the uncertainty in diffraction correction, $u(\Delta t^{diff})$ accounts for 0.4% of the total uncertainty with $u(\Delta t^{diff}) = 1.5 \cdot 10^{-10}$ s. Based on these numbers, it is thus assumed that the uncertainty in diffraction correction will be significantly lower than the preliminary standard uncertainty presented in Table 5.7, and $E_{\Delta t^{corr}}$ is thus reduced from the tentative 250 ppm.

The pulse-echo buffer rod method is prone to several coherent noise contributions [93] which could affect transit time calculations. Each of these noise sources may increase the uncertainty in transit time. Quantifying these contributions has not been done in the sensitivity analysis, but following Fosså [39], which found an uncertainty of $u(\Delta t) = 4.59 \cdot 10^{-8}$ s, an uncertainty larger than the uncertainty presented in Table 5.7 is chosen.

Based on the discussion above, a new sensitivity analysis is carried out, where the contribution of E_{K_T} and $E_{\Delta t^{corr}}$ is decreased and the contribution of E_L and $E_{\Delta t}$ is increased relative to Table 5.7. The result is presented in Table 5.8, and will serve as a basis for the project when designing the measurement cell.

Table 5.8: Preliminary uncertainty budget nr. 2 for the sound velocity using the pulse-echo buffer rod method when c_s = 1551.1 m/s and T = 60.0^oC if $E_c \leq 1000\ ppm = 0.1\%$ (95% confidence level).

Variable	**Rel. standard uncertainty (68% c.l.)**	**Typical value**	**Standard uncertainty (68% c.l.)**	**Expanded uncertainty (95% c.l.)**
L_0	630 ppm	25.00 mm	0.0158 mm	0.0316 mm
K_T	50 ppm	1.0028	$5.0 \cdot 10^{-5}$	$1.0 \cdot 10^{-4}$
Δt	320 ppm	32.3μs	0.01 μs	0.021 μs
Δt^{corr}	1793 ppm	0.5 μs	0.645 ns	1.290 ns
c_s	500 ppm	1551.1 m/s	0.776 m/s	1.551 m/s

The uncertainty in c_s as a function of temperature can further be studied using Eq. (5.2) in a temperature span of 20 to 60^oC. Each uncertainty contribution in Table 5.8 is assumed constant through the entire temperature span. The theoretical sound velocity is calculated as a function of temperature using Eq. (2.2) with P_M = 1.013 bar, which can be used to find the corresponding transit time (Eq. (2.12)). K_T is further found as a function of temperature following Eq. (2.54), and Δt^{corr} and L_0 are constants. The resulting $u(c_s)$ as a function of temperature is presented in Fig. 5.2

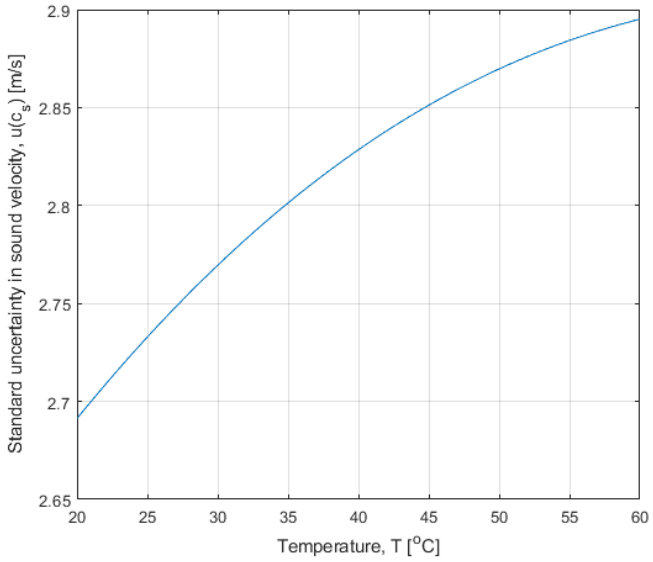

Figure 5.2: Uncertainty in c_s as a function of temperature, using Eq. (2.2). The uncertainty in $u(L_0)$, $u(\Delta t)$, $u(K_T)$, and $u(\Delta t^{corr})$ is set to constant.

From Fig. 5.2, it is evident that $u_c(c_s)$ increases with increasing temperature. Consequently will the uncertainty budgets in Chapter 6 be presented at maximum temperature throughout the project.

5.4 Uncertainty model for the theoretical sound velocities

5.4.1 Combined standard uncertainty in pressure

The theoretical sound velocity in distilled and saline water and the corresponding uncertainties will be dependent on the uncertainty in pressure, $u_c(P)$. A model for $u_c(P)$ will thus be presented here.

The gauge pressure, P_G, is given by Eq. (2.3). Differentiating Eq. (2.3) and setting $u(P)_{atm} = 0$, $u_c(P_G) = u_c(P)$ can be modelled as

$$\begin{aligned} u_c^2(P) = u_c^2(P)_M + \left(\rho g\right)^2 \cdot u_c^2(P)_d + \left(\rho h\right)^2 \cdot u^2(P)_{gravity} \\ + \left(gh\right)^2 \cdot u^2(P)_{density} + u^2(P)_{other}, \end{aligned} \tag{5.39}$$

where ρ is the density of the liquid, g is gravitational acceleration and h is the depth of the sound axis in meters. Note that hydrostatic pressure is given in Pascal, and pressure in bar. Thus must the sensitivity coefficients be converted to bar. Further,

$$u_c^2(P)_M = u^2(P)_{inst} + u^2(P)_{reading} + u^2(P)_{stability}, \tag{5.40}$$

and

$$u_c^2(P)_d = u^2(P)_{parallel} + u^2(P)_{caliper}. \tag{5.41}$$

All uncertainty contributions are described in Table 5.9.

Table 5.9: Description of uncertainty contributors when measuring the pressure using Paroscientific Model 740

Uncertainty contributor	**Uncertainty description**
$u(P)_{inst}$	Standard uncertainty in Paroscientific Model 740 pressure sensor.
$u(P)_{reading}$	Standard uncertainty due to observational fluctuations in analogue readings.
$u(P)_{stability}$	Standard uncertainty due to long term stability of pressure sensor.
$u(P)_{density}$	Standard uncertainty due to the deviation in sound velocity by assuming that the density of pure water is constant with increasing temperature.
$u(P)_{gravity}$	Standard uncertainty due to gravitational acceleration.
$u(P)_{parallel}$	Standard uncertainty in propagation depth below water surface.
$u(P)_{caliper}$	Standard uncertainty of the MarCal 16EWP digital caliper.
$u(P)_{other}$	Standard uncertainty due to other unknown contributions.

5.4.2 Combined standard uncertainty in theoretical sound velocity in distilled water

The measured sound velocity in distilled water is compared to the theoretical sound velocity, c_{td}, using Eq. (2.2). In this section, a model for the uncertainty of the theoretical sound velocity as a function of temperature in distilled water is presented.

Although T and P_G are correlated, they are here assumed to be uncorrelated as the increase in density with temperature is assumed negligible. The combined uncertainty can then be calculated using equation

$$u_c(c_t)^2 = \left(\frac{\partial c_t}{\partial T}u_c(T)\right)^2 + \left(\frac{\partial c_t}{\partial P}u_c(P)\right)^2 + \left(u(c_t^{model})\right)^2, \tag{5.42}$$

where the sensitivity coefficients are given as,

$$\frac{\partial c_t}{\partial T} = 4.88 - 0.0964 \cdot T + 4.05 \cdot 10^{-4} \cdot T^2 + (0.028 + 4.8 \cdot 10^{-4} \cdot T) \cdot \frac{P_G}{100}, \tag{5.43}$$

$$\frac{\partial c_t}{\partial P_G} = \frac{1}{100} \cdot (15.9 + 0.028 \cdot T + 2.4 \cdot 10^{-4} \cdot T^2). \tag{5.44}$$

5.4.3 Combined standard uncertainty in theoretical sound velocity in saline water

The measured sound velocity in saline water is compared with the UNESCO equation, Eq. (2.4), which is dependent on salinity, temperature and pressure. If the uncertainties are assumed uncorrelated, the combined uncertainty for theoretical saline water, c_{ts}, can be found as

$$u_c(c_{ts})^2 = \left(\frac{\partial c_{ts}}{\partial S}u(S)\right)^2 + \left(\frac{\partial c_{ts}}{\partial T}u_c(T)\right)^2 + \left(\frac{\partial c_{ts}}{\partial P}u_c(P)\right)^2, \tag{5.45}$$

where $\frac{\partial c_t^{sal.}}{\partial S}$, $\frac{\partial c_t^{sal.}}{\partial T}$ and $\frac{\partial c_t^{sal.}}{\partial P}$ are given in Appendix B, as Eqs. (B.2), (B.3) and (B.4) respectively.

Chapter 6

Experimental results

The experiments conducted throughout the project are presented in this chapter, together with the corresponding uncertainty when applicable. The uncertainty calculations will be based on the uncertainty models presented in Chapter 5, and the table set up for the uncertainty budgets is from [40].

The chapter consists of eight sections with corresponding subsections. The calibration results of the temperature sensor and calculated uncertainties concerning temperature and pressure measurements will be presented in Section 6.1. The results of the measured dimensions, the uncertainties in dimensions and uncertainty in thermal expansion of the sample length are presented in Section 6.2. Section 6.3 presents the results of the measured compressional and shear sound velocity. In Section 6.4, the directivity measurements are presented, and the effective element radius and transducer bandwidth is calculated. In Sections 6.5, 6.6, and 6.7 the experimental sound velocity measurements for distilled water, saline water and Extra Virgin olive oil are presented, respectively, together with the corresponding uncertainties. With the above-calculated uncertainties, the total uncertainty in experimental sound velocity can be calculated, presented in Section 6.8.

6.1 Temperature and Pressure

Temperature and pressure measurements are conducted throughout the project. Before temperature measurements are conducted, the temperature sensor is calibrated. This section will present the calculated uncertainties concerning temperature and pressure measurements and the calibration results.

6.1.1 Calibration of PT100

To calibrate the PT100 temperature sensor element used in this project, two sets of measurements are attained as explained in Section 3.1.7.
In the first set of measurements, the coefficients α, β and R_0 in Eq. (3.1) are set to $\alpha = 3.9083 \cdot 10^{-3}/^{o}C$,

$\beta = -5.775 \cdot 10^{-7}/^oC^2$ and $R_0 = 100\Omega$, corresponding to the standard coefficients for a regular platinum element[66]. The measured temperature of the PT100 sensor in the dry-well as a function of reference temperature in the dry-well is presented in black in Fig. 6.1, and the resulting deviation between the curves is presented in blue in Fig. (6.2). At 60^oC, the deviation between the two temperature sensors is at its highest at 0.4^oC.

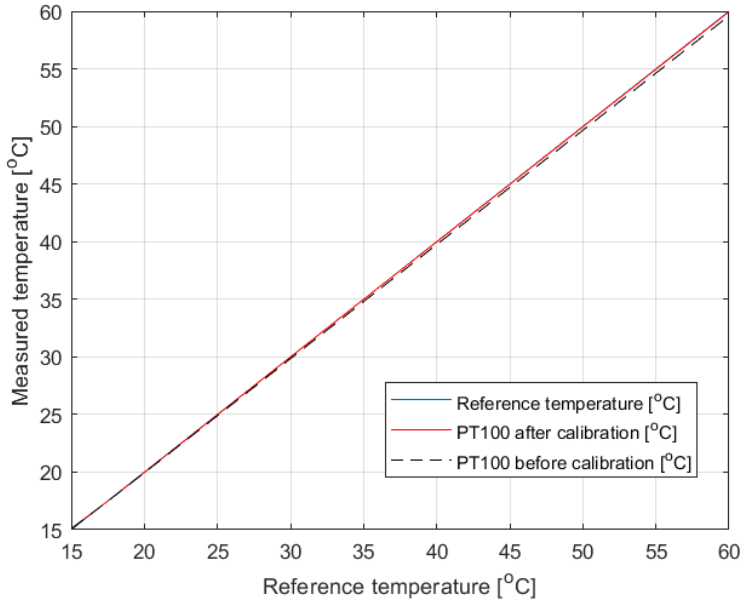

Figure 6.1: Result of the measured temperature before calibration (black dotted) and after calibration (red) with the PT100 temperature sensor. Plotted against the reference temperature in the dry-well, measured with the reference probe

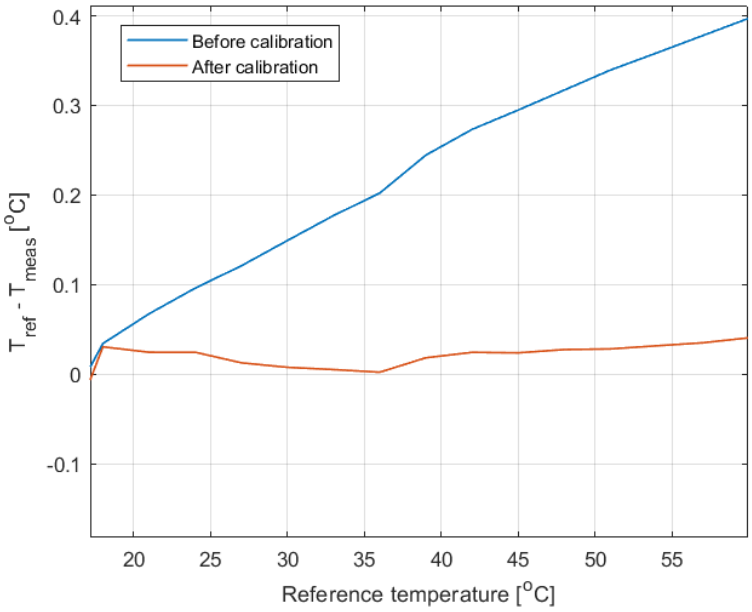

Figure 6.2: Deviation between the reference temperature, T_{ref} and the measured temperature by the PT100 temperature probe, T_{meas}, before (blue) and after calibration (red), as a function of T_{ref}.

The measured temperature with the original coefficients α, β and R_0 is transformed to resistance using Eq. (3.1), and the resulting plot is used to calculate the new coefficients by implementing Eq. (3.1) in Matlab's ready-made curve fitting tool, cftool [56].

The new coefficients are found to be $\alpha = 3.841 \cdot 10^{-3} {}^oC^{-1}$, $\beta = -2.095 \cdot 10^{-7} {}^oC^{-2}$ and $R_0 = 100.1\Omega$. These coefficients are implemented in the temperature scanner, and a new series of temperature measurements is conducted for a temperature span of 15-60 ${}^oC$. The resulting measured temperature from the PT100 sensor is presented in red in Fig.6.1 as a function of reference temperature, together with the reference temperature (in blue). The resulting deviation is presented in Fig. 6.2, now calculated to be 0.04 at 60^oC. The resulting coefficients are used throughout the project when measuring the temperature by applying Eq. (3.2).

The uncertainty due to deviation in calibration is found using the maximum deviation from calibration, corresponding to 0.04^oC at 60^oC with a confidence level of k =$\sqrt{3}$. This results in standard uncertainty $u(T)_{calibdev} = 0.023^oC$.

6.1.2 Uncertainty in temperature measurements

In Section 5.2.1, a model for the combined standard uncertainty of the temperature measurements is presented, $u_c(T)$. This model consists of contributions from the temperature sensor itself, uncertainties due to calibration, and uncertainty due to the RTD-USB adapter.

In Table 6.1 all uncertainties for the variables used in the uncertainty model are presented for T = T_0 = 22.94^oC, and for T = 45.7^oC, corresponding to the highest recorded temperature throughout the project. The description of each uncertainty contribution is presented in Table 5.2.

Using the tabulated values in Table 6.1 inserted into Eq. (5.9), the combined standard uncertainty in calibration is found to be $u_c(T)_{cal} = 0.034^oC$ at $T_0 = 22.94^oC$, and $u_c(T)_{cal} = 0.072^oC$ at $T = 45.7^oC$.

This can in turn be used to calculate the total standard uncertainty in temperature measurements, $u_c(T)$, using Eq. (5.8), and is presented as an uncertainty budget for $T = 45.7^oC$ in Table 6.2. The same equation can be applied for T_0 with uncertainty values presented in Table 6.1, resulting in $u_c(T_0) = 0.143^oC$.

Table 6.1: Standard uncertainty for the uncertainty contributions when measuring the temperature in the sample area using JUMO STEAMTemp Temperaturgiver RTD (902830), presented for $T_0 = 22.94^oC$ and $T = 45.7^oC$. All values are presented with 68% confidence level, k = 1. Description of each variable is presented in Table5.2. Note that tabulated uncertainties for $u(T)_{Tref}$ and $u(T)_{element}$ are assumed a 95% c.l., k = 2, and are here divided by 2 for 68% c.l.

Uncertainty contributor	**Description**
$u(T)_{Tref}$	1/10 DIN Class B: 0.022^oC at $T = T_0 = 22.94^oC$ and 0.033^oC at $T = 45.7^oC$. Found by interpolating values presented in [67], which follows IEC 60751 [65].
$u(T)_{drift_{ref}}$	Set to 0.025^oC following [94] for the entire temperature range.
$u(T)_{scanner}$	Manufacturers specification: 0.005^oC for 4-wire PRT/RTD [95] at $T_0 = 22.94^oC$. Add 0.003^oC Temp. Comp. per ^oC outside 18^oC to 28^oC at medium sample rate.
$u(T)_{calibdev}$	Found to be 0.023^oC at most (ref. Section 6.1.1). Assumed for whole temperature range.
$u(T)_{element}$	Class A RTD, 0.098^oC at T = $T_0 = 22.94^oC$ and 0.121^oC at $T = 45.7^oC$, Found by interpolating values presented in [67], which follows IEC 60751 [65].
$u(T)_{drift_{JM}}$	Set to $\pm$ 0.025^oC following [94] for the entire temperature range.
$u(T)_{adapter}$	Specified by the manufacturer to be 0.06^oC at 25^oC [96]. Assumed valid throughout the temperature range.
$u(T)_{var}$	Observed to be $\pm 0.002^oC$. Assumed for the entire temperature range.
$u(T)_{other}$	Neglected.

Table 6.2: Uncertainty budget for the temperature measurements using the using JUMO STEAMTemp Temperaturgiver RTD 902830 at 45.7^oC.

Uncertainty Contributor	**Input uncertainty**				**Combined uncertainty**	
	Expanded uncertainty $[^oC]$	**Conf. level & distr.**	**Cov. fac., k**	**Standard uncertainty** $[^oC]$	**Sens. Coeff.**	**Variance**
Calibration	0.0720	68% (norm)	1	0.0720	1	$5.18{\cdot}10^{-3}(^oC)^2$
PT100 dev. from calibration	0.0230	68% (norm)	1	0.0230	1	$5.29{\cdot}10^{-4}(^oC)^2$
PT100 uncertainty	0.241	95% (norm)	2	0.121	1	$0.0146\ (^oC)^2$
Thermal drift	0.0250	68% (norm)	1	0.0250	1	$6.25{\cdot}10^{-4}(^oC)^2$
RTD to USB adapter	0.0600	68% (norm)	1	0.0600	1	$3.60{\cdot}10^{-3}(^oC)^2$
Stability	0.0100	68% (norm)	1	0.0100	1	$1.00{\cdot}10^{-4}(^oC)^2$
Other sources	n/a	n/a	n/a	n/a	n/a	N/A
Sum of variances, $u_c^2(T)$						$0.0246\ (^oC)^2$
Combined standard uncertainty, $u_c(T)$						$0.157\ ^oC$
Expanded uncertainty (95%, k = 2), U(T)						$0.314\ ^oC$
Relative expanded uncertainty (95%, k = 2), U(T)/T						0.69%

6.1.3 Uncertainty in pressure measurements

Pressure measurements are conducted using a Paroscientific Model 740. In the following, the calculated uncertainty in the measured pressure will be presented, which follows the model presented in Section 5.4.1. The results will be used to calculate the uncertainty in theoretical sound velocity for pure and saline water, Sections 6.5.3 and 6.6.3 respectively.

The standard uncertainty values for the uncertainty contributors in pressure measurements are presented in Table 6.3, where a description of each contributor is presented in Table 5.9.

The density of pure water, ρ_w, as a function of temperature can be expressed by the Kell formulation [28], and the density of saline water, ρ_s is a function of temperature, salinity, and ρ_w [34]. By assuming a constant density throughout the project, uncertainties of $0.5{\cdot}10^{-4}$ m/s and $6 \cdot 10^{-6}$ m/s for distilled and saline water has been found by inserting $\rho_w = 998 kg/m^3$ and $\rho_s = 1013.2 kg/m^3$, corresponding to densities at 20 ^oC, into Eqs. 2.2 and 2.4 respectively for T = 60^oC. The dependency of the theoretical sound velocities due to incremental changes in the density for distilled and saline water at increasing temperatures are thus assumed negligible for the temperature range in this project.

The uncertainty in pressure due to the uncertainty in sound propagation depth, $u_c^2(P)_d$, is dependent on the height measurements of the measurement cell. Inserting $u(P)_{parallel}$ and $u(P)_{caliper}$ from Table 6.3 into Eq. (5.41) yields $u_c(P)_d = 3.13 \cdot 10^{-5}$ m.

Using the sound velocity measurements for distilled water, Table 6.14, as an example with P_M = 1.0395 bar, and assuming $\rho_w = 998 kg/m^3$ and d = $55{\cdot}10^{-3}$ m, the uncertainty in pressure can be found, presented as an uncertainty budget in Table 6.4.

Table 6.3: Standard uncertainty for the uncertainty contributors when measuring the pressure using Paroscientific Model 740. All values are presented with 68% confidence level, and a description of each uncertainty contributor is presented in Table6.4.

Uncertainty contributor	**Uncertainty description**
$u(P)_{instr}$	Specified by manufacturer to be 0.015 % of reading [63].
$u(P)_{reading}$	Observed to be $6.5 \cdot 10^{-5}$ bar.
$u(P)_{stability}$	Not available.
$u(P)_{density}$	Negligible (cf. discussion above).
$u(P)_{gravity}$	Neglected.
$u(P)_{parallel}$	0.0313 mm. (Ref. Table6.5).
$u(P)_{caliper}$	Specified to be 0.03 mm following DIN 862 standard [68] assuming 95% c.l., k = 2, thus 0.015 mm at 68% c.l.
$u(P)_{other}$	Not available.

Table 6.4: Uncertainty budget for the measured pressure using Paroscientific Model 740 in distilled water with P_M = 1.0395 bar, $\rho_w = 998 kg/m^3$ and d = $55{\cdot}10^{-3}$ m.

Uncertainty contributor	**Input uncertainty**				**Combined uncertainty**	
	Exp. uncertainty [bar]	**Conf. level & distr.**	**Cov. fac., k**	**Standard uncertainty [bar]**	**Sens. coeff.**	**Variance**
Instrument	$1.56{\cdot}10^{-4}$	68% (norm)	1	$1.56{\cdot}10^{-4}$	1	$2.43{\cdot}10^{-8} bar^2$
Observational fluctuations	$6.50{\cdot}10^{-5}$	68% (norm)	1	$6.50{\cdot}10^{-5}$	1	$4.23{\cdot}10^{-9} bar^2$
Height	$3.13 \cdot 10^{-5}$	68%(norm)	1	$3.13 \cdot 10^{-5}$	0.0979	$9.39{\cdot}10^{-12} bar^2$
Density	n/a	n/a	n/a	n/a	n/a	n/a
Gravity	n/a	n/a	n/a	n/a	n/a	n/a
Sum of variances					$u_c^2(P)$	$2.85{\cdot}10^{-8} bar^2$
Combined standard uncertainty (68% confidence level, k = 1)					$u_c(P)$	$1.69{\cdot}10^{-4} bar$
Expanded uncertainty (95% confidence level, k = 2)					$U(P)$	$3.38{\cdot}10^{-4} bar$
Measured pressure					P	1.0395 bar
Relative expanded uncertainty					U(P)/P	0.033%

6.2 Measurement cell dimensions

This section presents the measured length of the sample area, together with the dimensions of the Plexiglas buffer, and the associated uncertainties. The accuracy of the calculated thermal expansion, K_T, is directly related to uncertainties provided below and will thus be presented in Section 6.2.3.

6.2.1 Measured dimensions

All measurements are taken at temperature, $T = 22.94^oC$, and will thus be used as reference temperature for the thermal expansion, i.e. $T_0 = 22.94^oC$.
In Table 6.5, the entire surface of interest is measured. Table 6.6 presents repeatability measurements of the length of the buffer and sample area, taken approximately at the sound axis.

The distances from the bolts to the sample area, used for thermal expansion in Section 2.5, are measured to be d_{b1} = 0.7 mm and d_{b2} = 0.11 mm on the left and right side on the measurement cell respectively, with a standard uncertainty of ≈ 0.05 mm. The average distance will be used for thermal expansion calculations, thus $d_b = 0.9mm \pm 0.214mm$. The uncertainty is at 68% confidence level, and includes the MarCal 16EWR digital caliper uncertainty of 0.03mm (95% confidence level).

Table 6.5: Measurements of the sample length, L_0, and the buffer length (D), width (W) and height (H) using a MarCal 16EWR digital caliper. All measurement series were taken across the entire surface of interest.$u_{parallel}$ corresponds to the standard deviation of the measurements.

Measurement number	L_0 **[mm]**	**D [mm]**	**W [mm]**	**H [mm]**
1	25.16	70.11	100.05	105.11
2	25.17	70.08	100.10	105.04
3	25.18	70.10	100.06	105.13
4	25.18	70.12	100.01	105.05
5	25.18	70.09	100.02	105.10
6	25.19	70.06	100.05	105.12
7	25.17	70.10	100.06	105.08
8	25.17	70.11	100.10	105.09
9	25.16	70.10	100.00	105.13
10	25.19	70.12	100.03	105.11
Average value	25.18	70.10	100.05	105.1
$u_{parallel}$	0.011	0.0185	0.0343	0.0313

Table 6.6: Measurements for the sample length, L, and the buffer length, D, using a MarCal 16EWR digital caliper. Both measurement series were taken at the approximate location of the sound axis, thus the center of the width. u_{rep} corresponds to the standard deviation of the measurements.

Measurement number	L_0 **[mm]**	**D [mm]**
1	25.18	70.11
2	25.17	70.09
3	25.18	70.10
4	25.18	70.10
5	25.18	70.10
6	25.17	70.11
7	25.17	70.10
8	25.18	70.11
9	25.19	70.10
10	25.18	70.11
Average value	25.18	70.10
u_{rep}	0.0063	0.0068

6.2.2 Uncertainty in measured dimensions

In Section 5.2.3, a model for the uncertainty in sample length is presented through Eq. (5.13). The standard uncertainty of all uncertainty variables needed to calculate $u_c(L_0)$ are summarized in Table 6.7, and the description of the variables can be found in Table 5.4. The reflector surface is assumed to be plane within an uncertainty of $0.02mm$ at 95% confidence level (ref. Section 3.1.8.) Using the standard uncertainties presented in Table 6.7, together with Eq. (5.15), $u_c(D) = 0.0165mm$. This, together with $u(R)$, can in turn be used to find the standard uncertainty in sample length due to non-parallelism in the vertical direction of the sample area by applying Eq. (5.14), which results in $u_c(L_0)_{vert} = 0.0193mm$. With a calculated $u_c(L_0)_{vert}$, the total uncertainty in sample length can be found, presented as an uncertainty budget in Table 6.8.

Table 6.7: Standard uncertainty of the uncertainty contributions used to calculate $u(L_0)$. All are found at $T = T_0 = 22.94^oC$ for a 68% confidence level, k = 1. Discription of the uncertainty contributors are found in Table5.4.

Uncertainty source	**Description**
$u_{caliper}$	Specified to be 0.03 mm following DIN 862 standard [68] assuming 95% c.l., k = 2, thus 0.015 mm at 68% c.l.
$u(L_0)_{rep}$	0.0063 mm, ref. Table 6.6.
$u_c(L_0)_{vert}$	0.0193 mm (cf. discussion above)
$u(R)$	Set to 0.01 mm
$u(D)_{rep}$	0.0068 mm, ref. Table 6.6.
u_{stab}	n/a.
$u(L_0)_{other}$	n/a.

Table 6.8: Uncertainty budget for the measured sample length, L_0, calculated with Eq. (5.13) at $T_0 = 22.94^oC$.

Uncertainty source	**Input uncertainty**				**Combined uncertainty**	
	Expand. unc.	**Conf. level & distr.**	**Cov. fact., k**	**Standard unc.**	**Sens. coeff.**	**Variance**
Caliper uncertainty	0.0300 mm	95% (norm)	2	0.0150 mm	1	$2.25{\cdot}10^{-4}mm^2$
Repeatability	$6.30{\cdot}10^{-3}$ mm	68% (norm)	1	$6.30{\cdot}10^{-3}$ mm	1	$3.97{\cdot}10^{-5}mm^2$
Uneven surfaces	0.019 mm	68% (norm)	1	0.0193 mm	1	$3.72{\cdot}10^{-4}mm^2$
Stability	n/a	n/a	n/a	n/a	n/a	n/a
Other sources	n/a	n/a	n/a	n/a	n/a	n/a
Sum of variances				$u_c^2(L_0)$		$6.37{\cdot}10^{-4}mm^2$
Combined standard uncertainty				$u_c(L_0)$		0.0252mm
Expanded uncertainty (95% conf. level, k = 2)				$U(L_0)$		0.0505mm
Measured length				L_0		25.18mm
Relative expanded uncertainty (95% confidence level)				$E_L = U(L_0)/L_0$		0.200%

6.2.3 Uncertainty in thermal expansion

To calculate the uncertainty in thermal expansion,K_T, the model presented in Section 5.2.2 will be applied with uncertainty contributors described in Table 5.3. A case of T = 45.7^oC, corresponding to the maximum recorded temperature throughout the project, will be studied as an example.

The sample length, L_0, has been measured to L_0 = 25.18mm (ref. Table 6.6) with $u_c(L)$ = 0.0252 mm (ref. Table 6.8).

The length between bolts and sample area, d_p, has been measured to d_p = 0.9mm with corresponding uncertainty $u_c(d_b)$ = 0.214 mm (ref. Section 6.2.1).

The uncertainty in temperature at 68% confidence level is calculated to 0.143^oC for T = 22.94^oC and 0.157^oC for T = 45.7^oC in Section 6.1.2, and the corresponding uncertainty in ΔT at 68% confidence level is thus $u_c(\Delta T)$ = 0.212^oC following Eq. (5.12) with sensitivity coefficients equal to 1.

Additionally, α_p = $70 \cdot 10^{-6}$[53] and α_a = $24 \cdot 10^{-6}$[52], with corresponding uncertainties of $u(\alpha_p)$ = $2.35 \cdot 10^{-6}$ and $u(\alpha_a) = 0.35 \cdot 10^{-6}$ (ref. Section 3.5.2).

The variables above with corresponding uncertainties can be used to calculate the uncertainty in K_T, presented as an uncertainty budget in Table 6.9.

Table 6.9: Uncertainty budget for the thermal expansion in L_0 at T = 45.8^oC, where T_0 = 22.94^oC, L_0 = 25.18 mm, d_p = 0.9 mm, $\alpha_p = 70 \cdot 10^{-6}$[53], and $\alpha_a = 24 \cdot 10^{-6}$[52].

Uncertainty Source	**Input uncertainty**				**Combined uncertainty**	
	Expanded unc.	**Conf. level & distr.**	**Cov. factor, k**	**Standard unc**	**Sens.coeff**	**Variance**
Temperature, ΔT	0.212 ^oC	68% (norm)	1	0.212^oC	$2.23 \cdot 10^{-5}$	$2.24 \cdot 10^{-11}$
Thermal ex. coeff. α_a	$3.50 \cdot 10^{-7}/(^oC)$	68% (norm)	1	$3.50 \cdot 10^{-7}/(^oC)$	23.57	$6.81 \cdot 10^{-11}$
Thermal ex. coeff, α_p	$2.40 \cdot 10^{-6}/(^oC)$	68% (norm)	1	$2.4 \cdot 10^{-6}/(^oC)$	0.812	$3.80 \cdot 10^{-12}$
Uncertainty in length, L_0	$2.52 \cdot 10^{-5}$ m	68% (norm)	1	$2.52 \cdot 10^{-5}$ m	0.0015	$1.43 \cdot 10^{-15}$
Uncertainty in d_p	$2.14 \cdot 10^{-4}$ m	68% (norm)	1	$2.14 \cdot 10^{-4}$ m	-0.042	$8.08 \cdot 10^{-11}$
Sum of variances					$u_c^2(K_T)$	$1.75 \cdot 10^{-10}$
Combined standard uncertainty (68 % confidence level, k = 1)					$u_c(K_T)$	$1.32 \cdot 10^{-5}$
Expanded uncertainty (95% **confidence level, k = 2)**					$U(K_T)$	$2.65 \cdot 10^{-5}$
Thermal expansion at T = 45.7^oC					K_T	1.0005
Relative expanded uncertainty (95% **confidence level, k = 2)**					$U(K_T)/K_T$	0.00265%

6.3 Sound velocity in Plexiglas

Using the experimental setup explained in Section 3.2 at $T_0 = 22.8^oC$, a waveform is sampled, shown in Fig. 6.3. By analyzing the steady-state portion of the two reflections from the buffer/air interface, the transit time and thereby the sound velocity can be calculated using the zero-crossing method (Section 3.4.2). 14 consecutive zero-crosses were chosen, located inside the red square in Fig. 6.3. The average sound velocity was then calculated using Eq. (3.3), with the measured transit times and buffer length, D = 70.1 mm. The resulting average compressional sound velocity corrected for diffraction in Plexiglas is found to be $c_b = 2711.2 m/s$ with a standard deviation of 0.232 m/s.

From the measured compressional sound velocity in the Plexiglas buffer, a new shear wave sound velocity can be calculated using Eq. (2.1) with $\nu = 0.4$ and $c_b = 2711$ m/s, resulting in $c_{shear} = 1106.8$ m/s at 22.8^oC.

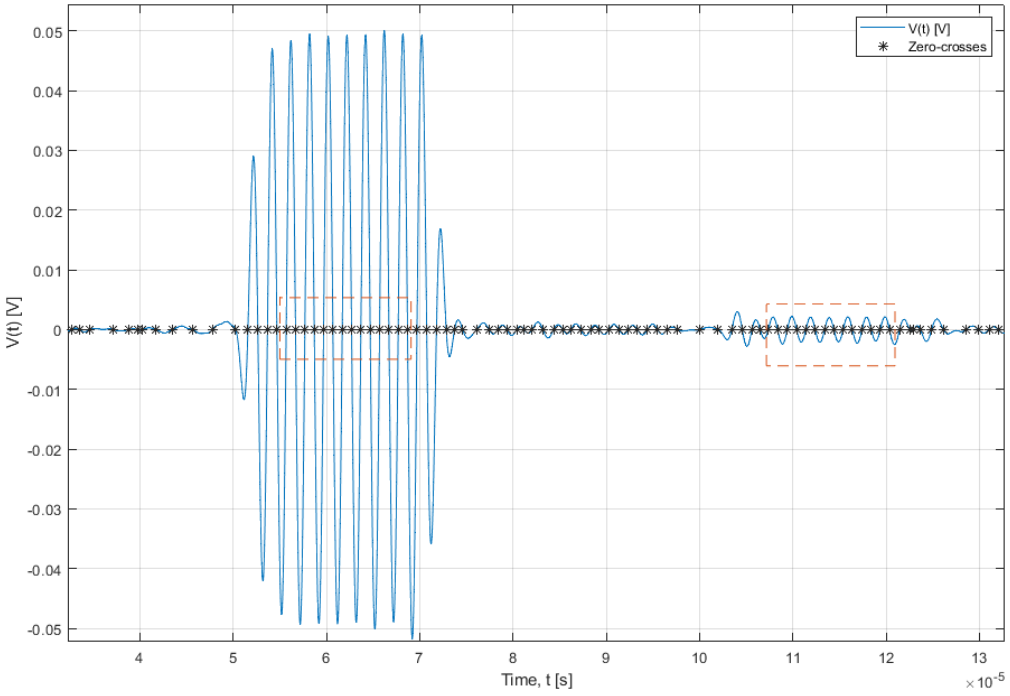

Figure 6.3: Resulting response using the measurement setup described in Section 3.2 with a f = 500kHz 10 period pulse. The calculated zero-crosses are shown with black marks, and the zero-crosses located inside the red squared are used for calculating the compressional sound velocity in Plexiglas.

The compressional sound velocity in Plexiglas as a function of temperature is measured using the experimental setup shown in Fig. 3.3 and the experimental method explained in Section 3.2.

To accurately account for thermal expansion, the Plexiglas used for the experiment is a Plexiglas block measured to 85.11 ± 0.1 mm at 22.10^oC. In steps of 3^oC, the waveform is recorded and the average sound velocity is calculated using the transit time between the two reflections for 14 consecutive zero-crosses, as shown in Fig. 6.3. To compensate for thermal expansion, the Plexiglas length as a function

of temperature can be expressed with Eq. (2.54), using $\alpha_b = 70 \cdot 10^{-6}$ [53] and $L_0^{buffer} = 85.11$ mm at $T_0 = 22.1^oC$.

$$L_{exp}^{buffer}(T) = L_0^{buffer} \cdot (1 + \alpha_b(T - T_0)) = 85.11 \cdot 10^{-3} \cdot (1 + 70.0 \cdot 10^{-6}(T - 22.1)) \tag{6.1}$$

In Table 6.10, the average sound velocity is presented for each temperature setpoint, together with the calculated standard deviation of the variation in sound velocity for the respective zero-crossing in each waveform, calculated using using Eq. (3.3). Both the sound velocity corrected for diffraction, and the undiffracted sound velocity is presented, thus where $t_{B2}^{corr} = t_{B1}^{corr} = 0$.

Table 6.10: Undiffracted and diffracted average sound velocity in Plexiglas, c_b, at temperature setpoints.

Temperature [^oC]	Undiffracted c_b [m/s]	c_b corrected for diffraction [m/s]	Std dev. [m/s]
22.10	2728.5	2725.0	0.5
25.67	2727.6	2724.1	0.4
28.62	2726.1	2722.6	0.4
31.39	2723.4	2719.9	0.3
34.51	2719.7	2716.2	0.4
37.41	2709.4	2706.0	0.4
40.24	2703.9	2700.5	0.4
43.48	2694.92	2691.5	0.4

A 2nd degree polynomial can be applied on the data poins in Table 6.10, resulting in a general equation for the decrease in sound velocity as a function of temperature. This is shown as the black line in Fig. 6.4, and can be expressed as

$$c_b^{85mm}(T) = -0.08415 \cdot T^2 + 3.912 \cdot T + 2680, \tag{6.2}$$

where $c_b^{85mm}(T)$ corresponds to the sound velocity for the 85 mm buffer as a function of temperature.

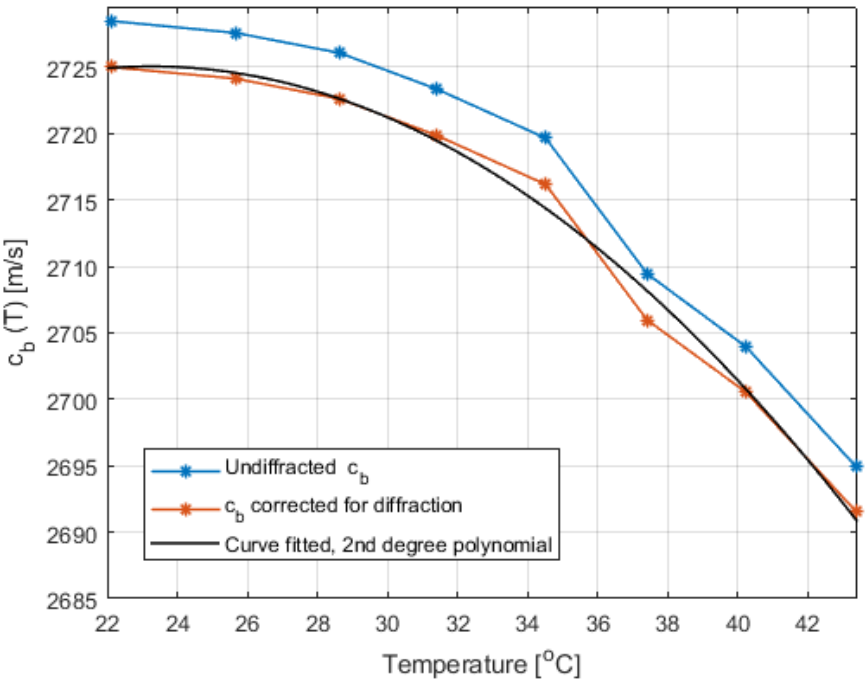

Figure 6.4: Blue curve: measured compressional sound velocity in Plexiglas as a function of temperature. Red curve: Curve fitted sound velocity, calculated with a 2nd degree polynomial.

Discrepancies are found between the measured sound velocities at room temperature for the buffer in the project (70 mm) and the 85 mm buffer. At 22.8^oC, the 70 mm buffer has a sound velocity of 2711.2 m/s, compared to 2725.3 m/s for the 85 mm buffer. As a result, c_b, measured with the 70 mm buffer is set to have an uncertainty of 14.1 m/s, assuming 100% confidence level (k = $\sqrt{3}$), thus is $u(c_b) = 8.14$ m/s.

The equation for the sound velocity in 70 mm Plexiglas as a function of temperature can be written:

$$c_b^{70mm}(T) = c_b^{85mm}(T) - (2725.3 - 2711.2) = -0.08415 \cdot T^2 + 3.912 \cdot T + 2666. \tag{6.3}$$

6.4 Directivity measurements and transducer properties

To calculate the effective radius, a_{eff}, the theory described in Section 2.4 and the experimental setup in Section 3.3 was used.

Further, using the measurement setup illustrated in Fig. 3.1, the sound velocity of the water used in the tank was measured to 1478±2.8 m/s using the ZCM at T = 19.8^oC. When the transducer and hydrophone were aligned, several series of measurements were performed. The signal generator was set to produce a 100 period sinusoidal burs with f = 500 kHz and 10 V amplitude. In steps of 0.1^o, 0.5^o and 0.05^o, the rotation stage was set to rotate from -7^o to 7^o. These measurements correspond to M1, M2 and M3, respectively. The results can be seen in Fig. 6.5.

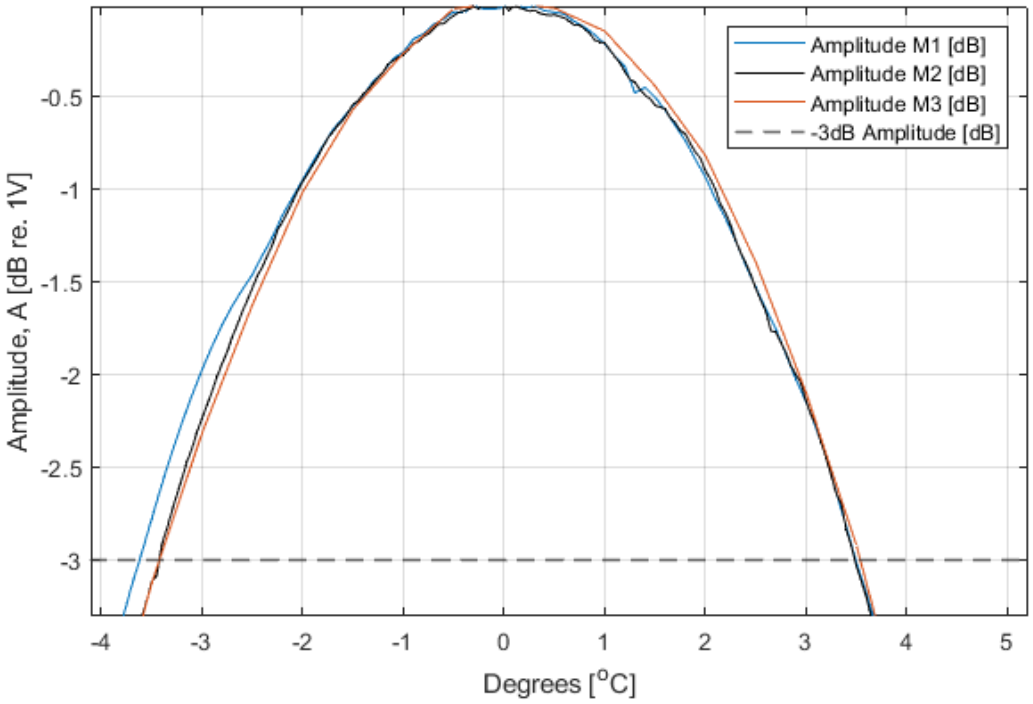

Figure 6.5: Results of three directivity measurements of the main lobe in steps of $0.1^o = M1$, $0.5^o = M2$ and $0.05^o = M3$, together with the line that corresponds to an amplitude reduction of 3 dB. The rotation stage is set to rotate from -7^o to 7^o, but for illustration proposes only -4^o to 4^o is shown.

There is little to no distortion in the amplitude signal in all three curves, but the curves do not line up perfectly. Therefore, the effective transducer radius is calculated for all three measurements, and the mean value will equal a_{eff}. This will consequently lead to uncertainty that will be included in Section 6.8.1.

The point where the amplitude has reduced by 3 dB is marked with a line in Fig. 6.5. By locating the intersection between the three curves and the line, θ_{3dB} can be found. Eq. (2.52) can then be applied to calculate the effective transducer radius, a_{eff}.

Table 6.11: List of calculated θ_{3dB} and resulting a_{eff} calculated from the results in Fig.6.5.

	θ_{3dB} <0 [^{o}]	θ_{3dB} >0 [^{o}]	Average $\overline{\lvert\theta_{3dB}\rvert}$[^{o}]	$a_{eff}[mm]$
Measurement 1	-3.612	3.494	3.553	12.22
Measurement 2	-3.424	3.485	3.455	12.58
Measurement 3	-3.422	3.539	3.481	12.48
Mean± std.dev.			3.496 ± 0.051	12.43 ± 0.18

From Table 6.11, the calculated effective transducer radius will henceforth be $a_{eff} = 12.43mm$ with an uncertainty of $u(a_{eff}) = 0.18mm$. More measurements would have been of interest to increase the credibility of the calculated a_{eff}.

However, in this project, the transducer is clamped on Plexiglas and not in direct contact with water.

Experimental data on the directivity in Plexiglas is not possible within the scope of this project. As a result, the theoretical directivity plot in Fig. 4.8 will be used throughout the project.

6.5 Sound velocity in distilled water

In this section, the experimental sound velocity measurements will be presented with varying nr. of periods and as a function of frequency and temperature. The uncertainty in theoretical sound velocity will also be presented, whereas the uncertainty in experimental sound velocity is calculated in Section 6.8.

6.5.1 Sound velocity measurements in distilled water

As to see how the sound velocity differed with pulse length, three measurements were taken with distilled water at room temperature using the measurement setup shown in Fig. 3.1 with f = 500 kHz. The Fourier Spectrum method (FSM) and the Zero-crossing method (ZCM) are used to calculate the resulting sound velocity, c_s, after applying a ten-period, six-period, and two-period pulse.

For the two-period and six-period pulse, the ZCM sound velocity was measured with the zero-crossings illustrated in Fig. 3.16, whereas zero-crossings 3 to 20 is used for the ten-period pulse, corresponding to the steady-state portion of the signal in Fig. 6.8. Each zero-crossing is marked with a circle.

The isolated pulses used for the FSM for the two-period and six-period pulses are shown in Fig. 3.17b and Fig. 3.19 respectively. Although not identical pulses, the same defined start and end will be used throughout all FSM sound velocity measurements for two-period and six-period pulses. The zero-padded pulses are shown in Fig. 6.8 for the ten-period pulse, and will be used to measure c_s according to Section 3.4.3.

The experimental sound velocities were then compared to the theoretical sound velocity, c_{td}, using Eq. (2.2). The results are presented in Figs. 6.6, 6.7, and 6.9. For the FSM, the sound velocity is a function of frequency, where c_s at 500 kHz is extracted and plotted together with the ZCM-results, and will thus be constant. The measured c_s for each measurement is presented in Table 6.12.

Table 6.12: Experimental sound velocity corrected for diffraction, c_s, in distilled water for 2, 6, and 10 period, measured with ZCM and FSM. For ZCM, the average c_s is presented (cf. discussion above). The results are compared with theoretical sound velocity, c_{td}, at temperature T with P_M = 1.0370 bar.

Nr. of periods	**Temp.** $[^oC]$	**Theoretical** c_{td} **[m/s]**	**FSM Sound velocity** c_s **[m/s]**	**FSM** c_{td}/c_s **[-]**	**ZCM Sound velocity** c_s **[m/s]**	**ZCM** c_{td}/c_s **[-]**
2	24.47	1495.25	1495.49	0.99984	1495.57	0.99979
6	24.18	1494.43	1494.85	0.99972	1494.84	0.99973
10	24.40	1495.05	1494.91	1.0001	1495.11	0.99996

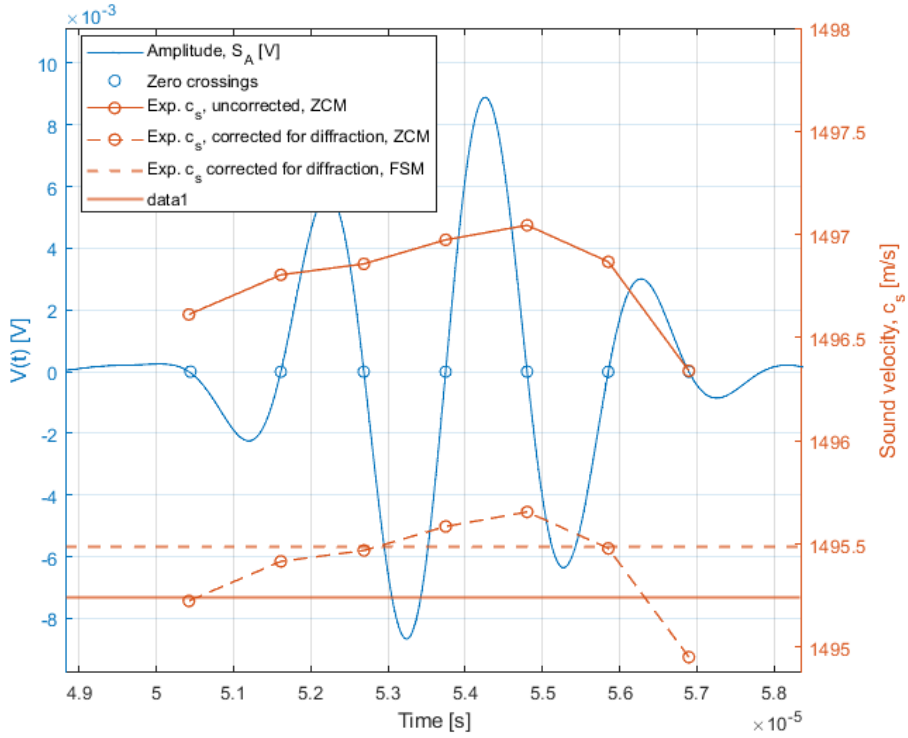

Figure 6.6: Left axis: Measured burst for distilled water at 24.47^oC using f = 500 kHz and a two-period pulse, with calculated zero-crosses. Right axis: Undiffracted and diffracted sound velocity as a function of zero-crossings for the ZCM, compared with the diffracted c_s using FSM, and theoretical sound velocity, c_{td}, using Kinsler and Frey [23].

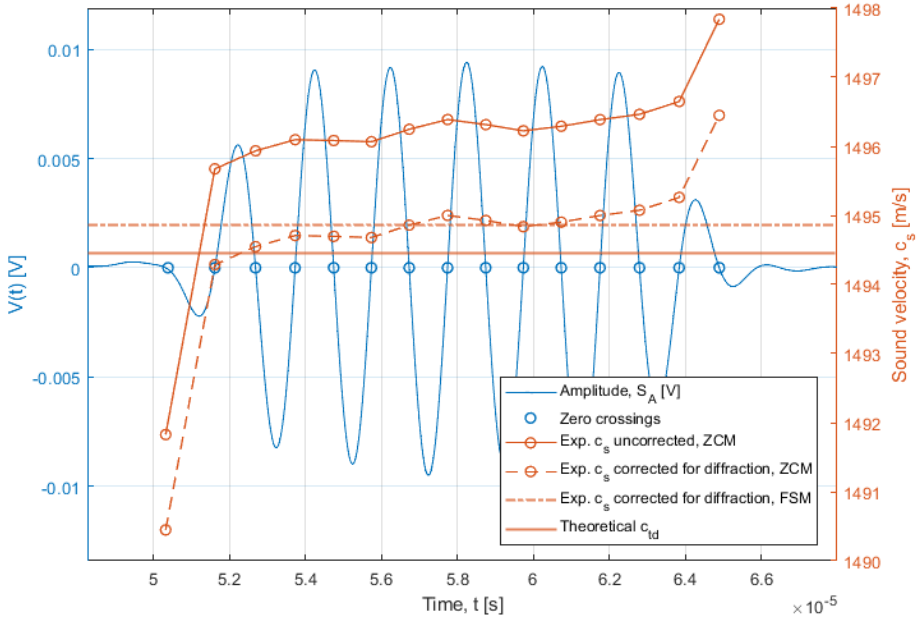

Figure 6.7: Left axis: S_A for distilled water at 24.18^oC using f = 500 kHz and a six-period pulse, with calculated zero-crosses. Right axis: Undiffracted and diffracted sound velocity as a function of zero-crossings for the ZCM, compared with the diffracted c_s using FSM, and theoretical sound velocity, c_{td}, using Kinsler and Frey [23].

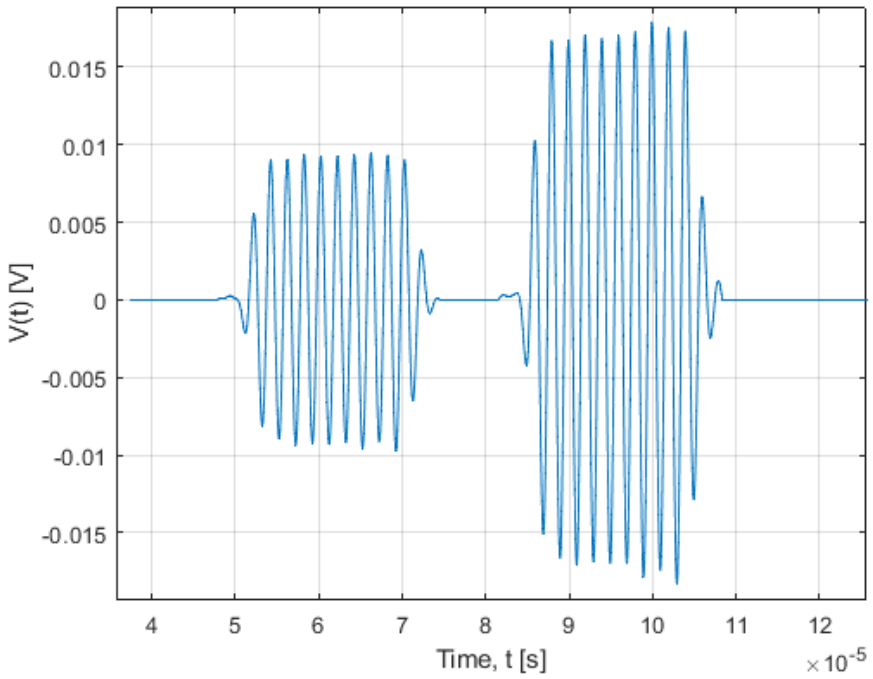

Figure 6.8: Zero-padded pulses for distilled water at 24.38^oC using f = 500 kHz and a ten-period pulse. Everything but the signals of interest is zero-padded, where the signals of interest will be used to measure c_S with the FSM according to Section 3.4.3. The resulting c_s is presented in Fig.6.9

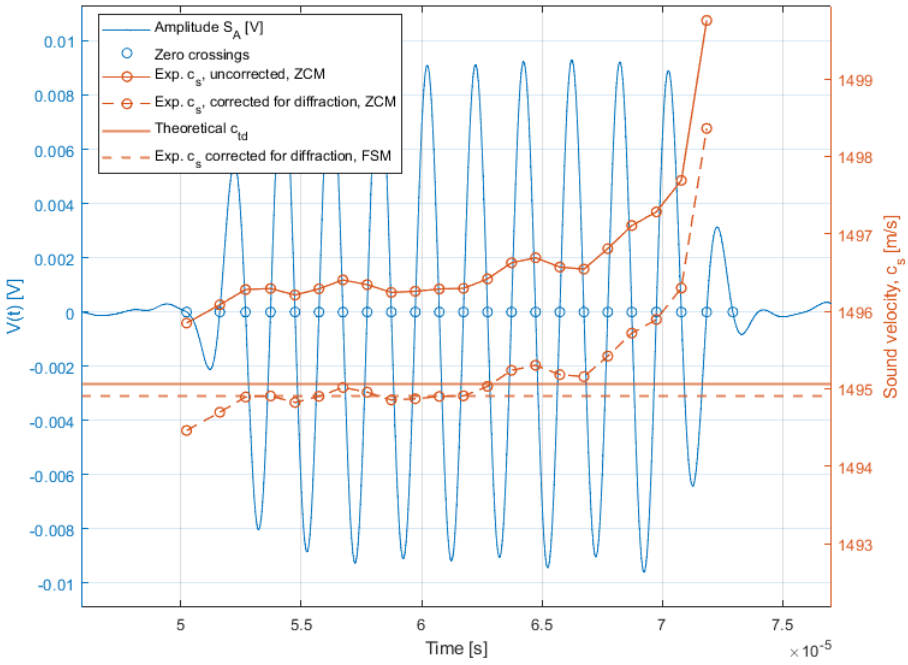

Figure 6.9: Left axis: S_A for distilled water at 24.38^oC using f = 500 kHz and a ten-period pulse, with calculated zero-crosses. Right axis: Undiffracted and diffracted sound velocity as a function of zero-crossings for the ZCM, compared with the diffracted c_s using FSM, and theoretical sound velocity, c_{td}, using Kinsler and Frey [23].

Table 6.12 clearly shows that, when using a two-period pulse, the FSM presents a more accurate c_s

than ZCM, which is expected as the ZCM has not reached a steady-state.

The six-period pulse has reached a distinct steady-state and agrees to within 281 ppm for the FSM and 271 for the ZCM. There is thus no substantial deviation between the signal processing methods for a six-period pulse, which will be confirmed later.

For the ten-period pulse, it can be observed that the ZCM deviates towards the end of the pulse, which is consistent with the arrival of coherent noise sources, shown in Fig. 3.33. From Table 6.12, it can however, be seen that this provides a c_s closest to the theoretical values. The presented results are further discussed in Chapter 7

Due to dispersion effects (ref. Section 2.1), it is of interest to see how accurate the measurement cell is at lower frequencies. Using the same experimental setup with a six-period signal, c_s was measured as a function of frequency for a frequency range 275-600 kHz, as lower frequencies would result in invalid measurements due to amplitude reduction. c_s was measured using the ZCM and the FSM for each frequency set-point. For the ZCM, the average c_s is found using the zero-crossings presented in Fig. 3.16, and the FSM is applied according to Fig. 3.19.

The uncorrected sound velocities and the sound velocities corrected for diffraction are presented in Fig. 6.10, together with the theoretical sound velocity for each measurement. The temperature range of the experiments varied from $T = 24.144^oC$ to $T = 24.095^oC$ within the time frame of the measurements, and $P_M = 1.0345$ bar. The uncertainty was calculated using the uncertainty budget presented later in Table 6.29 with updated values.

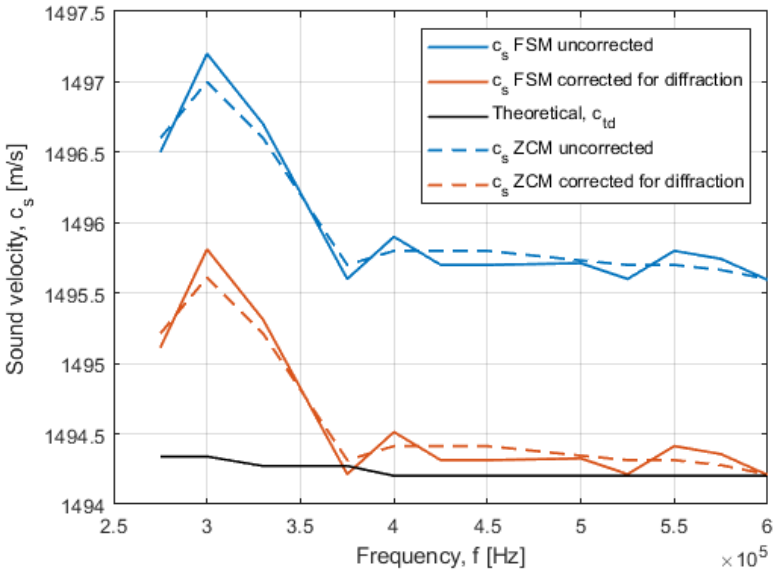

Figure 6.10: Experimental sound velocity in distilled water at room temperature as a function of frequency, measured using the ZCM and FSM for a six-period pulse. The diffracted c_s is shown in red, and undiffracted c_s is shown in blue. The theoretical sound velocity, compensated for temperature, is presented in black.

Table 6.13: Experimental sound velocity corrected for diffraction, c_s, in distilled water as a function of frequency for a frequency range of 275-600 kHz, measured with ZCM and FSM. Compared with theoretical sound velocity, c_{td}, with P_M = 1.0345 bar and T = 24.144^oC to T = 24.095^oC.

Frequency [kHz]	**Theoretical c_{td} [m/s]**	**FSM sound velocity c_s [m/s]**	**FSM Rel. expanded. unc. [ppm]**	**ZCM sound velocity c_s [m/s]**	**ZCM Rel. expanded. unc. [ppm]**
275	1494.34	1495.11	2215	1495.21	2256
300	1494.34	1495.81	2213	1495.61	2243
330	1494.27	1495.31	2214	1495.21	2241
375	1494.27	1494.21	2218	1494.31	2248
400	1494.20	1494.51	2218	1494.41	2229
425	1494.20	1494.31	2219	1494.41	2228
450	1494.20	1494.31	2218	1494.41	2222
500	1494.20	1494.33	2218	1494.35	2223
525	1494.20	1494.21	2217	1494.31	2220
550	1494.20	1494.41	2218	1494.31	2222
575	1494.20	1494.36	2219	1494.28	2224
600	1494.20	1494.21	2219	1494.21	2223

The presented results in Fig. 6.10 show that the sound velocity can be measured with accurate results down to 375 kHz before it deviates, resulting in a maximum deviation at 300 kHz. The relative expanded uncertainty for the ZCM has a slight increase with decreasing temperatures, which is found to be due to an increase in the spread in measured time shift, $u(\Delta t)_{var}$ (Section 5.2.4), with decreasing frequency with the ZCM. The results are further discussed in Chapter 7.

In a temperature range of 23.7-45.7^oC, a measurement series was carried out in $\approx 3^oC$ steps using the measurement setup shown in Fig. 3.3. For each temperature set-point, the measurements were stabilized for approx. ten minutes.

The sound velocities are measured continuously using ZCM and FSM with a six-period pulse. For the ZCM, the average c_s is found using the zero-crossings presented in Fig.3.16, and the FSM is applied according to Fig.3.19. Table 6.14 presents the resulting sound velocity, together with the theoretical sound velocity, c_{td}, using Eq. (2.2) with measured ambient air pressure, P_M = 1.0401 bar. For each sound velocity measurement, the corresponding uncertainty is calculated, where the uncertainty in sound velocity within the temperature set-point is included. The uncertainty calculations follow the uncertainty budget presented in Table 6.29.

A relationship between experimental sound velocity, c_s, and theoretical sound velocity, c_t can be obtained by dividing the theoretical sound velocity by the experimental sound velocity. The original c_S and c_s corrected for diffraction is presented in Fig. 6.11, together with an interval showing 1000 ppm = 0.1% uncertainty from the theoretical sound velocity.

Table 6.14: Mean sound velocity, $\overline{c_s}$, corrected for diffraction for a six-period pulse in distilled water for each temperature set-point, measured with ZCM and FSM, together with mean $\overline{c_{td}}$ at mean temperature $\overline{T}$ where P_M = 1.0401 bar. $U(\overline{c_s})$ includes std. dev. in c_s fluctuations at each temperature set-point.

		ZCM			**FSM**		
Temp., $\overline{T}$ [^oC]	**Theo. sound velocity $\overline{c_{td}}$ [m/s]**	**Sound velocity $\overline{c_s}$ [m/s]**	**Combined expanded unc., $U(\overline{c_s})$ [m/s]**	**Rel. expanded unc. $U(\overline{c_s})/\overline{c_s}$ [ppm]**	**Sound velocity $\overline{c_s}$ [m/s]**	**Combined expanded unc, $U(\overline{c_s})$ [m/s]**	**Rel. expanded unc. $U(\overline{c_s})/\overline{c_s}$ [ppm]**
23.66	1493.04	1493.19	3.32	2223	1493.25	3.31	2217
27.59	1503.55	1503.25	3.34	2222	1503.26	3.34	2222
30.31	1510.16	1509.83	3.36	2225	1509.79	3.35	2219
33.37	1516.96	1516.48	3.38	2229	1516.43	3.37	2222
36.07	1522.42	1522.00	3.39	2227	1521.98	3.39	2227
39.17	1528.09	1527.86	3.41	2232	1527.87	3.41	2232
42.26	1533.12	1532.81	3.42	2231	1532.86	3.42	2231
45.67	1537.98	1537.69	3.43	2231	1537.71	3.43	2231

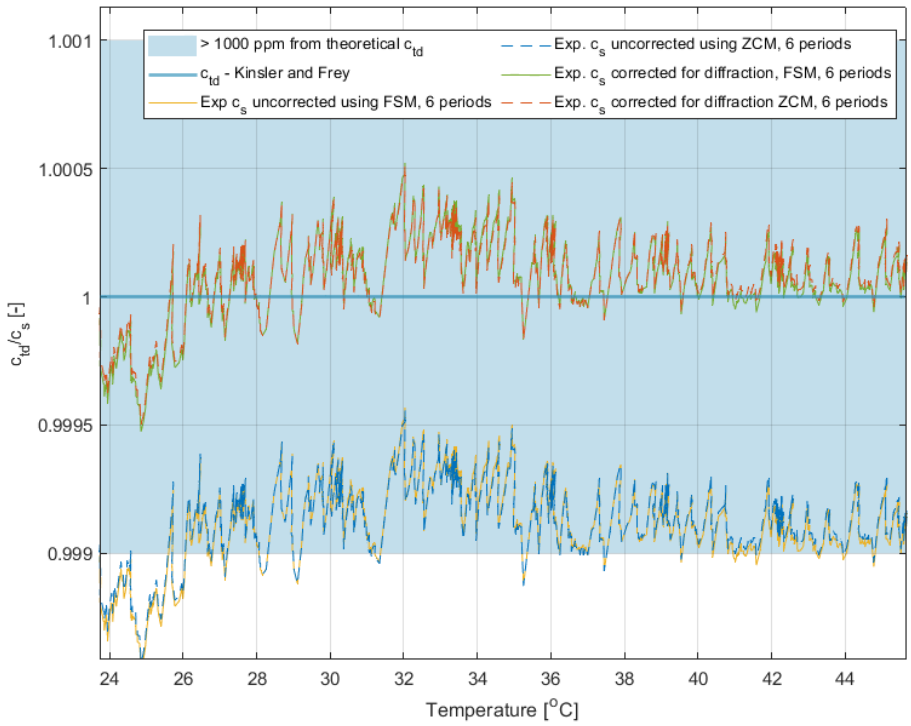

Figure 6.11: Sound velocity in distilled water as a function of temperature, using ZCM and FSM with a 6 period pulse, original and corrected for diffraction. The light blue shows the interval as within will result in an uncertainty < 1000ppm of c_{td}. The values are all presented as relative values, thus c_{td}/c_s [ppm], where c_{td} is calculated using Eq. (2.2) with P_M = 1.0401 bar.

From Fig. 6.11, it is evident that for a six-period pulse, the difference between using ZCM and FSM is incremental, which is consistent with previous measurements (cf. Fig. 6.7). At lower temperatures, an increase in deviation is observed compared to the remaining temperature span. It can also be seen that at $\approx 24^oC$, both signal processing methods approximates the deviation presented in Table 6.12. The results are further discussed in Chapter 7.

In the second series, the transducer is excited with a two-period burst, as to see how the FSM and ZCM works under no steady-state conditions. The sound velocity is measured continuously for a temperature span of 21.2 - 45.7^oC, and stabilized at approximately every third degree. c_s with the ZCM is found according to Fig. 3.16, and the FSM uses the analysis window presented in Fig. 3.17b.

The resulting experimental sound velocities corrected for diffraction are presented in Table 6.15 for each temperature set-point, together with the corresponding uncertainties. The uncertainty calculations follow the uncertainty budget in Table 6.29, where the sound velocity fluctuations within each temperature set-point is included. Sound velocity measurements as a function of temperature are shown in Fig. 6.12, presented as relative to the theoretical sound velocity, c_{td}. The 1000ppm interval is presented in light blue.

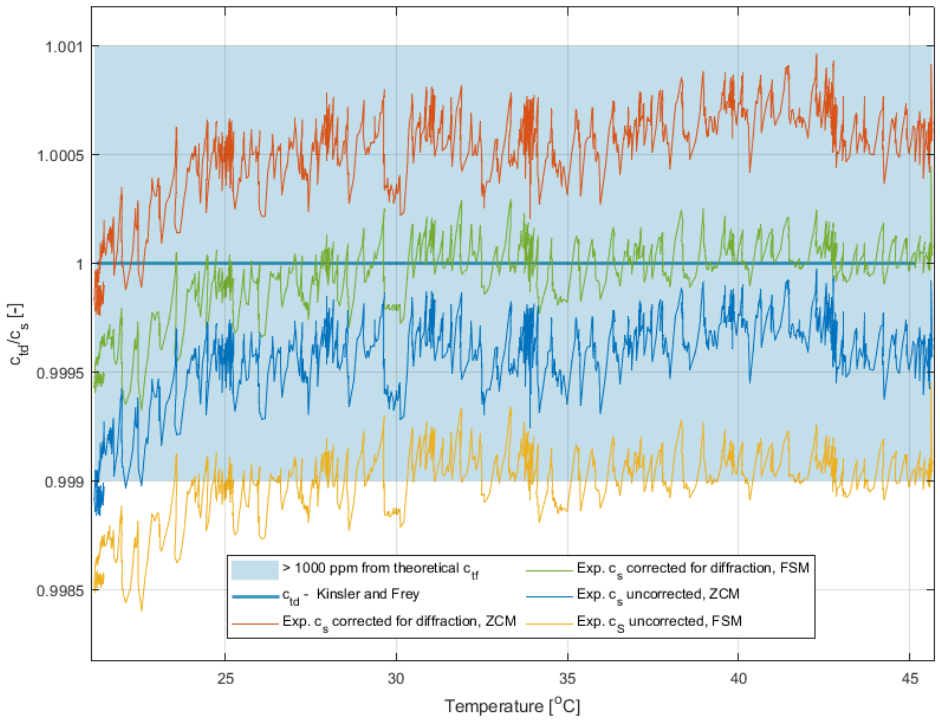

Figure 6.12: Sound velocity in distilled water as a function of temperature, using ZCM and FSM with a 2 period pulse, original and corrected for diffraction. The light blue shows the interval as within will result in sound velocity measurements less than 1000ppm of c_{td}. The values are all presented as relative values, thus c_{td}/c_s, where c_{td} is calculated using Eq. (2.2).

Table 6.15: Mean sound velocity, $\overline{c_s}$, corrected for diffraction for a two-period pulse in distilled water for each temperature set-point, measured with ZCM and FSM, together with mean $\overline{c_{td}}$ at mean temperature $\overline{T}$ where P_M = 1.0401 bar. $U(\overline{c_s})$ includes std. dev. in c_s fluctuations at each temperature set-point.

		ZCM			**FSM**		
Temp., $\overline{T}$ $[^oC]$	**Theo. sound velocity** $\overline{c_{td}}$ **[m/s]**	**Exp.** $\overline{c_s}$ **[m/s]**	**Combined expanded unc.,** $U(\overline{c_s})$ **[m/s]**	**Rel. expanded unc.** $U(\overline{c_s})/\overline{c_s}$ **[ppm]**	**Exp.** $\overline{c_s}$ **[m/s]**	**Combined expanded unc,** $U(\overline{c_s})$ **[m/s]**	**Rel. expanded unc.** $U(\overline{c_s})/\overline{c_s}$ **[ppm]**
21.20	1485.85	1485.97	3.30	2221	1486.55	3.29	2213
25.16	1497.20	1496.33	3.33	2225	1497.24	3.32	2217
28.00	1504.59	1503.64	3.35	2228	1504.56	3.34	2220
31.05	1511.87	1510.76	3.37	2231	1511.63	3.36	2223
33.93	1518.13	1517.11	3.38	2228	1517.96	3.38	2227
37.10	1524.37	1523.27	3.40	2228	1524.22	3.39	2227
39.84	1529.23	1528.04	3.41	2232	1529.10	3.40	2224
42.82	1533.96	1532.82	3.42	2231	1533.82	3.42	2230
45.66	1537.97	1536.90	3.43	2232	1537.77	3.43	2231

In Fig. 6.12, it can be seen that when using a two-period pulse, the ZCM and the FSM deviates significantly. Compared to c_{td}, it can be seen that the FSM provides accurate results, while the ZCM deviates from c_s for the entire temperature range. This is consistent with the results presented in Fig.6.6, and will be discussed further in Chapter 7.

6.5.2 Uncertainty in experimental sound velocity in distilled water

The uncertainty in the experimental sound velocity, c_s, follows the uncertainty model in Section 5.4.2. It is a product of several uncertainty contributions that have either been calculated previously or is yet to be found, and is thus presented as a result on its own in Section 6.8. The maximum temperature throughout the project will be used as an example, corresponding to $U(c_s)$ = 3.43 m/s at 45.67^oC for the ZCM using a six-period pulse .

6.5.3 Uncertainty in theoretical sound velocity in distilled water

An uncertainty model for the uncertainty in c_{td} was presented in Section 5.4.2, derived from Eq. (2.2).

Throughout the measurement series presented in Table 6.14, the maximum temperature recorded is $T = 45.7^oC$, with P_M = 1.0395 bar $\rightarrow$ P_G = 0.08 bar, and will be used as an example. Inserting these values into Eqs. 5.43 and 5.44 yields the sensitivity coefficients. The uncertainties in T and P_M can further be found in Tables 6.2 and 6.4 respectively.

The uncertainty of the sound velocity model, $u_c(c_{td}^{model})$, is given as 0.05% (500ppm) for $0 < T < 100^oC$ and $0 < P < 200bar$ [23], assuming a 95% confidence level. This corresponds to 0.769 m/s for c_{td} = 1537.7 m/s.

The resulting uncertainty budget for c_{td} at $T = 45.7^oC$ and P_M = 1.0395 bar is presented in Table 6.16.

Table 6.16: Uncertainty budget for theoretical sound velocity in distilled water at 45.7^oC and P_M = 1.0395 bar

Uncertainty source	**Input uncertainty**				**Combined uncertainty**	
	Expanded unc.	**Conf. level & distr.**	**Cov. factor, k**	**Standard unc.**	**Sens. coeff.**	**Variance**
Temperature, T	0.157 ^oC	68% (norm)	1	0.157 ^oC	1.320	$0.0429 m/s^2$
Gauge pressure, P_G	$1.69 \cdot 10^{-4}$ bar	68% (norm)	1	$1.69 \cdot 10^{-4}$ bar	0.177	$8.95 \cdot 10^{-10} (m/s)^2$
Model	0.769 m/s	95% (norm)	2	0.385 m/s	1	0.148 $(m/s)^2$
Sum of variances				$u_c^2(c_{td})$	0.191 $(m/s)^2$	
Combined standard uncertainty				$u_c(c_{td})$	0.437 m/s	
Expanded uncertainty (95% **confidence level, k = 2)**				$U(c_{td})$	0.874 m/s	
Theoretical sound velocity				c_{td}	1537.7 m/s	
Relative expanded uncertainty (95% **confidence level, k = 2)**				$k \cdot E_{c_{td}}$	568 ppm	

Using the uncertainty in temperature at $T_0 = 22.94^oC$, $u_c(T_0) = 0.143^oC$ (Section 6.1.2), c_{td} = 1490.90 m/s at T_0 (Eq. (2.2)), and $u_c(P) = 1.69 \cdot 10^{-4}$, a resulting uncertainty of $u_c(c_{td})$ = 0.579 m/s is calculated through Eq. (5.42). This results in a relative expanded uncertainty of 777 ppm, which shows that the uncertainty of the theoretical model will increase with decreasing temperatures.

6.6 Sound velocity in saline water

In the following, experimental sound velocity measurements for saline water using 20 ppt will be presented, together with the resulting uncertainty in theoretical and experimental sound velocity.

6.6.1 Sound velocity measurements in saline water

Using saline water with S = 20 ppt, a measurement series was conducted with f = 500kHz and a six-period pulse, where c_S was measured using the average transit time with the ZCM according to Fig. 3.16.

The sound velocity was measured continuously and stabilized in steps of 3^oC over a temperature range of 22-40^oC, limited by the range of the UNESCO equation. The results as a function of temperature are presented in Fig. 6.13, and the sound velocity measurements at each set-point are found in Table 6.18. For each measurement, the corresponding uncertainty is calculated, following the uncertainty budget presented in Table 6.29.

Before and after the measurement series, the conductivity was measured using a CMD210 conductivity meter with an accuracy of ±0.2% of reading ± 3 of the least significant digit[97]. This was to compensate for a possible increase in salinity due to evaporation at higher temperatures. The results are presented in Table6.17.

Table 6.17: Conductivity measurements before and after measuring the sound velocity as a function of temperature, using CMD210 conductivity meter

	Conductivity [mS/cm]
Before	32.04 ±0.04
After	32.12 ±0.04

It is from Table 6.17 evident that the increase in conductivity is minuscule, and falls within the uncertainty of the instrument. An increase in salinity can thus be neglected.

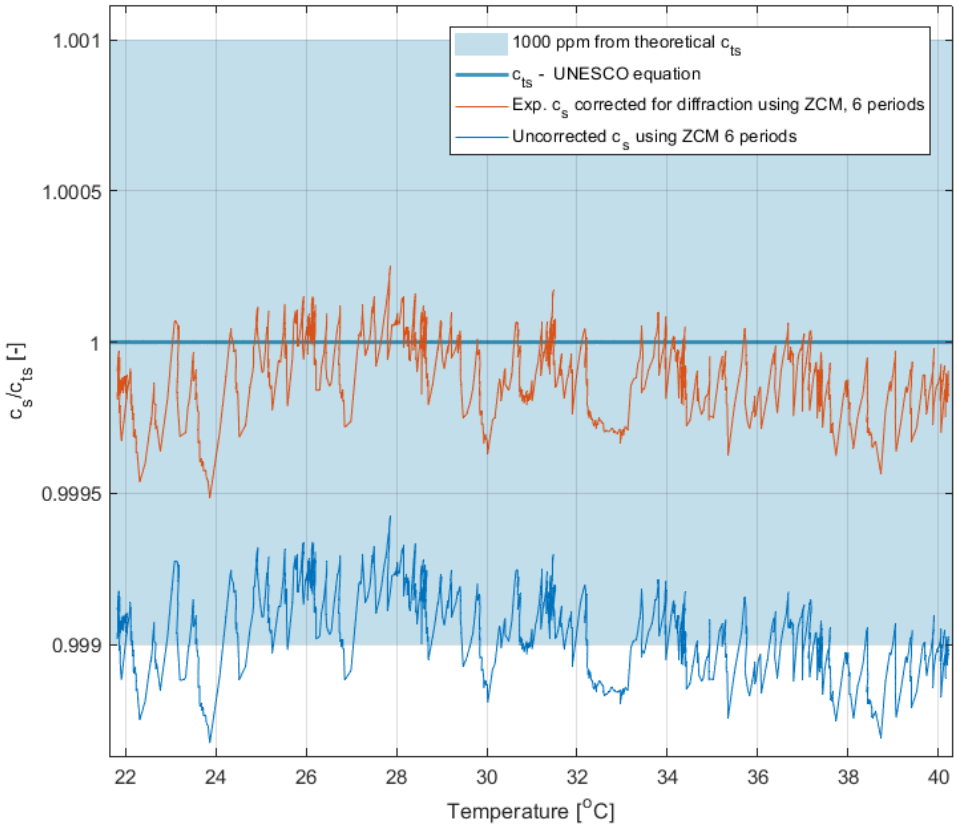

Figure 6.13: Sound velocity in saline water, S = 20ppt, as a function of temperature, using ZCM with a six-period pulse. The dark blue shows the original c_s, and the red curve presents c_s corrected for diffraction. The light blue shows the interval as within will result in an uncertainty < 1000ppm of c_{td}. The values are all presented as relative values, thus divided by the theoretical sound velocity, c_{ts}, using Eq. (2.4).

Fig. 6.13 presents sound velocity results closer to the theoretical values than the distilled water six-period signal. It can also be seen in Table 6.18 that the relative expanded uncertainty for saline water is higher as a consequence of a shorter transit time, and thus a higher sensitivity coeff. in Eq. (5.2).

The results will be further discussed in Chapter 7.

Table 6.18: Experimental sound velocity in saline water (20 ppt) for each temperature set-point, using the ZCM with a six-period pulse. Compared to theoretical values with P_M = 1.0310 bar. $U(\overline{c_s})$ includes std.dev. in c_s fluctuations at each temperature set-point.

Temperature, $\overline{T}$ $[^oC]$	**Theoretical** $\overline{c_{ts}}$ **[m/s]**	**Sound velocity,** $\overline{c_s}$ **[m/s]**	**Combined exp. uncertainty,** $U(\overline{c_s})$ **[m/s]**	**Relative exp. uncertanity** $U(\overline{c_s})/\overline{c_s}$ **[ppm]**
21.83	1510.18	1510.40	3.36	2225
26.16	1521.37	1521.29	3.39	2229
28.64	1527.20	1527.18	3.41	2233
31.40	1533.21	1533.22	3.42	2231
34.32	1539.02	1539.16	3.44	2236
37.39	1544.53	1544.74	3.45	2234
40.15	1549.00	1549.25	3.47	2241

6.6.2 Uncertainty in experimental sound velocity in saline water

In Section 6.8, the uncertainty in the experimental sound velocity will be calculated for distilled water, using the uncertainty model presented in Section same method is used to calculate the experimental sound velocity in saline water, where the combined expanded uncertainties for each set-point are shown in Table 6.18. Each uncertainty includes an uncertainty in sound velocity fluctuations at each temperature set-point.

6.6.3 Uncertainty in theoretical sound velocity in saline water

In Section 5.4.3, an uncertainty model for the uncertainty in c_{ts} was presented, derived from the UNESCO equation. This model will be implemented here.

In Table 6.18, a maximum uncertainty is found at T = 40.15^oC with P_M = 1.0310 bar, and will thus be used here as an example. In Table 6.1 and Table 6.4, $u_c(T)$ and $u_c(P)$ has been calculated for the case of T = 45.7^oC and P_M = 1.0395 bar. The same approach is applied here, with corrected values for T and P_M. The uncertainty in the salinity is given as the uncertainty of the scale when measuring the liquid solution. The scale in use is model UWE NJW-3000 and has a resolution of 0.1g. A datasheet (or website) of the scale has not been found, and the uncertainty is thus assumed to be the resolution, ±0.1g at 68% confidence level.

An uncertainty in the model itself is set to 0.15 m/s following [32]. The confidence level is not stated, and is thus assumed 68%.

Table 6.19: Uncertainty budget of the theoretical sound velocity in saline water using the UNESCO equation 2.4 where S = 20 ppt, T = 40.15^oC and P = 1.0310 bar.

Uncertainty source	Input uncertainty				Combined uncertainty	
	Expanded unc	Conf. level	Cov. factor, k	Standard unc.	Sens. coeff.	Variance
Temperature, T	0.157^oC	68%	1	0.157 ^oC	1.5436	0.0587 $(m/s)^2$
Pressure, P	$1.69 \cdot 10^{-4}$	68%	1	$1.69 \cdot 10^{-4}$	0.1753	$8.77 \cdot 10^{-10} (m/s)^2$
Salinity, S	0.1g	68%	1	0.1g	0.9733	$9.47 \cdot 10^{-3} (m/s)^2$
Model	0.15 m/s	68%	1	0.15 m/s	1	$0.0225 (m/s)^2$
Sum of variances					$u_c^2(c_{ts})$	0.0912 $(m/s)^2$
Combined standard uncertainty					$u_c(c_{ts})$	0.302 m/s
Expanded uncertainty (95% confidence level, k = 2)					$U(c_{t_s})$	0.604 m/s
Theoretical sound velocity					c_{ts}	1549.00 m/s
Relative expanded uncertainty					$k \cdot E_{c_{ts}}$	390 ppm

Using the uncertainty in temperature at T_0 = 22.94^oC, $u_c(T_0)$ = 0.143^oC (Section 6.1.2), c_{ts} = 1513.1 m/s at T_0 (Eq. (2.4)), and constant uncertainty in salinity, pressure and the model, a resulting uncertainty of $u_c(c_{ts})$ = 0.425 m/s is calculated through Eq. (5.45). This results in a relative expanded uncertainty of 562 ppm, which shows that the uncertainty in the theoretical model will increase with decreasing temperatures.

6.7 Sound velocity in Extra Virgin Olive Oil

It was of interest to see how the measurement cell behaved with decreasing temperatures. EVOO from Eldorado was chosen due to the lack of time and the necessary equipment to ventilate when heating crude oils (HSE regulations). By choosing a pure (100%) EVOO oil, measurements could be compared to other sources, as the author found no definite theoretical model for sound velocity in olive oils.

Using the measurement setup described in Section 3.1 and a six-period pulse, the change in sound velocity of EVOO was measured over a temperature range from 21 to 35 ^oC. The waveform was recorded every 3 seconds, and the temperature was stabilized for ten minutes in intervals of 3^oC. c_s was measured using the average transit time with the ZCM according to Fig. 3.16. The sound velocity corrected for diffraction, together with the uncorrected c_s, is presented in Fig. 6.14. c_s for each temperature set-point is presented in Table6.20 together with the corresponding uncertainties, where the uncertainty due to c_s fluctuations at each temperature set point is included. Using c_s corrected for diffraction, a linear regression line has been calculated using predefined tools in MATLAB. The regression line is shown in black in Fig. 6.14.

Two other sources have been used for comparison. Yan. et al. [98] measured the sound velocity in

EVOO from 21^oC to 36^oC using a pulse-echo system with the transducer directly immersed into the liquid with f = 5 MHz. A linear regression line of $c_s = -2.9292 \cdot T + 1522.7$ was found, with a claimed uncertainty of 2 m/s at room temperature. McClements and Povey [99] applied a pulse-echo method based on multiple reflections with f = 1.25 MHz and measured the sound velocity in olive oil (non-specific) for a temperature span of 20-70^oC with an uncertainty of 0.7 m/s. For the olive oil, a linear regression line of $c_s = -3.28 \cdot T + 1528.9$ was found. The linear regression line for both sources has been plotted as a function of temperature together with the experimental results of the project, presented in Fig. 6.14.

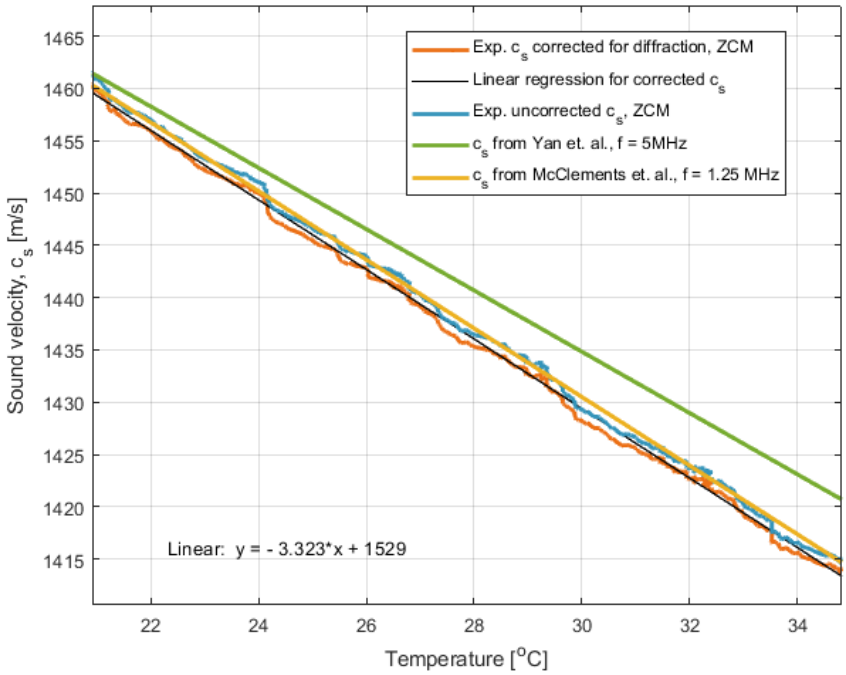

Figure 6.14: Experimental sound velocity in EVOO as a function of temperature and P_{meas} = 1.0310 bar. The uncorrected c_s (blue) and c_s corrected for diffraction are shown, together with the stated regression lines of [98] (green) and [99] (yellow). The calculated linear regression line for c_s corrected for diffraction is presented in black.

A linear regression line of $c_s(T) = -3.323 \cdot T + 1529$ has been calculated with a root mean square value of $R^2 = 0.9982$. The experimental sound velocity decreases with decreasing temperature, which is consistent with the linear regression lines of Yan. et al.[98] and McClements and Povey [99]. An increasing discrepancy with increasing temperature can further be seen between the experimental sound velocity and [98], while the linear regression line of [99] is consistent with the experimental values. With decreasing sound velocity, the uncertainty in sound velocity decreases due to a decrease in the sensitivity coefficients. The results are further discussed in Chapter 7.

Table 6.20: Experimental sound velocity corrected for diffraction in EVOO for each temperature set-point, using the ZCM with a 6-period pulse, together with the corresponding standard uncertainty (68% c.l.). $u_c(\overline{c_s})$ includes std. dev.in c_s fluctuations at each temperature set-point.

Temperature, $\overline{T}$ $[^oC]$	**Exp. sound velocity** $\overline{c_s}$ **[m/s]**	**Standard uncertainty** $u_c(\overline{c_s})$ **[m/s]**
20.88	1460.36	1.63
23.86	1450.31	1.61
26.54	1441.04	1.60
29.26	1432.22	1.59
32.09	1422.73	1.58
34.80	1413.64	1.57

6.8 Uncertainty in the experimental sound velocity

The uncertainty in the experimental sound velocity, c_s, will be presented as a result on its own here and will follow the uncertainty model presented in Section 5.4.2.

For distilled water, thus the reference liquid in the project, a maximum uncertainty is found at $T = 45.7^oC$, corresponding to c_s = 1537.7 m/s using the ZCM with a six-period pulse (ref. Table 6.14), and will thus be used here as an example.

The uncertainty in the experimental sound velocity is a product of several uncertainty contributions. The uncertainties in K_T and L_0 has been found in Tables 6.9 and 6.8, while uncertainties in transit time, $u_c(\Delta t)$, and correction term, $u_c(\Delta t^{corr})$, will be calculated in the following.

Each contribution will be presented here for T = 45.7^oC and c_s = 1537.7 m/s, and in Section 6.8.3 the total uncertainty in experimental sound velocity will be calculated using an uncertainty budget.

6.8.1 Uncertainty in correction term

The standard uncertainty in the correction term, $u(\Delta t^{corr})$, will only be dependent on the uncertainty in diffraction correction $u(\Delta t^{diff})$, which can be calculated with the model presented in Section 5.2.5.

In Section 4.1.2, the uncertainty in the diffraction correction model is found by taking the maximum difference between simulated results and the diffraction correction model presented in the project, assuming a confidence level of 100% (k = $\sqrt{3}$), resulting in $u(\Delta t^{diff})_{model} = 3.4 \cdot 10^{-9}$ s.

Uncertainties $u^2(\Delta t^{diff})_{a_{eff}}$, $u^2(\Delta t^{diff})_{c_b}$, $u_c^2(\Delta t^{diff})_L$, and $u^2(\Delta t^{diff})_D$ will be calculated using the approach explained in Section 5.2.5. The maximum sound velocity and temperature throughout the measurement series with distilled water will be applied, corresponding to T = 45.7^oC, and c_s = 1537.7 m/s for the ZCM (cf. Table 6.14). For simplicity, the variables and the corresponding uncertainties

needed for the uncertainty calculations are summarized in Table 6.21 in which those affected by temperature are compensated for.

Table 6.21: A summary of the numerical value and corresponding uncertainty for each variable needed in the calculation of the uncertainty in diffraction correction at T = 45.7^oC, together with the location of where the respective uncertainties are calculated.

Variable	**Value**	**Uncertainty**	**Conf. level & distr.**	**Coverage factor, k**	**Location**
a_{eff}	12.43 mm	0.18 mm	68% (norm)	1	Table6.11
$c_b(T)$	2669 m/s	8.14 m/s	68% (norm)	1	Section 6.3
L_0	25.18 mm	0.0252 mm	68% (norm)	1	Table6.8
$K_T(T)$	1.0005	$1.32{\cdot}10^{-5}$	68% (norm)	1	Table6.9
D	70.1 mm	0.0165 mm	68% (norm)	1	Section 6.2.2

The calculated uncertainties, $u^2(\Delta t^{diff})_{a_{eff}}$, $u^2(\Delta t^{diff})_{c_b}$, $u_c^2(\Delta t^{diff})_L$, and $u^2(\Delta t^{diff})_D$, are presented in Table 6.22.

Table 6.22: Calculated uncertainty in Δt^{diff} due to uncertainties in the diffraction correction variables for c_s = 1537.7 m/s at T = 45.7^oC. Subscript *var* stands for variable, and is thus dependent on the variable in question.

	Variables to calculate Δt^{diff}	$(\Delta t^{diff})_{var}$ [s]	$u\left(\Delta t^{diff}\right)_{var}$ [s]
	$\Delta t^{diff}\left(a_{eff}, c_b, D, L\right)$	$3.263{\cdot}10^{-8}$	-
a_{eff}	$\Delta t^{diff}\left(a_{eff}+u(a_{eff}), c_b, D, L\right)$	$3.336{\cdot}10^{-8}$	$\mathbf{7.3\cdot10^{-10}}$
	$\Delta t^{diff}\left(a_{eff}-u(a_{eff}), c_b, D, L\right)$	$3.190{\cdot}10^{-8}$	$\mathbf{7.3\cdot10^{-10}}$
c_b	$\Delta t^{diff}\left(a_{eff}, c_b+u(c_b), D, L\right)$	$3.256{\cdot}10^{-8}$	$\mathbf{7.0\cdot10^{-11}}$
	$\Delta t^{diff}\left(a_{eff}, c_b-u(c_b), D, L\right)$	$3.316{\cdot}10^{-8}$	$5.3\cdot10^{-11}$
D	$\Delta t^{diff}\left(a_{eff}, c_b, D+u(D), L\right)$	$3.258{\cdot}10^{-8}$	$\mathbf{5.0\cdot10^{-11}}$
	$\Delta t^{diff}\left(a_{eff}, c_b, D-u(D), L\right)$	$3.268{\cdot}10^{-8}$	$\mathbf{5.0\cdot10^{-11}}$
L	$\Delta t^{diff}\left(a_{eff}, c_b, D, L+u(L)\right)$	$3.720{\cdot}10^{-8}$	0
	$\Delta t^{diff}\left(a_{eff}, c_b, D, L-u(L)\right)$	$3.720{\cdot}10^{-8}$	0

The uncertainty in L is smaller than the amount of significant digits in Matlab and is thus negligible. The total uncertainty budget for Δt^{diff} with the calculated uncertainties in Table 6.22, is presented in Table 6.23.

Table 6.23: Uncertainty budget for $\Delta t^{diff} = \Delta t^{corr}$ when c_s = 1537.7 m/s and T = 45.7^oC

Uncertainty source	**Input uncertainty**				**Combined uncertainty**	
	Expand. unc.	**Conf. level & distr.**	**Cov. fact., k**	**Standard unc.**	**Sensit. coeff.**	**Variance**
Model	$6.0{\cdot}10^{-9}s$	100% (rect.)	$\sqrt{3}$	$3.4{\cdot}10^{-9}s$	1	$1.2{\cdot}10^{-17}s^2$
a_{eff}	$7.3{\cdot}10^{-10}s$	68%(norm.)	1	$7.3{\cdot}10^{-10}s$	1	$5.3{\cdot}10^{-19}s^2$
c_b	$7.0{\cdot}10^{-11}s$	68% (norm)	1	$7.0{\cdot}10^{-11}s$	1	$4.9{\cdot}10^{-21}s^2$
Buffer length, D	$5.0{\cdot}10^{-11}$ s	68% (norm)	1	$5.0{\cdot}10^{-11}$ s	1	$2.5{\cdot}10^{-21}s^2$
Sample length, L	n/a	n/a	n/a	n/a	n/a	n/a
Sum of variances				$u_c^2(\Delta t^{diff})$		$1.25{\cdot}10^{-17}s^2$
Combined standard uncertainty				$u_c(\Delta t^{diff})$		$3.54{\cdot}10^{-9}$ s
Expanded uncertainty (95% conf. level, k = 2)				$U(\Delta t^{diff})$		$7.08{\cdot}10^{-9}$ s
Theoretical diffraction correction at c_s = 1537.7 m/s				Δt^{diff}		$3.26{\cdot}10^{-8}$ s
Relative expanded uncertainty (95% confidence level)				$U(\Delta t^{diff})/\Delta t^{diff}$		**21.7%**

The above uncertainty budget is assumed for all measurements.

6.8.2 Uncertainty in transit time

In Section 5.2.4, two uncertainty models for the standard uncertainty in transit time, $u(\Delta t)$, are presented, depending on the signal processing method applied. In this section, the uncertainty in transit time for both scenario's will be calculated, where the c_s = 1537.7 m/s at T = 45.7^oC (cf. Table 6.14) will be used as an example.

Uncertainty due to coherent noise

Uncertainty in transit time due to coherent noise, $u_c(\Delta t)_{coh.noise}$, is given by Eq. (5.17) and consists of uncertainty contributions due to reflector reverberation, side lobe interference, mode-converted waves and the four times traversed buffer signal, which are all explained in detail in Section 3.5.

In Section 4.3, a numerical analysis calculating the uncertainty in transit time due to coherent noise sources was presented. Using this numerical analysis, it was shown that $u(\Delta t)_{sidelobe} = 9.4 \cdot 10^{-10}$s.

A pulse train will be studied using the experimental setup presented in Fig. 3.1 with distilled water at 22.1^oC. This waveform will be used to calculate $u_c(\Delta t)_{coh.noise}$ due to reflector reverberation, side lobe interference, and mode-converted waves. To inspect all noise contributions individually, the transducer is excited with a two-period 500 kHz pulse with a 10 V signal output from the signal generator. The result is presented in Fig. 6.15, and has also been used to identify all coherent noise sources in Fig. 3.26.

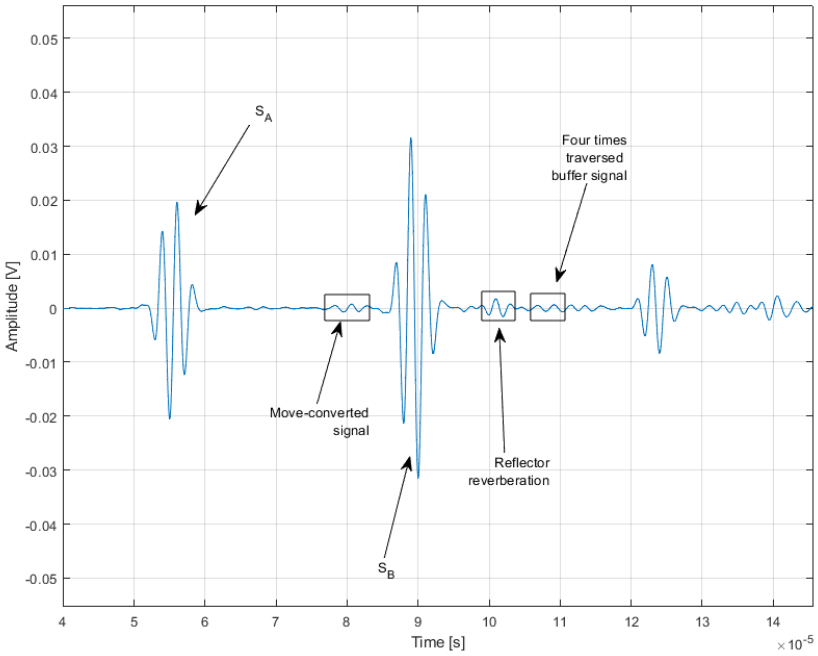

Figure 6.15: Measured pulse train using the experimental setup presented in Fig. 3.1 with f = 500 kHz and a two-period pulse.

In Fig. 6.15, the coherent noise sources of interest are identified, together with the signals of interest, S_A and S_B. Though these noise signals appear not to interfere with the signals of interest, they can do so if the sample velocity or pulse length is changed.

The signal-to-noise ratio (SNR) is of interest, and thus must the peak voltage amplitude of the signal, V_P^S, and for the noise, V_P^N, be found.

In Fig. 3.33 it is shown that the maximum voltage amplitude of the two-period pulse approximates the steady-state voltage amplitude of the six-period pulse. V_P^S for S_B will therefore be calculated using the local extremum in the pulse, resulting in $V_P^S = 0.0315$ V.

For the three coherent noise sources, the start and end of each pulse is harder to define, and the resulting V_P^N will thus only be an approximation. For each noise source, V_P^N is found by locating the maximum amplitude inside each of the respective rectangles. The resulting V_P^N, together with V_P^S, can then be used to calculate the SNR using $20\log(V_P^N / V_P^S)$. Then, using the numerical analysis in Section 4.3, where $V_P^S = A_S$, and $V_P^N = A_N$, the corresponding standard uncertainty of the time fluctuations can be calculated. The results for all coherent noise sources are presented in Table 6.24.

Table 6.24: Measured peak amplitude values of several coherent noise sources, together with calculated SNR and the resulting transit time uncertainty using the numerical analysis presented in 4.3. Subscript *var* represents the contribution to uncertainty in coherent noise due to the individual noise contributions.

	Mode-converted signal	**Reflector reverberation**	**Four times traversed buffer signal**
V_P^N [V]	$6.38{\cdot}10^{-4}$	$1.51{\cdot}10^{-3}$	$5.9\cdot10^{-4}$
SNR [dB]	32.3	24.8	32.9
$u(\Delta t)_{var}$ [s]	$5.5{\cdot}10^{-9}$	$1.3{\cdot}10^{-8}$	$5.1{\cdot}10^{-9}$

Using Eq. (5.17), the values presented in Table 6.24, together with the calculated $u(\Delta t)_{sidelobe}$, the combined standard uncertainty due to coherent noise is

$$u_c(\Delta t)_{coh.noise} = \sqrt{\left(9.4\cdot10^{-10}\right)^2 + \left(5.5\cdot10^{-9}\right)^2 + \left(1.3\cdot10^{-8}\right)^2 + \left(5.1\cdot10^{-9}\right)^2} = 1.5\cdot10^{-8}s \tag{6.4}$$

Uncertainty due to pump noise

During stable temperature conditions, 10 waveforms are collected with the measurement setup shown in Fig. 3.3, with and without the water pump turned on, using a six-period pulse at 500 kHz. The result is presented in Fig. 6.16, where the resulting waveform has been enlarged to properly inspect the zero-crossings.

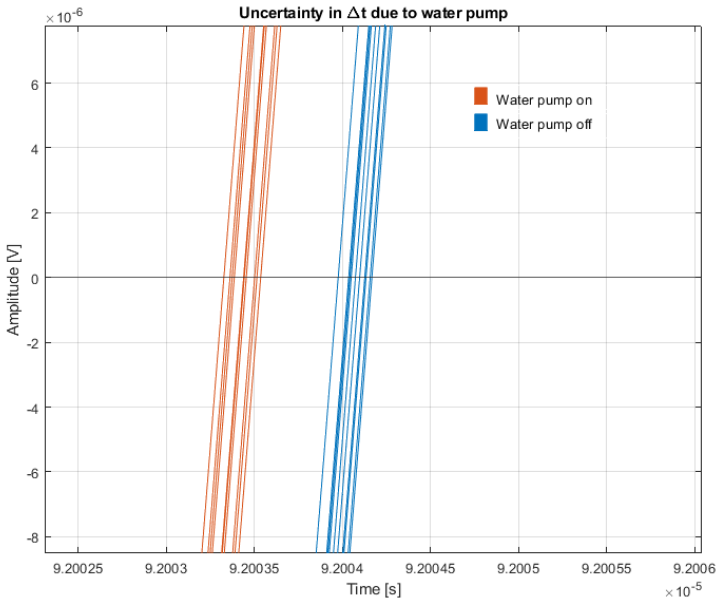

Figure 6.16: Measurement results showing the time shift of the zero-crossings due to noise from the water pump. A 500kHz 6 period pulse is acquired during stable temperature conditions. 10 measurements are collected when the water pump is turned on (marked in red) and similarly for when the pump is turned off (marked in blue). The waveform is enlarged to illustrate the difference.

From Fig. 6.16, the calculated uncertainty in transit time due to pump noise can be found. First, the

transit time for each zero-crossing is calculated for one waveform using the zero-crossing method. From the vector of transit times, the mean transit time is calculated. This is then done for all waveforms with the water pump turned off, resulting in a vector of ten mean transit time values, $(\Delta\overline{t}_n)_{off}$, where n = 1, 2, .., 10. The standard deviation, s_{off}, of $(\Delta\overline{t}_n)_{off}$ is then found.
The same calculations are then done for all ten waveforms with the water pump turned on, resulting in $(\Delta\overline{t}_n)_{on}$, where n = 1, 2, .., 10. A corresponding standard deviation,s_{on}, is then calculated from $(\Delta\overline{t}_n)_{on}$, resulting in a total uncertainty in transit time due to pump noise:

$$u(\Delta t)_{pump} = \sqrt{s_{off}^2 + s_{on}^2} = \sqrt{9.28\cdot10^{-11} + 1.50\cdot10^{-10}} = 1.56\cdot10^{-10}s. \tag{6.5}$$

Calculated uncertainty in transit time $u(\Delta t)$

With the above calculations, the total uncertainty in transit time can be found. A summary of the uncertainty values are presented in Table 6.25, where the description of each uncertainty contribution is presented in Table 5.5.

From Section 3.4.5, V_{RMS}^N is found to be $V_{RMS}^N = 1.498\cdot10^{-4}$V., which can be used to calculate the uncertainty in transit time due to bit resolution and incoherent noise, $u(\Delta t)_{res}$, for each acquisition (ref. Section 5.2.4).

Table 6.25: Standard uncertainty of the uncertainty contributions needed to find $u(\Delta t)_{ZCM}$ and $u(\Delta t)_{FSM}$, where all are found for a 68% confidence level, k = 1. Description of the contributions are presented in Table 5.5.

Uncertainty contributor	**Description**
$u(\Delta t)_{osc}$	Specified by manufacturer to 121.2·10^{-12}s [62].
$u_c(\Delta t)_{coh.noise}$	$1.5\cdot10^{-8}$s (cf. calculations above)
$u(\Delta t)_{ph.dist.}$	$3.18\cdot10^{-9}s$. (ref. Section 3.4.4).
$u(\Delta t)_{el}$	Not available.
$u(\Delta t)_{res}$	Measured for each acquisition (ref. Section 5.2.4)
$u(\Delta t)_{var}$	Measured for each acquisition.
$u(\Delta t)_{RFI}$	Not available.
$u(\Delta t)_{trunc}$	$9.0\cdot10^{-10}$s for two-period pulse, 1.8·10^{-10} s for a six-period pulse. (Ref. Section 3.4.3)
$u(\Delta t)_{pump}$	$1.56\cdot10^{-10}$s. (cf. calculations above)
$u(\Delta t)_{other}$	Not available

The total uncertainty due to a change in transit time is calculated for each sampled waveform. In Table 6.26, the uncertainty in transit time for the sound velocity measurement for distilled water at $T = 45.7^oC$ (ref. Table 6.14) will be presented for the ZCM, and Table 6.27 for the FSM.

Table 6.26: Uncertainty budget for $u(\Delta t)_{ZCM}$ when c_s = 1537.7 m/s, T = 45.7^oC for a six-period pulse

Uncertainty source	**Input uncertainty**				**Combined uncertainty**	
	Expand. unc.	**Conf. level & distr.**	**Cov. fact., k**	**Standard unc.**	**Sensit. coeff**	**Variance**
Oscilloscope, time resolution	$1.21\cdot10^{-10}$ s	68%(norm)	1	$1.21\cdot10^{-10}$ s	1	$1.46\cdot10^{-20}s^2$
Coherent noise	$1.5\cdot10^{-8}$ s	68%(norm)	1	$1.50\cdot10^{-8}$ s	1	$2.25\cdot10^{-16}s^2$
Sampling resolution	$4.25\cdot10^{-10}$s	68% (norm)	1	$4.25\cdot10^{-10}$ s	1	$1.81\cdot10^{-19}s^2$
Transit time variation	$3.50\cdot10^{-9}$ s	68%(norm)	1	$3.50\cdot10^{-9}$ s	1	$1.23\cdot10^{-17}s^2$
Pump noise	$1.56\cdot10^{-10}$ s	68%(norm)	1	$1.56\cdot10^{-10}$ s	1	$2.43\cdot10^{-20}s^2$
Sum of variances					$u_c^2(\Delta t)_{ZCM}$	$2.38\cdot10^{-16}s^2$
Combined standard uncertainty (68% confidence level, k = 1)					$u_c(\Delta t)_{ZCM}$	$1.54\cdot10^{-8}$
Expanded uncertainty (95% confidence level, k = 2)					$U(\Delta t)_{ZCM}$	$3.08\cdot10^{-8}$
Theoretical transit time at c_s = 1537.69 m/s					Δt	$3.27\cdot10^{-5}$
Relative expanded uncertainty (95% confidence level, k = 2)					$U(\Delta t)_{ZCM}/\Delta t$	0.09%

Table 6.27: Uncertainty budget for $u(\Delta t)_{FSM}$ when c_s = 1537.7 m/s, T = 45.7^oC for a six-period pulse

Uncertainty source	**Input uncertainty**				**Combined uncertainty**	
	Expand. unc.	**Conf. level & distr.**	**Cov. fact., k**	**Standard unc.**	**Sensit. coeff**	**Variance**
Oscilloscope, time resolution	$1.21\cdot10^{-10}$ s	68%(norm)	1	$1.21\cdot10^{-10}$ s	1	$1.46\cdot10^{-20}s^2$
Coherent noise	$1.5\cdot10^{-8}$ s	68%(norm)	1	$1.5\cdot10^{-8}$ s	1	$2.25\cdot10^{-16}s^2$
Sampling resolution	$4.25\cdot10^{-10}$s	68% (norm)	1	$4.25\cdot10^{-10}$ s	1	$1.81\cdot10^{-19}s^2$
Phase distortion	$3.18\cdot10^{-9}$ s	68%(norm)	1	$3.18\cdot10^{-9}$ s	1	$1.01\cdot10^{-17}s^2$
Truncating	$1.8\cdot10^{-10}$ s	68%(norm)	1	$1.8\cdot10^{-10}$ s	1	$3.24\cdot10^{-20}s^2$
Pump noise	$1.56\cdot10^{-10}$ s	68%(norm)	1	$1.56\cdot10^{-10}$ s	1	$2.43\cdot10^{-20}s^2$
Sum of variances					$u_c^2(\Delta t)_{FSM}$	$2.35\cdot10^{-16}s^2$
Combined standard uncertainty (68% confidence level, k = 1)					$u_c(\Delta t)_{FSM}$	$1.53\cdot10^{-8}$
Expanded uncertainty (95% confidence level, k = 2)					$U(\Delta t)_{FSM}$	$3.07\cdot10^{-8}$
Theoretical transit time at c_s = 1537.7 m/s					Δt	$3.27\cdot10^{-5}$
Relative expanded uncertainty (95% confidence level, k = 2)					$U(\Delta t)_{FSM}/\Delta t$	0.09%

6.8.3 Uncertainty budget for the experimental sound velocity

c_s is a product of sample length L_0, thermal expansion K_T, transit time Δt, and a time correction Δt^{corr}. The experimental uncertainties in L_0 and K_T are found earlier in Section 6.2, and the uncertainties in Δt^{corr} and Δt are found in Secs. 6.8.1 and 6.8.2 respectively. The standard deviation of all c_s measurements at each temperature set-point in the measurement series is further calculated to account for sound velocity fluctuations within the set-point. This is only applicable during the measurement series at increasing temperatures. A summary of the variables and corresponding uncertainties is presented in Table 6.28, and the total uncertainty in c_s is calculated in Table 6.29.

Table 6.28: Summary of values and corresponding combined std. uncertainty for each variable needed to calculate the combined std. uncertainty in c_s at T = 45.67 and c_s = 1537.7 m/s for ZCM, following Eq. (5.2)

Variable	**Value**	**Combined std. uncertainty**
L_0	25.18 mm	0.0252 mm
K_T	1.0005	$1.32 \cdot 10^{-5}$
Δt	$3.27 \cdot 10^{-5}$ s	$1.54 \cdot 10^{-8}$ s
Δt^{corr}	$3.26 \cdot 10^{-8}$ s	$3.54 \cdot 10^{-9}$ s

Table 6.29: Uncertainty budget for the sound velocity measured in distilled water using ZCM with a 6 period pulse at 45.67^oC.

Uncertainty source	**Input uncertainty**				**Combined uncertainty**	
	Expand. unc	**Conf. level & distr.**	**Cov. fact., k**	**Standard unc.**	**Sens. coeff.**	**Variance**
Sample length, L_0	$2.52 \cdot 10^{-5}$ m	68% (norm)	1	$2.52 \cdot 10^{-5}$ m	$6.12 \cdot 10^{4}$	2.38 $(m/s)^2$
Transit time, Δt	$1.54 \cdot 10^{-8}$ s	68% (norm)	1	$1.54 \cdot 10^{-8}$ s	$-4.71 \cdot 10^{7}$	0.526 (m/s^2)
Time correction, Δt^{corr}	$3.54 \cdot 10^{-9}$ s	68% (norm)	1	$3.54 \cdot 10^{-9}$ s	$4.71 \cdot 10^{7}$	0.0278 $(m/s)^2$
Thermal expansion, K_T	$1.32 \cdot 10^{-5}$	68% (norm)	1	$1.32 \cdot 10^{-5}$	$1.54 \cdot 10^{3}$	$4.13 \cdot 10^{-4}$ $(m/s)^2$
Fluctuations in temp. set-point	0.0310 m/s	68% (norm)	1	0.0310 m/s	1	$9.61 \cdot 10^{-4}$ $(m/s)^2$

Sum of variances	$u_c^2(c_s)$	2.94 $(m/s)^2$
Combined standard uncertainty (68% **confidence level, k = 1)**	$u_c(c_s)$	1.71 m/s
Expanded uncertainty (95% **confidence level, k = 2)**	$U(c_s)$	3.43 m/s
Experimental sound velocity	c_s	1537.69 m/s
Relative expanded uncertainty (95% **confidence level, k = 2)**	$k \cdot E_{c_s}$	**2231 ppm**

Chapter 7

Discussion

This project has aimed to create a measurement cell for high-precision sound velocity measurements using the pulse-echo buffer rod method. The results show that, compared with theoretical models, high precision is obtained, but the uncertainty of the measurements exceeds 1000 ppm, which was the initial maximum uncertainty limit for this work.

7.1 Sound velocity measurements

For this project, sound velocity measurements have been conducted for saline water, distilled water, and Extra Virgin Olive Oil as a function of temperature. It was desired to perform repeatability measurements along with measurements using crude oil, but time constraints prevented this.

Sound velocity measurements corrected for diffraction were obtained using the ZCM and FSM with a six-period pulse for temperatures between 23.6 and 45.7^oC and 1 atm. The experimental sound velocity measurements using the ZCM agreed to within 100 ppm at 23.66^oC with the output of the theoretical sound velocity using distilled water and 101 ppm for the FSM. For both the ZCM and the FSM, the deviation reached its maximum at 33.4^oC with an agreement of 316 ppm and 350 ppm, respectively.
A second independent measurement series was conducted for a temperature range of 21.2-45.7^oC and 1 atm using a two-period pulse. The FSM's experimental sound velocity agreed with the theoretical sound velocity within 471 ppm at 21.2^oC, the maximum deviation throughout the measurement series for the signal processing method, and decreased to 27 ppm and 20 ppm at 25.2^oC and 28.0^oC respectively. For the ZCM, a more significant discrepancy between the experimental and theoretical sound velocity has been identified, reaching 744 ppm at 42.8^oC. The increased deviation is expected as the signal has not reached a steady state.
For both measurement series using distilled water, it should be noted that the uncertainty in the theoretical model is 777 ppm at 22.9^oC to 568 ppm at 45.7^oC. This will be discussed in detail later.

Sound velocity measurements were performed with saline water with S = 20 ppt using the ZCM with a six-period pulse over a temperature range of 22-40^oC. The results were compared with the UNESCO

equation [31] and presented a better agreement with the theoretical sound velocity than the experiments with distilled water, with a maximum deviation of 213 ppm, measured at 40^oC. The relative expanded uncertainty in the theoretical model has further been calculated to 390 ppm at 40.15^oC, thus lower than the uncertainty in the theoretical model for distilled water. The uncertainty further increases with decreasing temperature, resulting in a relative expanded uncertainty of 562 ppm 22.9^oC. It was early suspected that the salinity in the water might change upon heating due to condensation. This would increase the sound velocity during measurements, increasing the deviation from the theoretical c_{ts}. Conductivity measurements were performed before and after the measurement series, indicating a negligible increase in salinity as the increase in conductivity fell within the uncertainty of the meter.

Except for the ZCM measurements for distilled water using a two-period pulse, all sound velocities measured at room temperature were observed to be higher than the theoretical sound velocity before the deviation decreased. Initially, the unstable variations with temperature were believed to be caused by bulging in the Plexiglas buffer not being compensated for (Fig. 2.12), or by uncertainty in the model for thermal expansion of the measurement cell. While these reasons may lead to errors throughout the series, the deviation does not increase with increasing temperature, and the variations are thus not explained by thermal expansion alone. At lower temperatures, the uncertainty in the theoretical models are higher, which could contribute to the increased deviation between c_s at theoretical sound velocities at lower temperatures. Further, in the case of coherent noise sources, the mode-converted shear wave will affect all measurement series and may cause a minor deviation. In contrast, the four times traversed propagation will not affect any measurements made throughout the experimental sound velocity range in the project. Therefore, the measurements with distilled water and saline are unlikely to differ due to the coherent noise sources. More measurements in the lower sound velocity range would be desirable to study the consistency between experimental results and the theoretical analysis of coherent noise.

At 40^oC, Kinsler and Frey's theoretical model [23] results in relative expanded uncertainty of 567 ppm (Section 5.4.2). In comparison, the UNESCO equation has a relative expanded uncertainty of 390 ppm at the respective temperature and S = 20 ppt (Section 5.4.3), both calculated with a 95% confidence level. Further, for distilled water (S = 0) at 40^oC and 1 atm, a discrepancy of 0.43 m/s can be calculated between the UNESCO equation and Kinsler and Frey's equation, thus the two theoretical models used in the project. The use of the UNESCO equation for distilled water is, however, debated [32].
Hence, uncertainties in the theoretical models and experimental sound velocity may be a reason for the increased deviation with distilled water compared to saline water.
There are several theoretical models for both distilled and saline water [32, 100, 30]. The accuracy of many of the exciting theoretical models is debated, as many models have been developed through experimental testing and may thus suffer from the lack of accurate measurements [32, 100]. Further investigation of the accuracy of the theoretical models is desirable to compare the experimental and theoretical sound velocities with more confidence, but this falls outside the scope of the project.

The sound velocity in EVOO was measured as a function of temperature for a temperature range of

21-35^oC, and linear regression of $c_s = -3.232T + 1529$ was found. As opposed to distilled and saline water, no general equation of state has been found for the temperature dependency of EVOO. However, it has been seen to exhibit similar acoustic behaviour to crude oils [101], where an increase in temperature and a decrease in pressure causes a reduction in sound velocity [6, 102]. The results were compared to previous measurements conducted on EVOO in Yan et al. [98] with an uncertainty of 2 m/s, and on (non-specified) olive oil in McClements and Povey [99] with a claimed uncertainty of 0.7 m/s. An increasing discrepancy was found between the experimental results and the measured values in [98], resulting in a deviation of 6.83 m/s at 34.7^oC. The deviation is beyond the uncertainty of c_s, and the uncertainty of 2 m/s reported in [98], combined. By comparing the uncorrected experimental values of the project with [99], it can be seen that the linear regression line of McClements and Povey closely resembles the experimental values of the project. The comparison of the experimental values above with the tabulated values by the authors has some limitations. In neither Yan et al. nor McClements and Povey is diffraction correction discussed, and this suggests that their sound velocity values may not be corrected for diffraction. Further, McClements and Povey use a frequency of 1.25MHz, while Yan et al. applies a frequency of 5MHz throughout the project. Dispersion effects of EVOO have not been investigated and may thus be a source of discrepancy between the models and experimental values. It is also worth noting that [99] do not specify the type of olive oil, and the chemical composition may vary from the EVOO used here.

At room temperature, it has been shown that a six-period pulse agreed to within 207 ppm for the FSM and 141 ppm for the ZCM in the frequency range of 375-600 kHz, and 515 and 582 ppm, respectively at 275 kHz with the output from the theoretical sound velocity model of Kinsler and Frey [23]. This is under the assumption of negligible dispersion effects in distilled water. By comparing the sound velocity at 500 kHz with the remainder of the interval 375-600 kHz, only a slight increase in deviation is observed. The results thus indicate a potential for using the measurement cell outside the project's chosen frequency, which can be of interest when measuring dispersive media. A thorough investigation of c_s measurements at higher frequencies than 600 kHz has not been investigated in this project, as the desired frequency range for XSENS Flow Solutions [2] is 200-500 kHz.

7.2 Pulse length and choice of signal processing method

A previous discussion (Section 3.5.6) argued why a six-period pulse was desirable, considering coherent noise sources and the need for steady-state to determine c_s using the ZCM accurately. c_s was measured as a function of zero-crossings for the ZCM using two, six and ten periods. Measured c_s using a two-period pulse clearly shows an increase in deviation from the theoretical model compared to six and ten periods. This is also evident in the temperature series, where the ZCM agrees to within 744 ppm at 42.8^oC, thus confirming that a steady-state is needed for the accurate use of the ZCM. For a ten-period pulse, c_s measurements nearing the transient end of the pulse rapidly diverge from the theoretical model. This is consistent with the arrival of reflector reverberation and the four times traversed signal (Fig. 3.33), and demonstrates how coherent noise sources significantly can affect

c_s measurements. Despite this, the ten-period ZCM provides accurate c_s measurements throughout the project compared to the theoretical model, which indicates that noise sources may lead to false accuracy when averaging consecutive zero-crossings.

When using a six-period pulse, the work agrees with the theoretical model to within 100 ppm at 23.66^oC for distilled water and as high as 7 ppm for saline water at 31.4^oC. This indicates good potential for the ZCM when a steady state is achieved and coherent noise sources are minimized. It can also be noted that when using the transient start of the signal in Figs. 6.6, 6.7, and 6.9 to measure c_s, the deviation between theoretical and experimental sound velocity increases, which is consistent with discussions presented in [36] and [37].

FSM exhibits a slightly lower agreement with the theoretical model than the ZCM for a six-period pulse at 23.66^oC, where an agreement of 101 ppm against 100 ppm is found compared to Kinsler and Frey [23]. For a six-period pulse in distilled water, however, the difference between c_s using the ZCM and the FSM, and the associated change in uncertainty, are incremental. Both models provide accurate results in comparison with the theoretical model. In this project, more confidence is given in the six-period ZCM for more extended measurement series as the phase unwrapping process of the FSM has been challenging for pulses containing many periods (ref. Section 3.4.3). The ZCM is thus used as the primary signal processing method in this project. The results, however, indicate that either method may be used for longer pulses.

The FSM is advantageous when short bursts are needed in cases where separating the acoustic signals from reflections and coherent noise sources is of interest. The work agreed with the theoretical model as high as 20 ppm at 28.0^oC in distilled water for a two-period pulse. The results provided in this project thus indicate that the method has good potential for accurate c_s measurements when short bursts are needed.

7.3 Diffraction correction

No good diffraction correction for low-frequency propagation through several mediums has been found by the author. Khimunin's diffraction correction model is valid for all ka-values but is limited to only one medium [43]. Rogers and Van Buren's model [103] is only valid for ka » 1, and Papadakis model [12] is only a function of S, and not ka, which is important at low frequencies. For this project, ka = 14.4, and as a result, Khimunin's model was adapted to work for several mediums, named the BPDC-MF model, described in Section 2.3.1.

Sound velocity measurements were acquired with high precision compared to theoretical models, and it was thus of interest to see how accurate the diffraction correction model was. Therefore, a simplified simulation of the measurement cell was simulated through Comsol in Section 4.1. The results yielded a discrepancy of 1^o, and the simulated diffraction correction for Signal B is thus seen to be reasonably well described by the BPDC-MF model within the sound velocity range 1320-1480 m/s. However, the results are suspected not yet to have converged, and indications are given to a

higher agreement when the results are converged based on a single measurement with higher spatial and temporal resolution. The real uncertainty in the model may therefore vary from the tabulated one in the project, $u(\Delta t)_{model} = 3.5 \cdot 10^{-9}$ s.

It is, however, shown in Section7.4.1, that the uncertainty in diffraction correction does not play a significant role in the total relative expanded uncertainty of the sound velocity in this project. However, if the pulse-echo solid buffer method is to be used as a method for high-precision sound velocity measurements, the diffraction correction method must be verified with more confidence than the results presented in this project.

7.4 Measurement cell and measurement setup

As part of the project, temperature measurements were needed. The liquid temperature was assessed by inserting a sensor directly into the sample area but leaving sufficient space on either side. The purpose was to reduce noise caused by reflections from the sensor while limiting temperature gradients caused by the surrounding metal. Due to the size of the water bath, spatial temperature variations were observed, as one side of the measurement cell was near the heater and thus heated more quickly. If the sample area was stirred at even intervals, a reduction in the spatial variation between set-points was observed but not eliminated. A reduction in temperature variations may have been possible if the size of the water bath was increased or the heat was more evenly distributed. In the current project, this was resolved by letting the water bath stabilize for several minutes at each temperature set-point. However, a more stable water bath would provide more confidence in the measurements taken between set-points.

Before conducting sound velocity measurements, air bubbles created upon heating were of concern. It would significantly reduce the amplitude of the sound wave and scatter the sound in all directions. The possibility of air bubbles and the temperature variations were reasons why a lid was not placed on the measurement cell. However, no air bubbles were observed throughout the measurement series. As the cell is designed with the intention of adding a lid, this can be done at a later stage.

The reflector was further shown to be a limiting factor to the number of pulses that could be used. The Department for Physics and Technology workshop tried to change the reflector without taking apart the measurement cell but did not succeed. The reflector should thus be made larger if longer pulses are needed in future work. If f = 500 kHz and the sound velocity in aluminium is assumed to be 6300 m/s (Table 3.6), the reflector should be increased by $(6300 \cdot 2 \cdot 10^{-6}) \cdot 0.5 = 6.3$ mm per extra period needed.

The current project aimed to determine if a high-precision sound velocity cell could be created using the pulse-echo buffer rod method, with size, sample volume, and frequency restrictions, and reach a relative expanded uncertainty of less than 1000 ppm (95% confidence level). A sensitivity analysis was performed prior to construction to see what the uncertainty contributions would have to be in order to fulfil these criteria, presented in Section 5.3. During the development of the measurement cell,

careful considerations were made in order to create a cell with as high precision as possible within the scope of the project.

Due to mode-converted shear waves and four times propagation in the buffer rod, the method suffers from coherent uncertainty contributions that are hard to reduce. Several studies have reported this [14, 16, 15, 13], and it can only be prevented or reduced through the choice of buffer material, buffer dimensions, or pulse length. In Section 3.5.4, an analysis is presented showing that, to achieve a small measurement cell with the chosen materials, the mode-converted shear wave or the four times traversed buffer signal must act as a permanent coherent noise source. In Bjørndal et al. [16], the mode-converted shear wave has a significantly lower amplitude, and based on this, the mode-converted shear wave has been chosen as a permanent coherent noise source, measured with an SNR of 33 dB (Fig. 3.26).

The construction of the measurement cell further made it challenging to determine the sample length with high precision. Initially, the chassis was intended to be carved out of an aluminium block in one go. Due to the lack of necessary tools in the workshop, the measurement cell was created from several individual parts. There is an associated degree of uncertainty in each part's length, height, and width, resulting in an overall more significant uncertainty of the cell's dimensions. In combination with the lack of high precision measuring tools to measure the sample length itself, the uncertainty in the sample length increased beyond the sensitivity analysis presented in Section 5.3. Further, when the temperature increases, the sample length is suspected to decrease due to a bulging in the Plexiglas, explained in Section 2.5. This thermal expansion was not quantifiable within the scope of this project and was too small to be measured with the measuring tools at hand.

7.4.1 Uncertainty discussion

The uncertainty budget presented in Table 6.29 will be used as a baseline for assessing the uncertainty in c_s. This corresponds to the uncertainty in sound velocity in distilled water at 45.7^oC using the ZCM with a six-period pulse, where a relative expanded uncertainty of 2231 ppm (95% confidence level) was calculated. There were no significant differences in FSM uncertainty at the chosen temperatures (also 2231 ppm), with the only difference being the contributions to transit time uncertainty in the total uncertainty budget. This discussion does not include uncertainty due to fluctuations in temperature set-points, which is independent of the general uncertainty in c_s.

In the resulting uncertainty budget, the most significant uncertainty contributor is the uncertainty of the sample length, calculated to be 0.0252 mm at 68% confidence level. This corresponds to 81% = 1811 ppm of the total uncertainty in sound velocity (95% confidence level) and exceeds the sample length uncertainty presented in the preliminary sensitivity analysis of $u(L_0)$ = 0.0151 mm at 68% confidence level. In cases of small distances, as in this project, it is often difficult to determine the length of the propagation path with adequate precision. Therefore, the different uncertainty contributions will be identified and assessed.

As is presented in Section 5.2.3, the length of the sample area is dependent on 1) the uncertainty of the

buffer length and the parallelism between buffer and reflector due to the construction method, 2) the caliper uncertainty, 3) and uncertainty due to repeatability in measurements. Therefore, reducing one or more of these uncertainty contributions is the most effective method for reducing the total relative expanded uncertainty.

This is illustrated in Fig. 7.1. The figure shows the change in the uncertainty budget in ppm when the uncertainty in sample length, $u_c(L_0)$, is changed, while the uncertainties $u_c(\Delta t)$, $u_c(K_T)$, and $u_c(\Delta t^{diff})$ are held constant.

By changing $u_c(L_0)$, and thereby the relative uncertainty in length, $E_L = u_c(L_0)/L_0$, the corresponding $E_c^{r.e.}$ can be calculated, where $E_c^{r.e.} = k \cdot E_c$ will serve as an abbreviation for the relative expanded uncertainty (95% confidence level, k = 2) for simplicity. A change in E_L will further cause a corresponding change in the contribution of the other relative uncertainties, $E_{\Delta t} = u(\Delta t)/\Delta t$, $E_{\Delta t^{corr}} = u(\Delta t^{corr})/\Delta t^{corr}$ and $E_{K_T} = u(K_T)/K_T$, to the total uncertainty budget. Since the contributions of $E_{\Delta t^{corr}}$ and E_{K_T} are minuscule compared to the other two, they are plotted on the right axis.

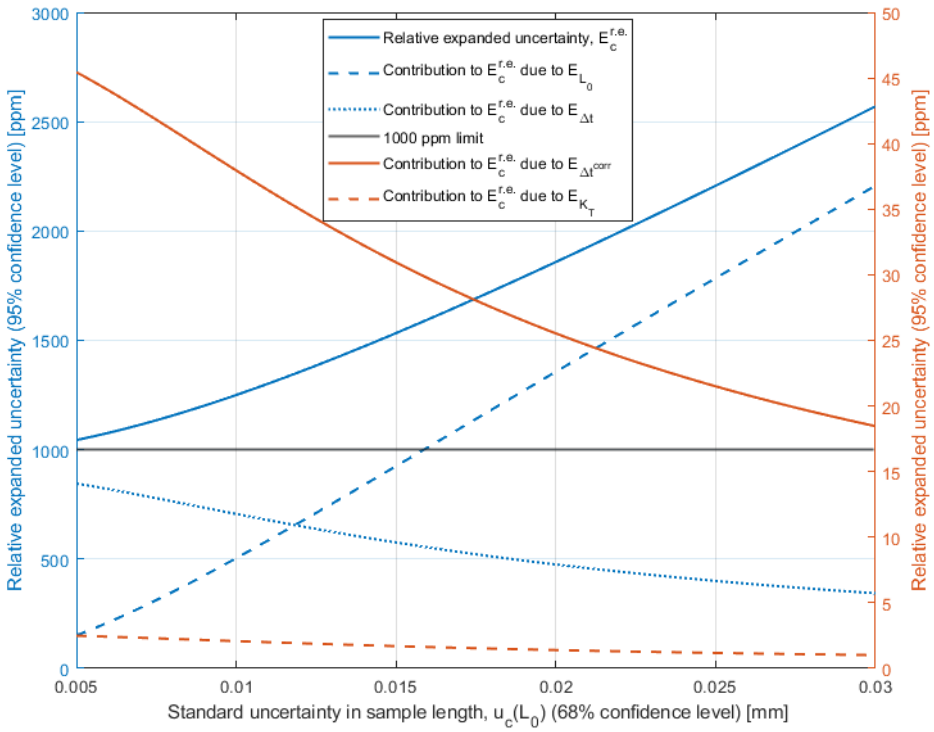

Figure 7.1: Change in the uncertainty budget as a function of uncertainty in sample length for the measurement cell constructed in the project. Blue solid curve is the total relative expanded uncertainty of the calculated sound velocity, $E_c^{r.e.} = k \cdot E_c$ (k = 2, 95% confidence level). The blue dashed line is the ppm contribution to the total $E_c^{r.e}$ due to uncertainty in the sample length, $u_c(L)$. Blue dashed line corresponds to the limit of 1000ppm set in the project. Red lines correspond to the ppm contribution to $E_c^{r.e}$ due to uncertainty in Δt, Δt^{corr} and K_T when E_L changes (68% confidence level). The uncertainties in Δt and Δt^{corr} are constant, calculated for a scenario of 1547 m/s.

In this project, $E_c^{r.e.}$ = 2231 ppm for c_s = 1547 m/s, with E_{L_0} contributing with 1811 ppm of the total 2231 ppm, while $E_{\Delta t}$ = 490 ppm. If the uncertainty in length is decreased to, say, $u(L_0)$ = 0.01 mm,

then $E_c^{r.e.}$ will decrease to ≈ 1250 ppm, while the contribution of $E_{\Delta t}$ will increase, accounting for 700 ppm of the total 1250 ppm. From Fig. 7.1, it is thus evident that a decrease in E_{L_0} will rapidly decrease $E_c^{r.e.}$, which can be done by decreasing $u(L_0)$ (as shown in Fig. 7.1), or by increasing the sample length.

To lower $E_c^{r.e.}$ to below 1000ppm for the current measurement cell, decreasing the standard uncertainty in sample length alone will, however, not be sufficient, and it is thus evident that the transit time uncertainty must be decreased as well. In Section 6.8.2, the uncertainty budget for the transit time uncertainty shows that coherent noise sources is the largest contributor. However, the most significant contribution to coherent noise is the reflector noise, which can easily be reduced or eliminated by increasing the reflector length. If coherent noise due to the reflector noise is eliminated, $u(\Delta t)_{coh.noise} = 7.59 \cdot 10^{-9}$s, and $E_c^{r.e.}$ is reduced with almost 200 ppm in the current uncertainty budget.

For the uncertainty budget presented in Table 6.29, only the uncertainty in thermal expansion is within the uncertainty of the sensitivity analysis presented in Section 5.3. For the transit time uncertainty, the sensitivity analysis presents an allowed uncertainty of $1 \cdot 10^{-8}$ s (68% c. l.). The experimental uncertainty budget in 6.29 shows that this is not achieved, as $u(\Delta t)_{zc} = 1.54 \cdot 10^{-8}$ s. Further, the experimental diffraction correction uncertainty is found to be $u(\Delta t^{corr}) = 3.54 \cdot 10^{-9}$ s against $6.45 \cdot 10^{-10}$ s in the sensitivity analysis. However, from Fig. 7.1, it is evident that $u(\Delta t^{corr})$ and $u(K_T)$ is negligible for the current uncertainty budget. It should be noted that the sensitivity analysis is carried out at 60^oC, but as the uncertainty increases with increasing temperature, the comparison is valid for lower temperatures.

It should be noted that the attained experimental uncertainty ought to be regarded as preliminary due to the diffraction correction uncertainty, and uncertainties not accounted for throughout the project, such as i) bulging in the Plexiglas buffer, ii) imperfect symmetry in the transducer or the mounting of the transducer, and iii) other unknown sources not accounted for.

7.4.2 Future improvements

Many of the presented uncertainty contributions in the project are due to the size of the measurement cell, restricted by preferences set by XSENS Flow Solutions. From previous discussions, it is evident that a future measurement cell, which includes the buffer, sample and reflector, should be enlarged. This will decrease the relative uncertainty in sample length and reduce or eliminate coherent noise sources.

A preliminary design of a new measurement cell can be presented using the analysis in Section 3.5.4. With no size limitations, as opposed to this project, the four times traversed buffer signal and the mode-converted wave can be chosen to arrive after both signals of interest. The new equation for the mode-converted shear wave, Eq.(7.1), will thus be

$$D > \frac{\frac{2L_0}{c_s} + \Delta t_{burst}}{\frac{1}{c_{shear}} - \frac{1}{c_b}}, \tag{7.1}$$

while the equation for the four times traversed buffer signal, Eq. (3.13), remains the same. Inserting the experimental c_b, and the corresponding theoretical c_{shear}, and choosing a 6 period pulse at 500 kHz corresponding to $\Delta t_{burst} = 1.2 \cdot 10^{-5} s$, new buffer and sample lengths can be found. A sound velocity range of c_s = 1250 - 1580 m/s is chosen, and the result is shown in Fig. 7.2.

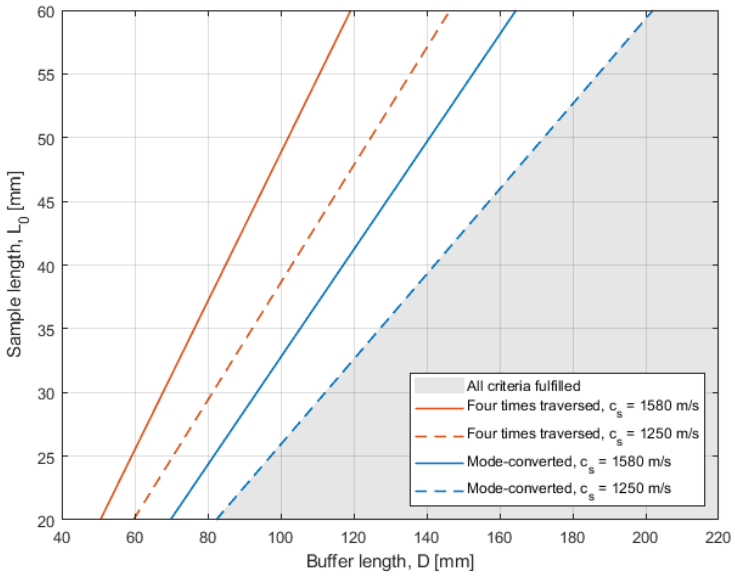

Figure 7.2: Minimum buffer length as a function of sample length (in grey) if the two coherent noise sources are to be removed form the signal of interest. Calculated with $c_b = 2711 m/s$, $c_{shear} = 1106.8 m/s$, and $\Delta t_{burst} = 1.2 \cdot 10^{-5}$ s for a sound velocity span of 1250-1580 m/s.

By applying the set parameters, Fig. 7.2 presents a large grey area that illustrates various combinations of buffer and sample lengths that result in propagation that avoids the two coherent noise sources. The mode-converted wave at low sound velocities will set the minimum sample and buffer length criteria. Thus must the measurement cell be increased with decreasing sound velocity. However, creating a measurement cell that avoids both noise contributions should be achievable with no size restrictions. Increasing the reflector size should further be possible to eliminate or reduce most coherent noise sources. The combination of Figs. 7.1 and 7.2 can be used as a starting point for creating a measurement cell using the solid buffer method with a relative expanded uncertainty of less than 1000 ppm.

Chapter 8

Conclusions and further work

8.1 Conclusions

In this project, a measurement cell was developed based on the pulse-echo solid buffer method in order to determine if the method can be utilized to construct a high precision sound velocity cell. Several preferences were given in advance by XSENS Flow Solutions which limited the design possibilities of the measurement cell.

A six-period pulse was found to be sufficient to avoid or limit coherent noise sources in the constructed measurement cell for a sound velocity range of 1250 m/s to 1580 m/s. This has been demonstrated experimentally to be sufficient to reach a steady-state and has thus been applied when measuring the sound velocity. Two different signal processing methods have been evaluated for experimental measurements; direct transit time measurements (ZCM) and the Fourier spectrum method (FSM). Both short bursts and six-period steady-state signals have been tested with these methods. The experimental results show that, compared with theoretical models, high precision measurements are obtained with both signal processing methods.
The present work demonstrated agreement within 100 ppm at 23.66^oC with the output of the theoretical sound velocity using the ZCM for the chosen steady-state pulse. A maximum deviation of 316 ppm at 33.4^oC was further reported throughout a temperature range of 23.6 and 45.7^oC. The FSM provides nearly identical results using the steady-state signal, while it demonstrates agreement within 20 ppm between measured sound velocity and the theoretical model at 28^oC using a short burst. This indicates that the method has good potential for accurate sound velocity measurements when short bursts are needed. It should here be noted that an uncertainty in the theoretical model for distilled water of 568 ppm is calculated. More confidence is given in the ZCM using the steady-state signal, as many assumptions and calculations throughout the thesis are based on continuous waves. This has thus been chosen as the primary signal processing method in this work. Due to the difficulty of phase unwrapping for longer pulses in this study, the FSM using a steady-state signal has not been further investigated.

Sound velocity measurements are further performed with saline water using the ZCM with a steady-

state pulse. The work demonstrated agreement within 7 ppm between the experimental sound velocity and the theoretical model at 31.40^oC and a maximum deviation of 161 ppm at 40^oC, corresponding to the maximum temperature in the measurement series. At 40^oC, an uncertainty in the theoretical model of 390 ppm is calculated. Saline water has better agreement with the theoretical model than distilled water, which is believed to be a combination of uncertainty within the theoretical models themselves and the calculated uncertainty of the experimental sound velocity.

A measurement series is further performed using Extra Virgin Olive oil as a liquid sample using the ZCM with a steady-state pulse. The experimental results demonstrated close agreement to the results presented in McClements and Povey [99], while a deviation of up to 6.8 m/s was found between the experimental results and the results presented in Yan et al.[98].

An adaptation of Khimunin's diffraction correction model has been introduced in the project for diffraction correction through multiple mediums, named the BPDC-MF model. Accurate sound velocity measurements were acquired compared to theoretical models, which motivated a careful analysis of the model through simulations in COMSOL. The preliminary results presented a deviation between the simulations and the diffraction correction model used in the project of 1^o, which indicates that the BPDC-MF model can be applied with little error when using the solid buffer method. The simulations are suspected to have yet to converge, and indications suggest even better agreement.

A traceable uncertainty budget is presented, which puts the total relative expanded uncertainty of the measurement cell at 2231 ppm (95% confidence level) with a sound velocity of 1538 m/s, corresponding to distilled water at 45.7^oC. The uncertainty analysis shows that uncertainties in the sample length contribute significantly to the overall uncertainty, accounting for 1811 ppm = 81 % of the total uncertainty budget. As a result, the main improvement from the current design is either a decrease in the sample length uncertainty or an increase in the sample length. Moreover, it was found that the uncertainty in transit time due to identified reflector reverberation accounted for more than 200 ppm of the total uncertainty budget, which can be reduced by increasing the size of the reflector. Errors known to affect the pulse-echo buffer rod method, such as the four-times traversed signal in the buffer and the mode-converted shear waves, are less critical than anticipated in this project.

Removing the size limitations only applicable for this project can reduce several sources of uncertainty, such as sample length uncertainty and uncertainty caused by coherent noise. With a few design alterations, it should be feasible to design a measurement cell using the pulse-echo buffer rod method with a relative expanded uncertainty within 1000ppm. It is, however, found that the candidate method may not be suited as a high-precision cell when small measurement cells are needed unless high-precision measuring tools are acquired.

8.2 Further work

A measurement cell that can measure the sound velocity in pressurized fluids and over a range of temperatures was initially desired. However, to measure the sound velocity in pressurized fluids, the chassis would have to be reinforced by expanding the thickness of the walls. Valves and pressure sensors would also have to be installed. This was not feasible within the project's scope and can thus be included in further work.

The measurements performed in this project for distilled and saline water present high accuracy compared to theoretical models. Validation through repeatability measurements would thus be of interest, together with a study of the accuracy of the theoretical models. Sound velocity measurements on crude oils were planned but unfortunately not performed due to lack of time. This may be included in further work. Additionally, by increasing the size of the water bath or by acquiring a more properly temperature-regulated bath, measurements could be conducted with more confidence outside the temperature set-points.

For the current measurement cell, the sample length uncertainty can be significantly reduced by acquiring a high-precision measuring tool. The length as a function of temperature can further be expressed with greater confidence if the change in sample length due to a possible bulging in the Plexiglas buffer is found with increasing temperatures.

The work assumes that the COMSOL simulations can be directly compared to the diffraction correction models presented in this project. A possible deviation due to the assumption should be studied in further work. The simulations are also suspected of not yet having converged, and more simulations with higher resolution would be of interest.

Finally, by removing the size restrictions on the construction of the measurement cell, a sound velocity cell measuring sound velocity with a relative expanded uncertainty within 1000 ppm is believed to be feasible. It would thus be of interest to create a new measurement cell to test if the proposed method can be applied when a sound velocity cell of high precision is needed.

References

[1] L. C. Lynnworth and Y. Liu, "Ultrasonic flowmeters: half-century progress report, 1955-2005," *Ultrasonics*, vol. 44, pp. e1371–e1378, 2008.

[2] XSENS Flow Solutions, Bergen, Norway, Available at: https://xsensflow.com/, Last Accessed: 09.04.22.

[3] V. K. Vidyarthi, P. Sagar, K. S. Harsha, S. Tripathi, N. Naik, and P. Munshi, "Ultrasonic Transit-time Flowmeters for Pipes: A Short Review," in *Flotek.g - Global Conference Exhibition*. FCRI, Aug. 2017, paper fg1797.

[4] J. P. Bentley, *Principles of Measurement Systems*, 4th ed. Pearson/Prentice Hall, 2005.

[5] Y. S. Yang, B. N. Scott, and B. B. Cregger, "The Design, Development, and Field Testing of a Water-Cut Meter Based on a Microwave Technique," *SPE Annual Technical Conference and Exhibition*, no. Paper Nr. SPE-20697-MS, 1990.

[6] M. Batzle and Z. Wang, "Seismic properties of pore fluids," *Geophysics*, vol. 57 (11), pp. 1396–1408, 1992.

[7] O. Nesse, "Sound Propagation in Emulsions," Ph.D. dissertation, University of Bergen, Dept. of Physics and Technology, Bergen, Norway, Jan. 1998.

[8] P. Lunde and M. Vestrheim, "Precision Sound Velocity Cell for Natural Gas at High Pressure. Phase 1- Feasibility study." *Christian Michelsen Research*, Ref. nr.: CMR-98-A10039, Bergen, Norway, Dec. 1998.

[9] P. Norli, "Sound Velocity Cell for Gas Characterization," Ph.D. dissertation, University of Bergen, Dept. of Physics and Technology, Bergen, Norway, Aug. 2007.

[10] E. Bjorndal, "Acoustic measurement of liquid density with applications for mass measurement of oil," Ph.D. dissertation, University of Bergen, Dept. of Physics and Technology, Bergen, Norway, Apr. 2007.

[11] S. Hoche, M. A. Hussein, and T. Becker, "Ultrasound-based density determination via buffer rod techniques: a review," *Journal of Sensors and Sensor Systems*, vol. 2, pp. 103–125, 2013.

[12] E. P. Papadakis, K. A. Fowler, and L. Lynnworth, "Ultrasonic attenuation by spectrum analysis of pulses in buffer rods: Method and diffraction corrections," *The Journal of the Acoustical Society of America*, vol. 53 (4), pp. 1336–1343, 1973.

[13] F. M. Foudzi and I. Ihara, "Development of Polygonal Buffer Rods for Ultrasonic Pulse-Echo Measurements," *Journal of Physics: Conference Series*, vol. 520, 2014.

[14] M. Saether, "Elastic wave velocities and attenuation under methane hydrate growth in Bentheim Sandstone - Measurements and modelling," Ph.D. dissertation, University of Bergen, Dept. of Physics and Technology, Bergen, Norway, Sep. 2018.

[15] S. J. Ball and J. P. M. Trusler, "Speed of sound of n-Hexane and n-Hexadecane at Temperatures Between 298 and 373 K and Pressure up to 100 MPa," *International Journal of Thermophysics*, vol. 22 (2), pp. 427–443, 2001.

[16] E. Bjørndal, K.-E. Frøysa, and S. Engeseth, "A Novel Approach to Acoustic Liquid Density Measurements Using a Buffer Rod Based Measuring Cell," *IEEE Transactions on Ultrasonic, Ferroelectric, and frequency Control*, vol. 55 (8), pp. 1794–1808, 2008.

[17] R. T. Higuti, "Energy Method to Calculate the Density of Liquids Using Ultrasonic Reflection Techniques," in *2001 IEEE Ultrasonic Symposium*, D. E. Yuhas and S. C. Schneider, Eds. Ultrasonics, Ferroelectrics, and Frequency Control Society, October 7-10, pp. 319–323.

[18] G. Tardajos, M. Diaz Pena, and E. Aicart, "Speed of sound in pure liquids by a pulse-echo-overlap method," *The Journal of Chemical Thermodynamics*, vol. 18, pp. 683–689, 1986.

[19] D. McClements and P. Fairley, "Ultrasonic pulse echo reflectometer," *Ultrasonic*, vol. 29, pp. 58–62, 1991.

[20] G. Benedetto, R. M. Gavioso, P. A. Giuliano Albo, S. Lago, D. Madonna Ripa, and S. R., "Speed of Sound in Pure Water at Temperatures between 274 to 394 K and at Pressures up to 90 MPa," *International Journal of Thermophysics*, vol. 26 (6), pp. 1667–1680, 2005.

[21] M. Solberg, "Absolute sound velocity measurements in liquid using the three-way three way pulse method," Master's thesis, University of Bergen, Dept. of Physics and Technology, Bergen, Norway, Sep. 2009.

[22] J. P. Petitet, R. Tufeu, and B. L. Neindre, "Determination of the Thermodynamic Properties of Water from Measurements of the Speed of Sound in the Temperature Range 251.15-293.15K and the Pressure Range 0.1-350 MPa," *International Journal of Thermophysics*, vol. 4 (1), pp. 1336–1343, 1983.

[23] L. E. Kinsler, A. R. Frey, A. B. Coppens, and J. V. Sanders, *Fundamentals of Acoustics*, 4th ed. John Wiley & Sons, Inc., 2000.

[24] W. Sachse and Y.-H. Pao, "On the determination of phase and group velocities of dispersive waves in solids," *Journal of Applied Physics*, vol. 49(8), pp. 4320–4327, 1978.

[25] F. Jacobsen and P. M. Juhl, *Fundamentals of General Linear Acoustics*, 1st ed. John Wiley Sons, New Jersey, USA, 2013.

[26] P. M. Shearer, *Introduction to Seismology*, 3rd ed. Cambridge University Press, 2019.

[27] H. D. Young and R. A. Freedman, *University Physics with Modern Physics*, 14th ed. Pearson Education Limited, Harlow, England.

[28] G. S. Kell, "Density, Thermal Expansivity, and Compressibility of Liquid Water from 0^oC to 150^oC: Correlations and Tables for Atmospheric Pressure and Saturation Reviewed and Expressed on 1968 Temperature Scale," *Journal of Chemical and Engineering Data*, vol. 20 (1), pp. 97–105, 1975.

[29] C.-T. Chen and F. J. Millero, "Speed of sound in seawater at high pressures," *The Journal of the Acoustical Society of America*, vol. 62(5), pp. 1129–1135, 1977.

[30] V. A. Del Grosso, "New equation for the speed of sound in natural waters (with comparison to other equations)," *The Journal of the Acoustical Society of America*, vol. 56(4), pp. 1084–1091, 1974.

[31] G. K. S. Wong and S. Zhu, "Speed of sound in seawater as a function of salinity, temperature and pressure," *The Journal of the Acoustical Society of America*, vol. 97 (3), pp. 1732–1736, 1995.

[32] C. C. Leroy, S. P. Robinson, and M. J. Goldsmidth, *The Journal of the Acoustical Society of America*, pp. 2274–2282.

[33] NPL- National Physics Laboratory, "Speed of sound in sea water- Underlying Physics," Available at: http://resource.npl.co.uk/acoustics/techguides/soundseawater/underlying-phys.html, Last Accessed: 21.04.22.

[34] UNESCO, "Tenth report of the joint panel on oceanographic tables and standards," *Unesco technical papers in marine science*, vol. 36, Sidney, B. C. Canada, 1-5 Sep. 1980.

[35] Lunde, P., Rommetveit, T. (XSENS AS), *Personal communication with supervisors*, University of Bergen, Dept. of Physics and Technology, Bergen, Norway, 2021-2022.

[36] J. B. Molyneux and D. R. Schmitt, "Compressional-wave velocities in attenuating media: A laboratory physical model study," *Geophysics*, vol. 65 (4), pp. 1162–1167, 2000.

[37] ——, "First-break timing: Arrival onset times by direct correlation," *Geophysics*, vol. 64 (5), pp. 1492–1501, 1999.

[38] A. Khimunin, "Numerical calculation of the diffraction corrections for the precise measurement of ultrasound absorption," *Acta Acustica united with Acustica*, vol. 27 (4), pp. 173–181, 1972.

[39] H. Fossaa, "Ultrasound Phantom for Myocardium," Master's thesis, University of Bergen, Dept. of Physics and Technology, Bergen, Norway, Oct 2011.

[40] P. Lunde and K.-E. Frøysa, "Handbook of Uncertainty Calculations. Ultrasonic Fiscal Gas Metering Stations," *Christian Michelsen Research AS*, Dec. 2001, bergen, Norway, Rapp. nr. ISBN: 82-556-1009-3.

[41] E. Storheim, P. Lunde, and M. Vestrheim, "Diffraction correction in ultrasonic fields for measurements of sound velocity in gas. conventional and alternative methods." in *Proc. of 34th Scandinavian Symposium on Physical Acoustics*. Norwegian Physical Society, January 3 - February 2. 2011, ISBN 978-82-8123-004-0.

[42] A. Williams Jr, "The piston source at high frequencies," *The Journal of the Acoustical Society of America*, vol. 23 (1), pp. 1–6, 1951.

[43] A. Khimunin, "Numerical calculation of the diffraction corrections for the precise measurement of ultrasound phase velocity," *Acta Acustica united with Acustica*, vol. 32 (3), pp. 192–200, 1975.

[44] M. Vestrheim, *Lecture notes in PHYS373- Acoustic measurement systems*. Course at the University of Bergen, Dept. for Physics and Technology, Bergen, Norway, 2013.

[45] M. Vestrheim, *Lecture notes in PHYS272- Acoustic Transducers*. Course at the University of Bergen, Dept. of Physics and Technology, Bergen, Norway, 2007.

[46] E. N. Mosland, E. Storheim, P. Lunde, M. Vestrheim, and J. Kocback, "Diffraction correction for precision measurements of sound velocity in gas. Is full receiver modelling needed?" vol. 42(4), 1999, pp. 406–413.

[47] J. P. M. Trusler, *Physical Acoustics and Metrology of Fluids*. New Jersey, USA: Bristol: Adam Hilger, 1991.

[48] A. D. Pierce, *Acoustics- An Introduction to Its Principles and Applications*, 3rd ed. Springer, Cham, Germany, 2019.

[49] E. E. Franco, M. A. B. Andrade, R. T. Higuti, J. C. Adamowski, and F. Buiochi, "Acoustic Transmission With Mode Conversion Phenomenon," *ABCM Symposium Series in Mechatronics*, vol. 2, pp. 113–120, 2006.

[50] K. W. Winkler and T. J. Plona, "Technique for Measuring Ultrasonic Velocity and Attenuation Spectra in Rocks Under Pressure," *Journal of Geophysical Research*, vol. 87 (B13), pp. 10 776–107 780, 1982.

[51] S. Fraser, "Acoustic investigation of the hydrodynamics and ecology of a tidal channel and the impacts of a marine renewable energy installation," Ph.D. dissertation, University of Aberdeen, Dept. of Geophysics, Apr. 2017.

[52] Thyssenkrupp, "Aluminium 6082," Available at: https://www.thyssenkrupp-materials.co.uk/aluminium-6082.html, Last Accessed: 20.01.22.

[53] Astrup, "Plast katalogen," Available at: https://astrup.no/Kataloger/Plastkatalogen, 2010, Last Accessed: 21.01.2022.

[54] J. H. McClellan, R. W. Schafer, and M. A. Yoder, *DSP First*, 2nd ed. Pearson Education Limited, USA, 2016.

[55] E. O. Brigham, *The Fast Fourier Transform and its applications*. Prentice Hall, Englewood Cliffs, NJ, 1988.

[56] MATLAB, *version 9.9.0 (R2020b)*. Natick, Massachusetts: The MathWorks Inc., 2020.

[57] KeySight Technologies, "33500B and 33600A Series Trueform Waveform Generators 20, 30, 80, 120 MHz," Aug. 2021, Available at: https://www.keysight.com/zz/en/assets/7018-05928/data-sheets/5992-2572.pdf, Last Accessed: 29.04.2022.

[58] A. O. Pedersen, *Personal communication*, University of Bergen, Dept. of Physics and Technology, Bergen, Norway, 2022.

[59] Elprocus- Electronic Projects for Engineering Students, "What is Knee Voltage of PN-Junction Diode," Available at: https://www.elprocus.com/knee-voltage-of-pn-junction-diode/, Last Accessed: 21.04.2022.

[60] P. Zhang, *Advanced Industrial Control Technology*, 1st ed. Binghamton: Elsevier Science, 2010, ISBN 9781437778076.

[61] Olympus, "Ultrasonic Transducers - Wedges, Cables, Test Blocks," Available at: http://www.materialevaluation.gr/pdf/Flaw_Detectors/Transducers_And_Probes/UltraSonic_Transducers_Pana_UT_EN_201603.pdf, July 2019, Last Accessed: 21.05.2022.

[62] Tektronix, "Mixed Signal Oscilloscopes MSO3000 Series, DPO3000 Series Datasheet," Sep. 2010, Available at: https://www.farnell.com/datasheets/866445.pdf, Last Accessed: 01.05.2022.

[63] Paroscientific, Inc. Digiquartz Pressure Instrumentation, "Digiquartz Intelligent Barometers and Barometric Standards," Available at: http://www.coastal-usa.com/paros.pdf, Last Accessed: 21.04.2022.

[64] JUMO, "Push-in resistance thermometers in steam-tight version," Available for download: http://www.jumo.no/produkter/sensorer-og-automatisering/temperatur/rtd-temperaturf%C3%B8lere/oversikt-over-rtd-temperaturf%C3%B8lere/902830/jumo-steamtemp-temperaturgiver-rtd-pt100---pt1000-i-vann--og-damptett-utf%C3%B8relse-902830.html, Last Accessed: 02.05.2022.

[65] The International Electrotechnical Commission (IEC), "Industrial platinum resistance thermometers and platinum temperature sensors (IEC 60751:2008)," Standard, July 2008, DIN EN 60751:2009-05.

[66] H. Preston-Thomas, "The International Temperature Scale of 1990 (ITS-90)," *Metrologia*, vol. 27, pp. 3–10, 1990.

[67] ATP Instrumentation Ltd, "Pt100 Accuracy and Probe Classification," Available at: https://atp-instrumentation.co.uk/blogs/articles/pt100-accuracy-and-probe-classification, Last Accessed: 28.04.2022.

[68] Mahr Group, "Digital Caliper 16 EWR with data output," Available at: https://metrology.mahr.com/en-int/products/article/4103301-digitaler-messschieber-marcal-16-ewr, Last Accessed: 29.04.2022.

[69] M. Aanes, "Interaction of piezoelectric transducer excited ultrasonic pulsed beams with a fluid-embedded viscoelastic plate. Finite element modeling, angular spectrum modeling and measurements," Ph.D. dissertation, University of Bergen, Dept. of Physics and Technology, Bergen, Norway, 2013.

[70] P. He and J. Zheng, "Acoustic dispersion and attenuation measurement using both transmitted and reflected pulses," *Ultrasonic*, vol. 39 (1), pp. 27–32, 2001.

[71] R. A. Kline, "Measurement of attenuation and dispersion using an ultrasonic spectroscopy technique," *The Journal of the Acoustical Society of America*, vol. 76 (2), pp. 498–504, 1984.

[72] J. Wu, "Determination of velocity and attenuation of shear waves using ultrasonic spectroscopy," *The Journal of the Acoustical Society of America*, vol. 99 (5), pp. 2871–2875, 1996.

[73] R. A. Adams and C. Essex, *Calculus - A complete course*, 8th ed. Pearson, Toronto, Canada, 2014.

[74] NASPI Engineering Analysis Task Team (EATT), "Phase angle calculations: Considerations and use cases," North American Synchro Phasor Initiative, Tech. Rep. NASPI-2016-TR-006, Sep. 2016.

[75] S. Zhou and L. Rongfang, "Efficient and accurate frequency estimator under low snr by phase unwrapping," *Mathematical Problems in Engineering*, vol. Article ID 7396074, 2019.

[76] D. Zheng-Miao and H. Xiao-Hong, "A simple phase unwrapping algorith and its application to phase-based frequency estimation," *Recent Patents on Signal Processing*, vol. 2, pp. 63–71, 2010.

[77] N.-K. Chen and P.-H. Wu, "The use of fourier-domain analyses for unwrapping phase images of low signal-to-.noise ratio," *Magnetic Resonance in Medicine*, vol. 2, pp. 356–366, 2019.

[78] M. M. Sæther, *Personal communication*, University of Bergen, Dept. of Physics and Technology, Bergen, Norway, 2022.

[79] M. R. Ebadi, "Coherent and incoherent seismic noise attenuation using parabolic radon transform and its applications in environmental geophysics," *Modelling Earth Systems and Environments*, vol. 3(18), 2017.

[80] The Engineering Toolbox, "Coefficients of linear thermal expansion," Available at: https://www.engineeringtoolbox.com/linear-expansion-coefficients-d_95.html, Last Accessed: 19.09.21.

[81] ——, "Young's Modulus, Tensile Strength and Yield Strength Values for some Materials," Available at: https://www.engineeringtoolbox.com/young-modulus-d_417.html, Last Acessed: 17.08.21.

[82] Aalco, "Aluminium Alloy 6082 T6 T651 Plate," Available at:https://www.aalco.co.uk/datasheets/Aluminium-Alloy_6082-T6~T651_148.ashx, Last Accessed: 20.01.22.

[83] N. Aluminium, "Alloy Data Sheet EN-AW6082," Available at:https://www.nedal.com/wp-content/uploads/2016/11/Nedal-alloy-Datasheet-EN-AW-6082.pdf?fbclid=IwAR0J7toAY5Sk-aFcT8v5zSASMjoLLTwaYE0Vu_R4rfAQJPZcac7FV8x2zkE, Last Accessed: 11.05.22.

[84] E. N. Mosland, *Personal communication*, PhD candidate, University of Bergen, Dept. of Physics and Technology, Bergen, Norway, 2022.

[85] B. Ghose, K. Balasubramaniam, C. V. Krishnamurthy, and A. Subhananda Rao, "Two Dimensional FEM Simulation of Ultrasonic Wave Propagation in Isotropic Solid Media using COMSOL," in *Proc. of the COMSOL Conference 2010 India*, October 7-9 2010.

[86] D. Wotzka, D. Zmarzły, and T. Boczar, "Numerical Simulation of Acoustic Wave Propagating in a Spherical Object Filled with Insulating Oil," *Acta Physica Polonica*, vol. 118 (6), pp. 1272–1275, 2010.

[87] COMSOL Inc., "Comsol Multiphysics, Version 5.6, Structural Mechanics User's Guide," Stockholm, Sweden.

[88] R. Kazys, L. Mazeika, R. Barauskas, E. Jasiuniene, and V. Daniulaitis, "Evaluation of diffraction errors in precise pulse-echo measurements of ultrasound velocity in chambers with waveguide," *Ultrasonics*, vol. 40, pp. 853–858, 2002.

[89] P. Lunde, "PHYS374- Theoretical Acoustics," *University of Bergen, Dept. of Physics and Technology, Bergen, Norway*, 2008.

[90] P. Lunde, K.-E. Frøysa, and M. Vestrheim, "GARUSO - Version 1.0. Uncertainty model for Multipath Ultrasonic Transit Time Gas Flow Meters," Christian Michelsen Research AS, Bergen, Norway, Tech. Rep. CMR-97-A10014, Sept 1997.

[91] ISO, *Guide to the expression of uncertainty in measurement (GUM)* . Geneva, Switzerland: International Organisation for Standardisation, First edition, 1995, ISBN 92-67-10188-9.

[92] Olympus IMS, "Material sound velocities," Available at: https://www.olympus-ims.com/en/ndt-tutorials/thickness-gauge/appendices-velocities/, Last Accessed: 15.09.21.

[93] E. Bjørndal and K.-E. Frøysa, "Acoustic Methods for Obtaining the Pressure Reflection Coefficient from a Buffer Rod Based measurement Cell," *IEEE Transactions on Ultrasonic, Ferroelectric, and frequency Control*, vol. 55 (8), pp. 1781–1793, 2008.

[94] Acromag, "Criteria for Temperature Sensor Selection of T/C and RTD Sensor Types - The Basics of Temperature Measurement using RTDs," Tech. Rep., Wixom, USA, 8500-917A.

[95] Fluke Corporation, "Fluke 1586A Super-DAQ Precision Temperature Scanner," Available at: https://www.fluke.com/en-us/product/calibration-tools/temperature-calibrators/fluke-calibration-1586a, Last Accessed: 05.05.2022.

[96] Dracal Technologies, "USB 2/3 Wire RTD Sensor To USB Adapter ," Available at: https://www.dracal.com/wp-content/uploads/2021/09/Dracal-RTD_23-Datasheet.pdf, Last Accessed: 27.04.2022.

[97] MeterLab, "CMD210 Conductivity meter- Operating instructions," Available at: https://pdf.indiamart.com/impdf/24943910855/MY-96244901/meterlab-cmd-210-conductivity-meter.pdf, Last Accessed: 20.04.2022.

[98] J. Yan, W. M. D. Wright, J. A. O'Mahony, Y. Roos, E. Cuijpers, and S. M. van Ruth, "A sound approach: Exploring a rapid and non-destructive ultrasonic pulse echo system for vegetable oils characterization," *Food Research International*, vol. 125, pp. 1–9, 2019.

[99] D. J. McClements and M. J. W. Povey, "Ultrasonic Velocity Measurements in Some Liquid Triglycerides and Vegetable Oils," *Journal of the American Oil Chemists' Society*, vol. 65 (11), pp. 1787–1790, 1988.

[100] V. A. Belogol'skii, S. S. Sekoyan, L. M. Samorukova, S. R. Stefanov, and V. I. Levtsov, "Acoustical measurements - pressure dependence of the sound velocity in distilled water," *Measurement Techniques*, vol. 42(4), pp. 406–413, 1999.

[101] T. Sankarappa, M. Kumar, and A. Ahmad, "Ultrasound velocity and density studies in some refined and unrefined edible oils," *Physics and Chemistry of liquids*, vol. 43 (6), pp. 507–514, 2005.

[102] Z. Wang, "Wave velocities in Hydrocarbons and Hydrocarbon saturated rocks - with application to EOR monitoring," Ph.D. dissertation, Standford University- Dept. of Geophysics, California, USA, Apr. 1988.

[103] P. H. Rogers and A. L. Van Buren, "An exact expression for the Lommel-diffraction correction integral," *The Journal of the Acoustical Society of America*, vol. 55(4), pp. 724–728, 1974.

Appendix A

Numerical diffraction correction calculations

A.1 Numerical solution of Khimunin's diffraction correction integral

As part of this project, Khimunin's diffraction correction integral (BPDF model) is utilized to calculate diffraction correction, shown in Sec. 2.3.1. To confirm that the calculations used in this project are correct, the tabulated data of Khimunin is compared to the calculated data, using MatLab. This section describes the approach and the resulting numerical values. The script used to calculate the numerical values is found in Ap. D.5.

For a single fluid medium, Khimunin expressed the deviation from plane-wave propagation for a uniformly vibrating plane piston as [38]

$$H^{diff} = \frac{\langle p \rangle_A}{p^{plane}}, \tag{A.1}$$

where p^{plane} is the plane-wave pressure at distance z = d, and $\langle p \rangle_A$ is the average sound pressure over the measurement area (in the absence of the receiver) at distance z = d, with area equal to the sound source, $A = \pi a^2$.

Based on Williams theory for a baffled piston [42], Khimunin formulated the equation [38]

$$H^{diff}(L,f) = 1 - \frac{4}{\pi}\int_0^{\pi/2} e^{-ikL\left(\sqrt{1+4(\frac{a}{L})^2 cos^2\theta}-1\right)} sin^2\theta d\theta. \tag{A.2}$$

Here, the plane wave expression has been extracted, $k = \omega/c$ is the wave number, a is the radius of the transducer and θ is an integration variable. Khimunin further expressed the modulus of ratio of the average pressure to the pressure of the continuous plane wave [38]

$$|H_{diff}| = \frac{\langle p(L,f) \rangle_A}{p_p(L,f)} = \sqrt{A^2 + B^2}, \tag{A.3}$$

where A and B is stated as

$$A = 1 - C\frac{4}{\pi}cos(kL) - D\frac{4}{\pi}sin(kL), \tag{A.4}$$

$$B = D\frac{4}{\pi}cos(kL) - C\frac{4}{\pi}sin(kL). \tag{A.5}$$

In equations A.4 and A.5, the constants C and D are expressed as

$$C = \int_0^{\pi/2} cos[k\sqrt{L^2 + 4a^2cos^2\theta}]sin^2\theta d\theta, \tag{A.6}$$

$$D = \int_0^{\pi/2} sin[k\sqrt{L^2 + 4a^2cos^2\theta}]sin^2\theta d\theta, \tag{A.7}$$

where L is the distance between transmitter and receiver.

Equations A.4 and A.5 were further used to calculate the deviation of phase of average pressure from the phase of plane wave pressure [43]

$$\angle H_{diff} = \phi = tan^{-1}\left(\frac{B}{A}\right) \tag{A.8}$$

To calculate the amplitude and phase, equations A.6 and A.7 must be solved numerically. To do so, Simpsons integration method is utilized [73]

$$\int_a^b f(x)dx \approx \frac{\Delta x}{3}[y_0 + 4(y_1 + y_3 + y_5 + ..) + 2(y_2 + y_4 + y_6 + ...) + y_n] \tag{A.9}$$

The Simpsons method is thus based on a subdivision of the interval [a,b] into n subintervals. Each subinterval is of equal length $\Delta x = (b-a)/n$ [73]. To calculate equations A.6 and A.7, $\Delta x = d\theta = \pi/2n$ must be determined. Using MatLab and comparing the results with [38], n = 1000 was found to be sufficient for the diffraction integral to converge.

In order to compare the calculated values with those tabulated by Khimunin, some small modifications were needed. Khimunin used the rounded off ka-values to calculate the tabulated data (table 1 in [38, 43]). The exact values were therefore determined by the Fresnel parameter [44]

$$S = \frac{2\pi z}{ka^2} \tag{A.10}$$

Equation A.10 was solved for k, where z is found by the rounded off ka-values. Thus, if ka = 20, a = 10mm and S = 1, z is calculated to be 31.8mm ≈ 32mm using equation A.10. Then, by inserting the rounded off z-value into $k = 2\pi z/(Sa^2)$, the exact wave number k = 2.01062 mm^{-1} is found and thus is the exact ka-number given as ka = 20.106. Khimunin uses the rounded of ka-values = [10, 15, 20, 25, 30, 40, 60, 100, 200, 400, 1000] and S-values from 0.01 to 10. The amplitude and phase calculations are therefore done for the same ka-numbers and S-values using MatLab. A synopsis of the calculated amplitude and phase is presented in table A.1 and table A.3 respectively, and Khimunin's tabulated amplitude and phase data is presented in tables A.2 and A.4

Khimunin reports an uncertainty using the Simpsons method of $1 \cdot 10^{-4}$. The difference between Khimunin's tabulated data and the calculated data using MatLab is within the uncertainty with a few exceptions. The excess difference is believed to be rounding errors.

In the project, equation A.2 is implemented. It was therefore necessary to see how the amplitude and phase would vary using equation A.2 directly compared to the method described above. Equation A.2 is implemented in MatLab, where the integral is evaluated using the Simpsons integration method with n = 1000. The amplitude and phase is calculated and compared to the calculated amplitude and phase in table A.1 and A.3 respectively. The difference is, at most, found to be $1.3 \cdot 10^{-4}$ and $9.223 \cdot 10^{-4}$ rad for the amplitude and phase respectively. The difference due to the method used to calculate the amplitude and phase of the diffraction correction is thus negligible.

Table A.1: Synopsis of the calculated amplitude of the BPDF model, using equation A.3 and Simpsons integration method. The ka-values are rounded off, exact values are used in the calculations.

	ka										
S	**10**	**15**	**20**	**25**	**30**	**40**	**60**	**100**	**200**	**400**	**1000**
0.05	0.97128	0.95467	0.96250	0.95141	0.95153	0.95456	0.95142	0.95134	0.95120	0.95103	0.95077
0.1	0.96040	0.93075	0.93034	0.93261	0.93233	0.93008	0.93212	0.93072	0.93089	0.93116	0.93173
0.15	0.94731	0.92835	0.92272	0.92293	0.92111	0.91845	0.91869	0.91663	0.91746	0.91630	0.91596
0.2	0.92906	0.91902	0.91032	0.90184	0.90750	0.90699	0.90393	0.90399	0.90552	0.90549	0.90525
0.25	0.90741	0.89689	0.88980	0.90020	0.89142	0.89370	0.89616	0.89341	0.89557	0.89513	0.89493
0.3	0.88616	0.87862	0.89044	0.88365	0.88993	0.88223	0.88629	0.88232	0.88437	0.88504	0.88521
0.35	0.86897	0.87441	0.88457	0.87514	0.87333	0.88052	0.87322	0.87493	0.87700	0.87745	0.87756
0.4	0.85799	0.87744	0.86573	0.87598	0.86939	0.86431	0.87051	0.87149	0.87047	0.87009	0.86998
0.45	0.85333	0.87617	0.85517	0.86058	0.86687	0.86406	0.85778	0.85677	0.85725	0.85746	0.85752
0.5	0.85344	0.86601	0.85719	0.84786	0.85019	0.85691	0.85913	0.85792	0.85690	0.85661	0.85652
0.55	0.85601	0.85016	0.85861	0.84894	0.84310	0.84172	0.84480	0.84725	0.84830	0.84856	0.84863
0.6	0.85872	0.83494	0.85084	0.85085	0.84643	0.84023	0.83660	0.83564	0.83550	0.83549	0.83548
0.65	0.85981	0.82511	0.83639	0.84345	0.84476	0.84298	0.83975	0.83764	0.83670	0.83647	0.83640
0.7	0.85821	0.82191	0.82251	0.82936	0.83356	0.83677	0.83774	0.83765	0.83747	0.83742	0.83740
0.75	0.85358	0.82357	0.81447	0.81641	0.81939	0.82329	0.82623	0.82764	0.82819	0.82832	0.82836
0.8	0.84610	0.82707	0.81305	0.80974	0.80966	0.81101	0.81283	0.81400	0.81454	0.81467	0.81471
0.85	0.83631	0.82964	0.81576	0.80950	0.80689	0.80525	0.80481	0.80486	0.80494	0.80497	0.80498
0.9	0.82495	0.82951	0.81920	0.81269	0.80909	0.80577	0.80370	0.80279	0.80244	0.80235	0.80233
0.95	0.81282	0.82602	0.82071	0.81580	0.81260	0.80917	0.80666	0.80538	0.80485	0.80471	0.80468
1	0.80069	0.81934	0.81894	0.81642	0.81438	0.81188	0.80985	0.80874	0.80825	0.80813	0.80810
1.1	0.77888	0.79951	0.80560	0.80728	0.80775	0.80785	0.80768	0.80751	0.80741	0.80739	0.80738
1.2	0.76296	0.77736	0.78472	0.78809	0.78983	0.79145	0.79251	0.79302	0.79323	0.79328	0.79330
1.3	0.75398	0.75896	0.76412	0.76702	0.76871	0.77044	0.77170	0.77235	0.77263	0.77270	0.77271
1.4	0.75123	0.74729	0.74898	0.75038	0.75131	0.75235	0.75316	0.75360	0.75379	0.75383	0.75385
1.5	0.75306	0.74251	0.74097	0.74077	0.74081	0.74095	0.74112	0.74123	0.74128	0.74129	0.74130
1.6	0.75761	0.74315	0.73932	0.73787	0.73719	0.73658	0.73620	0.73602	0.73594	0.73593	0.73592
1.7	0.76329	0.74720	0.74209	0.73989	0.73875	0.73766	0.73691	0.73653	0.73637	0.73633	0.73632
1.8	0.76888	0.75280	0.74723	0.74470	0.74335	0.74202	0.74109	0.74061	0.74041	0.74036	0.74035
1.9	0.77356	0.75853	0.75305	0.75050	0.74912	0.74774	0.74676	0.74625	0.74604	0.74599	0.74597
2	0.77688	0.76344	0.75839	0.75600	0.75469	0.75338	0.75244	0.75196	0.75175	0.75170	0.75169
2.1	0.77860	0.76698	0.76252	0.76039	0.75921	0.75803	0.75718	0.75675	0.75656	0.75652	0.75650
2.2	0.77868	0.76888	0.76507	0.76324	0.76223	0.76120	0.76047	0.76009	0.75993	0.75989	0.75987
2.3	0.77716	0.76910	0.76593	0.76439	0.76354	0.76268	0.76206	0.76174	0.76161	0.76157	0.76156
2.4	0.77419	0.76769	0.76511	0.76385	0.76315	0.76245	0.76194	0.76168	0.76157	0.76154	0.76153
2.5	0.76989	0.76478	0.76272	0.76172	0.76116	0.76060	0.76019	0.75998	0.75989	0.75987	0.75986
2.6	0.76446	0.76054	0.75894	0.75816	0.75772	0.75728	0.75696	0.75679	0.75672	0.75670	0.75670
2.7	0.75803	0.75513	0.75393	0.75334	0.75300	0.75267	0.75242	0.75230	0.75224	0.75223	0.75223
2.8	0.75079	0.74874	0.74787	0.74744	0.74719	0.74695	0.74677	0.74667	0.74663	0.74663	0.74662
2.9	0.74285	0.74152	0.74093	0.74063	0.74047	0.74029	0.74017	0.74010	0.74007	0.74007	0.74007
3	0.73437	0.73363	0.73327	0.73308	0.73298	0.73287	0.73279	0.73274	0.73273	0.73272	0.73272
3.5	0.68719	0.68811	0.68840	0.68853	0.68859	0.68866	0.68870	0.68873	0.68874	0.68874	0.68874
4	0.63812	0.63952	0.64001	0.64023	0.64035	0.64047	0.64055	0.64059	0.64061	0.64062	0.64062
4.5	0.59147	0.59291	0.59341	0.59364	0.59377	0.59389	0.59398	0.59403	0.59405	0.59405	0.59405
5	0.54882	0.55013	0.55059	0.55080	0.55091	0.55103	0.55111	0.55115	0.55117	0.55118	0.55118
5.5	0.51047	0.51161	0.51201	0.51220	0.51230	0.51240	0.51247	0.51251	0.51252	0.51253	0.51253
6	0.47622	0.47720	0.47754	0.47770	0.47779	0.47787	0.47794	0.47797	0.47798	0.47798	0.47798
6.5	0.44568	0.44651	0.44681	0.44694	0.44702	0.44709	0.44714	0.44717	0.44718	0.44718	0.44718
7	0.41842	0.41913	0.41938	0.41949	0.41955	0.41962	0.41966	0.41968	0.41969	0.41970	0.41970
7.5	0.39402	0.39462	0.39483	0.39493	0.39499	0.39504	0.39508	0.39510	0.39511	0.39511	0.39511
8	0.37211	0.37262	0.37280	0.37289	0.37293	0.37298	0.37301	0.37303	0.37303	0.37304	0.37304
8.5	0.35235	0.35280	0.35295	0.35303	0.35306	0.35310	0.35313	0.35315	0.35315	0.35315	0.35315
9	0.33448	0.33487	0.33500	0.33506	0.33510	0.33513	0.33516	0.33517	0.33517	0.33517	0.33517
9.5	0.31826	0.31859	0.31870	0.31876	0.31879	0.31882	0.31884	0.31885	0.31885	0.31886	0.31886
10	0.30347	0.30376	0.30386	0.30390	0.30393	0.30396	0.30397	0.30398	0.30399	0.30399	0.30399

Table A.2: Synopsis of table 1 in [38], the tabulated amplitude values versus the dimensionless distance S. Ka-values are rounded off.

	ka										
S	**10**	**15**	**20**	**25**	**30**	**40**	**60**	**100**	**200**	**400**	**1000**
0.05	0.9713	0.9547	0.9625	0.9514	0.9517	0.9546	0.9514	0.9514	0.9512	0.9511	0.9509
0.1	0.9605	0.9308	0.9304	0.9327	0.9324	0.9301	0.9323	0.9308	0.9308	0.9312	0.9318
0.15	0.9473	0.9284	0.9228	0.9229	0.9216	0.9185	0.9188	0.9164	0.9175	0.9165	0.9161
0.2	0.9292	0.9191	0.9104	0.9010	0.9075	0.9068	0.9040	0.9040	0.9056	0.9055	0.9053
0.25	0.9075	0.8969	0.8899	0.9003	0.8914	0.8937	0.8962	0.8937	0.8956	0.8952	0.8950
0.3	0.8862	0.8787	0.8905	0.8837	0.8900	0.8823	0.8863	0.8824	0.8844	0.8851	0.8853
0.35	0.8690	0.8744	0.8846	0.8752	0.8732	0.8809	0.8735	0.8750	0.8770	0.8775	0.8776
0.4	0.8581	0.8774	0.8657	0.8760	0.8685	0.8644	0.8705	0.8713	0.8705	0.8701	0.8701
0.45	0.8534	0.8762	0.8552	0.8606	0.8669	0.8642	0.8578	0.8568	0.8573	0.8577	0.8577
0.5	0.8533	0.8660	0.8572	0.8480	0.8502	0.8569	0.8592	0.8580	0.8569	0.8566	0.8566
0.55	0.8560	0.8501	0.8586	0.8490	0.8431	0.8417	0.8449	0.8473	0.8483	0.8486	0.8487
0.6	0.8587	0.8350	0.8509	0.8509	0.8465	0.8403	0.8367	0.8357	0.8352	0.8355	0.8356
0.65	0.8598	0.8252	0.8367	0.8435	0.8447	0.8430	0.8398	0.8367	0.8367	0.8365	0.8364
0.7	0.8582	0.8219	0.8225	0.8294	0.8336	0.8368	0.8377	0.8376	0.8374	0.8374	0.8375
0.75	0.8536	0.8236	0.8146	0.8166	0.8194	0.8233	0.8262	0.8277	0.8282	0.8283	0.8284
0.8	0.8461	0.8271	0.8131	0.8098	0.8097	0.8111	0.8128	0.8140	0.8146	0.8147	0.8147
0.85	0.8363	0.8297	0.8158	0.8096	0.8069	0.8052	0.8048	0.8049	0.8048	0.8050	0.8050
0.9	0.8250	0.8296	0.8192	0.8127	0.8092	0.8058	0.8038	0.8028	0.8024	0.8024	0.8024
0.95	0.8129	0.8262	0.8207	0.8158	0.8127	0.8092	0.8068	0.8054	0.8049	0.8046	0.8048
1	0.8007	0.8194	0.8190	0.8165	0.8144	0.8119	0.8097	0.8088	0.8083	0.8082	0.8082
1.1	0.7789	0.7996	0.8056	0.8074	0.8077	0.8079	0.8077	0.8076	0.8074	0.8074	0.8074
1.2	0.7632	0.7774	0.7847	0.7882	0.7899	0.7915	0.7927	0.7930	0.7933	0.7933	0.7933
1.3	0.7541	0.7591	0.7642	0.7671	0.7690	0.7706	0.7717	0.7724	0.7727	0.7727	0.7727
1.4	0.7513	0.7474	0.7490	0.7503	0.7514	0.7525	0.7532	0.7536	0.7538	0.7538	0.7538
1.5	0.7531	0.7425	0.7409	0.7408	0.7409	0.7410	0.7412	0.7413	0.7413	0.7413	0.7413
1.6	0.7577	0.7432	0.7393	0.7379	0.7373	0.7366	0.7362	0.7361	0.7358	0.7360	0.7360
1.7	0.7633	0.7473	0.7421	0.7399	0.7388	0.7377	0.7369	0.7366	0.7364	0.7364	0.7364
1.8	0.7689	0.7529	0.7473	0.7448	0.7428	0.7421	0.7411	0.7407	0.7405	0.7404	0.7404
1.9	0.7736	0.7586	0.7531	0.7505	0.7491	0.7478	0.7468	0.7463	0.7461	0.7460	0.7461
2	0.7769	0.7635	0.7584	0.7560	0.7547	0.7534	0.7525	0.7520	0.7518	0.7517	0.7517
2.1	0.7786	0.7670	0.7626	0.7604	0.7592	0.7581	0.7573	0.7568	0.7566	0.7565	0.7565
2.2	0.7787	0.7689	0.7652	0.7633	0.7622	0.7613	0.7605	0.7601	0.7599	0.7599	0.7599
2.3	0.7772	0.7691	0.7660	0.7647	0.7636	0.7627	0.7621	0.7618	0.7616	0.7617	0.7616
2.4	0.7740	0.7677	0.7652	0.7639	0.7630	0.7625	0.7620	0.7618	0.7616	0.7616	0.7615
2.5	0.7699	0.7648	0.7628	0.7617	0.7612	0.7606	0.7602	0.7600	0.7599	0.7599	0.7599
2.6	0.7645	0.7605	0.7590	0.7582	0.7577	0.7573	0.7570	0.7568	0.7567	0.7568	0.7567
2.7	0.7580	0.7551	0.7540	0.7533	0.7530	0.7527	0.7525	0.7523	0.7523	0.7522	0.7522
2.8	0.7508	0.7488	0.7479	0.7474	0.7472	0.7470	0.7468	0.7467	0.7464	0.7466	0.7466
2.9	0.7429	0.7415	0.7409	0.7407	0.7405	0.7403	0.7406	0.7398	0.7401	0.7397	0.7401
3	0.7341	0.7336	0.7333	0.7331	0.7330	0.7329	0.7328	0.7328	0.7327	0.7327	0.7327
3.5	0.6972	0.6881	0.6884	0.6883	0.6886	0.6887	0.6886	0.6887	0.6887	0.6888	0.6888
4	0.6380	0.6394	0.6399	0.6406	0.6404	0.6403	0.6406	0.6406	0.6406	0.6406	0.6406
4.5	0.5915	0.5929	0.5934	0.5936	0.5937	0.5939	0.5938	0.5941	0.5941	0.5941	0.5941
5	0.5488	0.5501	0.5504	0.5507	0.5508	0.5511	0.5511	0.5512	0.5512	0.5512	0.5512
5.5	0.5105	0.5117	0.5120	0.5121	0.5122	0.5124	0.5125	0.5125	0.5125	0.5125	0.5125
6	0.4762	0.4772	0.4775	0.4776	0.4778	0.4779	0.4780	0.4780	0.4780	0.4780	0.4780
6.5	0.4456	0.4466	0.4468	0.4469	0.4470	0.4471	0.4472	0.4472	0.4472	0.4472	0.4472
7	0.4184	0.4191	0.4194	0.4195	0.4196	0.4196	0.4196	0.4197	0.4198	0.4198	0.4197
7.5	0.3940	0.3947	0.3949	0.3949	0.3950	0.3950	0.3950	0.3951	0.3951	0.3951	0.3951
8	0.3722	0.3726	0.3728	0.3729	0.3729	0.3729	0.3730	0.3731	0.3731	0.3731	0.3731
8.5	0.3523	0.3529	0.3530	0.3530	0.3531	0.3531	0.3531	0.3532	0.3532	0.3532	0.3532
9	0.3345	0.3348	0.3350	0.3351	0.3351	0.3351	0.3351	0.3352	0.3352	0.3352	0.3352
9.5	0.3183	0.3186	0.3188	0.3188	0.3188	0.3188	0.3188	0.3189	0.3189	0.3189	0.3189
10	0.3035	0.3037	0.3038	0.3039	0.3039	0.3039	0.3040	0.3040	0.3040	0.3040	0.3040

Table A.3: Synopsis of the calculated phase (in radians) of the BPDF model using equation A.8 and Simpsons integration method. The ka-values are rounded off, exact values are used in the calculations.

	ka										
S	**10.053**	**15.079**	**20.106**	**25.133**	**30.159**	**40.212**	**60.319**	**100.53**	**201.06**	**402.12**	**1005.3**
0.05	0.0603	0.0727	0.0574	0.0535	0.0586	0.0537	0.0522	0.0538	0.0531	0.0531	0.0529
0.1	0.0839	0.0780	0.0846	0.0838	0.0819	0.0771	0.0753	0.0766	0.0764	0.0768	0.0762
0.15	0.1116	0.0925	0.0919	0.0943	0.0991	0.0932	0.0956	0.0963	0.0953	0.0942	0.0947
0.2	0.1373	0.1212	0.1209	0.1150	0.1084	0.1093	0.1095	0.1097	0.1118	0.1105	0.1102
0.25	0.1567	0.1417	0.1272	0.1242	0.1291	0.1228	0.1244	0.1277	0.1254	0.1245	0.1243
0.3	0.1677	0.1451	0.1341	0.1463	0.1380	0.1420	0.1366	0.1398	0.1414	0.1413	0.1412
0.35	0.1712	0.1451	0.1589	0.1466	0.1566	0.1512	0.1502	0.1547	0.1544	0.1540	0.1539
0.4	0.1707	0.1559	0.1732	0.1650	0.1580	0.1658	0.1672	0.1627	0.1609	0.1606	0.1605
0.45	0.1701	0.1770	0.1725	0.1839	0.1793	0.1703	0.1714	0.1751	0.1767	0.1771	0.1772
0.5	0.1726	0.1991	0.1770	0.1849	0.1921	0.1921	0.1862	0.1828	0.1817	0.1815	0.1814
0.55	0.1799	0.2141	0.1946	0.1877	0.1910	0.1982	0.2021	0.2025	0.2022	0.2021	0.2020
0.6	0.1920	0.2198	0.2160	0.2041	0.1991	0.1985	0.2016	0.2041	0.2052	0.2055	0.2056
0.65	0.2080	0.2192	0.2306	0.2249	0.2189	0.2125	0.2093	0.2084	0.2083	0.2083	0.2082
0.7	0.2264	0.2179	0.2354	0.2386	0.2370	0.2329	0.2287	0.2264	0.2254	0.2251	0.2251
0.75	0.2455	0.2204	0.2343	0.2424	0.2454	0.2464	0.2456	0.2446	0.2441	0.2440	0.2440
0.8	0.2640	0.2286	0.2336	0.2410	0.2455	0.2497	0.2521	0.2530	0.2533	0.2534	0.2534
0.85	0.2809	0.2421	0.2379	0.2411	0.2443	0.2483	0.2514	0.2531	0.2537	0.2539	0.2539
0.9	0.2952	0.2589	0.2482	0.2468	0.2474	0.2491	0.2510	0.2521	0.2526	0.2528	0.2528
0.95	0.3066	0.2771	0.2632	0.2584	0.2567	0.2558	0.2558	0.2560	0.2561	0.2562	0.2562
1	0.3151	0.2947	0.2807	0.2743	0.2712	0.2685	0.2669	0.2663	0.2660	0.2660	0.2659
1.1	0.3238	0.3230	0.3145	0.3090	0.3058	0.3024	0.2999	0.2986	0.2981	0.2980	0.2979
1.2	0.3247	0.3390	0.3381	0.3361	0.3346	0.3328	0.3313	0.3305	0.3301	0.3301	0.3300
1.3	0.3225	0.3441	0.3489	0.3502	0.3506	0.3508	0.3507	0.3507	0.3506	0.3506	0.3506
1.4	0.3211	0.3429	0.3505	0.3537	0.3553	0.3568	0.3578	0.3582	0.3584	0.3585	0.3585
1.5	0.3233	0.3409	0.3484	0.3520	0.3540	0.3559	0.3573	0.3580	0.3583	0.3584	0.3584
1.6	0.3303	0.3416	0.3475	0.3506	0.3523	0.3540	0.3553	0.3560	0.3563	0.3563	0.3564
1.7	0.3422	0.3471	0.3507	0.3527	0.3539	0.3552	0.3561	0.3566	0.3568	0.3568	0.3569
1.8	0.3584	0.3578	0.3591	0.3600	0.3606	0.3613	0.3618	0.3620	0.3622	0.3622	0.3622
1.9	0.3780	0.3731	0.3725	0.3725	0.3725	0.3726	0.3728	0.3728	0.3729	0.3729	0.3729
2	0.4002	0.3921	0.3901	0.3893	0.3890	0.3887	0.3885	0.3884	0.3883	0.3883	0.3883
2.1	0.4242	0.4140	0.4109	0.4096	0.4090	0.4083	0.4079	0.4077	0.4076	0.4076	0.4076
2.2	0.4494	0.4378	0.4341	0.4324	0.4315	0.4307	0.4301	0.4298	0.4297	0.4296	0.4296
2.3	0.4752	0.4628	0.4587	0.4568	0.4558	0.4548	0.4541	0.4537	0.4536	0.4536	0.4536
2.4	0.5011	0.4885	0.4841	0.4821	0.4811	0.4800	0.4792	0.4789	0.4787	0.4787	0.4786
2.5	0.5270	0.5144	0.5099	0.5079	0.5068	0.5057	0.5049	0.5045	0.5044	0.5043	0.5043
2.6	0.5526	0.5401	0.5357	0.5337	0.5326	0.5315	0.5307	0.5303	0.5302	0.5301	0.5301
2.7	0.5776	0.5656	0.5613	0.5593	0.5582	0.5571	0.5563	0.5559	0.5558	0.5557	0.5557
2.8	0.6021	0.5905	0.5863	0.5844	0.5833	0.5823	0.5816	0.5812	0.5810	0.5810	0.5810
2.9	0.6259	0.6148	0.6108	0.6089	0.6079	0.6069	0.6062	0.6058	0.6057	0.6056	0.6056
3	0.6490	0.6384	0.6346	0.6328	0.6318	0.6309	0.6302	0.6298	0.6297	0.6296	0.6296
3.5	0.7529	0.7449	0.7420	0.7407	0.7400	0.7392	0.7387	0.7385	0.7383	0.7383	0.7383
4	0.8391	0.8332	0.8310	0.8300	0.8295	0.8290	0.8286	0.8284	0.8283	0.8283	0.8283
4.5	0.9106	0.9061	0.9045	0.9037	0.9033	0.9029	0.9026	0.9025	0.9024	0.9024	0.9024
5	0.9702	0.9668	0.9655	0.9650	0.9647	0.9644	0.9641	0.9640	0.9640	0.9640	0.9640
5.5	1.0205	1.0178	1.0169	1.0164	1.0162	1.0159	1.0158	1.0157	1.0156	1.0156	1.0156
6	1.0633	1.0612	1.0604	1.0601	1.0599	1.0597	1.0596	1.0595	1.0595	1.0595	1.0595
6.5	1.1001	1.0985	1.0979	1.0976	1.0974	1.0973	1.0972	1.0971	1.0971	1.0971	1.0971
7	1.1322	1.1308	1.1303	1.1301	1.1300	1.1298	1.1298	1.1297	1.1297	1.1297	1.1297
7.5	1.1602	1.1591	1.1587	1.1585	1.1584	1.1583	1.1582	1.1582	1.1582	1.1582	1.1581
8	1.1849	1.1840	1.1836	1.1835	1.1834	1.1833	1.1833	1.1832	1.1832	1.1832	1.1832
8.5	1.2069	1.2061	1.2058	1.2057	1.2056	1.2056	1.2055	1.2055	1.2055	1.2055	1.2055
9	1.2265	1.2259	1.2256	1.2255	1.2255	1.2254	1.2254	1.2253	1.2253	1.2253	1.2253
9.5	1.2442	1.2436	1.2434	1.2433	1.2433	1.2432	1.2432	1.2432	1.2432	1.2431	1.2431
10	1.2601	1.2596	1.2595	1.2594	1.2593	1.2593	1.2593	1.2593	1.2592	1.2592	1.2592

Table A.4: Synopsis of table 1 in [43], the tabulated diffraction phase shifts (in radians) versus the dimensionless distance S. Ka-values are rounded off.

	ka										
S	**10.053**	**15.079**	**20.106**	**25.133**	**30.159**	**40.212**	**60.319**	**100.53**	**201.06**	**402.12**	**1005.3**
0.05	0.0604	0.0727	0.0575	0.0535	0.0584	0.0537	0.0523	0.0538	0.0532	0.053	0.053
0.1	0.0839	0.078	0.0846	0.0836	0.0819	0.0771	0.0753	0.0765	0.0762	0.0767	0.0762
0.15	0.1116	0.0925	0.0919	0.0943	0.0991	0.0931	0.0956	0.0962	0.0953	0.0941	0.0947
0.2	0.1373	0.1212	0.1209	0.1154	0.1084	0.1094	0.1094	0.1097	0.1119	0.1105	0.1101
0.25	0.1566	0.1416	0.1271	0.1243	0.1291	0.1228	0.1243	0.1275	0.1254	0.1245	0.1243
0.3	0.1677	0.1451	0.1341	0.1463	0.138	0.1421	0.1366	0.1398	0.1415	0.1413	0.1412
0.35	0.1713	0.1451	0.1589	0.1466	0.1572	0.1505	0.1505	0.1547	0.1543	0.154	0.1535
0.4	0.1707	0.1559	0.1732	0.165	0.1581	0.1657	0.1673	0.1625	0.1608	0.1606	0.1605
0.45	0.1701	0.177	0.1725	0.1839	0.1793	0.1703	0.1714	0.1751	0.1767	0.1769	0.1772
0.5	0.1727	0.1991	0.177	0.1848	0.192	0.1921	0.1862	0.1828	0.1817	0.1815	0.1814
0.55	0.18	0.2141	0.1946	0.1877	0.1909	0.1981	0.2022	0.2024	0.202	0.2021	0.202
0.6	0.1921	0.2197	0.216	0.2041	0.1991	0.1985	0.2016	0.2041	0.2056	0.2055	0.2056
0.65	0.208	0.2193	0.2308	0.2251	0.2186	0.2126	0.2093	0.2084	0.2083	0.2082	0.2082
0.7	0.2264	0.218	0.2354	0.2386	0.237	0.2329	0.2287	0.2264	0.2254	0.2252	0.2251
0.75	0.2454	0.2204	0.2343	0.2423	0.2453	0.2464	0.2455	0.2446	0.2441	0.2439	0.2439
0.8	0.2264	0.2286	0.2336	0.2411	0.2455	0.2497	0.2521	0.2535	0.2533	0.2535	0.2534
0.85	0.2808	0.2421	0.2379	0.2411	0.2443	0.2483	0.2514	0.2531	0.2539	0.2539	0.2539
0.9	0.2954	0.2589	0.2482	0.2468	0.2474	0.2491	0.251	0.2521	0.2528	0.2528	0.2528
0.95	0.3066	0.277	0.2632	0.2584	0.2567	0.2558	0.2555	0.256	0.2561	0.2562	0.2563
1	0.3149	0.2946	0.2806	0.2743	0.2712	0.2685	0.2668	0.2663	0.266	0.266	0.2659
1.1	0.3237	0.3229	0.3144	0.309	0.3061	0.3024	0.2999	0.2986	0.2981	0.2979	0.2979
1.2	0.3248	0.3389	0.3381	0.336	0.3345	0.3327	0.3314	0.3305	0.3301	0.3301	0.33
1.3	0.3222	0.344	0.3489	0.3502	0.3505	0.3508	0.3508	0.3507	0.3505	0.3506	0.3505
1.4	0.3211	0.3429	0.3505	0.3536	0.3554	0.3565	0.3578	0.3582	0.3584	0.3584	0.3586
1.5	0.3233	0.3409	0.3484	0.352	0.3539	0.3559	0.3573	0.3579	0.3583	0.3584	0.3584
1.6	0.3302	0.3418	0.3475	0.3505	0.3522	0.354	0.3553	0.356	0.3562	0.3564	0.3565
1.7	0.3421	0.3471	0.3507	0.3527	0.3539	0.3551	0.356	0.3566	0.3568	0.3569	0.3568
1.8	0.3583	0.3577	0.3591	0.36	0.3611	0.3613	0.3617	0.362	0.3623	0.3622	0.3622
1.9	0.3779	0.373	0.3725	0.3724	0.3725	0.3726	0.3727	0.3728	0.3728	0.3728	0.3729
2	0.4002	0.3925	0.3901	0.3893	0.389	0.3886	0.3884	0.3884	0.3884	0.3884	0.3884
2.1	0.4242	0.4139	0.411	0.4096	0.4089	0.4084	0.4089	0.4077	0.4076	0.4075	0.4076
2.2	0.4494	0.4378	0.4341	0.4324	0.4315	0.4307	0.4302	0.4298	0.4297	0.4296	0.4297
2.3	0.4751	0.4628	0.4587	0.4569	0.4558	0.4548	0.4541	0.4538	0.4536	0.4536	0.4536
2.4	0.5016	0.4884	0.4842	0.4821	0.4812	0.48	0.4792	0.4788	0.4787	0.4786	0.4786
2.5	0.527	0.5143	0.5099	0.5079	0.5098	0.5056	0.5049	0.5045	0.5044	0.5043	0.5043
2.6	0.5525	0.5401	0.5357	0.5338	0.5326	0.5315	0.5307	0.5304	0.5301	0.5301	0.53
2.7	0.5776	0.5655	0.5612	0.5592	0.5582	0.5571	0.5564	0.5559	0.5558	0.5557	0.5557
2.8	0.6021	0.5905	0.5863	0.5843	0.5833	0.5823	0.5815	0.5812	0.5814	0.581	0.5809
2.9	0.6259	0.6148	0.6108	0.609	0.6079	0.6069	0.6053	0.6057	0.6056	0.6055	0.6056
3	0.6488	0.6383	0.6346	0.6328	0.6318	0.6309	0.6302	0.6298	0.6297	0.6296	0.6296
3.5	0.7529	0.7449	0.742	0.7404	0.7399	0.7392	0.7384	0.7384	0.7383	0.7383	0.7383
4	0.8394	0.8328	0.8309	0.8299	0.8295	0.8291	0.8286	0.8283	0.8283	0.8283	0.8283
4.5	0.9105	0.9061	0.9043	0.9036	0.9033	0.9027	0.9028	0.9025	0.9024	0.9024	0.9024
5	0.9702	0.9668	0.9658	0.9649	0.9644	0.9641	0.964	0.964	0.964	0.964	0.964
5.5	1.0204	1.0178	1.0169	1.0165	1.0164	1.0159	1.0156	1.0157	1.0156	1.0156	1.0156
6	1.0631	1.0612	1.0604	1.0602	1.0601	1.0597	1.0599	1.0595	1.0595	1.0595	1.0595
6.5	1.1	1.0983	1.0979	1.0977	1.0974	1.0975	1.0972	1.0971	1.0971	1.0971	1.0971
7	1.132	1.1308	1.1301	1.1303	1.1299	1.1301	1.1298	1.1298	1.1297	1.1297	1.1299
7.5	1.1602	1.1589	1.1587	1.1587	1.1584	1.1583	1.1583	1.1583	1.1583	1.1583	1.1583
8	1.185	1.184	1.1835	1.1834	1.1832	1.1833	1.1834	1.1834	1.1834	1.1834	1.1843
8.5	1.2068	1.206	1.2059	1.2055	1.2057	1.2054	1.2056	1.2055	1.2055	1.2055	1.2055
9	1.2266	1.2258	1.2255	1.2254	1.2255	1.2254	1.2254	1.2254	1.2254	1.2254	1.2254
9.5	1.2443	1.2435	1.2434	1.2432	1.2433	1.2431	1.243	1.2432	1.2432	1.2432	1.2432
10	1.2602	1.2596	1.2595	1.2593	1.2594	1.2594	1.2593	1.2593	1.2593	1.2592	1.2592

Appendix B

The UNESCO equation

The UNESCO equation is given by [31]

$$c(S,T,P) = Cw(T,P) + A(T,P)\cdot S + B(T,P)\cdot S^{3/2} + D(T,P)\cdot S^2 \tag{B.1}$$

Where the coefficients are given by

$$\begin{aligned} Cw(T,P) = &\left(C_{00} + C_{01}\cdot T + C_{02}\cdot T^2 + C_{03}\cdot T^3 + C_{04}\cdot T^4 + c_{05}\cdot T^5\right) \\ &+\left(C_{10} + C_{11}\cdot T + C_{12}\cdot T^2 + C_{13}\cdot T^3 + C_{14}\cdot T^4\right)\cdot P \\ &+\left(C_{20} + C_{21}\cdot T + C_{22}\cdot T^2 + C_{23}\cdot T^3 + C_{24}\cdot T^4\right)\cdot P^2 + \left(C_{30} + C_{31}\cdot T + C_{32}\cdot T^2\right)\cdot P^3 \end{aligned}$$

$$\begin{aligned} A(T,P) = &\left(A_{00} + A_{01}\cdot T + A_{02}\cdot T^2 + A_{03}\cdot T^3 + A_{04}\cdot T^4\right) + \left(A_{10} + A_{11}\cdot T + A_{12}\cdot T^2 + A_{13}\cdot T^3 + A_{14}\cdot T^4\right)\cdot P \\ &+\left(A_{20} + A_{21}\cdot T + A_{22}\cdot T^2 + A_{23}\cdot T^3\right)\cdot P^2 + \left(A_{30} + A_{31}\cdot T + A_{32}\cdot T^2\right)\cdot P^3 \end{aligned}$$

$$B(T,P) = B_{00} + B_{01}\cdot T + \left(B_{10} + B_{11}\cdot T\right)\cdot P$$

$$D(T,P) = D_{00} + D_{10}\cdot P$$

The numerical values are given in table B.1.

Table B.1: Numerical values for the UNESCO equation

Coefficients	Numerical values	Coefficients	Numerical values
C_{00}	1402.388	A_{02}	$7.166 \cdot 10^{-5}$
C_{01}	5.03830	A_{03}	$2.008 \cdot 10^{-6}$
C_{02}	-5.81090·10^{-2}	A_{04}	$-3.21 \cdot 10^{-8}$
C_{03}	3.3432·10^{-4}	A_{10}	$9.4742 \cdot 10^{-5}$
C_{04}	-1.47797·10^{-6}	A_{11}	-1.2583·10^{-5}
C_{05}	3.1419·10^{-9}	A_{12}	-6.4928·10^{-8}
C_{10}	0.153563	A_{13}	1.0515·10^{-8}
C_{11}	$6.8999 \cdot 10^{-4}$	A_{14}	-2.0142·10^{-10}
C_{12}	-8.1829·10^{-6}	A_{20}	-3.9064·10^{-7}
C_{13}	1.3632·10^{-7}	A_{21}	9.1061·10^{-9}
C_{14}	-6.1260·10^{-10}	A_{22}	-1.6009·10^{-10}
C_{20}	3.1260·10^{-5}	A_{23}	7.994·10^{-12}
C_{21}	-1.7111·10^{-6}	A_{30}	1.100·10^{-10}
C_{22}	2.5986·10^{-8}	A_{31}	6.651·10^{-12}
C_{23}	-2.5353·10^{-10}	A_{32}	-3.391·10^{-13}
C_{24}	1.0415·10^{-12}	B_{00}	-1.922·10^{-2}
C_{30}	-9.7729·10^{-9}	B_{01}	-4.42·10^{-5}
C_{31}	3.8513·10^{-10}	B_{10}	7.3637·10^{-5}
C_{32}	-2.3654·10^{-12}	B_{11}	1.7950·10^{-7}
A_{00}	1.389	D_{00}	1.727·10^{-3}
A_{01}	-1.262·10^{-2}	D_{10}	-7.9836·10^{-6}

B.1 Partial derivative of the UNESCO equation

To calculate the uncertainty in the UNESCO equation, equation B.1 must be differentiated with respect to salinity (S), temperature (T) and pressure (P). The equations are presented below, where the tabulated values are found in table B.1.

Salinity

The sound velocity differentiated with respect to salinity is given as

$$\frac{\partial c}{\partial S} = A(T,P) + \frac{3}{2} \cdot B(T,P) \cdot S^{1/2} + 2 \cdot D(T,P) \cdot S, \tag{B.2}$$

where the equations for A(T,P), B(T,P) and D(T,P) are given above.

Temperature

The sound velocity differentiated with respect to temperature is given as

$$\frac{\partial c}{\partial T} = \frac{\partial CW}{T} + \frac{\partial A}{\partial T} \cdot S + \frac{\partial B}{\partial T} \cdot S^{3/2} + \frac{\partial D}{\partial T}. \tag{B.3}$$

Where

$$\begin{aligned}\frac{\partial Cw}{\partial T} = &\left(C_{01} + 2 \cdot C_{02} \cdot T + 3 \cdot C_{03} \cdot T^2 + 4 \cdot C_{04} \cdot T^3 + 5 \cdot c_{05} \cdot T^4\right) \\ &+\left(C_{11} + 2 \cdot C_{12} \cdot T + 3 \cdot C_{13} \cdot T^2 + 4 \cdot C_{14} \cdot T^3\right) \cdot P \\ &+\left(C_{21} + 2 \cdot C_{22} \cdot T + 3 \cdot C_{23} \cdot T^2 + 4 \cdot C_{24} \cdot T^3\right) \cdot P^2 + \left(C_{31} + 2 \cdot C_{32} \cdot T\right) \cdot P^3.\end{aligned}$$

$$\begin{aligned}\frac{\partial A}{\partial T} = &\left(A_{01} \cdot T + 2 \cdot A_{02} \cdot T + 3 \cdot A_{03} \cdot T^2 + 4 \cdot A_{04} \cdot T^3\right) + \left(A_{11} + 2 \cdot A_{12} \cdot T + 3 \cdot A_{13} \cdot T^2 + 4 \cdot A_{14} \cdot T^3\right) \cdot P \\ &+\left(A_{21} + 2 \cdot A_{22} \cdot T + 3 \cdot A_{23} \cdot T^2\right) \cdot P^2 + \left(A_{31} + 2 \cdot A_{32} \cdot T\right) \cdot P^3.\end{aligned}$$

$$\frac{\partial B}{\partial T} = B_{01} + B_{11} \cdot T \cdot P, \qquad \frac{\partial D}{\partial T} = 0.$$

Pressure

The sound velocity differentiated with respect to pressure is given as

$$\frac{\partial c}{\partial P} = \frac{\partial CW}{\partial P} + \frac{\partial A}{\partial P} \cdot S + \frac{\partial B}{\partial P} \cdot S^{3/2} + \frac{\partial D}{\partial P}. \tag{B.4}$$

where

$$\begin{aligned}\frac{\partial C}{\partial P} = &\left(C_{10} + C_{11} \cdot T + C_{12} \cdot T^2 + C_{13} \cdot T^3 + C_{14} \cdot T^4\right) \\ &2 \cdot \left(C_{20} + C_{21} \cdot T + C_{22} \cdot T^2 + C_{23} \cdot T^3 + C_{24} \cdot T^4\right) \cdot P + 3 \cdot \left(C_{30} + C_{31} \cdot T + C_{32} \cdot T^2\right) \cdot P^2.\end{aligned}$$

$$\begin{aligned}\frac{\partial A}{\partial P} = &\left(A_{10} + A_{11} \cdot T + A_{12} \cdot T^2 + A_{13} \cdot T^3 + A_{14} \cdot T^4\right) \\ &+2 \cdot \left(A_{20} + A_{21} \cdot T + A_{22} \cdot T^2 + A_{23} \cdot T^3\right) \cdot P + 3 \cdot \left(A_{30} + A_{31} \cdot T + A_{32} \cdot T^2\right) \cdot P^2.\end{aligned}$$

$$\frac{\partial B}{\partial P} = \left(B_{10} + B_{11} \cdot T\right). \qquad \frac{\partial D}{\partial P} = D_{10}.$$

Appendix C

Uncertainty standards

Uncertainty and uncertainty calculations are a large part of this project. As to clarify the notations used and equations applied, a short description will be given here. The uncertainty calculations follows the *International Bureau of Weights and Measures* [91].

C.1 Distributions

Various probability distributions are used in statistics to provide the probabilities for all the possible outcomes of a random variable. The most common once are the normal and the rectangular distributions.

C.1.1 Normal distribution

The normal distribution, also known as the Gaussian distribution, governs the behaviour of random variables associated with random measurement errors [73]. It is the most common distribution, and follows the central limit theorem which states that the mean of a samples distribution will approximate a normal distribution with enough independent random variables [91]. An illustration of a normal distribution is shown in figure C.1.

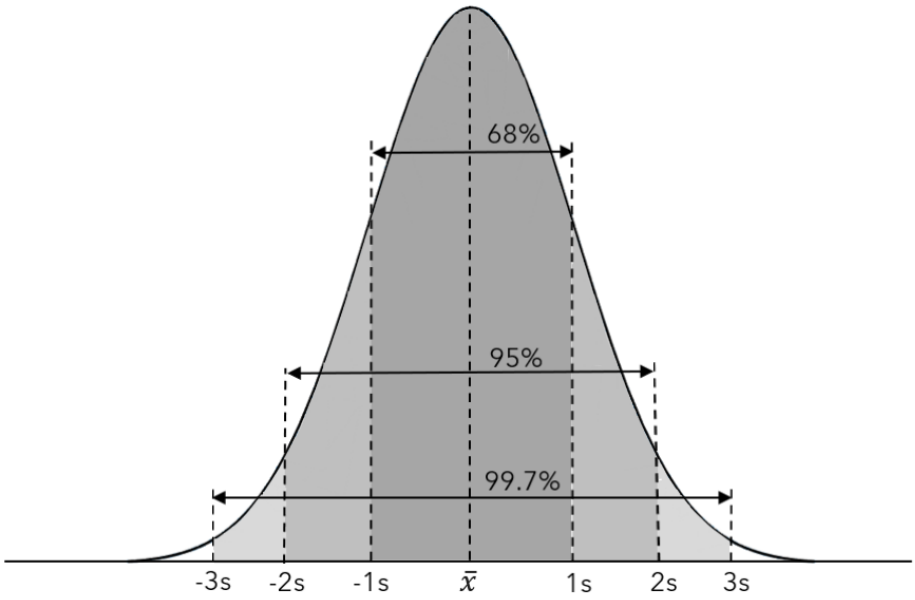

Figure C.1: Illustration of a normal distribution.

Coverage factor, k, defines the level of confidence for a parameter measured in a normal distribution. As can be seen in figure C.1, a coverage factor of k = 1 corresponds to a confidence level of approximately 68% and values within ± 1 standard deviation, s, of the mean value $\overline{x}$. k = 2 and k = 3 further corresponds to approximately 95% and 99% confidence levels and values within ± 2 and ± 3 standard deviations respectively [91].

C.1.2 Rectangular distribution

With a rectangular uncertainty distribution for variable x, any observation x_n will fall between values -a < x < +a with a confidence level of 100 %, corresponding to a coverage factor k =$\sqrt{3}$ [73]. A variable a with rectangular uncertainty distribution is converted to standard uncertainty through [91]

$$u(x) = \frac{a}{\sqrt{3}}. \tag{C.1}$$

C.2 Type A evaluation of uncertainty

Type A uncertainty evaluation is the process of assessing uncertainty through the statistical analysis of a series of observations [91]. The collected data from a series of measurements is thus evaluated using statistical methods.

The arithmetic mean or average, $\overline{x}$ for n independent observations is defined as [91]

$$\overline{x} = \frac{1}{n}\sum_{k=1}^{n} x_k. \tag{C.2}$$

The mean thus provides a statistical center of distribution. How each individual observation, x_k, differs from the mean value is often of interest. The **variance** of the n experimental observations is given by

$$s^2 = \frac{1}{n-1}\sum_{j=1}^{n}\left(x_j - \overline{x}\right)^2. \tag{C.3}$$

From equation C.3, the **experimental standard deviation** can be found, which characterizes the dispersion about the mean, or how accurately the mean represents the sample data

$$s = \sqrt{s^2} = \sqrt{\frac{1}{n-1}\sum_{j=1}^{n}\left(x_j - \overline{x}\right)^2}. \tag{C.4}$$

The experimental standard deviation is henceforth used as **standard uncertainty**, u(x) = s, following Lunde and Frøysa [40]. To obtain the **expanded uncertainty**, $U(x)$, the standard uncertainty must be multiplied with a coverage factor

$$U(x) = k \cdot u(x), \tag{C.5}$$

where k = 2 for a 95% confidence level.

C.3 Type B evaluation of uncertainty

Type B evaluation of uncertainty consists of evaluating uncertainty by means other than statistical analysis of observation sequences. These uncertainties are thus based on manufacturer's specifications, previously measured data and other available information. A probability density function is still assumed, thus must the available data lie within a specific confidence level.
In this project, the manufacturers specification is commonly used to assess type B uncertainties. The confidence level of the uncertainties are often not provided and must therefore be assumed. Unless otherwise specified, a confidence level of k = 1 is assumed to overestimate the uncertainty rather than underestimate it.

Appendix D

MATLAB-functions

D.1 Sensitivity Analysis

Sensitivityanalysis_relative.m

```
%Sensitivity analysis, relative uncertainty
%Hannah D. S. Benus, May 2021

f = 500000; %frequency
L_0 = 20e-3; %Width of sample
c_w = 1480; %Speed of sound in water
alpha_T = 71.5e-6;
T = 21;
T_0 = 24;
t_corr = (1/f)/4; %Due to diffraction correction etc
%%-----------%%
Delta_T = T - T_0;
K_T = 1 + (T-T_0)*alpha_T;
Delta_t = 2*(L_0)/c_w; %Difference between signal from buffer/sample interface and ...
    signal from reflector

%%------------%%
ppmL_0 = 32.5; %How much L_0 should contribute to total uncertainty
u_L0 = (ppmL_0/1000000)*L_0;
u_L0_mm = u_L0/10e-4;
u_L0_expanded = u_L0_mm*2;

%%-------------%%
ppmE_KT = 12.5; %How much K_T should contribute to total uncertainty
ppm_DeltaT = ppmE_KT/(alpha_T*abs(T-T_0));
u_DeltaT = (ppm_DeltaT/1000000)*abs(T-T_0)
u_KT = (ppmE_KT/1000000)*K_T;
u_KT_expanded = u_KT*2;

%% ---------- %%
ppmDelta_t = 32.5; %How much Δ_t should contribute to total uncertainty
u_Delta_t = (ppmDelta_t/1000000)*Delta_t;
u_Delta_t_microseconds = u_Delta_t/10e-6;
u_Delta_t_expandend = u_Delta_t_microseconds*2;%Shown in microseconds

%%% ---------%%
ppm = 25; %How much the correction term should contribute to total uncertainty
ppmt_corr = ppm/(t_corr/Delta_t);
u_t_corr = (ppmt_corr/1000000)*t_corr;
u_t_corr_microseconds = u_t_corr/10e-7;
u_t_corr_expanded = 2*u_t_corr_microseconds; %Shown in microseconds
```

D.2 Signal processing scripts

Sound velocity measurements, data collection and storage, diffraction corrections, and uncertainty calculations are all run through the main script presented below.

Main_script.m

```
clear all
%%%%% Running osccilloscope, saving data and plotting waveform live %%%%%
%%% Script for Master thesis
%%% Created by: Hannah D. S. Benus
%%% Last edited: 05.03.2022
%%% Information:
%%% Main script for data collection. It connectects to the oscilloscope,
%%% and then, through a timer, collects data every -period- seconds.
%%% For each execution, new data is collected and the temperature is measured.
%%% A signal processing scrip calculates the sound velocity from the waveforms ...
    collected using
%%% transit time (FSM and ZCM). The original waveforms are saved in a .txt document,
%%% and the calculated sound velocities, temperature, uncertainty,
%%% theoretical sound velocity etc. is saved in another .txt document.
%%% The waveform is shown live to see the evolution of the sampled waveform
%%% throughout the measurement series.
%%% The program can be canceled at any time without loss of data.
%%%-------------------------------------------------------------%%%
%See if oscilloscope is communicating with MATLAB
if exist("id_scope")
    disp("Oscilloscope is running")
else
    disp("Connecting to oscilloscope")
    [id_scope] = InitScope(); %Connecting to oscilloscope
    disp("Oscilloscope is running")
end

ch = 2; %Oscilloscope channel

SOS = ['SOS_distilled_6p',datestr(now,'dd_mm_HH_MM_SS'),'.txt']; %Create filename for ...
    SOS-info
fileID_SOS = fopen(SOS,'at');
WF = ['Waveform_distilled_6p',datestr(now,'dd_mm_HH_MM_SS'),'.txt']; %Create filename ...
    for waveform

period = 3; %Seconds between runs

t_obj = timer; %Timer is created, as well as parameters for timer
set(t_obj, 'StartDelay', period);
set(t_obj, 'Period', period);
set(t_obj, 'TasksToExecute',5000); %600 = 40 mminutes, 2500 = approx two hours
set(t_obj, 'ExecutionMode', 'fixedRate');

%Appends function StartDataCollection
t_obj.StartFcn = {@StartDataCollection,id_scope,ch,WF,fileID_SOS};
%Appends function RunDatacollection, runs "count" times
t_obj.TimerFcn = {@RunDatacollection,id_scope,ch,WF,fileID_SOS};
%Appends function StopDatacollection, runs last time to close the .txt
t_obj.StopFcn = {@StopDatacollection,id_scope,ch,WF,fileID_SOS};
start(t_obj); %Timer is started
pause(period);
stop(t_obj);
delete(t_obj); %Timer is deleted after finished

%Plotting the resulting variation in SOS and temperature when the program
%is finished
PlotSOS(SOS)

%Is run after timer is initiated:
function[c_zerocrosses,c_zc_corrected]= StartDataCollection(¬, ¬, id_scope,ch, ...
    WF,fileID_SOS) %
    [x,wf] = DPORead(id_scope,ch); %Collecting data from oscilloscope, wf = waveform [V]

    %Communicating with temperature sensor, "usbtenkiget -h" for information:
    [¬,temp] = system(['usbtenkiget -s E16381 -i 0 -x 3']);
    findtemp = regexp(temp,"\d+.\d*","Match");%locating the numbers in the output
    T_original = str2double(findtemp{1});%The first number is the temperature

    %Calculating SOS using sampled waveform from oscilloscope and temperature from ...
        sensor :
    [c_Frey, c_FSM, c_FSM_corrected ,c_zerocrosses, c_zc_corrected,y,Signallength, ...
        uncertainty_sos, u_sos_theoretical, std_zc] = Signalprocessing(x,wf,T_original);

    %Plotting live waveform
    hLine = plot(y);
    StripChart("initialize",gca) %Initializing liveplot
    err = 0 ; %If errors occur, err = 1 in .txt file

    %Opening file and write SOS to file
    fprintf(fileID_SOS,'%s %s %s %s %s %s %s %s %s %s %s %s %s %s ...
        \n',"Date","Time","Signal_length","c_zc","c_zc_corrected", ...
        "c_FSM","c_FSM_corrected","c_Frey","Temp", "Totalerror", "Theoreticalerror", ...
        "Std_zc", "Error");
    fprintf(fileID_SOS,'%s %s %d %d %d %d %d %d %d %d %d %d %d ...
        %d\n',datestr(now,'dd_mm_yyyy'),...
    datestr(now,'HH_MM_SS'),Signallength, c_zerocrosses,c_zc_corrected, c_FSM, ...
        c_FSM_corrected,c_Frey,T_original, uncertainty_sos, u_sos_theoretical, std_zc,err);

    %Write waveform to file
    writematrix(y,WF);

    %Output Command window
    info = sprintf("Time = %s SOS_t = %s SOS_zc = %s SOS_FSM = %s Temp = ...
        %s",datestr(now,'HH_MM_SS'),c_Frey, c_zc_corrected,c_FSM_corrected, T_original);
    disp(info);
end
```

```
85
86  function [c_zerocrosses,c_zc_corrected] = RunDatacollection(¬, ¬, id_scope,ch,WF, ...
        fileID_SOS)
87      [x,wf] = DPORead(id_scope,ch);
88
89       %Communicating with temperature sensor:
90      [¬,temp] = system(['usbtenkiget -s E16381 -i 0 -x 3']);
91      findtemp = regexp(temp,"\d+.\d*","Match");
92      T_original = str2double(findtemp{1});
93
94      [c_Frey, c_FSM, c_FSM_corrected ,c_zerocrosses, c_zc_corrected,y,Signallength, ...
            uncertainty_sos, u_sos_theoretical,std_zc] = Signalprocessing(x,wf, T_original);
95
96      %Updating live waveform
97      hLine = plot(y);
98      StripChart('Update',hLine,y)
99      err = 0;% No error in writing waveform, used to track waveform to temperature
100     try
101         writematrix(y,WF,"WriteMode","Append");
102     catch
103         disp('Error: Could not write waveform');
104         err = 1; %Error is logged in the SOS.txt document
105     end
106
107     %Writing SOS to .txt
108     fprintf(fileID_SOS,'%s %s %d %d %d %d %d %d %d %d %d ...
            %d\n',datestr(now,'dd_mm_yyyy'),...
109     datestr(now,'HH_MM_SS'),Signallength, c_zerocrosses,c_zc_corrected, c_FSM, ...
            c_FSM_corrected,c_Frey,T_original, uncertainty_sos, u_sos_theoretical, std_zc, ...
            err);
110
111     %Output command window
112     info = sprintf("Time = %s SOS_t = %s SOS_zc = %s SOS_FSM = %s Temp = ...
            %s",datestr(now,'HH_MM_SS'),c_Frey, c_zc_corrected,c_FSM_corrected, T_original);
113     disp(info);
114
115     pause(1)
116 end
117 %Run the last time of the timer to close everything:
118 function [c_zerocrosses,c_zc_corrected]=StopDatacollection(¬, ¬, id_scope,ch,WF, ...
        fileID_SOS)
119     [x,wf] = DPORead(id_scope,ch);
120     [¬,temp] = system(['usbtenkiget -s E16381 -i 0 -x 3']); %Communicating with Dracal
121     findtemp = regexp(temp,"\d+.\d*","Match"); %Finding temperature output
122     T_original = str2double(findtemp{1});
123     [c_Frey, c_FSM, c_FSM_corrected ,c_zerocrosses, c_zc_corrected,y,Signallength, ...
            uncertainty_sos, u_sos_theoretical,std_zc] = Signalprocessing(x,wf, T_original);
124
125     %Plotting waveform
126     hLine = plot(y);
127     StripChart('Update',hLine,y)
128     err = 0;
129     fprintf(fileID_SOS,'%s %s %d %d %d %d %d %d %d %d %d ...
            %d\n',datestr(now,'dd_mm_yyyy'),...
130     datestr(now,'HH_MM_SS'),Signallength, c_zerocrosses,c_zc_corrected, c_FSM, ...
            c_FSM_corrected,c_Frey,T_original, uncertainty_sos, u_sos_theoretical, std_zc,err);
131
132
133     writematrix(y,WF,"WriteMode","Append");
134     fclose(fileID_SOS);
135     info = sprintf("Time = %s SOS = %s Temp = ...
            %s",datestr(now,'HH_MM_SS'),c_zc_corrected, T_original);
136     disp(info);
137 end
```

DPOread.m

```
%% DPORead.m
% Created by Magne Vestrheim, edited by Mathias Saether
% Adjusted 2021-11-04 by Audun Oppedal Pedersen:
% - Byte order and word length controlled by InitScope (16-bit)
% - Cleaned up old code (still found in GitLab)
% - Using visadev in InitScope instead of the deprecated visa statement:
% => Update from the deprecated binblockread function to readbinblock
% => Update from fprintf and freadf to write and read
% - Corrected an error in the calculation of wf. Now including YOF.

% Use the DPO3000 Series Programmer Guide when editing the script.

function [x,wf,tidsskala] = DPORead(id_scope,ch,samples)

noB = 2; % Number of bytes per word (8-bit if 1, 16-bit if 2, ...)
% set(id_scope,'InputBufferSize',noB*samples); % Buffer size in the computer

% fopen(id_scope);
% fprintf(id_scope,['DAT:SOU CH' num2str(ch)]); % Velge kanal. ch=1 betyr CH1
write(id_scope,['DAT:SOU CH' num2str(ch)]); % Velge kanal. ch=1 betyr CH1

% Record length per visible time interval, affecting the sample rate
rec_len = str2double(writeread(id_scope,'HOR:RECO?'));
if nargin() == 3
    if samples > rec_len
        warning('The record length is set too low. Adjusting and waiting 10 s...')
        write(id_scope,['HOR:RECO ' num2str(samples)]); % New record length
        pause(10);
    elseif samples < rec_len
        warning('Retrieving less than the record length (full view).')
    end
else
    samples = rec_len;
end

% Set what samples to retrieve
write(id_scope,'DAT:START 1');
write(id_scope,['DAT:STOP ' num2str(samples)]);

% Read the data
write(id_scope,'CURV?');
% dd = query(id_scope,'CURV?');
% pause(.2);
% ff = query(id_scope,'BUSY?');
if noB == 2
    ydata = readbinblock(id_scope,'int16');
elseif noB == 1
    ydata = readbinblock(id_scope,'int8');
else
    error('Unsupported word length');
end
flush(id_scope); % Flush the termination character from the scope

%% Scaling of the data
% Horizontal scaling
tidsskala = str2double(writeread(id_scope,'HOR:SCA?'));
% Horizontal offset
xze = str2double(writeread(id_scope,'WFMO:XZE?'));
% Horizontal increment
xin = str2double(writeread(id_scope,'WFMO:XIN?'));
% Vertical multiplying factor
ymu = str2double(writeread(id_scope,'WFMO:YMU?'));
% Vertical offset
yze = str2double(writeread(id_scope,'WFMO:YZE?'));
% Digital vertical offset
yof = str2double(writeread(id_scope,'WFMO:YOF?'));

% Time vector
x = (0:(length(ydata)-1))*xin + xze;
% Voltage/current vector
wf = (ydata-yof)*ymu + yze;
```

Signalprocessing.m

```
%Signal processing of waveform to calculate the sound velocity using FSM
%and ZCM. The calculates sound velocity values are compensated for
%diffraction.
% Includes temperature calibration, theoretical sound velocity calculation,
% uncertainty calculation, and the variables are compensated for temperature
% Hannah D. S. Benus, 2021/2022

function [c_Frey, c_FSM, c_FSM_corrected ,c_zerocrosses, c_zc_corrected,y,Signallength, ...
    uncertainty_sos, u_sos_theoretical, std_zc] = Signalprocessing(x,wf, T_original)

%% -------- Variables to change --------- %%%
pumpon = 1; %1 = Yes, 0 = No (for uncertainty)
Oscillocope_amplitude_span = -0.01 - (-0.09); %[V] Zoom of oscilloscope screen, manually
```

```
P_meas = 1.02077; %[bar], pressure measured in lab before start of experiment
%% ------------------------------------- %%%

fs = (length(x)-1)/(x(end-1)-x(1)); %Sampling frequency
Upper_freq = 8e5;%For filtering
Lower_freq = 2.5e5;%For filtering
freq =500000; %Sent frequency
Bufferlength = 70.1e-3; %At reference temperature 22.94 degrees
a = 12.427e-3; %Effective radius of transducer [m]

treshold = 0.5; %Treshold for chosing the value of the sum for which the pulse starts
ZC_interest = 3; %Chosing which zerocross in the pulse is of interest, 0 is start of pulse
steady_state = 3; %Chosing, when signal is longer than 3 wavelengths, when steady-state ...
    starts
stop_steady_state = 2; %Chosing which zerocross will be the last in steady-state, ...
    subtract last zero-cross with nr

f_min = 250000;% Hz, minimum frequency of interest when calculating FFT
f_max = 700000; %Hz, maximum frequency of interest when calculating FFT
%
%% ------ Correction of sample length due to thermal expansion ----- %
L_0 = 25.18e-3; %mm, length of sample area at 21.94 degrees, reference temperature
T_0 = 22.94; %Reference temperature
Samplelength = L_0 + (Temperature-T_0)*(26.08e-3*24e-6 - 0.9e-3*70e-6); %Thermal expansion


%% --------------- Temperature calibration ------------------------- %%

alpha_original = 0.003908299841; %original coefficient  [^oC]
beta_original = -5.7749974e-7; %original coefficient [^oC]
R = 100*(1 + alpha_original*T_original + beta_original*T_original^2);

alpha = 3.841e-3; %New coeeficient [^oC]
beta = -2.095e-7; %New coeeficient [^oC]
R_0 = 100.1; %New coefficient [Ohm]

T = (-alpha*R_0 + sqrt(alpha^2*R_0^2 - 4*beta*R_0*(R_0 - R)))/(2*beta*R_0);

%%  Sound velocity in Plexiglas as a function of temperature  %%

c_b_70 = 2711.2; %70mm buffer sos at 22.8oC
c_b_85 = 2725.3; %85mm buffer sos at 22.8oC
c_b = -0.08415*T^2 + 3.912*T + 2680 - (c_b_85 - c_b_70); %Sound velocity in 70mm buffer ...
    as a function of temperature

%% ------ Pressure calculations ------------------------- %%
rho = 997.05; %Density of pure water at 1atm and 25C
rho = 913; %Density of raffined olive oil
g = 9.81; %Gravity acceleration [m/s^2]
h = 55e-3; %Distance below water, sound axis [m]
P_atm = 1.01325; %Atmospheric pressure [bar]
conv_bar = 10e-5; %Pascal to bar conversion
hydrostatic_P = rho*g*h*conv_bar; %[bar] Hydrostatic pressure
P_tot = P_meas + hydrostatic_P; %Total pressure [bar]
P_gauge = P_tot - P_atm; %Gauge pressure [bar]



%% ----Signal manipulation and calculating variables used for uncertainty calculations ...
    later --- %%
wf = wf(12000:66000);%Eliminating the transducer signal and the DC-component
wf = wf - wf(1); %Moving the amplitude signal up to start at 0
y = bandpass(wf,[Lower_freq,Upper_freq],fs); %Filtering out the low and high frequencies


bits = 16; %Vertical resolution

ΔV_q = Oscillocope_amplitude_span/(2^bits - 1); %After eliminating transducer signal ...
    and filtering
u_bit = ΔV_q/2; %Uncertainty due to bit resolution
t_s = (x(end) - x(1))/10000; %Sampling period

x = x(12000:66000);%Eliminating the transducer signal and the DC-component



%%------------ Finding zero-crosses -------------------------%%
findzerocrosses = @(v) find(v(:).*circshift(v(:), [-1 0]) ≤ 0);
zerocrosses = findzerocrosses(y); %Vector that contains the indices corresponding to ...
    zero-crossings

for zc = 1:numel(zerocrosses) %Looping through the length of vector zxidx
    idex = zerocrosses(zc)-1:zerocrosses(zc) + 1; %Makes a vector of the index ...
        corresponding to a "zero cross", the index before and the index after
    if idex > 0 & idex < length(y)
        xrng = x(idex); %Finds the corresponding values in time
        yrng = y(idex); %Finds the corresponding values in amplitude

        ΔV = yrng(end)-yrng(1); %Calculating the span from zc to nearest point
        error(zc) = sqrt((t_s*u_bit/ΔV)^2 + (2.118e-4)^2); %Calculating the error for ...
            each zc due to resolution [V]

        ZC(zc) = interp1( yrng(:), xrng(:), 0, 'linear', 'extrap' ); %Linear ...
            interpolation around point 0, extrapolation outside the range

    end
end

%Explanation zero-crossing
%zci = Circshift circullary shifts the values of the data in the vector one to
%the left (in this case). Thus it takes one value in the vector v and
%multiplies it with the value to the left. If both of these values are
%negative, the resulting value will be positive and thereby not ≤ 0. If
```

```
%one value is negative and one value positive, the result will be negative
%and one therefore has a zero-crossing.

%%-------------------- Zero-crossing------------------------------ %%

%Uses the indexes found corresponding to zero-crosses (before
%interpolation) to calculate the sum between two zero-crosses. This can be
%used to determine when the pulse starts.

for i = 1:length(zerocrosses) - 1
    len  = zerocrosses(i):zerocrosses(i+1);
    parts = y(len);
    s(i) = sum(abs(parts)); %Summing the area between two zero-crossings
    if s(i) > treshold %Separating the zerocrosses corresponding to noise to ...
        zerocrosses corresponding to pulse by treshold value
        pulse_zerocrosses(i) = x(zerocrosses(i));
        count(i) = 1;
    end
end

sA = 0 ;
for A = 1:length(count) - 1 %Finding start of Signal A
    sA = sA + 1;
    if count(A) == 1
        break
    end
end
Signal_A_time = ZC(sA + ZC_interest);

end_A = 0;
for t = 1:length(count)-1
   end_A = end_A + 1;
   if count(t) ==1 && count(t+1) == 0  %Located the end of signal A, next 1 in count ...
       will be start of signal B
       end_A = end_A + 1; %Include the last pulse
       break
   end
end
%end_A = end_A + 1;% To include signal beyond treshold if needed

count(1:end_A) = 0; %First pulse is eliminated so second pulse can be found

sB = 0 ;
for B = 1:length(count) - 1 %Finding start for Signal B
    sB = sB + 1;
    if count(B) == 1
        break
    end
end
Signal_B_time = ZC(sB + ZC_interest);

end_B = 0;
for t = 1:length(count)-1
   end_B = end_B + 1;
   if count(t) ==1 && count(t+1) == 0  %Located the end of signal B
       end_B = end_B + 1; %Include the last pulse
       break
   end
end
%end_B = end_B + 1 % To include signal beyond treshold if needed

%% ---------- Fourier spectrum method ------------------ %%

%Creating x-axis of interest
N1=2^nextpow2(length(x));% returns the first P such that 2.^P ≥ abs(N)
freq_whole = fs*(0:N1/2-1)/N1; %One-sided spectrum

f_1M = find(freq_whole ≤ f_max);%Maximum signal of interest
f_100k = find(freq_whole ≥ f_min); %Minimum signal of interest
f = freq_whole(f_100k(1):f_1M(end));

Signal = zeros(size(x)); %For plotting

%%%%% Signal A %%%%%
SignalA = zeros(size(x));

i_A = find(x ≥ ZC(sA)& x ≤ ZC(end_A)); % Finding all the indexes for Signal A
Signal(i_A) = y(i_A);
SignalA(i_A) = y(i_A);
RA = circshift(SignalA,-i_A(1)); %Move pulse to start of signal, start defined by start ...
    of x-vector
t_shiftA = x(i_A(1)) - x(1);

fourier_A = fft(RA, N1);
fourier_A = fourier_A(f_100k(1):f_1M(end));

mag_A = abs(fourier_A);
phase_A_shifted = angle(fourier_A);%Retrieving the wrapped phase
%pa = phase_A_shifted - 2*pi.*f.*t_shiftA; %Comparing wrapped vs unwrapped phase

pAs_unwrapped = unwrap(phase_A_shifted); %Unwrapping the phase
phase_A = pAs_unwrapped - 2*pi.*f.*t_shiftA; %Correcting for shift

%%%%% Signal B %%%%%
SignalB = zeros(size(x));

i_B = find(x ≥ ZC(sB)& x ≤ ZC(end_B));
SignalB(i_B) = -y(i_B); %Negative to flip the signal, 90 degree difference
Signal(i_B) = -y(i_B);
RB = circshift(SignalB,-i_B(1)); %Move pulse to start of signal, source [72] in Mathias PhD
t_shiftB= x(i_B(1)) - x(1);

fourier_B = fft(RB, N1);
```

```
fourier_B = fourier_B(f_100k(1):f_1M(end));

mag_B = abs(fourier_B);
phase_B_shifted = angle(fourier_B); %Retrieving the wrapped phase
%pb = phase_B_shifted- 2*pi.*f.*t_shiftB; %To compare wrapped and unwrapped phase
pBs_unwrapped = unwrap(phase_B_shifted); %Unwrapping the phase

phase_B = pBs_unwrapped - 2*pi.*f.*t_shiftB; %Correcting for shift

%% -------Speed of sound calculations ---------------- %%

%Calculating speed of sound using FFT
c_shift = (2*Samplelength)./(pb./(2*pi.*f) - pa./(2*pi.*f));
c_FSM = interp1(f,c_shift,500000); %Finding the speed of sound at 500000kHz using ...
    linear interpolation

%Calculating the speed of sound using zero_crossing
ca = sA + steady_state;
cb = sB + steady_state;

if end_A - sA < 10 %Short pulse, 10 approximates to a pulselength of 4 periods

    %Corresponding to the middle of the pulse
  Signal_A_time1 = ZC(sA+6);
  Signal_A_time2 = ZC(sA+7);

    %Corresponding to the middle of the pulse
  Signal_B_time1 = ZC(sB+6);
  Signal_B_time2 = ZC(sB+7);

  Signal_A_time = (Signal_A_time1 + Signal_A_time2)/2;
  Signal_B_time = (Signal_B_time1 + Signal_B_time2)/2;
  c_zerocrosses  = 2*Samplelength/(Signal_B_time-Signal_A_time);
  Signallength = 2;

  std_zc = 0;
else %Long pulse, calculating the mean
   while ca ≤ (end_A - stop_steady_state)
       Signal_A_time = ZC(ca);
       Signal_B_time = ZC(cb);
       c_zerocross_vector(ca) = 2*Samplelength/(Signal_B_time-Signal_A_time);
       ca = ca + 1;
       cb = cb + 1;
       Signallength = 6;
   end
   positions = find(c_zerocross_vector > 0);
   c_zerocrosses  = mean(c_zerocross_vector(positions));
   std_zc = std(c_zerocross_vector(positions));
end


%Calculating the theoretical speed of sound using the equation found in "Fundementals ...
    of Acoustics, 4th ed." from Kinsler et. al.
c_Frey = 1402.7 + 488 * (T/100) - 482 * (T/100)^2 + 135 * (T/100)^3 + ...
 (15.9 + 2.8 * (T/100) + 2.4 * (T/100)^2) * (P_gauge/100);

%% ------------------- Diffraction correction ------------------- %%
n = 1000;
theta = (0:(pi/2)/n:(pi/2)); %[radians]

%Diffraction correction for signal A
for zc = 1:length(theta)
    H_diff_zerocross_A(zc) = exp(-1i*((2*pi*freq)/c_b)*2*Bufferlength*...
    ((sqrt(1+4*(a/(2*Bufferlength))^2*(cos(theta(zc)))^2))-1))*(sin(theta(zc)))^2; ...
        %Echo A
end
H_diff_A_zerocross = 1 - 4/pi*((2*sum(H_diff_zerocross_A((3:2:end-2))) + ...
    4*sum(H_diff_zerocross_A(2:2:end)) + H_diff_zerocross_A(1) + ...
    H_diff_zerocross_A(length(theta)))*theta(2)/3);
phase_diff_A = angle(H_diff_A_zerocross);

%Diffraction correction for signal B - Fourier
[H_diff_B_FSM] = Diffraction_signalB(a,c_b,L_0,c_FSM);
phase_diff_B = H_diff_B_FSM;

%c_phase_corrected = (2*Samplelength)./(phase_A./(2*pi.*f) - phase_B./(2*pi.*f) - ...
    phase_diff_d./(2*pi.*f) + phase_diff_D./(2*pi.*f));

phase_BB = -interp1(f,phase_B,500000);
phase_AA = -interp1(f,phase_A,500000);

c_FSM_corrected = (2*Samplelength)./(phase_BB./(2*pi.*freq) - phase_AA./(2*pi.*freq) + ...
    phase_diff_B./(2*pi.*freq) - phase_diff_A./(2*pi.*freq));

%H_diff_B_zerocross = 1 - 4/pi*(2*sum(H_diff_zerocross_B((3:2:end-2))) + ...
    4*sum(H_diff_zerocross_B(2:2:end)) + H_diff_zerocross_B(1) + ...
    H_diff_zerocross_B(length(theta))*theta(2)/3);

%Diffraction Zerocrossing method
t_A_zerocross = angle(H_diff_A_zerocross)/(2*pi*freq);
[H_diff_B_zerocross] = Diffraction_signalB(a,c_b,L_0,c_zerocrosses); %Script ...
    calculating the diffraction correction in signal A
t_B_zerocross = H_diff_B_zerocross/(2*pi*freq);
c_zc_corrected =  2*Samplelength/(Signal_B_time - Signal_A_time + t_B_zerocross - ...
    t_A_zerocross);
%% ---------------------------------------------------- %%

totalerror = sum(error)/length(error); %Error due to bit resolution [v]
%totalerror = (2.118e-4)^2;
[uncertainty_sos, u_sos_theoretical] = ...
    Uncertainty_calculations(totalerror,Signal_B_time,Signal_A_time,...
t_B_zerocross,t_A_zerocross,L_0, T, P_gauge, c_Frey, pumpon, Samplelength, P_meas);
```

Diffraction_signalB.m

```
function [diff_signalB] = Diffraction_signalB(a,c_b,L_0,c_zerocrosses)
%Calculating the diffraction correction for Signal B using the method
%Described in section 2.3. Based on Khimunin's diffraction correction
%method

Buffer = 70.1e-3;
Bufferlength = linspace(0,70.07e-3, 1000); %Through buffer
Samplelength = linspace(0,500e-3, 1000); %Through Sample twice
Bufferlength_back = linspace(0,500e-3, 1000); %Through Buffer back
n = 1000;
theta = (0:(pi/2)/n:(pi/2)); %[radians]
freq = 500000;
for r = 1:length(Bufferlength)
    for i = 1:length(theta)
        %Diffraction one way buffer:
        H_diff1(i) = exp(-1i*((2*pi*freq)/c_b)*Bufferlength(r)*...
        ((sqrt(1+4*(a/(Bufferlength(r)))^2*(cos(theta(i)))^2))-1))*...
        (sin(theta(i)))^2;
        %Diffraction two way sample:
        H_diff2(i) = exp(-1i*((2*pi*freq)/c_zerocrosses)*Samplelength(r)*...
        ((sqrt(1+4*(a/(Samplelength(r)))^2*(cos(theta(i)))^2))-1))*...
        (sin(theta(i)))^2;
        %Diffraction one way buffer back:
        H_diff3(i) = exp(-1i*((2*pi*freq)/c_b)*Bufferlength_back(r)*...
        ((sqrt(1+4*(a/(Bufferlength_back(r)))^2*(cos(theta(i)))^2))-1))*...
        (sin(theta(i)))^2;


    end
    H_diff_1_sum(r) = 1 - 4/pi*((2*sum(H_diff1((3:2:end-2))) + 4*sum(H_diff1(2:2:end)) ...
        + H_diff1(1) + H_diff1(length(theta)))*theta(2)/3);
    H_diff_2_sum(r) = 1 - 4/pi*((2*sum(H_diff2((3:2:end-2))) + 4*sum(H_diff2(2:2:end)) ...
        + H_diff2(1) + H_diff2(length(theta)))*theta(2)/3);
    H_diff_3_sum(r) = 1 - 4/pi*((2*sum(H_diff3((3:2:end-2))) + 4*sum(H_diff3(2:2:end)) ...
        + H_diff3(1) + H_diff3(length(theta)))*theta(2)/3);

end

%One way buffer:
DiffA = angle(H_diff_1_sum);

%Two-way sample:
B = angle(H_diff_2_sum);
y_start = find(B ≥ DiffA(end)); %index
x_start = Samplelength(y_start(1));
x_end = x_start + 2*L_0;
x_end_index = find(Samplelength ≥ x_end);
x_sampletot = Samplelength(y_start(1):x_end_index(1)); %Distance for sample
x_sample = linspace(Bufferlength(end), Bufferlength(end) + 2*L_0, length(x_sampletot));
DiffB = B(y_start(1):x_end_index(1)); %Diffraction correction for sample

%Back one way buffer
C = angle(H_diff_3_sum);
y_start_C = find(C ≥ DiffB(end));
x_start_C = Bufferlength_back(y_start_C(1));
x_end_C = x_start_C + Buffer;
x_end_C_index = find(Bufferlength_back ≥ x_end_C);
x_buffertot = Bufferlength_back(y_start_C(1):x_end_C_index(1));
x_buffer = linspace(Bufferlength(end) + 2*L_0, 2*Bufferlength(end) + 2*L_0, ...
    length(x_buffertot));
DiffC = C(y_start_C(1):x_end_C_index(1));

diff_signalB = DiffC(end);
end
```

Uncertainty_calculations.m

```
function [uncertainty_sos, u_sos_theoretical] = ...
    Uncertainty_calculations(totalerror,standd,...
Signal_B_time,Signal_A_time,t_B_zerocross,t_A_zerocross,L_0, T, P_G, c_Frey, pumpon, ...
    Samplelength,P)
%UNCERTAINTY_CALCULATIONS
%This function calculates the uncertainty in the calculated sound
%velocity based on the uncertainty analysis in Chapter 5.

%% Uncertainty in length measurements

u_caliper = 0.03e-3; %Uncertainty in caliper, specified by manufacturer, k = 2
u_L_repeatibility = 0.0063e-3; %Uncertainty due to repetability in measurements, k = 1
u_uneven = 0.019e-3; %Uncertainty due to uneven surfaces k = 1
u_L_67confidence = sqrt((u_caliper/2)^2 + u_L_repeatibility^2 + u_uneven^2); %Total ...
    uncertainty in length measurements

%% Uncertainty in transit time measurements
u_osc = 121.2e-12; %Time resolution of oscilloscope, k = 1
u_coh = 1.5e-8; %Uncertainty due to coherent noise, k = sqrt(3)
u_variations = standd;%std. of zerocrosses, k = 1
```

```
u_pump =  1.56e-10; %Uncertainty due to pump noise, k = 1
u_trunc = 9.01e-10; %Uncertainty due to truncating the signal (FSM), manually changed ...
    between two and six period, k = 1
u_ph_dist = totalerror; %Uncertainty due to phase distortions (FSM), k = 1

if pumpon == 1
    u_tt_67 = sqrt(u_osc^2 + (u_coh/sqrt(3))^2 + totalerror^2 + u_variations^2 + ...
        u_pump^2); %Total uncertainty in transit time measurements, 67% confidence
    u_tt_FSM = sqrt(u_trunc^2 + u_osc^2 + u_ph_dist + (u_coh/sqrt(3))^2 + totalerror^2 ...
        + u_variations^2 + u_pump^2); %Total uncertainty in transit time measurements, ...
        67% confidence

else
    u_tt_67 = sqrt(u_osc^2 + (u_coh/sqrt(3))^2 + totalerror^2 + u_variations^2 ); ...
        %Total uncertainty in transit time measurements
    u_tt_FSM = sqrt(u_trunc^2 + u_osc^2 + u_ph_dist + (u_coh/sqrt(3))^2 + totalerror^2 ...
        + u_variations^2); %Total uncertainty in transit time measurements, 67% confidence
end

%% Uncertainty in time correction
u_tcorr = 3.538e-9;%Not dependent on waveform

%% Uncertainty in K_T - thermal expansion (including sensitivity coefficients, already ...
    calculated)
u_ΔT = 0.212; %[^oC] Uncertainty in T - T_0
u_alu = 3.5e-7; %[m/m^oC]Uncertainty in the thermal expansion coefficient of aluminium
u_plexi = 2.4e-6; %[m/m^oC]Uncertainty in thermal expansion coefficient of Plexiglas
u_db = 2.14e-4; % [m] Uncertainty due to measured distance from bolt to sample area
u_K_T = sqrt((u_ΔT*2.23e-5)^2 + (u_alu*38.39)^2 + (4.5e-6*1.325)^2 + ...
(u_L_67confidence*6.09e-5)^2 + (u_db*(-0.068))^2);

%% Uncertainty in calculated sound velocity
K_T = Samplelength/L_0;
Delta_t = Signal_B_time - Signal_A_time;
Delta_t_corr = t_B_zerocross- t_A_zerocross ;
k = 2; %95% confidence level

%Uncertainty in ZCM
uncertainty = (((2*K_T)/(Delta_t - Delta_t_corr)*u_L_67confidence)^2 +...
((-2*K_T*L_0/(Delta_t - Delta_t_corr)^2)*u_tt_67)^2 ...
    + (((2*K_T*L_0)/(Delta_t - Delta_t_corr)^2)*u_tcorr)^2...
 + ((2*L_0/(Delta_t - Delta_t_corr))*u_K_T)^2);
uncertainty_sos = k*sqrt(uncertainty);

%Uncertainty in FSM
uncertainty_FSM = k*(((2*K_T)/(Delta_t - Delta_t_corr)*u_L_67confidence)^2 +...
((-2*K_T*L_0/(Delta_t - Delta_t_corr)^2)*u_tt_FSM)^2 ...
    + (((2*K_T*L_0)/(Delta_t - Delta_t_corr)^2)*u_tcorr)^2 + ...
((2*L_0/(Delta_t - Delta_t_corr))*u_K_T)^2);
uncertainty_FSM_sos = k*sqrt(uncertainty);

%% Uncertainty in theoretical sos - distilled water
dc_dt = 4.88 - 0.0964*T + (4.05e-4)*T^2 + (0.028 + (4.8e-4)*T)*P_G/100; %Sensitivity coeff
dc_dp = 1/100*(15.9 + 0.028*T + (2.4e-4)*T^2); %Sensitivity coeff
u_T = 0.156; %[^oC] 67% confidence level

u_p_meas = P*0.00015; %0.015% of reading
u_reading = 6.5e-5; %bar, fluctuations due to analog readings
u_density = 4.3e-5; %bar, deviation from assumed constant density
u_height = 4.21e-5; %bar, uncertianty due to height of sound axis
u_P = sqrt(u_p_meas^2 + u_reading^2 + u_density^2 + u_height^2); %[bar], 67% confidence ...
    level
u_model = 0.5*(c_Frey*0.05/100); %Uncertainty of model, 67% confidence level

u_sos_theoretical = sqrt((dc_dt*u_T)^2 + (dc_dp*u_P)^2 + u_model^2);
u_sos_theoretical = u_sos_theoretical*2;% 95% confidence level, k = 2

end
```

D.3 Simulation

The below script simulates the propagation of the side lobes inside a measurement cell with two layers. It is based on ray-tracing and assumes plane waves.

beamdirectivity.m

```
clear all
clear figure
%%%%%% A matlab program for plotting propagation in measurement cell %%%%%
%%% Hannah Benus, 25.04.2021 %%%

%%% Dimensions of box %%%
Bufferlength = 85e-3;
Bufferwidth = 100e-3;
```

```
Samplelength = 25e-3;
Totallength = Bufferlength + Samplelength ;
Transducer_position = Bufferwidth/2;
transducer_diameter= 25e-3;
trans_r = transducer_diameter/2; % radius of transducer [mm]
%trans_r = 15.875e-3;
c_buffer = 2716.1468; %m/s
c_sample = 1481; %m/s

f = 500000; %[Hz]
Rayleigh =  pi*trans_r^2*f/c_buffer;

%%%%%% calculate the angles of the lobes %%%%%%%%%
theta_one = asind(5.15/(2*pi*f*trans_r/c_buffer)); %MAX sidelobe 1
theta_two = asind(8.42/(2*pi*f*trans_r/c_buffer)); %MAX sidelobe 2
theta_three = asind(11.62/(2*pi*f*trans_r/c_buffer)); %MAX sidelobe 3
theta_four = asind(14.7/(2*pi*f*trans_r/c_buffer));

node_1 = asind(3.8316/(2*pi*f*trans_r/c_buffer));
node_2 = asind(7.0156/(2*pi*f*trans_r/c_buffer));
node_3 = asind(10.17/(2*pi*f*trans_r/c_buffer));
node_4 = asind(13.32/(2*pi*f*trans_r/c_buffer));

sidelobe1 = [node_1:1.5:node_2];
sidelobe2 = [node_2:1.5:node_3];
main_lobe = [0:2.5:node_1];
%angle_2 = [node_3:2.5:node_4]; %Change this to either sidelobes or only max
angle_2 = sidelobe1;


%%% Colors for plot %%%
b = [0 0.4470 0.7410];
o = [0.8500 0.3250 0.0980];
y = [0.9290 0.6940 0.1250];
p = [0.4940 0.1840 0.5560];
g = [0.4660 0.6740 0.1880];
lb = [0.3010 0.7450 0.9330];
r = [0.6350 0.0780 0.1840];
grey = [0.75 0.75 0.75];
vector_colors = {b,o,y,p,g,lb,r,b,o,y,p,g,lb,r,b,o,y,p,g,lb,r,b,o,y,p,g,lb,r};
%%%%%%%%%%%%%%%%%%%%%%%%%%

angle_1 = 90 - angle_2;

%create plot
figure, plot((Bufferwidth/2+(trans_r)),0,"b*")
hold on
xlabel("Width of box [m]")
ylabel("Length of box [m]")
title("Transducer radius [m]:",trans_r)
plot((Bufferwidth/2-(trans_r)),0,"b*")
yline(Bufferlength)
xline(Bufferwidth)
yline(Totallength)
xline(0)

%%%%%%% Calculating time for main lobe %%%%%%%%
t_mainbuffer = 2*Bufferlength/c_buffer;
t_mainsample = 2*Samplelength/c_sample;
t_main = t_mainbuffer + t_mainsample;


%%%%% The plotting %%%%%%%%%
for i = 1:length(angle_2)


    t2(i) = 0;
    t3(i) = 0;
    t_b(i) = 0;
    t_b1(i)  = 0;
    t_s(i)= 0;
    t_s1(i)= 0;
    t_s2(i) = 0;
    t_buffer_down(i) = 0;
    t_buffer_down_1(i) = 0;
    t_buffer_down_2(i) = 0;
    t_up_buffer(i)= 0;
    t_up_buffer_1(i)= 0;

    length_tr_1(i) = tand(angle_1(i))*Transducer_position;
    %%%%%%%%%%%%%%%%%%%%%%%%%%%%%%%%
    if length_tr_1(i) < Bufferlength %&& length_tr_1(i) > Bufferlength/2 % Reflects ...
        side wall in buffer from transducer above half-way point
        s_up_buffer(i) = Transducer_position/cosd(angle_1(i));
        t_up_buffer(i) = s_up_buffer(i)/c_buffer; %Time to first reflection
        length_r1(i) = length_tr_1(i); %Plot from transducer position to y = length_r1
        plot([Transducer_position,0],[0,length_r1(i)],"color",vector_colors{i})
        plot([Transducer_position, Bufferwidth], [0,length_r1(i)],"color",vector_colors{i})
        length_r2(i) = Bufferlength - length_r1(i);

        %Reflection with buffer/sample
        width_r1(i) = tand(angle_2(i))*length_r2(i); %plot where y = buffer/samle and x ...
            = width
        plot([0,width_r1(i)],[length_r1(i),Bufferlength],"color",vector_colors{i})
        plot([Bufferwidth,Bufferwidth-width_r1(i)],[length_r1(i),Bufferlength],...
        "color",vector_colors{i})
        s_up_buffer_1(i) = sqrt(length_r2(i)^2 + width_r1(i)^2);
        t_up_buffer_1(i) = s_up_buffer_1(i)/c_buffer;

        length_r3(i) = tand(angle_1(i))*(Bufferwidth-width_r1(i));

        %Propagation up into sample %%%%%%%%%%%%%%%%%%%%%
        %Snells law
```

```
110             snells_angle(i) = asind(sind(angle_2(i))*c_sample/c_buffer);
111             angle_3(i) = 90-snells_angle(i);
112
113             length_sample_1(i) = tand(angle_3(i))*(Bufferwidth-width_r1(i));
114
115             if length_sample_1(i) > Samplelength %Reflection right into Reflector
116                 length_above_buffer(i) = length_sample_1(i) - Samplelength;
117                 width_sample_1(i) = length_above_buffer(i)/tand(angle_3(i));
118                 s_s(i) = sqrt(Samplelength^2 + (Bufferwidth-width_r1(i) -width_sample_1(i)));
119                 t_s(i) = s_s(i)/c_sample;
120
121                 plot([width_r1(i), Bufferwidth-width_sample_1(i)],[Bufferlength, ...
                        Totallength],"color",vector_colors{i})
122                 plot([Bufferwidth-width_r1(i),width_sample_1(i)],[Bufferlength, ...
                        Totallength],"color",vector_colors{i})
123
124                 length_s1(i) = tand(angle_3(i))*width_sample_1(i);
125
126                 if length_s1(i) > Samplelength %Straight down again
127                     width_sample_2(i) = (length_s1(i) - Samplelength)/tand(angle_3(i));
128                     plot([Bufferwidth-width_sample_1(i), Bufferwidth - ...
                            width_sample_2(i)],[Totallength,Bufferlength],...
129                     "color",vector_colors{i})
130                     plot([width_sample_1(i), width_sample_2(i)],[Totallength,Bufferlength],...
131                     "color",vector_colors{i})
132                     s_s1(i) = s_s(i); %Length up = length down
133                     t_s1(i) = t_s(i);
134
135                     %Plot in buffer again:
136                     bufferlength_1(i) = tand(angle_1(i))*width_sample_2(i);
137
138                     if bufferlength_1(i) > Bufferlength %Straight down to transducer
139                         bufferwidth_1(i) = (bufferlength_1(i) - Bufferlength)/tand(angle_1(i));
140                         s_b(i) = sqrt(Bufferlength^2 + ...
                                (width_sample_2(i)-bufferwidth_1(i))^2 );
141                         t_b(i) = s_b(i)/c_buffer;
142
143                         plot([Bufferwidth - width_sample_2(i), ...
                                Bufferwidth-bufferwidth_1(i)],[Bufferlength, ...
                                0],"color",vector_colors{i})
144                         plot([width_sample_2(i), bufferwidth_1(i)],[Bufferlength, ...
                                0],"color",vector_colors{i})
145
146
147                     else %Reflection in sidewall
148                         s_b(i) = sqrt(bufferlength_1(i)^2 + width_sample_2(i)^2);
149                         t_b(i) = s_b(i)/c_buffer;
150                         plot([Bufferwidth - width_sample_2(i), Bufferwidth],[Bufferlength, ...
                                Bufferlength - bufferlength_1(i)],"color",vector_colors{i})
151                         plot([width_sample_2(i), 0],[Bufferlength, ...
                                Bufferlength-bufferlength_1(i)],"color",vector_colors{i})
152
153                         bufferwidth_1(i) = tand(angle_1(i))*(Bufferlength-bufferlength_1(i));
154                         if bufferwidth_1 > Bufferwidth %Reflection into next sidewall
155                             bufferlength_2(i) = ...
                                    (bufferwidth_1(i)-Bufferwidth)*tand(angle_2(i));
156                             s_b1(i) = sqrt(Bufferlength^2 + (bufferlength_1(i) - ...
                                    bufferlength_2(i))^2);
157                             t_b1(i) = s_b1(i)/c_buffer;
158
159                             plot([Bufferwidth,0],[ bufferlength_1(i), ...
                                    bufferlength_2(i)],"color",vector_colors{i})
160                             plot([0,Bufferwidth],[ bufferlength_1(i), ...
                                    bufferlength_2(i)],"color",vector_colors{i})
161
162                             bufferwidth_2(i) = tand(angle_2(i))*bufferlength_2(i);
163
164                             s_b2(i) = sqrt(bufferwidth_2(i)^2 + bufferlength_2(i)^2);
165                             t_b2(i) = s_b2(i)/c_buffer;
166
167                             plot([0, bufferwidth_2(i)],[bufferlength_2(i),0],...
168                             "color",vector_colors{i})
169                             plot([Bufferwidth, ...
                                    Bufferwidth-bufferwidth_2(i)],[bufferlength_2(i),0],...
170                             "color",vector_colors{i})
171
172
173                         else %Straigth down
174                             s_b1(i) = sqrt((Bufferlength-bufferlength_1(i))^2 + ...
                                    bufferwidth_1(i)^2);
175                             t_b1(i) = s_b1(i)/c_buffer;
176
177                             plot([Bufferwidth, Bufferwidth-bufferwidth_1(i)],...
178                             [Bufferlength-bufferlength_1(i), 0],"color",vector_colors{i})
179                             plot([0, bufferwidth_1(i)],[Bufferlength - bufferlength_1(i), ...
                                    0],"color",vector_colors{i})
180                         end
181
182                     end
183
184
185                 else %Reflection into right sidewall
186                     s_s1(i) = sqrt(width_sample_1(i)^2 + length_s1(i)^2);
187                     t_s1(i) = s_s1(i)/c_sample;
188                     plot([Bufferwidth-width_sample_1(i),Bufferwidth], ...
                            [Totallength,Totallength-length_s1(i)],"color",vector_colors{i})
189                     plot([width_sample_1(i), 0], ...
                            [Totallength,Totallength-length_s1(i)],"color",vector_colors{i})
190
191                     width_sample_2(i) = tand(snells_angle(i))*(Samplelength-length_s1(i));
192                     plot([Bufferwidth, ...
                            Bufferwidth-width_sample_2(i)],[Totallength-length_s1(i),...
193                     Bufferlength],"color",vector_colors{i})
194                     plot([0,width_sample_2(i)],[Totallength-length_s1(i),...
```

```
                Bufferlength],"color",vector_colors{i})

                s_s2(i) = sqrt(width_sample_2(i)^2 + (Samplelength-length_s1(i))^2);
                t_s2(i) = s_s2(i)/c_sample;

                %into buffer again
                bufferlength_1(i) = tand(angle_1(i))*(Bufferwidth-width_sample_2(i));

                if bufferlength_1(i) < Bufferlength %Reflection in sidewall
                    s_b(i) = sqrt((Bufferwidth-width_sample_2(i))^2 + bufferlength_1(i)^2);
                    t_b(i)= s_b(i)/c_buffer;

                    plot([Bufferwidth-width_sample_2(i), 0],[Bufferlength,Bufferlength ...
                        - bufferlength_1(i)],"color",vector_colors{i})
                    plot([width_sample_2(i), Bufferwidth],[Bufferlength,Bufferlength - ...
                        bufferlength_1(i)],"color",vector_colors{i})

                    bufferwidth_1(i) = tand(angle_2(i))*(Bufferlength-bufferlength_1(i));
                    s_b1(i)= sqrt(bufferwidth_1(i)^2 + (Bufferlength-bufferlength_1(i))^2);
                    t_b1(i) = s_b1(i)/c_buffer;

                    plot([0,bufferwidth_1(i)],[Bufferlength - ...
                        bufferlength_1(i),0],"color",vector_colors{i})
                    plot([Bufferwidth,Bufferwidth-bufferwidth_1(i)],[Bufferlength - ...
                        bufferlength_1(i),0],"color",vector_colors{i})


                else %Straight down
                    bufferwidth_1(i) = tand(angle_2(i))*Bufferlength;
                    s_b(i) = sqrt(Bufferlength^2 + bufferwidth_1(i)^2);
                    t_b(i) = s_b(i)/c_buffer;
                    plot([Bufferwidth-width_sample_2(i),...
                    (Bufferwidth-bufferwidth_1(i)-width_sample_2(i))],...
                    [Bufferlength,0],"color",vector_colors{i})
                    plot([width_sample_2(i),bufferwidth_1(i)+ ...
                        width_sample_2(i)],[Bufferlength,0],"color",vector_colors{i})

                end

            end

        else %Reflection into right sidewall inside sample
            s_s(i) = sqrt(length_sample_1(i)^2 + (Bufferwidth- width_r1(i))^2);
            t_s(i) = s_s(i)/c_sample;
            plot([width_r1(i), Bufferwidth],[Bufferlength,Bufferlength + ...
                length_sample_1(i)], "color",vector_colors{i})
            plot([Bufferwidth-width_r1(i), 0],[Bufferlength,Bufferlength + ...
                length_sample_1(i)],"color",vector_colors{i})

            width_r2(i) = tand(snells_angle(i))*(Samplelength-length_sample_1(i));
            s_s1(i) = sqrt(width_r2(i)^2 + (Samplelength-length_sample_1(i))^2);
            t_s1(i) = s_s1(i)/c_sample;
            plot([Bufferwidth, Bufferwidth - width_r2(i)],[Bufferlength + ...
                length_sample_1(i), Totallength] ,"color",vector_colors{i})
            plot([0, width_r2(i)],[Bufferlength + length_sample_1(i), ...
                Totallength],"color",vector_colors{i})

            length_sample_2(i) = tand(angle_3(i))*(Bufferwidth- width_r2(i));

            if length_sample_2 > Samplelength %Straight down to buffer-sample-interface
                length_into_buffer(i) = length_sample_2(i) - Samplelength;
                width_sample_3(i) = length_into_buffer(i)/tand(angle_3(i));

                plot([Bufferwidth - width_r2(i), width_sample_3(i)], [Totallength, ...
                    Bufferlength],"color",vector_colors{i})
                plot([width_r2(i), Bufferwidth -width_sample_3(i)],[Totallength, ...
                    Bufferlength],"color",vector_colors{i})
                s_s2(i) = sqrt(Samplelength^2 + (Bufferwidth - ...
                    width_sample_3(i)-width_r2(i))^2);
                t_s2(i) = s_s2(i)/c_sample;

                length_buffer(i) = tand(angle_1(i))*width_sample_3(i);

                %%Into buffer again
                if length_buffer(i) > Bufferlength %Staight down to transducer again
                    bufferwidth_1(i) = (length_buffer(i)-Bufferlength)/tand(angle_1(i));
                    s_b(i) = sqrt(Bufferlength^2 + (width_sample_3(i) - ...
                        bufferwidth_1(i))^2);
                    t_b(i) = s_b(i)/c_buffer;

                    plot([width_sample_3(i), bufferwidth_1(i)],[Bufferlength, ...
                        0],"color",vector_colors{i})
                    plot([Bufferwidth-width_sample_3(i), ...
                        Bufferwidth-bufferwidth_1(i)],[Bufferlength, ...
                        0],"color",vector_colors{i})
                else
                    s_b(i) = sqrt(length_buffer(i)^2 + width_sample_3(i)^2 );
                    t_b(i) = s_b(i)/c_buffer;

                    plot([width_sample_3(i),0], [Bufferlength, ...
                        Bufferlength-length_buffer(i)],"color",vector_colors{i})
                    plot([Bufferwidth-width_sample_3(i),Bufferwidth], [Bufferlength, ...
                        Bufferlength-length_buffer(i)],"color",vector_colors{i})

                    bufferwidth_1(i)= tand(angle_1(i))*(Bufferlength-length_buffer(i));
                    s_b1(i) = sqrt(bufferwidth_1(i)^2 + (Bufferlength-length_buffer(i))^2);
                    t_b1(i) = s_b1(i)/c_buffer;

                    plot([0,bufferwidth_1(i)],[Bufferlength-length_buffer(i),0],...
                    "color",vector_colors{i})
                    plot([Bufferwidth,bufferwidth-bufferwidth_1(i)],...
                    [Bufferlength-length_buffer(i),0],...
                    "color",vector_colors{i})
```

```
281                 end
282
283             else %Reflection into left sidewall inside sample
284                 s_s2(i)= sqrt(length_sample_2(i)^2 + (Bufferwidth-width_r2(i))^2);
285                 t_s2(i) = s_s2(i)/c_sample;
286                 plot([Bufferwidth - width_r2(i), 0],[Totallength, ...
                        Totallength-length_sample_2(i)],"color",vector_colors{i})
287                 plot([width_r2(i), Bufferwidth],[Totallength, ...
                        Totallength-length_sample_2(i)],"color",vector_colors{i})
288
289                 width_sample_3(i) = ...
                        tand(snells_angle(i))*(Samplelength-length_sample_2(i));
290
291                 s_s3(i) = sqrt(width_sample_3(i)^2 + (Samplelength-length_sample_2(i))^2);
292                 t_s3(i) = s_s3(i)/c_sample;
293
294                 plot([0,  width_sample_3(i)],[ Totallength-length_sample_2(i), ...
                        Bufferlength],"color",vector_colors{i})
295                 plot([Bufferwidth, Bufferwidth-width_sample_3(i)],[ ...
                        Totallength-length_sample_2(i), Bufferlength],"color",vector_colors{i})
296
297                 %%%%% Propagation into buffer again
298
299                 length_buffer(i) = tand(angle_1(i))*(Bufferwidth-width_sample_3(i));
300
301                 if length_buffer(i) > Bufferlength %Propagation right back to ...
                        transducer, 4A12
302                     bufferwidth_1(i) = tand(angle_2(i))*Bufferlength;
303
304                     s_b(i) = sqrt(bufferwidth_1(i)^2 + Bufferlength^2);
305                     t_b(i) = s_b(i)/c_buffer;
306
307                     plot([width_sample_3(i), width_sample_3(i)+ bufferwidth_1(i)], ...
                            [Bufferlength,0],"color",vector_colors{i})
308                     plot([Bufferwidth-width_sample_3(i), ...
                            Bufferwidth-(width_sample_3(i)+ bufferwidth_1(i))], ...
                            [Bufferlength,0],"color",vector_colors{i})
309
310                 else %reflecton in side walls
311                     s_b(i) = sqrt((Bufferwidth-width_sample_3(i))^2 + ...
                            (length_buffer(i))^2);
312                     t_b(i) = s_b(i)/c_buffer;
313
314                     plot([width_sample_3(i), Bufferwidth],[Bufferlength, ...
                            Bufferlength-length_buffer(i)],"color",vector_colors{i})
315                     plot([Bufferwidth-width_sample_3(i), 0],[Bufferlength, ...
                            Bufferlength-length_buffer(i)],"color",vector_colors{i} )
316
317                     bufferwidth_1(i) = tand(angle_2(i))*(Bufferlength-length_buffer(i));
318                     s_b1(i) = sqrt(bufferwidth_1(i)^2 ...
                            +(Bufferlength-length_buffer(i))^2 );
319                     t_b1(i) = s_b1(i)/c_buffer;
320
321                     plot([ Bufferwidth, Bufferwidth- ...
                            bufferwidth_1(i)],[Bufferlength-length_buffer(i),0],...
322                     "color",vector_colors{i})
323                     plot([ 0, bufferwidth_1(i)],[Bufferlength-length_buffer(i),0],...
324                     "color",vector_colors{i})
325
326
327                 end
328
329             end
330         end
331         %%%%%%% inside buffer %%%%%%%%%%%%%
332         if length_r3(i) < Bufferlength %Reflects into the sidewall
333
334             length_r4(i) = length_r3(i); %Plot: x = Bufferwidth, y = length_r4
335             plot([width_r1(i),Bufferwidth],[Bufferlength, ...
                    Bufferlength-length_r4(i)],"color",vector_colors{i})
336             plot([Bufferwidth-width_r1(i),0],[Bufferlength, ...
                    Bufferlength-length_r4(i)],"color",vector_colors{i})
337             width_r2(i) = tand(angle_1(i))*(Bufferlength - length_r4(i));
338             s_buffer_down(i) = length_r4(i)/sind(angle_2(i));
339             t_buffer_down(i) = s_buffer_down(i)/c_buffer;
340             %%%%%%%%%%%%%%
341             if width_r2 > Bufferwidth %Reflects into sidewall on other side
342                 length_r5(i) = (width_r2(i) - Bufferwidth(i))/tand(angle_2(i)); %Plot y ...
                        = length_r5, x = 0
343                 plot([Bufferwidth, 0],[Bufferlength-length_r4(i),length_r5(i)],...
344                 "color",vector_colors{i})
345                 plot([0, Bufferwidth],[Bufferlength- ...
                        length_r4(i),length_r5(i)],"color",vector_colors{i})
346                 s_buffer_down_1(i) = Bufferwidth/sind(angle_2(i));
347                 t_buffer_down_1(i) = s_buffer_down_1(i)/c_buffer;
348
349                 %Reflects to transducer
350                 width_r3(i) = tand(angle_1(i))*length_r5(i);
351                 s_buffer_down_2(i) = sqrt(length_r5(i)^2 + width_r3(i)^2);
352                 t_buffer_down_2(i) = s_buffer_down_2(i)/c_buffer;
353
354             else
355                 width_r3(i) = Bufferwidth - width_r2(i); %Back at transducer, y = 0, x ...
                        = width_r3
356                 plot([Bufferwidth, width_r3(i)],[Bufferlength-length_r4(i),0],...
357                 "color",vector_colors{i})
358                 plot([0, Bufferwidth-width_r3(i)],[Bufferlength-length_r4(i),0],...
359                 "color",vector_colors{i})
360                 s_buffer_down_3(i) = width_r3(i)/sind(angle_2(i));
361                 t_buffer_down_3(i) = s_buffer_down_3(i)/c_buffer;
362             end
363             %%%%%%%%%%%%%%
364         else
```

```
365             length_r4(i) = length_r3(i)- Bufferlength;
366             width_r3(i) = length_r4(i)/tand(angle_1(i));
367             width_r4(i) = Bufferwidth - width_r3(i); %Plot y = 0, x = width_r4
368             plot([width_r1(i),width_r4(i)],[Bufferlength,0],"color",vector_colors{i})
369             plot([Bufferwidth-width_r1(i),Bufferwidth-width_r4(i)],...
370             [Bufferlength,0],"color",vector_colors{i})
371             s_buffer_down_2(i)= Bufferlength/sind(angle_1(i));
372             t_buffer_down_2(i) = s_buffer_down_2(i)/c_buffer;
373
374
375         end
376     %%%%%%%%%%%%%%%%%%%%%%%%%%%%%%%
377     elseif length_tr_1(i) < Bufferlength && length_tr_1(i) < Bufferlength/2 %Reflects ...
            side wall in buffer under halv the length of buffer
378         %Not implemented as this has not been the applicable to the project
379
380     %%%%%%%%%%%%%%%%%%%%%%%%%%%%%%%
381     else %Straight up into buffer/sample
382         width_a1(i) = (length_tr_1(i) - Bufferlength)/tand(angle_1(i)) ;
383         plot([Transducer_position, width_a1(i)], [0,Bufferlength],"color",vector_colors{i})
384         plot([Transducer_position, ...
                Bufferwidth-width_a1(i)],[0,Bufferlength],"color",vector_colors{i})
385         s_up_buffer(i)= Bufferlength/sind(angle_1(i));
386         t_up_buffer(i) = s_up_buffer(i)/c_buffer;
387         length_a2(i) = tand(angle_1(i))*width_a1(i);
388
389         %Propagation into sample%%%
390         snells_angle(i) = asind(sind(angle_2(i))*c_sample/c_buffer);
391         angle_3(i) = 90-snells_angle(i);
392
393         length_sample_1(i) = tand(angle_3(i))*width_a1(i);
394
395         if length_sample_1(i) > Samplelength %Straight into reflector
396             length_above_sample(i) = length_sample_1(i) - Samplelength;
397             width_sample_1(i) = length_above_sample(i)/tand(angle_3(i));
398             s_s(i)= sqrt(Samplelength^2 + (width_a1(i)-width_sample_1(i))^2);
399             t_s(i)= s_s(i)/c_sample;
400
401             plot([width_a1(i), width_sample_1(i)], [Bufferlength, ...
                    Totallength],"color",vector_colors{i})
402             plot([Bufferwidth-width_a1(i), Bufferwidth-width_sample_1(i)], ...
                    [Bufferlength, Totallength],"color",vector_colors{i})
403
404             length_sample_2(i) = tand(angle_3(i))*width_sample_1(i);
405
406             if length_sample_2(i) > Samplelength %Straight down again
407                 s_s1(i) = s_s(i);
408                 t_s1(i) = t_s(i);
409
410                 widthdiff(i) = width_sample_1(i) - (width_a1(i)-width_sample_1(i));
411                 plot([width_sample_1(i),widthdiff(i)],[Totallength, ...
                        Bufferlength],"color",vector_colors{i})
412                 plot([Bufferwidth-width_sample_1(i),Bufferwidth-widthdiff(i)],...
413                 [Totallength, Bufferlength],"color",vector_colors{i})
414
415                 widthdiff(i) = width_sample_1(i) - (width_a1(i)-width_sample_1(i));
416                 bufferlength_1(i) = tand(angle_1(i))*widthdiff(i);
417
418                 %%%Propagation back into buffer
419
420                 if bufferlength_1(i) > Bufferlength %Propagation straight down to ...
                        transducer
421                     bufferwidth_1(i) = tand(angle_2(i))*Bufferlength;
422                     s_b(i) = sqrt(bufferwidth_1(i)^2 + Bufferlength^2);
423                     t_b(i) = s_b(i)/c_buffer;
424
425                     plot([widthdiff(i), (widthdiff(i) - ...
                            bufferwidth_1(i))],[Bufferlength,0],"color",vector_colors{i})
426                     plot([Bufferwidth-widthdiff(i), ...
                            Bufferwidth-(widthdiff(i)-bufferwidth_1(i))],...
427                     [Bufferlength,0],"color",vector_colors{i})
428
429                 else %Propagation into side wall
430                   s_b(i) = sqrt(widthdiff(i)^2 + bufferlength_1(i)^2);
431                   t_b(i) = s_b(i)/c_buffer;
432
433                   plot([widthdiff(i),0],...
434                   [Bufferlength,Bufferlength-bufferlength_1(i)],"color",...
435                   vector_colors{i})
436                   plot([Bufferwidth-widthdiff(i),Bufferwidth],...
437                   [Bufferlength,Bufferlength-bufferlength_1(i)],"color",...
438                   vector_colors{i})
439
440                   bufferwidth_1(i) = tand(angle_2(i))*(Bufferlength-bufferlength_1(i));
441                   s_b1(i) = sqrt(bufferwidth_1(i) + (Bufferlength-bufferlength_1(i))^2);
442                   t_b1(i) = s_b1(i)/c_buffer;
443
444                   plot([0,bufferwidth_1(i)], [(Bufferlength-bufferlength_1(i)), ...
                          0],"color",vector_colors{i})
445                   plot([Bufferwidth,Bufferwidth-bufferwidth_1(i)], ...
                          [(Bufferlength-bufferlength_1(i)), 0],"color",vector_colors{i})
446
447                 end
448
449             else %Reflection in sidewall
450                 s_s1(i) = sqrt(width_sample_1(i)^2 + length_sample_2(i)^2);
451                 t_s1(i) = s_s1(i)/c_sample;
452                 plot([width_sample_1(i), 0], [Totallength, ...
                        Totallength-length_sample_2(i)],"color",vector_colors{i})
453                 plot([Bufferwidth-width_sample_1(i), Bufferwidth], [Totallength, ...
                        Totallength-length_sample_2(i)],"color",vector_colors{i})
454
```

```
455                 width_sample_2(i) = tand(snells_angle(i))*(Samplelength - ...
                        length_sample_2(i) );
456                 s_s2(i) = sqrt(width_sample_2(i)^2 + (Samplelength - length_sample_2(i) ...
                        )^2);
457                 t_s2(i) = s_s2(i)/c_sample;
458
459                 plot([0, width_sample_2(i)], [Totallength-length_sample_2(i), ...
                        Bufferlength],"color",vector_colors{i})
460                 plot([Bufferwidth, Bufferwidth-width_sample_2(i)], ...
                        [Totallength-length_sample_2(i), ...
                        Bufferlength],"color",vector_colors{i})
461
462                 %%%% Propagation back into buffer
463                 bufferlength_1(i) = tand(angle_1(i))*(Bufferwidth-width_sample_2(i));
464
465                 if bufferlength_1(i) > Bufferlength %Propagation straight down
466
467                     bufferwidth_1(i) = tand(angle_2(i))*Bufferlength;
468                     s_b(i) = sqrt(bufferwidth_1(i)^2 + Bufferlength^2);
469                     t_b(i) = s_b(i)/c_buffer;
470
471                     plot([width_sample_2(i), ...
                            width_sample_2(i)+bufferwidth_1(i)],[Bufferlength,0],...
472                     "color",vector_colors{i})
473                     plot([Bufferwidth-width_sample_2(i),Bufferwidth- ...
                            width_sample_2(i)-bufferwidth_1(i)],[Bufferlength,0],...
474                     "color",vector_colors{i})
475
476                 else
477                     s_b(i) = sqrt(bufferlength_1(i)^2 + (Bufferlength-width_sample(i))^2);
478                     t_b(i) = s_b(i)/c_buffer;
479
480                     plot([width_sample_2(i),Bufferwidth],...
481                     [Bufferlength,Bufferlength-bufferlength_1(i)],...
482                     "color",vector_colors{i})
483                     plot([Bufferwidth-width_sample_2(i),0],...
484                     [Bufferlength,Bufferlength-bufferlength_1(i)],...
485                     "color",vector_colors{i})
486
487                     bufferwidth_2(i) = tand(angle_2(i))*(Bufferlength-bufferlength_1);
488                     s_b1(i) = sqrt(bufferwidth_2(i)^2 + (Bufferlength-bufferlength_1)^2);
489                     t_b1(i) = s_b1(i)/c_buffer;
490
491                     plot([Bufferwidth, Bufferwidth-bufferwidth_2(i)],...
492                     [Bufferlength-bufferlength_1(i),0],"color",vector_colors{i})
493                     plot([0, bufferwidth_2(i)],...
494                     [Bufferlength-bufferlength_1(i),0],"color",vector_colors{i})
495                 end
496             end
497
498         else
499             s_s(i) = sqrt(length_sample_1(i)^2 + width_a1(i)^2);
500             t_s(i) = s_s(i)/c_sample;
501
502             plot([width_a1(i), 0], [Bufferlength, Bufferlength + length_sample_1(i)], ...
                    "color",vector_colors{i})
503             plot([Bufferwidth-width_a1(i), Bufferwidth], [Bufferlength, Bufferlength + ...
                    length_sample_1(i)], "color",vector_colors{i})
504
505             width_s1(i) = tand(snells_angle(i)*(Samplelength - length_sample_1(i)));
506             s_s1(i) = sqrt(width_s1(i)^2 + (Samplelength-length_sample_1(i))^2)
507             t_s1(i) = s_s1(i)/c_sample;
508
509             plot([0,width_s1(i)],[Bufferlength + length_sample_1(i),Totallength], ...
                    "color", vector_colors{i})
510             plot([Bufferwidth,Bufferwidth- width_s1(i)],[Bufferlength + ...
                    length_sample_1(i),Totallength], "color", vector_colors{i})
511
512             width_s2(i) = tand(snells_angle(i))*Samplelength;
513             s_s2(i) = sqrt(width_s2(i)^2 + Samplelength^2)
514             t_s2(i) = s_s2(i)/c_sample;
515
516             plot([width_s1(i), width_s1(i) + width_s2(i)],[Totallength, Bufferlength], ...
                    "color",vector_colors{i})
517             plot([Bufferwidth-width_s1(i),Bufferwidth - ( width_s1(i) + ...
                    width_s2(i))],[Totallength, Bufferlength], "color",vector_colors{i})
518
519             %%%% Back into buffer
520
521             width_a2(i) = tand(angle_2(i))*Bufferlength;
522             s_b(i) = sqrt(width_a2(i)^2 + Bufferlength^2);
523             t_b(i) = s_b(i)/c_buffer;
524
525             plot([width_s1(i) + width_s2(i), width_s1(i) + width_s2(i) + width_a2(i)], ...
                    [Bufferlength, 0], "color",vector_colors{i})
526             plot([Bufferwidth-(width_s1(i) + width_s2(i)), Bufferwidth-(width_s1(i) + ...
                    width_s2(i) + width_a2(i))], [Bufferlength, 0], "color",vector_colors{i})
527
528         end
529
530         %%%%%%%
531         if length_a2(i) < Bufferlength %Reflection into sidewall to the left
532             s_buffer_down(i) = sqrt(length_a2(i)^2 + width_a1(i)^2);
533             t_buffer_down(i) = s_buffer_down(i)/c_buffer;
534             length_a3(i) = Bufferlength - length_a2(i);
535             plot([width_a1(i),0],[Bufferlength, length_a3(i)],"color",vector_colors{i})
536             plot([Bufferwidth-width_a1(i),Bufferwidth],[Bufferlength, ...
                    length_a3(i)],"color",vector_colors{i})
537             length_a4(i) = Bufferlength-length_a2(i);
538             width_a2(i) = tand(angle_2(i))*length_a4(i);
539             %%%
540             if width_a2(i) > Bufferwidth %Reflection in sidewall to the right
541                 length_a5(i) = (width_a2(i) - Bufferwidth)/tand(angle_2(i));
```

```
                plot([0,Bufferwidth], [length_a3(i),length_a5(i)],"color",vector_colors{i})
                plot([Bufferwidth,0], [length_a3(i),length_a5(i)],"color",vector_colors{i})
                s_buffer_down_1(i) = sqrt(Bufferwidth^2 + (length_a3(i)- length_a5(i)^2));
                t_buffer_down_1(i) = s_buffer_down_1(i)/c_buffer;

                width_a3(i) = tand(angle_2(i))*length_a5(i);
                width_a4(i) = Bufferwidth - width_a3(i);
                plot([Bufferwidth,width_a4(i)],[length_a5(i),0],...
                "color",vector_colors{i})
                plot([0,Bufferwidth-width_a4(i)],[length_a5(i),0],...
                "color",vector_colors{i})
                s_buffer_down_2(i) = sqrt(width_a3(i)^2 + length_a5(i)^2);
                t_buffer_down_2(i) = s_buffer_down_2(i)/c_buffer;


            else %Reflection straigth down to transducer
                width_a3(i) = width_a2(i); %Plotting y = 0, x = width_a3
                plot([0,width_a3(i)],[length_a3(i),0],...
                "color",vector_colors{i})
                plot([Bufferwidth,Bufferwidth-width_a3(i)],[length_a3(i),0],...
                "color",vector_colors{i})
                s_buffer_down_1(i)= width_a3(i)/sind(angle_2(i));
                t_buffer_down_1(i) = s_buffer_down_1(i)/c_buffer;

            end
            %%%

        else %Reflection straight down again
            s_buffer_down(i) = s_up_buffer(i);
            t_buffer_down(i)= t_up_buffer(i);
            width_a2(i) = width_a1(i) - sqrt(s_buffer_down(i)^2-Bufferlength^2); %Plot ...
                y = 0, x = width_a2
            plot([width_a1(i),width_a2(i)],[Bufferlength, 0],"color",vector_colors{i})
            plot([Bufferwidth-width_a1(i),Bufferwidth-width_a2(i)],...
            [Bufferlength, 0],"color",vector_colors{i})
        end
        %%%%%%%
    end


    %%%% Calculating time
    %Two-way signal
    total_time_large(i) = t_up_buffer(i)+ t_up_buffer_1(i) + t2(i) + t3(i) + t_b(i) + ...
        t_b1(i) + t_s(i) + t_s1(i) + t_s2(i);
    t_diff(i) = total_time_large(i) - t_main;

    %One-way signal
    total_time_small(i) = t_up_buffer(i)+ t_up_buffer_1(i) + ...
        t_buffer_down(i)+t_buffer_down_1(i) + t_buffer_down_2(i);
    t_diff_small(i) = total_time_small(i) - t_mainbuffer;

end
```

D.4 Numerical analysis of noise

numerical_analysis_noise.m

```
%Numerical analysis, coherent noise
clear all
omega = 2*pi*500000;
t = 4e-4:1e-7:6e-4;
vector = linspace(0,180,5000); %Phase difference from 0 to 180 degrees
phi = vector*2*pi/180;

%A = 3.1622766; %10dB
%A = 10; %20 dB
%A = 31.62277; %30dB
A = 100; %40dB
%A = 125.892541;%42dB
%A = 316.2277; %50dB
%A = 1000; %60dB
%A_vector = [3.1622766,10,31.62277,100, 316.2277, 1000];

B = 1;
SignalB =A*sin(omega.*t);

for i = 1:length(phi)
   Buffer(:,i)= B.*sin(omega.*t + phi(i));
   C(i) = A.*sqrt(1 + (B/A)^2 + 2*(B/A).*cos(phi(i)));
   angle(i) = atan(((B/A).*sin(phi(i)))/(1 + (B/A).*cos(phi(i))));%Radians
   time(i) = angle(i)/omega;
   angledegrees(i) = angle(i)*180/(pi); %Degrees
   ratio(i) =20*log10(C(i)/A);
end

standard_angle = std(angledegrees)
standard_ratio = std(ratio)
standard_noise = standard_angle/(360*500000)

figure, plot(vector, angleplot)
```

```
title("Angle")
figure,plot(vector,ratio)
title("SNR")
figure, plot(vector, time)
title("time")
```

D.5 Diffraction correction

Diffraction_correction_Khimunin.m

```
%Numerical analysis of the diffraction correction
%Using Khimunins diffraction correction method
%The integration is carried out using the Simpsons integration method

ka = [10,15,20,25,30,40,60,100,200,400,1000];
n = 100000;
theta = (0:pi/n:pi/2);

S1 = (0.05:0.05:1);
S2 = (1.1:0.1:3);
S3 = (3.5:0.5:10);

S = [S1,S2,S3];

a = 10; %radius [mm], following Khimunin
k = [1.0053,1.5079,2.0106,2.5133, 3.0159, 4.0212, 6.0319, 10.053,20.106,40.212, ...
    100.53]; %The exact wave number values
for j = 1:length(S)
    for m = 1:length(k)
        %Calculating z by using the equation S = z*lambda/a^2 = z*2pi/ka^2
        z(j,m) = (S(j)*k(m)*a^2/(2*pi));
        for n = 1:length(theta)

            C(j,m,n)= cos(k(m)*sqrt((z(j,m))^2 + ...
                4*a^2*(cos(theta(n))^2)))*(sin(theta(n)))^2;
            D(j,m,n)= sin(k(m)*sqrt((z(j,m))^2 + ...
                4*a^2*(cos(theta(n))^2)))*(sin(theta(n)))^2;

            h_diff(j,m,n) = exp(-1i*k(m)*z(j,m)*((sqrt(1+4*(a/z(j,m))^2*...
            (cos(theta(n)))^2))-1))*(sin(theta(n)))^2;


        end
        C_integral_sum(j,m) = ((C(j,m,1))+ 2*sum(C(j,m,(3:2:end-2)))+ ...
            4*sum(C(j,m,(2:2:end)))...
            + C(j,m,length(theta)))*theta(2)/3; %Simpsons integration
        D_integral_sum(j,m) = ((D(j,m,1))+ 2*sum(D(j,m,(3:2:end-2)))+ ...
            4*sum(D(j,m,(2:2:end)))+...
            D(j,m,length(theta)))*theta(2)/3; %Simpsons integration

        A(j,m) = 1- C_integral_sum(j,m)*(4/pi)*cos(k(m)*z(j,m))-...
        D_integral_sum(j,m)*(4/pi)*sin(k(m)*z(j,m));
        B(j,m) = D_integral_sum(j,m)*(4/pi)*cos(k(m)*z(j,m))-...
        C_integral_sum(j,m)*(4/pi)*sin(k(m)*z(j,m));

        Diff_abs(j,m) = sqrt((A(j,m))^2 + (B(j,m))^2);
        phase(j,m) = atan(B(j,m)/A(j,m));

        H_diff(j,m) = 1 - 4/pi*((2*sum(h_diff(j,m,(3:2:end-2))) + ...
            4*sum(h_diff(j,m,2:2:end)) ...
            + h_diff(j,m,1) + h_diff(j,m,length(theta)))*theta(2)/3);

    end


end
Dne2 = abs(H_diff);
Difference = abs(Dne2 - Diff_abs);

angle1 = angle(H_diff);
Difference_angle = abs(angle1-phase);
```